Computing Rates and Distributions of Rock Recovery in Subduction Zones

Buchanan C Kerswell[1], Matthew J Kohn[2], and Taras V. Gerya[3]

[1]Miami University
[2]Boise State University
[3]Swiss Federal Institute of Technology (ETH-Zurich)

December 21, 2022

Abstract

Bodies of rock that are detached (recovered) from subducting oceanic plates, and exhumed to Earth's surface, become invaluable records of the mechanical and chemical processing of rock along subduction interfaces. Exposures of interface rocks with high-pressure (HP) mineral assemblages provide insights into the nature of rock recovery, yet various interpretations concerning thermal gradients, recovery rates, and recovery depths arise when directly comparing the rock record with numerical simulations of subduction. Constraining recovery rates and depths from the rock record presents a major challenge because small sample sizes of HP rocks makes statistical inference weak. As an alternative approach, this study implements numerical simulations of oceanic-continental convergence and applies a classification algorithm to identify rock recovery. Over one million markers are classified from 64 simulations representing a large range of subduction zones. We find recovery P's (depths) correlate strongly with convergence velocity and moderately with oceanic plate age, while PT gradients correlate strongly with oceanic plate age and upper-plate thickness. Recovery rates strongly correlate with upper-plate thickness, yet show no correlation with other boundary conditions. Likewise, PT distributions of recovered markers vary among numerical experiments and generally show poor overlap with the rock record. A significant gap in predicted marker recovery is found near 2 GPa and 550 @C, coinciding with the highest density of exhumed HP rocks. Implications for such a gap in marker recovery include numerical modeling uncertainties, petrologic uncertainties, selective sampling of exhumed HP rocks, or natural geodynamic factors not accounted for in numerical experiments.

Computing Rates and Distributions of Rock Recovery in Subduction Zones

Buchanan C. Kerswell [1] Matthew J. Kohn [2] Taras V. Gerya [3]

[1] Department of Geology & Environmental Earth Science, Miami University, Oxford, OH 45056

[2] Department of Geosicences, Boise State University, Boise, ID 83725

[3] Department of Earth Sciences, ETH-Zurich, Sonneggstrasse 5, Zurich 8092, Switzerland

Key Points:

- Simulated rocks detach at depths consistent with major mechanical transitions along subduction interfaces
- Simulated rock PT distributions and recovery rates correlate with boundary conditions
- Few simulated rocks detach from the PT region of highest natural sample density

Corresponding author: Buchanan C. Kerswell, `buchanankerswell@u.boisestate.edu`

Abstract

Bodies of rock that are detached (recovered) from subducting oceanic plates, and exhumed to Earth's surface, become invaluable records of the mechanical and chemical processing of rock along subduction interfaces. Exposures of interface rocks with high-pressure (HP) mineral assemblages provide insights into the nature of rock recovery, yet various interpretations concerning thermal gradients, recovery rates, and recovery depths arise when directly comparing the rock record with numerical simulations of subduction. Constraining recovery rates and depths from the rock record presents a major challenge because small sample sizes of HP rocks makes statistical inference weak. As an alternative approach, this study implements numerical simulations of oceanic-continental convergence and applies a classification algorithm to identify rock recovery. Over one million markers are classified from 64 simulations representing a large range of subduction zones. We find recovery P's (depths) correlate strongly with convergence velocity and moderately with oceanic plate age, while PT gradients correlate strongly with oceanic plate age and upper-plate thickness. Recovery rates strongly correlate with upper-plate thickness, yet show no correlation with other boundary conditions. Likewise, PT distributions of recovered markers vary among numerical experiments and generally show poor overlap with the rock record. A significant gap in predicted marker recovery is found near 2 GPa and 550 °C, coinciding with the highest density of exhumed HP rocks. Implications for such a gap in marker recovery include numerical modeling uncertainties, petrologic uncertainties, selective sampling of exhumed HP rocks, or natural geodynamic factors not accounted for in numerical experiments.

Plain language summary

Converging tectonic plates leads to subduction of the denser plate beneath the other. Bodies of subducted rock that return to Earth's surface bring information about the deep subduction interface, yet the rates, depths, and mechanisms that detach rock from the subducting plate are not well-understood. As an alternative to studying rock samples, this study implements a machine learning algorithm to identify rock detachment in numerical simulations. Over one million simulated rocks are classified from 64 simulations representing a large range of possible subduction zones. Marker pressure-temperature (PT) conditions are compared across models and with the rock record. Correlations are drawn among important model parameters, including plate velocities and plate thickness, that reveal strong and weak effects on marker detachment. Recovery rates strongly correlate with upper-plate thickness, yet show no correlation with other parameters. Likewise, PT distributions of markers show variable compatibility with the rock record depending on the comparison. A significant gap marker recovery coincides with a large proportion of exhumed HP rocks. Implications for such a gap in marker recovery include numerical modeling uncertainties, petrologic uncertainties, selective sampling of exhumed HP rocks, or natural geodynamic factors not accounted for in numerical experiments.

1 Introduction

Maximum pressure-temperature (PT) conditions have been estimated for hundreds of high-pressure (HP) metamorphic rocks exhumed from subduction zones (Figure 1, Agard et al., 2018; Hacker, 1996; Penniston-Dorland et al., 2015). These samples represent fragments of oceanic crust, continental crust, seafloor sediments, and upper mantle that have detached from subducting oceanic and continental lithospheres at various depths along the interface between subducting and overriding tectonic plates (referred to as "recovery" after Agard et al. (2018). This *rock record* is the only tangible evidence of PT-strain fields, deep seismic cycling, and fluid flow within Earth's lithosphere during deformation and chemical processing in subduction zones. Together with geophysical imaging (e.g. Bostock, 2013; Ferris et al., 2003; Hyndman & Peacock, 2003; Mann et al., 2022; Naif et al., 2015; Rondenay et al., 2008; Syracuse & Abers, 2006), analysis of surface heat flow data (e.g. Currie & Hyndman, 2006; Gao & Wang, 2014; Hyndman et al., 2005; Kohn et al., 2018; Morishige & Kuwatani, 2020; Wada & Wang, 2009), and forward numerical geodynamic modeling (e.g. Gerya et al., 2002, 2008; Gerya & Stöckhert, 2006; Hacker et al., 2003; Kerswell et al., 2021; McKenzie, 1969; Peacock, 1990, 1996; Sizova et al., 2010; Syracuse et al., 2010; Yamato et al., 2007, 2008), investigation of the rock record underpins contemporary understandings of subduction geodynamics (e.g. Agard et al., 2009; Agard, 2021; Bebout, 2007).

However, it remains difficult to directly interpret the rock record in terms of recovery rates and distributions along the subduction interface. For example, compilations of PT estimates representing the global distribution of HP rocks exhumed during the Phanerozoic (the pd15 and ag18 datasets, Agard et al., 2018; Penniston-Dorland et al., 2015) reveal an abrupt decrease in relative sample abundance at P's above 2.3-2.4 GPa (Figure 1). For pd15 and ag18, a nearly-constant cumulative distribution (CDF) curve interrupted

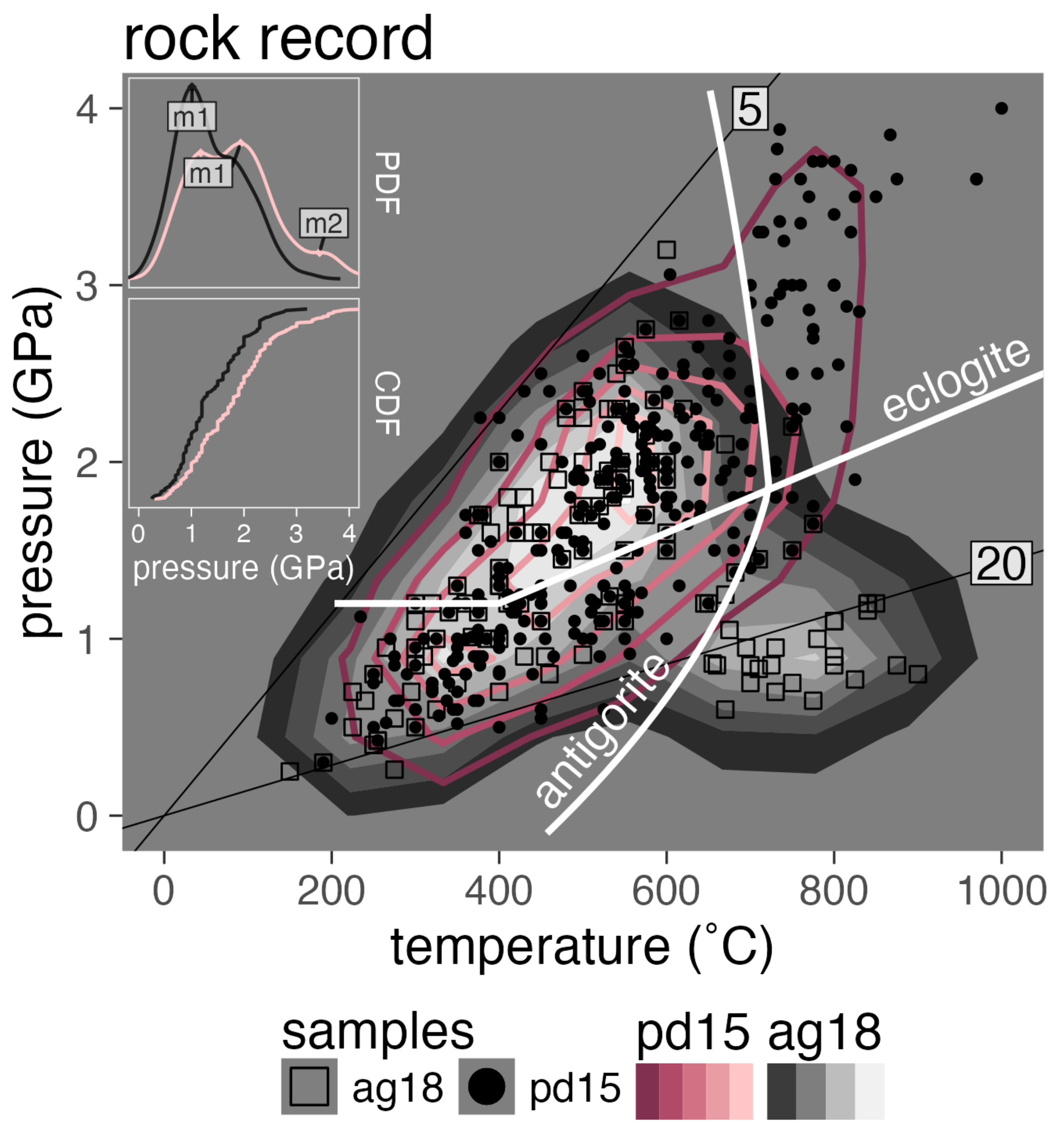

Figure 1: PT diagram showing distributions of PT estimates for exhumed HP metamorphic rock samples compiled in the pd15 (solid contours, Penniston-Dorland et al., 2015) and ag18 (filled contours, Agard et al., 2018) datasets. (insets) Probability distribution diagrams of pd15 and ag18 samples showing broad bimodal and trimodal sample distributions with respect to P (top inset) and a kinked CDF (bottom inset) indicating that a substantial proportion of markers are recovered from P's between 0.5-2.5 GPa with very few rocks reaching maximum P's above 3 GPa. Thin lines are thermal gradients labeled in °C/km. Reaction boundaries for eclogitization of oceanic crust and antigorite dehydration are from Ito & Kennedy (1971) and Schmidt & Poli (1998), respectively.

by a sharp change in slope around 2.3-2.4 GPa implies relatively uniform recovery of subducting material up to 2.3-2.4 GPa, but increasingly rare recovery above 2.3-2.4 GPa (Agard et al., 2018; Kerswell et al., 2021; Monie & Agard, 2009; Plunder et al., 2015). On the one hand, evidence for common mechanical coupling depths near 2.3 GPa (Furukawa, 1993; Kerswell et al., 2021; Wada & Wang, 2009) suggests an upper-limit to recovery depths that is consistent with the scarcity of (ultra-)HP samples in the rock record and invariant with respect to key thermo-kinematic parameters (convergence velocity, subduction geometry, plate thickness; Figure 1). On the other hand, substantial variations in lateral (along-strike) upper-plate surface heat flow patterns suggest coupling depths also vary substantially among subduction zone segments (Kerswell & Kohn, 2022) and do impose an invariant upper-limit to recovery depths. Moreover, geophysical constraints on the depths of key mechanical transitions likely to induce rock recovery (e.g. Abers et al., 2020; Audet & Kim, 2016; Audet & Schaeffer, 2018; Morishige & Kuwatani, 2020) suggest high recovery rates should cluster around discrete depths, rather than uniform and widespread recovery along the subduction interface implied by the pd15 and ag18 datasets.

Difficulties in relating complex polymetamorphic rocks from different environments challenge the use of PT distributions of exhumed HP rock samples as robust constraints on key subduction zone parameters. Interpretations of rock recovery mechanisms, subduction interface behavior, metamorphic reactions, seismic cycling, and subduction geodynamics might vary depending on metamorphic terrane (local tectonic environment), sampling strategy (random or targeted outcrops), sample size (how many outcrops were observed and sampled in the field), and analytical sample selection (investigating PT's and deformation histories for a subset of samples with a specific scientific question in mind). Different compilations of PT estimates can show different density distributions, in terms of relative abundances of samples across PT space, and thus imply different depths of rock recovery along the subduction interface. For example, Agard et al. (2018) noted that compilations from Plunder et al. (2015) and Groppo et al. (2016) show less dispersion (i.e. a more step-like CDF) than ag18 with tighter bimodal or trimodal distributions clustering around inferred depths of important mechanical transitions along the subduction interface. These peaks (modes) in distributions of exhumed HP rocks coincide with the continental Moho at approximately 25-35 km and the transition to mechanical plate coupling at approximately 80 km (Agard et al., 2018; Monie & Agard, 2009; Plunder et al., 2015). Less consensus explains a smaller, yet significant, intermediate mode at 55-

60 km (Agard et al., 2009, 2018; Plunder et al., 2015), although it is consistent with a high- density region of PT estimates in the pd15 dataset.

Differences in compiled PT datasets notwithstanding, key observations regarding rock recovery in subduction zones emerge from pd15 and ag18:

1. Rocks are recovered with relatively similar frequency up to 2.5 GPa
2. 64-66% of recovered rocks equilibrated between 1-2.5 GPa
3. 5-19% of recovered rocks equilibrated above 2.5 GPa
4. 32-34% of recovered rocks equilibrated between 350-525 °C
5. 50-56% of recovered rocks equilibrated above 525 °C
6. 52-62% of recovered rocks record gradients between 5-10 °C/km
7. 18-31% of recovered rocks record gradients between 10-15 °C/km
8. 6-30% of recovered rocks record gradients above 15 °C/km

These ranges in the relative abundances of exhumed HP rocks compiled in different datasets raise important questions in subduction zone research: are rocks recovered broadly and uniformly along the subduction interface or discretely from certain depths? How do recovery rates and distributions vary among diverse subduction zone settings and through time?

Previous work comparing the rock record directly with numerical models has generally produced ambiguous interpretations concerning recovery rates and distributions along the subduction interface. For example, comparisons of different numerical geodynamic codes with subsets of the rock record show variable agreement in terms of overlapping PT paths and thermal gradients (e.g. Angiboust et al., 2012b; Burov et al., 2014; Holt & Condit, 2021; Penniston-Dorland et al., 2015; Plunder et al., 2018; Roda et al., 2010, 2012, 2020; Ruh et al., 2015; Yamato et al., 2007, 2008). Initial setups for numerical experiments (oceanic plate age, convergence velocity, subduction dip angle, upper-plate thickness, and heating sources; Kohn et al., 2018; Penniston-Dorland et al., 2015; Ruh et al., 2015; van Keken et al., 2019), differential recovery rates from subduction zones with favorable thermo-kinematic boundary conditions (Abers et al., 2017; van Keken et al., 2018), and comparisons among suites of undifferentiated HP rocks (e.g. grouping rocks recovered during subduction initiation with rocks recovered during "steady-state" subduction, see Agard et al., 2018, 2020) all potentially contribute to nonoverlapping PT distributions and thermal gradients between exhumed HP rocks and numerical geodynamic models. Compounding the ambiguity are arguments that material is sporadically recovered during short-lived mechanical transitions (Agard et al., 2016) and/or geodynamic changes (Monie & Agard, 2009)—implying exhumed HP rocks are not random samples of the subduction interface during steady-state subduction. Such ambiguities warrant further investigation into the general response of recovery rates and distributions to broad ranges of thermo-kinematic boundary conditions and various implementations of subduction interface rheologies.

Fortunately, clues about the nature and PT limits of rock recovery are provided by many extensively studied examples of exhumed subduction interfaces (e.g. Agard et al., 2018; Angiboust et al., 2011; 2015; Cloos & Shreve, 1988; Fisher et al., 2021; Ioannidi et al., 2020; Kitamura & Kimura, 2012; Kotowski & Behr, 2019; Locatelli et al., 2019; Monie & Agard, 2009; Okay, 1989; Platt, 1986; Plunder et al., 2013, 2015; Tewksbury-Christle et al., 2021; Wakabayashi, 2015). However, these type localities represent an unknown fraction of subducted material and differ significantly in terms of their geometry (field relationships), composition (rock types), and interpreted deformation histories (both detachment and exhumation). It is also unclear to what extent ag18 and pd15 (and other compilations) represent the full range of recovery conditions and/or represent scientific sampling bias (e.g. undersampling low-grade rocks or oversampling high-grade rocks from the same pristine exposures, Agard et al., 2018). Thus, a primary challenge to inferring recovery rates and distributions accurately from the rock record fundamentally stems from sparse nonrandom samples (typically less than a few dozen PT estimates from any given exhumed terrane) compared to the diversity of thermo-kinematic parameters characterizing subduction zones and petro-thermo-mechanical conditions suitable for rock recovery along the subduction interface.

This study aims at addressing the sparsity and nonrandomness of exhumed HP rock samples by tracing numerous (1,341,729) Lagrangian markers from 64 numerical geodynamic simulations of oceanic-continental subduction (Kerswell et al., 2021). We first generate a PT dataset from instantiations of a particular numerical geodynamic code so large that it was insensitive to noise and outliers—thus representing a statistically robust picture of recovery rates and PT distributions in subduction zones. From such a large dataset of generated samples, we identify correlations among recovery rates, PT distributions, and thermo-kinematic boundary conditions that quantify parameter sensitivities and indicate ranges of plausible conditions for reproducing the rock record. In fact, surprisingly low densities of generated samples, in terms of their relative abundances across PT space, were found coinciding with the highest-density regions of natural samples around 2 GPa and 550 °C. We then discuss implications for poor overlap between generated sample densities and exhumed HP rock densities, including insufficient implementation of recovery mechanisms in numerical geodynamic models (numerical bias) and a potential overabundance of natural samples collected from similar metamorphic grades around 2 GPa and 550 °C (empirical bias).

2 Methods

This study presents a dataset of Lagrangian markers (described below) from numerical experiments that simulated 64 oceanic-continental convergent margins with thermo-kinematic boundary conditions (oceanic plate age, convergence velocity, and upper-plate lithospheric thickness) closely representing the range of presently active subduction zones (Syracuse & Abers, 2006; Wada & Wang, 2009). Initial conditions were modified from previous studies of active margins (Gorczyk et al., 2007; Sizova et al., 2010) using the numerical geodynamic code I2VIS (Gerya & Yuen, 2003). I2VIS models visco-plastic flow of geological materials by solving conservative equations of mass, energy, and momentum on a fully-staggered finite difference grid with a *marker-in-cell* technique (Gerya, 2019; Gerya & Yuen, 2003; e.g. Harlow & Welch, 1965). Complete details about the initial setup, boundary conditions, and rheological model are presented in Kerswell et al. (2021). Complete details about I2VIS and example code are presented in Gerya & Yuen (2003) and Gerya (2019).

The following section defines Lagrangian markers (now referred to as *markers*) and briefly elaborates on their usefulness in understanding flow of geological materials, followed by a description of the marker classification algorithm. A complete mathematical description of the classification algorithm is presented in Appendix A.1.

2.1 Lagrangian Markers

Markers are mathematical objects representing discrete parcels of material flowing in a continuum (Harlow, 1962, 1964). Tracing markers (saving marker information at each timestep) is distinctly advantageous for investigating subduction dynamics in the following two ways.

First, modeling subduction requires solving equations of mass, motion, and heat transport in a partly layered, partly heterogeneous, high-strain region known as the *plate interface*, *subduction interface*, or *subduction channel* (Gerya et al., 2002). Current conceptual models regard the subduction interface as a visco-plastic continuum with complex geometry and structure, sharp thermal, chemical, and strain gradients, strong advection, and abundant fluid flow (Agard et al., 2016, 2018; Bebout, 2007; Bebout & Barton, 2002; Cloos & Shreve, 1988; Gerya & Yuen, 2003; Penniston-Dorland et al., 2015; Shreve & Cloos, 1986; Stöckhert, 2002; Tewksbury-Christle et al., 2021). Finite-difference numerical approaches do not perform well with strong local gradients, and interpolating and updating T, strain, and chemical fields with markers greatly improves accuracy and stability of numerical solutions (Gerya, 2019; Gerya & Yuen, 2003; Moresi et al., 2003).

Second, tracing a marker closely proxies for tracing a rock's PT-time history. Strictly speaking, deviations between calculated PT-time histories of markers and rocks are possible because our numerical geodynamic simulations assume: (1) markers move in an incompressible continuum (Batchelor, 1953; Boussinesq, 1897), (2) material properties are governed by a simplified petrologic model describing eclogitization of oceanic crust (Ito & Kennedy, 1971) and (de)hydration of upper mantle ($antigorite \Leftrightarrow olivine + orthopyroxene + H_2O$, Schmidt & Poli, 1998), and (3) marker stress and strain are related by a highly non-linear rheological model derived from empirical flow laws (Hilairet et al., 2007; Karato & Wu, 1993; Ranalli, 1995; Turcotte & Schubert, 2002). For example, if rocks within a subduction interface shear zone were highly compressible or could sustain large deviatoric stresses, P's and T's might be different from markers. The hydrological model implemented in our numerical simulations, embodied by assumptions 2 and 3, exert particularly strong control on subduction interface strength, and thus the probability and style of detachment. Our simulations developed stable subduction channels (tectonic-mélanges, e.g. Gerya et al., 2002) instead of discrete shear zones that detach large coherent slices of oceanic lithosphere (e.g. Ruh et al., 2015) primarily due to our choice of hydrological model. However, insofar as subduction interface shear zones closely behave as mélange-like channels of incompressible visco-plastic fluids (under the assumptions above, Gerya, 2019; Gerya & Yuen, 2003; Kerswell et al., 2021), comparisons between marker PT distributions and the rock record may be made.

2.2 Marker Classification

For each numerical experiment, 20,986 markers were initially selected from within a 760 km-long and 8 km-deep section of oceanic crust and seafloor sediments at $t = 0$ Ma. Tracing proceeded for 115 timesteps (between 9.3-54.7 Ma depending on convergence velocity), which was sufficient for markers to be potentially subducted very deeply (up to 300 km) from their initial positions. However, only markers that detached from the subducting oceanic plate were relevant for comparison with PT estimates of exhumed HP rocks (because these markers and rocks were not subducted). The main challenge, therefore, was to first develop a method for determining which markers among 20,986 detached and moved away from the subducting plate without knowing their fate *a priori*. Moreover, the method needed to be generalizable to a large range of numerical experiments. Note that detached markers were classified as "recovered" even if they did not exhume to the surface within the modeling domain. Diverse processes can cause exhumation of subduction zone rocks, including later tectonic events, and our goal was to compare only the maximum metamorphic conditions of markers and rocks along their prograde paths.

Classifying unlabelled markers as either "recovered" or "not recovered" based solely on their undifferentiated traced histories defines an unsupervised classification problem (Barlow, 1989). Many methods can be applied to solve the unsupervised classification problem, yet this study implemented a Gaussian mixture model (Reynolds, 2009)—a type of "soft" clustering algorithm used extensively for pattern recognition, anomaly detection, and estimating complex probability distribution functions (e.g. Banfield & Raftery, 1993; Celeux & Govaert, 1995; Figueiredo & Jain, 2002; Fraley & Raftery, 2002; Vermeesch, 2018). "Hard" classification is possible by directly applying simple rules to markers without clustering (e.g. Roda et al., 2012). However, "hard" methods are less generalizable than "soft" approaches like Gaussian mixture models, which can be implemented to study many possible features in numerical simulations with Lagrangian reference frames—not just recovery of subducted material. In this case, a Gaussian mixture model organized markers into groups (clusters) by fitting $k = 14$ bivariate Gaussian ellipsoids to the distribution of markers in PT space. "Fitting" refers to adjusting parameters (centroids and covariance matrices) of all k Gaussian ellipsoids until the ellipsoids and data achieved maximum likelihood (see Appendix A.1 for a complete mathematical description). Finally, marker clusters with centroids located within certain bounds were classified as "recovered". The entire classification algorithm can be summarized as follows:

0. Select markers within a 760 km $\times$ 8 km section of oceanic crust
1. Trace markers for 115 timesteps
2. Identify maximum marker PT conditions (at either maxT or maxP)
3. Apply Gaussian mixture modeling to maximum marker PT conditions
4. Check for cluster centroids within the bounds:
   - ≥ 3 °C/km AND
   - ≤ 1300 °C AND
   - ≤ 120 km (3.4 GPa)
5. Classify marker clusters found in step 4 as "recovered"
6. Classify all other markers as "not recovered"

Note that maximum marker PT conditions used for clustering were assessed before markers transformed (dehydrated or melted) and before the accretionary wedge toe collided with the high-viscosity convergence region positioned at 500 km from the left boundary (to avoid spurious maximum PT conditions from sudden isothermal burial). We also tried applying different prograde PT path positions in step 2 by determining maximum marker T's (maxT) and maximum P's (maxP) independently. Applying maxP vs. maxT conditions to the classifier resulted in distinct PT distributions of recovered markers and distinct correlations among thermo-kinematic boundary conditions and marker recovery modes. For natural samples of exhumed HP rocks, compilations emphasize maxP, not maxT, (Penniston-Dorland et al., 2015), and thus empirical PT estimates are best compared with maxP conditions. Also, many PT paths for exhumed HP rocks have "hairpin" or isothermal decompression retrograde PT paths without significant heating during exhumation (Agard et al., 2009). Figures 2 & 3 illustrate marker classification for 1 of 64 numerical experiments. All other experiments are presented in Supplementary **??**.

2.3 Recovery Modes

To better quantify how rock recovery can vary among subduction zones with different boundary conditions, marker recovery modes (density peaks) were determined with respect to absolute PT and PT gradients. The highest-density peak (mode1) shows where the greatest abundance of markers are recovered. The deepest, or warmest, density peak (mode2) shows where the most deeply subducted markers (or markers with the highest PT gradients) are recovered. In other words, changes in the positions of mode1 and mode2 reflect variations in recovery conditions for "normal" recovery and "extreme cases", respectively.

Note that correlations are not presented here with respect to the thermal parameter Φ (Φ = oceanic plate age $\cdot$ convergence velocity), unlike many studies. The rationale is three-fold: (1) the aim was to understand how oceanic plate age and convergence velocity affect marker recovery independently, (2) sample sizes of recovered markers were larger when grouped by oceanic plate age and convergence velocity (n = 335,788) compared to grouping by Φ (n = 83,947; implying they do not correlate well with Φ), and (3) and combining oceanic plate age and convergence velocity can draw unnecessarily ambiguous associations with other geodynamic features of subduction zones (e.g. Φ vs. H from England et al., 2004; Wada & Wang, 2009).

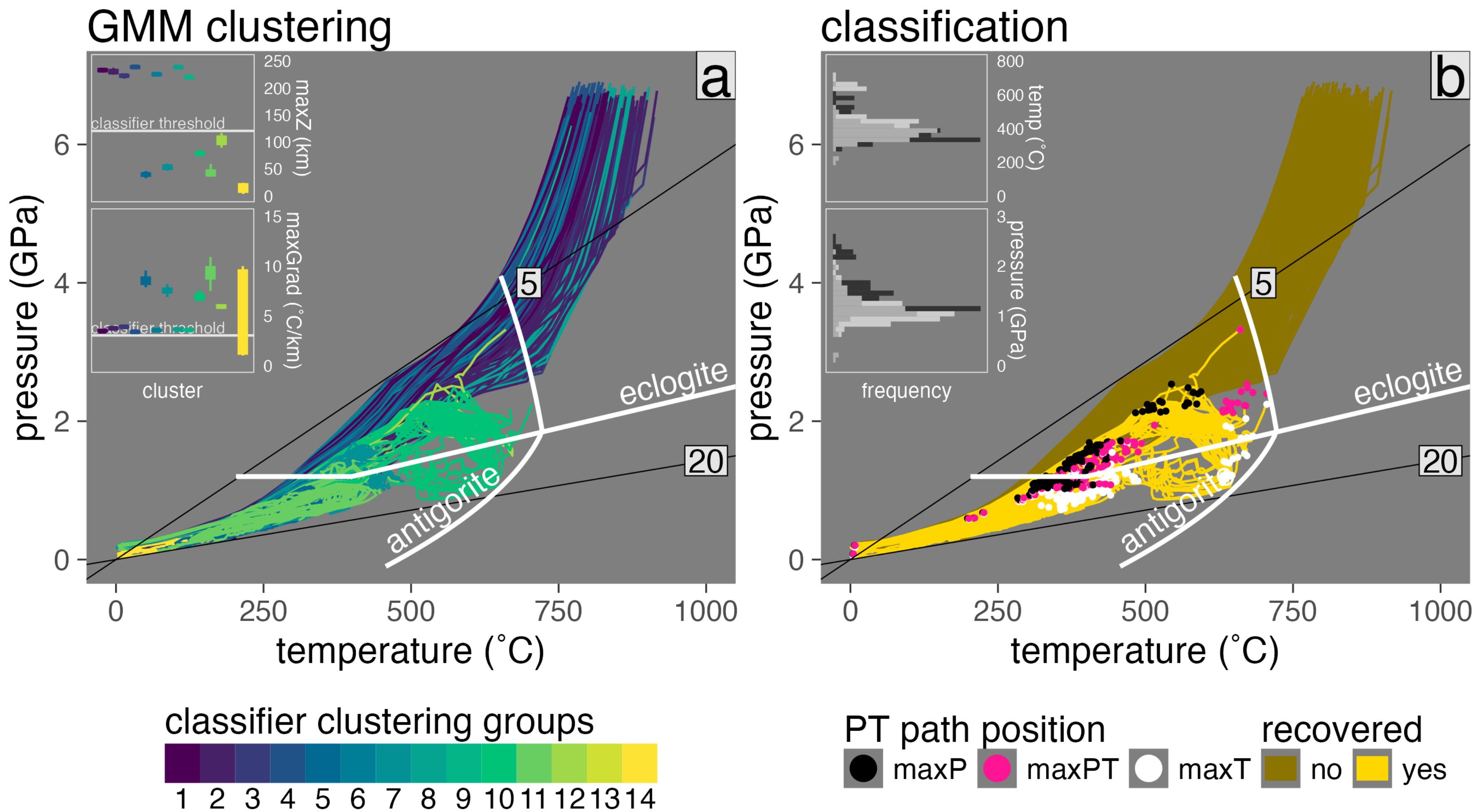

Figure 2: Example of marker classification for model cda62. (a) PT diagram showing marker clusters as assigned by Gaussian mixture modeling (GMM; colored PT paths). Boxplots showing depth and thermal gradient distributions of marker clusters assigned by GMM. Markers belonging to clusters with centroids (means) positioned at $\leq$ 120 km (top inset) and $\geq$ 5 °C/km (bottom inset) are classified as recovered. All others are classified as not recovered. (b) PT diagram showing marker classification results (colored PT paths) and various marker positions along their PT paths (black, white, and pink points). (insets) Histograms showing the distribution of T's (top inset) and P's (bottom inset) for recovered markers at maxP (black bars) and maxT (white bars) conditions. In this experiment, a significant number of markers have different peak metamorphic conditions between their maxT and maxP positions. Thin lines are thermal gradients labeled in °C/km. Only a random subset of markers are shown.

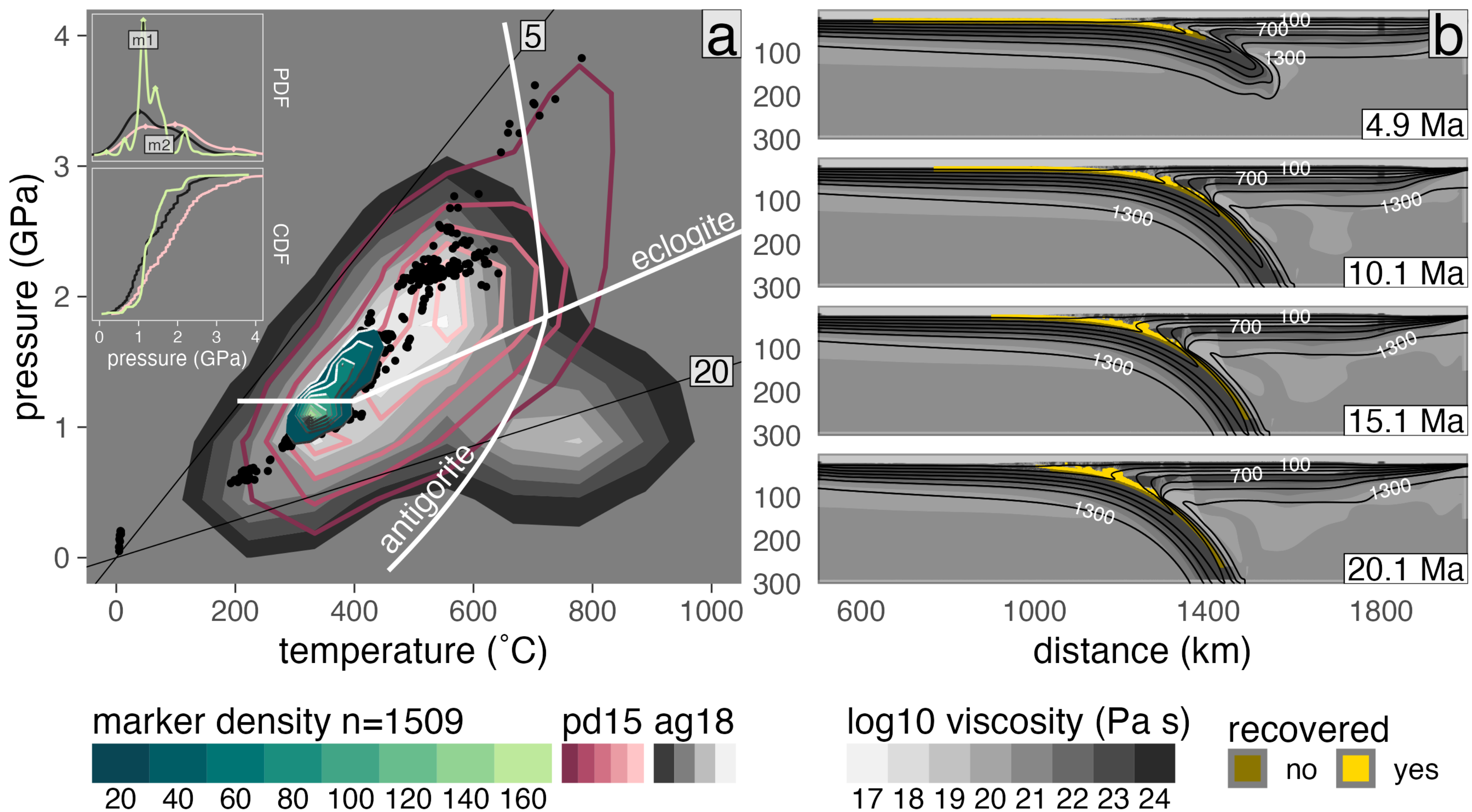

Figure 3: Summary of marker recovery for model cda62. (a) PT diagram showing the density of recovered markers (black points and green Tanaka contours) in comparison with the pd15 (solid red density contours) and ag18 (filled gray density contours) datasets. (insets) Probability distribution diagrams showing trimodal recovery P's (top inset) and a step-like CDF (bottom inset) indicating that a substantial proportion of markers are recovered from depths between 0.5-1.5 GPa. Thin lines are thermal gradients labeled in °C/km. Reaction boundaries for eclogitization of oceanic crust and antigorite dehydration are from Ito & Kennedy (1971) and Schmidt & Poli (1998), respectively. (b) Visualization of log viscosity in the model domain showing the major modes of marker recovery along a relatively thick subduction interface that tapers near the viscous coupling depth.

3 Results

3.1 Comparing Marker PT Distributions with the Rock Record

3.1.1 Global Markers from all Numerical Experiments

While marker recovery can occur at all P's recorded by exhumed metamorphic rocks (Figure 4), large disparities between recovered markers and the rock record are found if considering sample densities with respect to P. For example, pd15 and ag18 show high sample densities centered at 1 GPa—a shared feature common to all 64 numerical experiments—yet sample densities above 1 GPa are much greater in pd15 and ag18 compared to simulations (relative to the total number of samples in each dataset; Figure 4). Samples compiled in pd15 and ag18 also show much broader bimodal or trimodal density distributions across P's compared to a narrow and strong unimodal P distribution centered at 1 GPa for recovered markers. With respect to T, thermal gradients of recovered markers are significantly lower than natural samples. On average, markers recovered from $<$ 2 GPa differ by 173 °C and 3-4 °C/km compared to rocks exhumed from $<$ 2 GPa (excluding the highest-T samples in ag18 that relate to subduction initiation, Agard et al., 2018, 2020; Soret et al., 2022). In fact, relatively poor overlap exists between the high-density peak of recovered markers centered at 1 GPa & 300° C and either high-density peaks of natural sample centered at 1 GPa & 350° C and 2 GPa & 550° C (Figure 4).

3.1.2 Markers from Individual Numerical Experiments

For most experiments, marker recovery is localized and discrete with peaky multimodal density distributions and step-like CDFs. The PT positions of recovery cluster centroids depend on thermo-kinematic boundary conditions, however, so marker PT distributions vary. A few experiments show broad marker distributions that resemble the rock record with respect to P, but not with respect to thermal gradients (Supplementary **??**). Other experiments show the opposite. To compare marker recovery among various subduction zone settings, we combined recovered markers from multiple numerical experiments with similar thermo-kinematic boundary conditions—–analogous to randomly sampling exhumed HP rocks from similar subduction zones (Figures 5 & 6).

Whether comparing the rock record with recovered markers from individual numerical experiments, suites of experiments, or all numerical experiments, several key observations emerge (Figure 4):

1. Recovered markers from most individual numerical experiments show discrete multimodal PT distributions with steep step-like CDFs (Figure 3 & Supplementary **??**)
2. Relatively few markers are recovered from PT regions coinciding with high-densities of natural samples around 2 GPa and 550 °C
3. Markers are recovered from a single major P mode near 1 GPa and minor P mode near 2.5 GPa with a higher rate of recovery from lower P's (79% from $\leq$ 1.5 GPa) compared to natural samples (36-59% from $\leq$ 1.5 GPa)
4. Markers are recovered from a single major T mode near 300 °C and minor T mode near 525 °C with a higher rate of recovery from lower T's (97% from $\leq$ 525 °C) compared to natural samples (44-50% from $\leq$ 525 °C)
5. The relative abundance of markers recovered along "typical" thermal gradients for subduction zones (87% from 5-12 °C/km) is high compared to natural samples (59-78% from 5-12 °C/km)
6. Many markers are recovered from the forbidden zone (11% from $\leq$ 5 °C/km)
7. Virtually no markers (0.002%) are recovered from $\geq$ 15 °C/km compared to natural samples (6-30% from $\geq$ 15 °C/km, Figure 4)

3.2 Correlations with Boundary Conditions

3.2.1 Oceanic Plate Age Effect

Thermal gradients of recovered markers respond strongly to changes in oceanic plate age (Figure 7, Table 1). Both PT gradient modes are strongly inversely correlated with oceanic plate age, showing a mean increase from about 5.88 ± 0.17 °C/km (Grad mode1) and 6.91 ± 0.68 °C/km (Grad mode2) for older plates ($\geq$ 85 Ma) to about 7.25 ± 0.05 °C/km (Grad mode1) and 8.84 ± 0.56 °C/km (Grad mode2) for younger plates ($\leq$ 55 Ma). The dominant P mode (P mode1) moderately correlates with oceanic plate age, indicating a slightly higher possibility of recovering material from beyond the continental Moho for the oldest oceanic plates ($\geq$ 85 Ma). Neither T modes, nor recovery rate

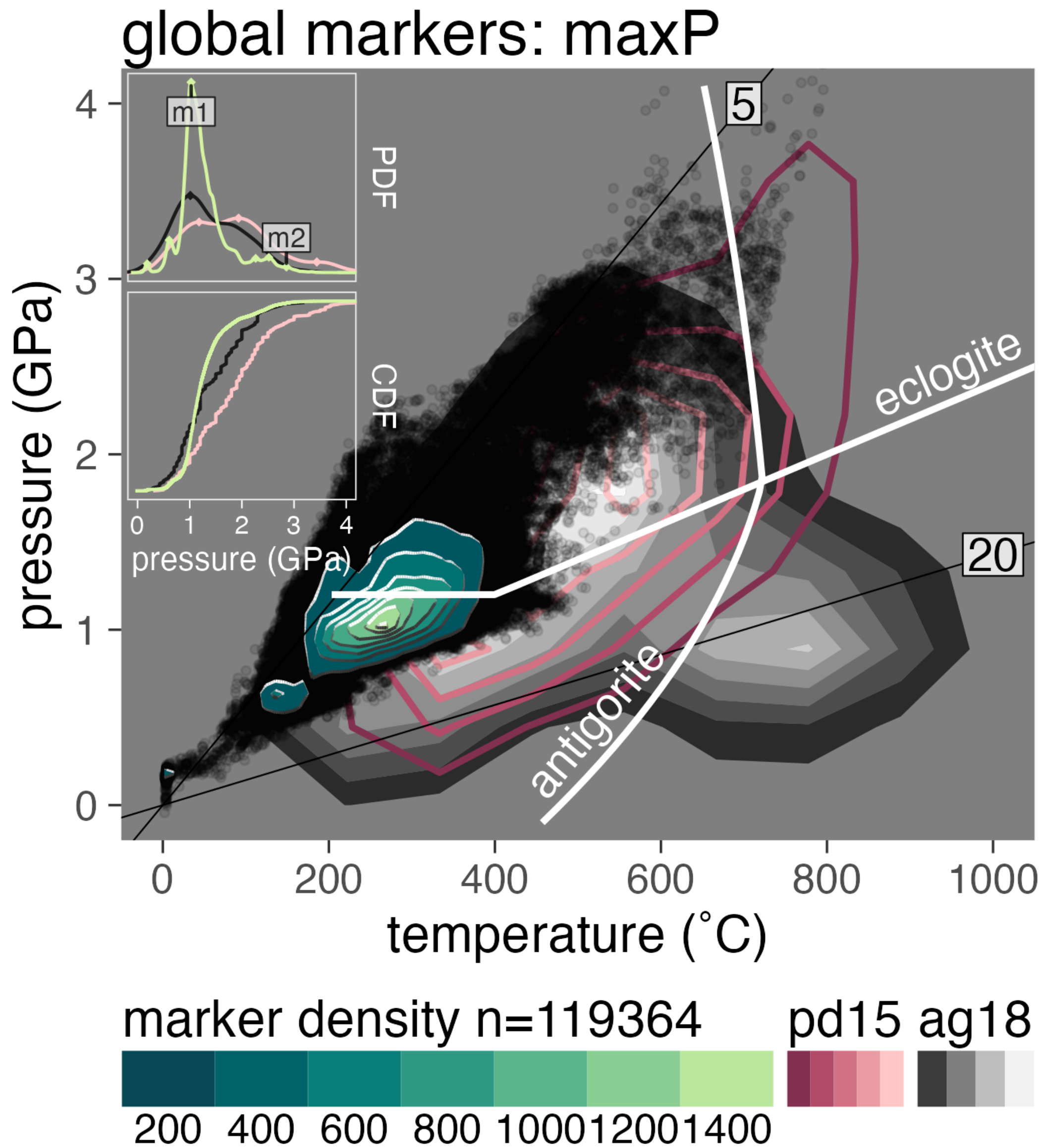

Figure 4: Recovered markers from all 64 numerical experiments. (a) PT diagram showing the density of recovered markers (black points and green Tanaka contours) in comparison with the pd15 (solid red density contours) and ag18 (filled gray density contours) datasets. Marker density is concentrated along relatively cool thermal gradients, primarily near the continental Moho (1 GPa), with minor recovery modes centered near the onset of plate coupling (2.3-2.5 GPa). (insets) Probability distribution diagrams showing discrete multimodal recovery P's (top inset) and a steep CDF (bottom inset) indicating that a substantial proportion of markers are recovered from depths between 0.5-1.5 GPa. Note the higher-abundance of pd15 and ag18 samples at $>$ 1.5 GPa compared to markers. Thin lines are thermal gradients labeled in °C/km. Reaction boundaries for eclogitization of oceanic crust and antigorite dehydration are from Ito & Kennedy (1971) and Schmidt & Poli (1998), respectively.

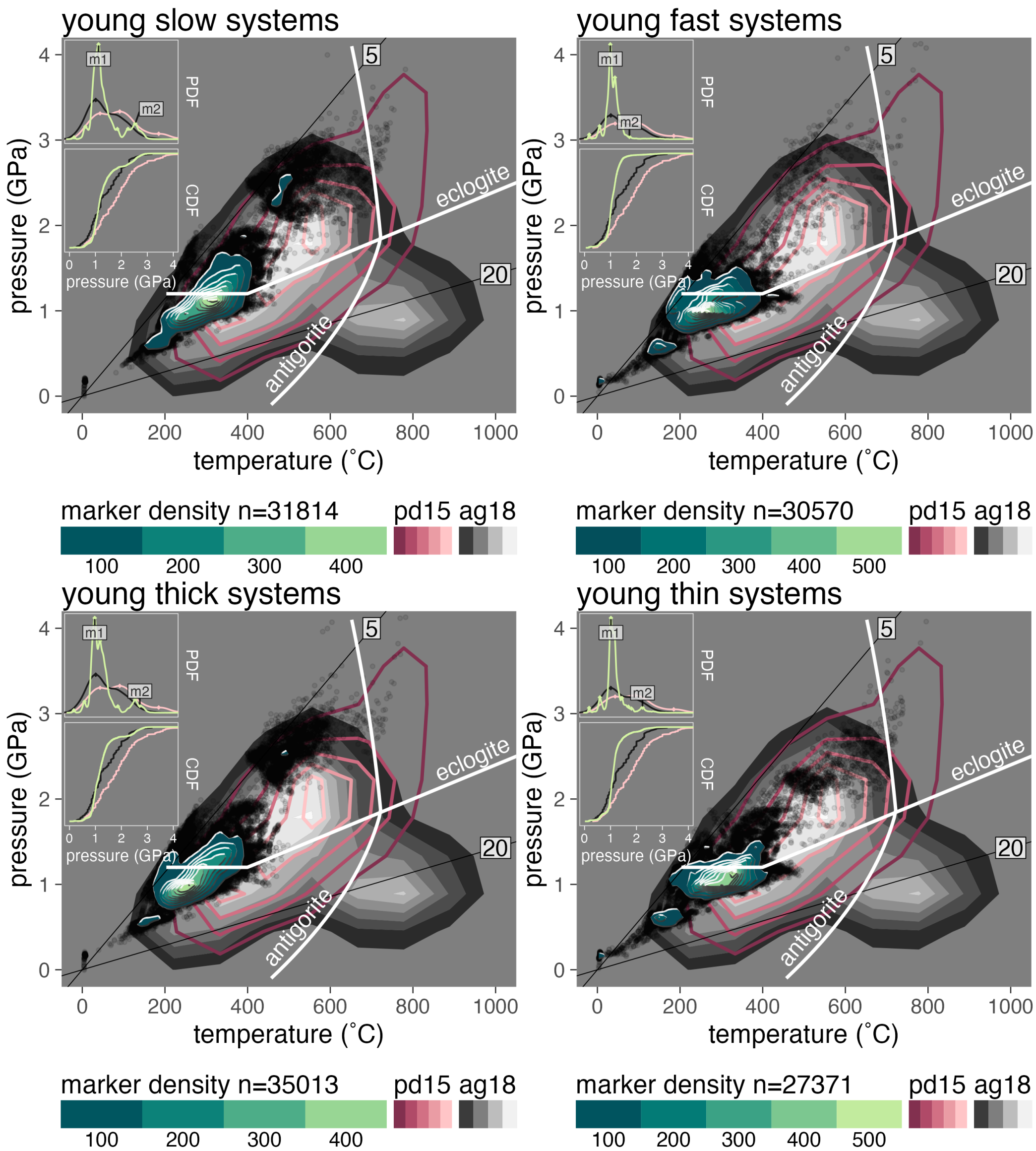

Figure 5: Recovered markers from numerical experiments with young oceanic plates (32.6-55 Ma). PT diagrams showing the densities of recovered markers (black points cloud and green Tanaka contours) in comparison with the pd15 (solid red density contours) and ag18 (filled gray density contours) datasets, grouped by thermo-kinematic boundary conditions (16 experiments per plot; boundary conditions summarized in Kerswell et al., 2021). (insets) Probability distribution (top inset) and CDF diagrams with respect to P. Thin lines are thermal gradients labeled in °C/km. Reaction boundaries for eclogitization of oceanic crust and antigorite dehydration are from Ito & Kennedy (1971) and Schmidt & Poli (1998), respectively.

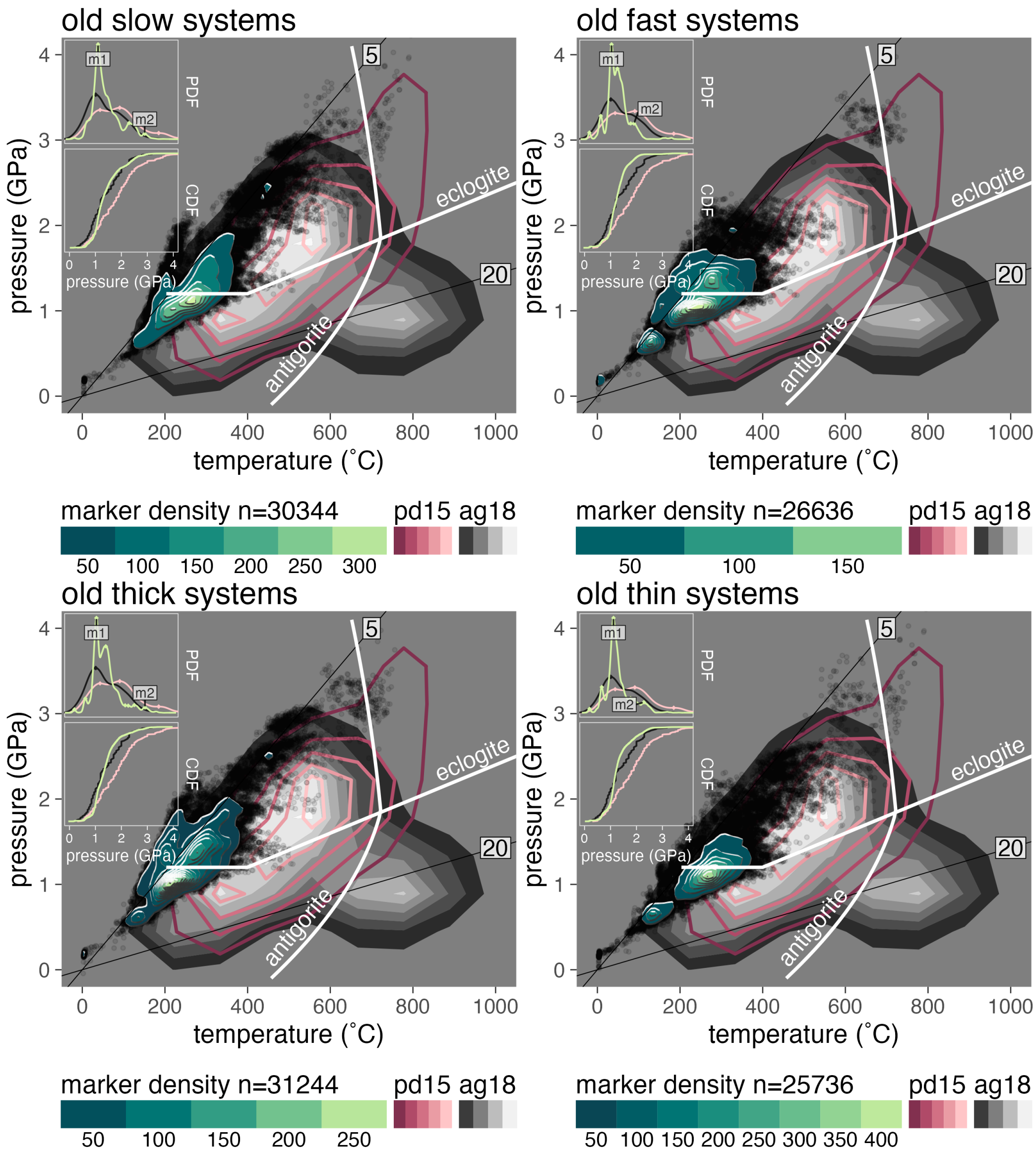

Figure 6: Recovered markers from numerical experiments with older oceanic plates (85-110 Ma). PT diagrams showing the densities of recovered markers (black points cloud and green Tanaka contours) in comparison with the pd15 (solid red density contours) and ag18 (filled gray density contours) datasets, grouped by thermo-kinematic boundary conditions (16 experiments per plot; boundary conditions summarized in Kerswell et al., 2021). (insets) Probability distribution (top inset) and CDF diagrams with respect to P. Thin lines are thermal gradients labeled in °C/km. Reaction boundaries for eclogitization of oceanic crust and antigorite dehydration are from Ito & Kennedy (1971) and Schmidt & Poli (1998), respectively.

correlate with oceanic plate age. Although oceanic plate age strongly affects the average PT gradients of recovered material, it does not strongly shift marker recovery up or down the subduction interface.

3.2.2 Convergence Velocity Effect

P's and T's of recovered markers respond strongly to changes in convergence velocity (Figure 7, Table 1). Both P modes are strongly inversely correlated with convergence velocity, showing a mean increase from 1.09 ± 0.03 GPa (P mode1) and 1.91 ± 0.33 GPa (P mode2) for fast moving plates (100 km/Ma) to about 1.37 ± 0.06 GPa (P mode1) and 2.64 ± 0.08 GPa (P mode2) for slow moving plates (40 km/Ma). However, the dominant P mode (P mode1) does not change significantly until convergence velocity drops below 66 km/Ma (Table 1). Both T modes are strongly inversely correlated with convergence velocity, showing a mean increase from 249.3 ± 6.6 °C (T mode1) and 371.8 ± 60.8 °C (T mode2) for fast moving plates (100 km/Ma) to about 311.6 ± 1.5 °C (T mode1) and 542.5 ± 74.3 °C (T mode2) for slow moving plates (40 km/Ma). Neither PT gradient modes, nor recovery rate correlate with convergence velocity. In summary, decreasing convergence velocity shifts marker recovery to warmer and deeper conditions along the subduction interface without significantly changing the average thermal gradient of subducted material.

3.2.3 Upper-plate Thickness Effect

From the same numerical experiments used to trace markers, an association between upper-plate thickness and mechanical coupling depths was demonstrated (Kerswell et al., 2021). P distributions of markers were thus expected to respond strongly to changes in upper-plate thickness. However, a surprisingly negligible effect was observed (Figure 7). For example, neither of the P modes, nor T mode2 (usually the most deeply subducted markers) correlate with upper-plate thickness. In contrast, both PT gradient modes and the dominant T mode (T mode1) inversely correlate with upper-plate thickness. Recovery rate is correlated with upper-plate thickness and not with any other boundary condition, indicating higher recovery rates are more likely underneath thick upper-plates. Recovery rates show a mean decrease from 10.65 ± 0.32 % for thicker plates (≥ 78 km-thick) to 8.09 ± 0.3 % for thinner upper-plates (≤ 62 km-thick). In summary, thin upper-plates are more likely to produce warmer thermal gradients, higher T's, and lower recovery rates.

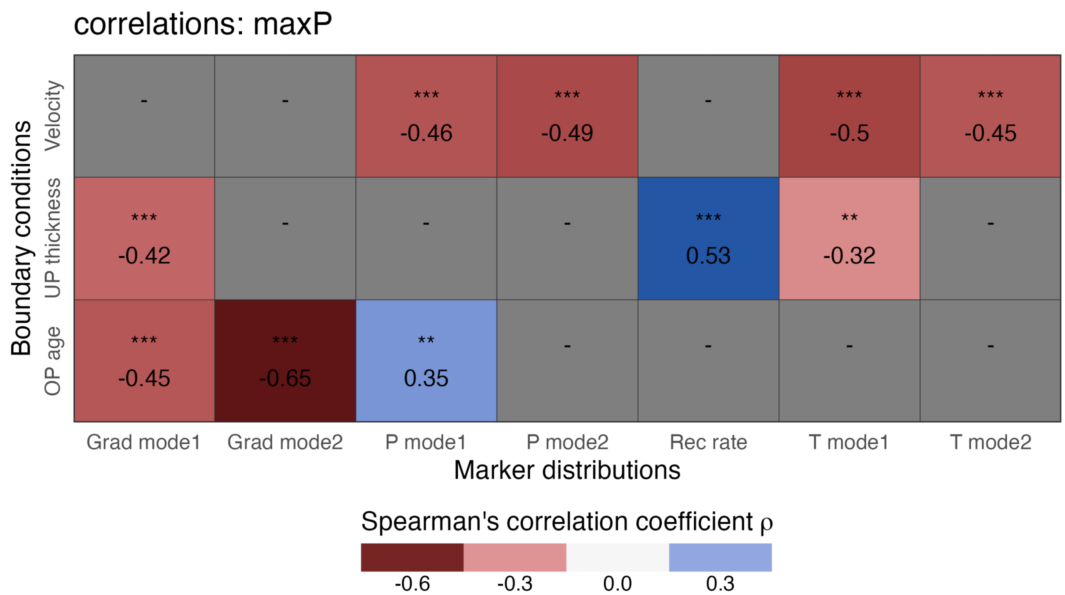

Figure 7: Correlations among marker recovery modes and thermo-kinematic boundary conditions. The dominant recovery mode (mode1) indicates the position of the tallest density peak with respect to P, T, or thermal gradient (i.e. conditions from which the greatest number of markers are recovered), while mode2 indicates the position of the warmest, deepest, or highest gradient density peak (i.e. conditions from which deeply subducted markers are recovered). While oceanic plate age and upper-plate thickness more strongly affect the average thermal gradients of recovered markers (stronger correlations with gradient modes and T mode1), convergence velocity more strongly affects the depths of recovery along the subduction interface, especially for deeply subducted markers (stronger correlation with P modes and T mode2). The dominant T mode (T mode1) and recovery rate are correlated with upper-plate thickness, but not with any other boundary condition. Symbols indicate the Spearman's rank correlation coefficient that measures the significance of monotonic correlations. *** $\rho \leq 0.001$, ** $\rho \leq 0.01$, * $\rho \leq 0.05$, - $\rho \geq 0.05$.

Table 1: Subduction zone parameters and marker classification summary

Initial Boundary Conditions					Marker Classification Summary							
model	Φ	Z_{UP}	age	$\vec{v}$	recovered	rec. rate	P mode1	P mode2	T mode1	T mode2	grad mode1	grad mode2
	km	km	Ma	km/Ma		%	GPa	GPa	°C	°C	°C/km	°C/km
cda46	13.0	46	32.6	40	1482±28	7.8±0.14	1.12±0.00	2.46±0.04	336±2	584±138	8.2±0.02	9.5±0.04
cda62	13.0	62	32.6	40	1351±24	7.2±0.12	1.12±0.00	2.24±0.26	332±2	534±36	8.3±0.02	8.3±0.02
cda78	13.0	78	32.6	40	1863±30	9.9±0.16	1.39±0.00	2.38±0.02	352±2	477±2	5.9±0.02	9.3±1.66
cda94	13.0	94	32.6	40	1932±28	10.2±0.14	1.24±0.00	2.65±0.02	341±2	502±26	5.6±0.02	7.8±0.04
cdb46	21.5	46	32.6	66	1806±34	9.6±0.18	1.04±0.00	2.37±0.74	334±2	657±2	8.3±0.04	8.4±0.38
cdb62	21.5	62	32.6	66	1405±20	7.4±0.10	1±0.00	2.16±0.00	281±2	531±32	7.8±0.04	10±0.06
cdb78	21.5	78	32.6	66	1884±32	10±0.18	0.92±0.00	2.49±0.08	264±2	541±6	8.1±0.04	8.1±0.04
cdb94	21.5	94	32.6	66	2330±124	12.3±0.66	1.16±0.16	2.64±0.12	291±2	464±44	7.5±0.02	7.9±1.10
cdc46	26.1	46	32.6	80	1736±46	9.2±0.24	1.02±0.00	1.27±0.68	320±0	475±162	8.8±0.40	9.1±0.98
cdc62	26.1	62	32.6	80	1288±28	6.8±0.16	0.99±0.00	2.01±0.00	264±2	531±2	6.7±0.02	8.6±0.92
cdc78	26.1	78	32.6	80	1801±24	9.5±0.14	0.94±0.10	2.88±0.16	283±2	519±28	7.8±0.02	8.1±2.00
cdc94	26.1	94	32.6	80	2158±26	11.4±0.14	1.14±0.00	3.01±0.02	274±0	533±2	6.7±0.04	9.8±0.04

Table 1: Subduction zone parameters and marker classification summary *(continued)*

Initial Boundary Conditions					Marker Classification Summary							
model	Φ	Z_{UP}	age	$\vec{v}$	recovered	rec. rate	P mode1	P mode2	T mode1	T mode2	grad mode1	grad mode2
	km	km	Ma	km/Ma		%	GPa	GPa	°C	°C	°C/km	°C/km
cdd46	32.6	46	32.6	100	1055±58	5.6±0.30	1±0.00	1.76±0.14	226±0	465±50	5.9±0.02	8.5±0.06
cdd62	32.6	62	32.6	100	1365±28	7.2±0.14	0.99±0.00	1.63±0.16	262±2	342±30	5.6±0.04	8.9±0.04
cdd78	32.6	78	32.6	100	1889±28	10±0.16	1±0.00	1.93±0.08	264±2	512±2	7.5±0.04	11.8±1.56
cdd94	32.6	94	32.6	100	2716±32	14.4±0.16	1.23±0.00	2.9±0.00	242±38	660±6	7.3±0.02	7.3±0.02
cde46	22.0	46	55.0	40	1612±36	8.5±0.18	1.11±0.00	2.83±0.54	315±2	675±90	6.7±0.02	7.9±0.94
cde62	22.0	62	55.0	40	1794±50	9.5±0.26	1.08±0.00	2.24±0.00	285±2	485±2	6.1±0.00	7.4±0.64
cde78	22.0	78	55.0	40	1866±34	9.9±0.18	1.37±0.00	2.52±0.00	315±2	507±98	5.9±0.06	7.5±0.02
cde94	22.0	94	55.0	40	1808±20	9.6±0.10	2.33±0.86	2.54±0.00	319±2	431±0	5±0.02	7.2±0.02
cdf46	36.3	46	55.0	66	2246±56	11.9±0.30	1.11±0.04	2.68±0.28	308±2	673±14	7.6±0.02	7.6±0.02
cdf62	36.3	62	55.0	66	1569±38	8.3±0.20	1.14±0.00	2.2±0.06	265±2	582±130	6.9±0.02	6.9±0.02
cdf78	36.3	78	55.0	66	1621±26	8.6±0.14	0.99±0.00	2.75±0.18	228±2	545±8	7±0.02	7.5±1.16
cdf94	36.3	94	55.0	66	1964±30	10.4±0.16	0.93±0.00	2.79±0.02	216±0	597±212	6.6±0.02	6.6±0.02

Table 1: Subduction zone parameters and marker classification summary *(continued)*

Initial Boundary Conditions					Marker Classification Summary							
model	Φ	Z_{UP}	age	$\vec{v}$	recovered	rec. rate	P mode1	P mode2	T mode1	T mode2	grad mode1	grad mode2
	km	km	Ma	km/Ma		%	GPa	GPa	°C	°C	°C/km	°C/km
cdg46	44.0	46	55.0	80	2101±74	11.1±0.40	1.2±0.00	1.96±0.04	338±2	338±2	8.1±0.16	8.2±1.26
cdg62	44.0	62	55.0	80	1334±24	7.1±0.12	1±0.00	1.74±0.06	218±4	277±48	5.2±0.02	7.5±0.04
cdg78	44.0	78	55.0	80	1585±26	8.4±0.14	1.01±0.00	2.21±0.02	238±2	529±210	4.9±0.02	7.1±0.02
cdg94	44.0	94	55.0	80	2132±22	11.3±0.12	0.98±0.00	2.69±0.02	209±0	402±36	6.4±0.02	9.4±0.10
cdh46	55.0	46	55.0	100	947±16	5±0.08	0.95±0.00	1.63±0.26	273±4	368±98	7±0.18	9.2±0.48
cdh62	55.0	62	55.0	100	1448±24	7.7±0.12	0.99±0.00	1.73±0.00	237±36	243±2	6.9±1.46	7.1±0.02
cdh78	55.0	78	55.0	100	1631±22	8.6±0.12	0.99±0.02	1.59±0.26	215±10	256±84	6.6±1.36	6.8±0.16
cdh94	55.0	94	55.0	100	2281±28	12.1±0.14	0.88±0.00	1.24±0.14	203±0	275±2	6.7±0.02	10.3±0.62
cdi46	34.0	46	85.0	40	1275±24	6.8±0.14	1.17±0.00	3.55±0.32	287±2	721±72	6.6±0.02	6.6±0.02
cdi62	34.0	62	85.0	40	1915±34	10.1±0.18	1.09±0.00	2.28±0.00	257±2	494±286	5.6±0.76	6.7±0.04
cdi78	34.0	78	85.0	40	2043±24	10.8±0.12	1.65±0.02	2.56±0.00	320±2	443±4	5.4±0.02	6.5±0.02
cdi94	34.0	94	85.0	40	2007±38	10.6±0.20	1.66±0.02	2.94±0.00	292±2	493±6	5.1±0.02	6.4±0.02

Table 1: Subduction zone parameters and marker classification summary *(continued)*

Initial Boundary Conditions					Marker Classification Summary								
model	Φ	Z_{UP}	age	$\vec{v}$	recovered	rec. rate	P mode1	P mode2	T mode1	T mode2	grad mode1	grad mode2
	km	km	Ma	km/Ma		%	GPa	GPa	°C	°C	°C/km	°C/km
cdj46	56.1	46	85.0	66	1656±100	8.8±0.52	1.07±0.00	2.55±0.58	273±2	616±318	6.4±0.06	7.4±0.12
cdj62	56.1	62	85.0	66	1364±28	7.2±0.14	1.09±0.00	2.13±0.04	238±2	516±24	6.3±0.02	6.3±0.02
cdj78	56.1	78	85.0	66	1326±28	7±0.14	1.22±0.00	1.97±0.02	202±0	315±0	4.5±0.02	6.5±0.06
cdj94	56.1	94	85.0	66	1849±26	9.8±0.14	1.03±0.00	1.52±0.00	206±0	206±0	5.9±0.02	5.9±0.02
cdk46	68.0	46	85.0	80	1463±24	7.8±0.14	1.06±0.02	1.11±0.26	270±2	400±120	7.5±0.02	7.5±0.02
cdk62	68.0	62	85.0	80	1204±20	6.4±0.10	1.07±0.00	1.83±0.00	220±2	452±170	4.7±0.02	6.7±0.04
cdk78	68.0	78	85.0	80	1540±36	8.2±0.20	1.02±0.04	1.78±0.34	214±8	214±8	6±1.58	6.9±0.90
cdk94	68.0	94	85.0	80	2032±32	10.8±0.16	1.04±0.00	3.19±0.06	265±2	677±30	6±0.02	6±0.02
cdl46	85.0	46	85.0	100	714±16	3.8±0.08	1.1±0.00	1.56±0.02	268±2	268±2	6±0.06	6.5±2.78
cdl62	85.0	62	85.0	100	1096±22	5.8±0.12	1.02±0.00	2.23±0.02	246±2	466±126	6.8±0.18	6.8±0.18
cdl78	85.0	78	85.0	100	1663±42	8.8±0.22	1.08±0.18	1.94±0.02	273±2	273±2	4±0.02	8.9±2.46
cdl94	85.0	94	85.0	100	1508±218	8±1.16	1.23±0.16	1.27±0.08	225±4	370±70	5.8±0.06	7.4±2.74

Table 1: Subduction zone parameters and marker classification summary *(continued)*

Initial Boundary Conditions					Marker Classification Summary								
model	Φ	Z_{UP}	age	$\vec{v}$	recovered	rec. rate	P mode1	P mode2	T mode1	T mode2	grad mode1	grad mode2
	km	km	Ma	km/Ma		%	GPa	GPa	°C	°C	°C/km	°C/km
cdm46	44.0	46	110.0	40	1390±24	7.4±0.12	1.39±0.00	3.14±0.02	320±2	711±6	6.1±0.02	8.1±1.94
cdm62	44.0	62	110.0	40	2326±28	12.3±0.14	1.21±0.00	2.45±0.00	281±0	439±2	5.5±0.38	5.7±0.04
cdm78	44.0	78	110.0	40	1828±36	9.7±0.18	1.48±0.00	2.51±0.00	331±4	668±208	5.5±0.02	6.4±1.04
cdm94	44.0	94	110.0	40	1901±28	10.1±0.14	1.53±0.00	2.87±0.00	302±2	517±210	5.3±0.02	6±0.02
cdn46	72.6	46	110.0	66	1942±88	10.3±0.46	1.25±0.00	2.3±0.08	283±2	637±70	7.1±0.06	7.1±0.06
cdn62	72.6	62	110.0	66	1217±24	6.5±0.14	1.13±0.00	2.15±0.24	269±0	559±136	6.9±0.06	6.9±0.06
cdn78	72.6	78	110.0	66	1684±38	8.9±0.20	1.38±0.00	1.38±0.00	212±2	429±4	3.9±0.02	7±1.22
cdn94	72.6	94	110.0	66	1685±26	8.9±0.14	1.06±0.00	1.77±0.36	203±2	299±144	5.6±0.04	6.6±0.44
cdo46	88.0	46	110.0	80	1476±128	7.8±0.68	1.21±0.04	1.75±0.86	280±2	343±74	7.4±0.08	7.4±0.08
cdo62	88.0	62	110.0	80	1328±82	7.1±0.44	1.06±0.02	2.31±0.60	252±4	577±230	7.1±0.08	7.1±0.08
cdo78	88.0	78	110.0	80	1629±34	8.7±0.18	0.92±0.00	1.38±0.02	194±2	376±90	4.1±0.02	6.9±1.58
cdo94	88.0	94	110.0	80	1997±152	10.6±0.80	1.07±0.22	2.68±1.86	252±26	526±410	5.7±0.02	6.9±2.58

Table 1: Subduction zone parameters and marker classification summary *(continued)*

Initial Boundary Conditions					Marker Classification Summary							
model	Φ	Z_{UP}	age	$\vec{v}$	recovered	rec. rate	P mode1	P mode2	T mode1	T mode2	grad mode1	grad mode2
	km	km	Ma	km/Ma		%	GPa	GPa	°C	°C	°C/km	°C/km
cdp46	110.0	46	110.0	100	1518±144	8±0.76	1.27±0.00	2.15±3.24	301±2	306±30	7±0.06	7±0.06
cdp62	110.0	62	110.0	100	1371±114	7.3±0.60	1.12±0.00	2.06±0.00	234±2	346±312	5.2±0.78	9.6±1.62
cdp78	110.0	78	110.0	100	1650±36	8.8±0.20	1.11±0.00	1.82±0.24	274±2	541±70	6.1±1.08	6.3±0.06
cdp94	110.0	94	110.0	100	1848±156	9.8±0.84	1.41±0.12	3.17±0.66	244±0	259±90	5.7±0.02	5.7±0.02

Classifier uncertainties (2σ) estimated by running the classifier 30 times with random marker samples (jackknife sample proportion: 90%)

4 Discussion

4.1 Thermo-Kinematic Controls on Rock Recovery

While the combined distribution of markers recovered from all numerical experiments shows appreciable deviations from PT estimates compiled by Penniston-Dorland et al. (2015) and Agard et al. (2018), markers recovered from simulations with the youngest oceanic plates (32.6-55 Ma) and the slowest convergence velocities (40-66 km/Ma) begin to resemble the distribution of exhumed HP rocks (compare Figure 4 with Figures 5 & 6) with respect to thermal gradients and P distributions. Slower subduction of younger plates increases marker thermal gradients and strongly shifts marker recovery down the subduction interface (strong correlations with Grad mode1 and P mode1 & mode2, Figure 7). The correlations in Figure 7 also suggest a shift towards warmer recovery conditions should be complemented by thin upper-plates—implying systems with thin upper-plates, slow convergence, and young oceanic plates should be most consistent with the distribution of rock recovery implied by pd15 and ag18 (Figure 5). This correspondence might appear consistent with inferences that the rock record is composed primarily of rock bodies exhumed from "warm" subduction settings (Abers et al., 2017; van Keken et al., 2018). However, our numerical experiments also show that recovery rates do not correlate with oceanic plate age or convergence velocity, and that recovery rates are poorer for thinner upper-plates (Figure 7). Correlations between thermo-kinematic boundary conditions and recovery rates drawn from many tens of thousands of recovered markers across numerous simulations counter the notion that preferential recovery is happening in "warm" subduction settings.

Besides recovery rates of subducting markers, other dynamic characteristics appear to correlate with oceanic plate age and convergence velocity. For example, simulations with slow convergence velocities (e.g. models: cda, cde, cdi, cdm) tend to have higher subduction angles (see Supplementary **??**)with thicker subduction interfaces that allow more markers to subduct to deeper, and thus warmer, conditions compared to other experiments (e.g. models: cdd, cdh, cdl, cdp) that form narrow interfaces with shallow choke points (e.g. see Supplementary **??**). Observationally, the angle of subduction does not correlate significantly with oceanic plate age or convergence velocity, but rather inversely with the duration of subduction (Hu & Gurnis, 2020). Thus, the rock record might indicate preferential exhumation during the earlier stages of subduction when subduction angles were steeper (although not necessarily during subduction initiation), even for older oceanic plates. More generally, differences in plate flexibility, overall subduction geometry, and velocity of plate motions strongly affect PT distributions of rock recovery (Monie & Agard, 2009)—rather than strictly "warm" versus "cool" subduction settings *per se*. In other words, thermo-kinematic boundary conditions typically inferred to strictly regulate *thermal* effects (e.g. young-slow oceanic plates supporting warmer thermal gradients) may indeed be regulating more *dynamic* effects (e.g. young-slow oceanic plates flexibly rolling back to support deeper subduction of material along thicker interfaces) that are subsequently *observed* as thermal effects (average increase in marker PT's).

4.2 Comparison with other Numerical Experiments

Marker PT distributions and their correlations with thermo-kinematic boundary conditions presented above are determined directly from large samples of recovered material evolving dynamically in a deforming subduction interface (analogous to reconstructing thermal gradients from large random samples of exhumed HP rocks). In contrast, other studies investigating thermal responses to variable boundary conditions typically determine PT gradients statically along discrete surfaces representing megathrust faults (e.g. Abers et al., 2006; Currie et al., 2004; Davies, 1999; Furukawa, 1993; Gao & Wang, 2014; McKenzie, 1969; Molnar & England, 1990; Peacock & Wang, 1999; Syracuse et al., 2010; van Keken et al., 2011, 2019; Wada & Wang, 2009) or dynamically by "finding" the subduction interface heuristically at each timestep (e.g. Arcay, 2017; Holt & Condit, 2021; Ruh et al., 2015). Other studies using similar geodynamic codes have traced many fewer markers (typically dozens vs. ˜ 120,000; Faccenda et al., 2008; Gerya et al., 2002; Sizova et al., 2010; Yamato et al., 2007, 2008) from a narrower range of thermo-kinematic boundary conditions, so they implicitly have less statistical rigor. This study stresses the importance of large sample sizes because individual marker PT paths can vary considerably within a single simulation, yet important modes of recovery become apparent from density peaks as more markers are traced. Furthermore, most other studies make no attempt to determine peak PT conditions related to detachment and *recovery* (with some exceptions, e.g. Roda et al., 2012, 2020), so marker PT paths are less analogous to PT paths determined by applying petrologic modeling.

4.3 Comparison with Geophysical Observations

The locations of important recovery modes determined from numerical experiments correspond closely with the depths of important mechanical transitions inferred from seismic imaging studies and surface heat flow observations. For example, the dominant recovery mode common among all numerical experiments at about 1 GPa (Table 1 & Figure 4) is consistent with a layer of low seismic velocities and high V_p/V_s ratios observed at numerous subduction zones between 20-50 km depth (Bostock, 2013). While considerable unknowns persist about the nature of deformation in this region (Bostock, 2013; Tewksbury-Christle & Behr, 2021), the low-velocity zone, accompanied by low-frequency and slow-slip seismic events, is often interpreted as a transitional brittle-ductile shear zone actively accommodating underplating of subducted material and/or formation of a tectonic mélange around the base of the continental Moho (Audet & Kim, 2016; Audet & Schaeffer, 2018; Bostock, 2013; Calvert et al., 2011, 2020; Delph et al., 2021).

Formation of low-velocity zones and their geophysical properties are generally attributed to high pore-fluid pressures caused by metamorphic reactions relating to the dehydration of oceanic crust (Hacker, 2008; Rondenay et al., 2008; van Keken et al., 2011). Surprisingly, despite our numerical implementation of a relatively simple model for dehydration of oceanic crust (Ito & Kennedy, 1971; Kerswell et al., 2021), and a relatively simple visco-plastic rheological model (Gerya & Yuen, 2003; Kerswell et al., 2021), the primary mode of marker recovery at 1.15 $\pm$ 0.46 GPa (2 σ, Table 1) coincides closely with the expected region for shallow underplating according to geophysical constraints (35 $\pm$ 15 km or 1.0 $\pm$ 0.4 GPa). The size of the markers dataset (n = 119,364 recovered markers) and prevalence of marker recovery from 1 GPa suggest that although dehydration may indeed trigger detachment of subducting rocks, other factors—notably the compositional and mechanical transition in the upper-plate across the Moho—also influence detachment at this depth.

The termination of the low-velocity zone at depths beyond the continental Moho marks another important mechanical transition. This second transition is often interpreted as the onset of mechanical plate coupling near 80 km (or 2.3 GPa) and coincides well with the deeper recovery modes determined from recovered markers at 2.2 $\pm$ 1.1 GPa (2 σ, Table 1). Between these two modes of recovery at $\sim$ 40 and $\sim$ 80 km lies a gap that coincides with the highest sample density of exhumed HP rocks compiled in pd15 and ag18 (Figure 4). This recovery gap is discussed in the following section.

4.4 The Marker Recovery Gap

Although recovered markers partially overlap with the range of PT estimates compiled in the pd15 and ag18 datasets, the differences between distributions of recovered markers and natural samples are numerous, including: (1) an obvious lack of markers recovered from ≥ 15 °C/km (0.002%) compared to pd15 and ag18 (37-48%, Figure 4), (2) recovery of markers from a single dominant mode near 1 GPa and 300 °C compared to more broadly distributed multimodal recovery across PT space for natural samples (Figure 4), (3) a general shift towards lower T's and cooler thermal gradients for markers compared to natural samples, and (4) a remarkable gap in marker recovery near 2 GPa and 550 °C that coincides with the highest density of natural samples (Figure 4). In fact, across 64 numerical experiments with wide-ranging initial conditions less than 1% (0.63%) of markers are recovered from between 1.8-2.2 GPa and 475-625 °C. Why might this gap occur? Four possibilities are considered:

1. Simple rheological models preclude certain recovery mechanisms (poor implementation of subduction interface mechanics, i.e., modeling uncertainty, Section 4.3)
2. Peak metamorphic conditions are systematically misinterpreted (peak metamorphic conditions do not correspond to maxP or PT paths are not well constrained, i.e., petrologic uncertainties, e.g., see Penniston-Dorland et al., 2015)
3. Rocks are frequently (re)sampled from the same peak metamorphic conditions and other rocks from different metamorphic grades are infrequently sampled (selective nonrandom sampling, i.e., scientific bias, e.g., see Agard et al., 2018)
4. Rocks are recovered during short-lived events (e.g., subduction of seamounts, Agard et al., 2009) that are not implemented in our numerical experiments, rather than recovered during steady-state subduction within a serpentine-rich tectonic mélange that is characteristic of our numerical experiments (i.e., geodynamic uncertainties)

4.4.1 Numerical Modeling Uncertainties

Simplifying assumptions in our numerical experiments influence thermal gradients and dynamics of rock recovery from the subducting oceanic plate. Substantially lower T's and thermal gradients in numerical experiments compared to natural samples (Figure 4) might indicate imperfect implementation of heat generation and transfer (Kohn et al., 2018; Penniston-Dorland et al., 2015). Our hydrologic model and implementation of serpentine rheology in the numerical experiments creates a weak interface. A stronger rheology (e.g., quartz or a mixed melange zone Beall et al., 2019; Ioannidi et al., 2021), or a stronger serpentine flow law (Burdette & Hirth, 2022), would yield greater heating and higher T's from enhanced viscous dissipation along the subduction interface (Kohn et al., 2018). In principle, a stronger rheology might shift the overall PT distribution of markers to higher T's and help fill in the marker recovery gap around 2 GPa and 550 °C, and/or possibly change flow to extract rocks more broadly along the subduction interface. Although the effects of different interface rheologies on thermal structure or rock recovery were not explicitly explored in this study, even numerical simulations with the smallest PT discrepancies between markers and natural samples (youngest oceanic plates and slowest convergence velocities, Figures 5 & 6) exhibit the same sizeable gap in marker recovery around 2 GPa and 550 °C. Thus, higher T's alone would not seem to close the gap.

4.4.2 Petrologic Uncertainties

Interpreting peak metamorphic conditions of complex polymetamorphic rocks is challenging with many sources of uncertainties. However, a global shift in PT estimates of natural samples towards warmer conditions compared to recovered markers would imply that decades of field observations, conventional thermobarometry (e.g. Spear & Selverstone, 1983), phase equilibria modeling (e.g. Connolly, 2005), trace element thermometry (e.g. Ferry & Watson, 2007; Kohn, 2020), and Raman Spectroscopy of Carbonaceous Material thermometry (Beyssac et al., 2002) from many independent localities worldwide (e.g. Agard et al., 2009, 2018; Angiboust et al., 2009, 2012a, 2016; Avigad & Garfunkel, 1991; Monie & Agard, 2009; Plunder et al., 2013, 2015) have systematically misinterpreted the prograde and retrograde histories of exhumed HP rocks. The consistency of independent analytical techniques suggests systematic bias is unlikely and estimated uncertainties are generally too small for this argument to be viable (Penniston-Dorland et al., 2015).

4.4.3 Selective Sampling and Scientific Bias

At least two factors might lead to scientific bias. First, the application of conventional thermobarometry is easier for certain rock types and mineral assemblages (e.g. eclogite-facies metabasites and metapelitic schists) than for others (e.g. quartzites, metagraywackes). Second, certain subduction complexes expose more rocks than others. These factors lead to sampling bias, both in the rocks that are selected for analysis and which subduction complexes contribute most to compilations. For example, a PT condition of ~ 2 GPa and 550 °C typically yields assemblages that are both recognizable in the field (eclogites, *sensu stricto*, and kyanite- or chloritoid-schists) and amenable to thermobarometric calculations and petrologic modeling. This fact may lead to oversampling of the rocks that yield these PT conditions and the subduction zones that expose these rocks. In Penniston-Dorland et al. (2015), the western and central European Alps, which contain many rocks that equilibrated near this PT condition, represented ~ 90 samples across < 1000 km (~ 1 sample per 100 km), whereas the Himalaya and Andes, which contained more diverse PT conditions, represented only ~ 1 sample per 300-400 km. Some subduction zones are not represented at all in these datasets (e.g. central and western Aleutians, Kamchatka, Izu-Bonin-Marianas, Philippines, Indonesia, etc.), either because metamorphic rocks are not exposed or rock types are not amenable to petrologic investigation. Correcting for this type of bias is challenging because it would require large random samples of exhumed HP rocks from localities worldwide and development of new techniques for quantifying PT conditions in diverse rock types.

4.4.4 Short-lived Events and Geodynamic Uncertainties

Detachment of rocks from the subducting slab might not occur randomly, but rather in response to specific events, such as subduction of asperities or seamounts (e.g. Agard et al., 2009) or abrupt fluid events. Yet no numerical models have attempted to model these events. In the case of seamounts, high surface roughness correlates with higher coefficients of friction (Gao & Wang, 2014). Higher friction increases heating and T's, driving subduction interface thermal gradients into the field of PT conditions defined by the pd15 and ag18 datasets (Kohn et al., 2018). If asperities become mechanically unstable at depths of $\sim$ 50-70 km, preferential detachment would create an "overabundance" of recorded PT conditions at moderate T ($\sim$ 550 °C) at $\sim$ 2 GPa, as observed.

Alternatively, although fluid release is modeled in our numerical experiments as continuous, it may occur sporadically. Two dehydration reactions along the subduction interface are particularly relevant: the transformation of lawsonite to epidote, and the transformation of chlorite (plus quartz) to garnet. Although dehydration of lawsonite is nearly discontinuous in PT space, few rocks show clear evidence for lawsonite immediately prior to peak metamorphism (although such evidence can be subtle). In the context of equilibrium thermodynamics, chlorite dehydration should occur continuously below depths of $\sim$ 35 km, consistent with assumptions of many numerical geodynamic models. However, research suggests substantial overstepping of this reaction, resulting in the abrupt formation of abundant garnet and release of water (Castro & Spear, 2017). Direct geochronology of garnet growth rates in subduction complexes also suggests abrupt growth and water release (Dragovic et al., 2015). Because fluids are thought to help trigger brittle failure (earthquakes) that could detach rocks from the subducting slab surface, abrupt release at a depth of $\sim$ 50-70 km might again result in an "overabundance" of recorded PT conditions at P's of $\sim$ 2 GPa. This mechanism would require relatively consistent degrees of overstepping in rocks of similar bulk composition and would not directly explain higher T's, however.

5 Conclusion

This study traces PT paths of more than one million markers from 64 subduction simulations representing a large range of presently active subduction zones worldwide. Marker recovery is identified by implementing a "soft" clustering algorithm, and PT distributions of recovered markers are compared among models and with the rock record. Such a large dataset presents a statistically-robust portrait of important recovery modes (where most markers are detached) along the subduction interface. The three most important findings are as follows:

1. Numerical simulations with relatively simple (de)hydration models and visco-plastic interface rheologies simulate important recovery mechanisms near the base of the continental Moho around 1 GPa and 300 °C (underplating and/or formation of

tectonic mélanges) and near the depth of mechanical plate coupling around 2.5 GPa and 525 °C.

2. Subduction systems with young oceanic plates, slow convergence velocities, and thin upper-plate lithospheres are most consistent with the rock record, but it is unclear to what extent kinematic effects (young flexible oceanic plates with high subduction angles accommodating deeper subduction of material) rather than thermal effects (young oceanic plates supporting higher thermal gradients) drive changes in marker PT distributions. Comparing young-slow-thin numerical experiments to the rock record is not straightforward, however, because recovery rates do not correlate with either oceanic plate age or convergence velocity, and warmer subduction zones yield poorer recovery rates.
3. A gap in marker recovery near 2 GPa and 550 °C coinciding with the highest densities of natural samples suggests an "overabundance" of samples are studied from this PT region. Explanations for this "overabundance" might include selective sampling of rocks amenable to petrologic investigation (scientific bias), reaction overstepping (abrupt release of water triggering detachment of rock near 2 GPa and 550 °C), or processes such as subduction of seamounts that are not included in numerical simulations. Future work investigating natural samples from a larger range of peak PT conditions and analyzing marker recovery from numerical geodynamic models that include new hydrologic models and interface rheologies might help resolve this discrepancy.

Open Research

All data, code, and relevant information for reproducing this work can be found at `https://github.com/buchanankerswell/kerswell_et_al_marx`, and at `https://doi.org/10.17605/OSF.IO/3EMWF`, the official Open Science Framework data repository. All code is MIT Licensed and free for use and distribution (see license details).

Acknowledgments

We gratefully acknowledge high-performance computing support from the Borah compute cluster (DOI: `10.18122/oit/3/boisestate`) provided by Boise State University's Research Computing Department. This work was supported by the National Science Foundation grant OIA1545903 to M. Kohn, S. Penniston-Dorland, and M. Feineman.

References

Abers, G., Keken, P. van, Kneller, E., Ferris, A., & Stachnik, J. (2006). The thermal structure of subduction zones constrained by seismic imaging: Implications for slab dehydration and wedge flow. *Earth and Planetary Science Letters*, *241*(3-4), 387–397.

Abers, G., van Keken, P., & Hacker, B. (2017). The cold and relatively dry nature of mantle forearcs in subduction zones. *Nature Geoscience*, *10*(5), 333–337.

Abers, G., Keken, P. van, & Wilson, C. (2020). Deep decoupling in subduction zones: Observations and temperature limits. *Geosphere*, *16*(6), 1408–1424.

Agard, P. (2021). Subduction of oceanic lithosphere in the alps: Selective and archetypal from (slow-spreading) oceans. *Earth-Science Reviews*, *214*, 103517.

Agard, P., Yamato, P., Jolivet, L., & Burov, E. (2009). Exhumation of oceanic blueschists and eclogites in subduction zones: Timing and mechanisms. *Earth-Science Reviews*, *92*(1-2), 53–79.

Agard, P., Yamato, P., Soret, M., Prigent, C., Guillot, S., Plunder, A., et al. (2016). Plate interface rheological switches during subduction infancy: Control on slab penetration and metamorphic sole formation. *Earth and Planetary Science Letters*, *451*, 208–220.

Agard, P., Plunder, A., Angiboust, S., Bonnet, G., & Ruh, J. (2018). The subduction plate interface: Rock record and mechanical coupling (from long to short time scales). *Lithos*, *320-321*, 537–566.

Agard, P., Prigent, C., Soret, M., Dubacq, B., Guillot, S., & Deldicque, D. (2020). Slabitization: Mechanisms controlling subduction development and viscous coupling. *Earth-Science Reviews*, *208*, 103259.

Angiboust, S., Agard, P., Jolivet, L., & Beyssac, O. (2009). The zermatt-saas ophiolite: The largest (60-km wide) and deepest (c. 70–80 km) continuous slice of oceanic lithosphere detached from a subduction zone? *Terra Nova*, *21*(3), 171–180.

Angiboust, S., Agard, P., Raimbourg, H., Yamato, P., & Huet, B. (2011). Subduction interface processes recorded by eclogite-facies shear zones (monviso, w. alps). *Lithos*, *127*(1-2), 222–238.

Angiboust, S., Langdon, R., Agard, P., Waters, D., & Chopin, C. (2012a). Eclogitization of the monviso ophiolite (w. Alps) and implications on subduction dynamics. *Journal of Metamorphic Geology*, *30*(1), 37–61.

Angiboust, S., Wolf, S., Burov, E., Agard, P., & Yamato, P. (2012b). Effect of fluid circulation on subduction interface tectonic processes: Insights from thermo-mechanical numerical modelling. *Earth and Planetary Science Letters*, *357*, 238–248.

Angiboust, S., Kirsch, J., Oncken, O., Glodny, J., Monié, P., & Rybacki, E. (2015). Probing the transition between seismically coupled and decoupled segments along an ancient subduction interface. *Geochemistry, Geophysics, Geosystems*, *16*(6), 1905–1922.

Angiboust, S., Agard, P., Glodny, J., Omrani, J., & Oncken, O. (2016). Zagros blueschists: Episodic underplating and long-lived cooling of a subduction zone. *Earth and Planetary Science Letters*, *443*, 48–58.

Arcay, D. (2017). Modelling the interplate domain in thermo-mechanical simulations of subduction: Critical effects of resolution and rheology, and consequences on wet mantle melting. *Physics of the Earth and Planetary Interiors*, *269*, 112–132.

Audet, P., & Kim, Y. (2016). Teleseismic constraints on the geological environment of deep episodic slow earthquakes in subduction zone forearcs: A review. *Tectonophysics*, *670*, 1–15.

Audet, P., & Schaeffer, A. (2018). Fluid pressure and shear zone development over the locked to slow slip region in cascadia. *Science Advances*, *4*(3), eaar2982.

Avigad, D., & Garfunkel, Z. (1991). Uplift and exhumation of high-pressure metamorphic terrains: The example of the cycladic blueschist belt (aegean sea). *Tectonophysics*, *188*(3-4), 357–372.

Banfield, J., & Raftery, A. (1993). Model-based gaussian and non-gaussian clustering. *Biometrics*, 803–821.

Barlow, H. (1989). Unsupervised learning. *Neural Computation*, *1*(3), 295–311.

Batchelor, G. (1953). *The theory of homogeneous turbulence*. Cambridge university press.

Beall, A., Fagereng, Å., & Ellis, S. (2019). Strength of strained two-phase mixtures: Application to rapid creep and stress amplification in subduction zone mélange. *Geophysical Research Letters*, *46*(1), 169–178.

Bebout, G. (2007). Metamorphic chemical geodynamics of subduction zones. *Earth and Planetary Science Letters*, *260*(3-4), 373–393.

Bebout, G., & Barton, M. (2002). Tectonic and metasomatic mixing in a high-t, subduction-zone mélange—insights into the geochemical evolution of the slab–mantle interface. *Chemical Geology*, *187*(1-2), 79–106.

Beyssac, O., Goffé, B., Chopin, C., & Rouzaud, J. (2002). Raman spectra of carbonaceous material in metasediments: A new geothermometer. *Journal of Metamorphic Geology*, *20*(9), 859–871.

Bostock, M. (2013). The moho in subduction zones. *Tectonophysics*, *609*, 547–557.

Boussinesq, J. (1897). *Théorie de l'écoulement tourbillonnant et tumultueux des liquides dans les lits rectilignes a grande section* (Vol. 1). Gauthier-Villars.

Burdette, E., & Hirth, G. (2022). Creep rheology of antigorite: Experiments at subduction zone conditions. *Journal of Geophysical Research: Solid Earth*, *127*(7), e2022JB024260.

Burov, E., François, T., Agard, P., Le Pourhiet, L., Meyer, B., Tirel, C., et al. (2014). Rheological and geodynamic controls on the mechanisms of subduction and HP/UHP exhumation of crustal rocks during continental collision: Insights from numerical models. *Tectonophysics*, *631*, 212–250.

Calvert, A., Preston, L., & Farahbod, A. (2011). Sedimentary underplating at the cascadia mantle-wedge corner revealed by seismic imaging. *Nature Geoscience*, *4*(8), 545–548.

Calvert, A., Bostock, M., Savard, G., & Unsworth, M. (2020). Cascadia low frequency earthquakes at the base of an overpressured subduction shear zone. *Nature Communications*, *11*(1), 1–10.

Castro, A., & Spear, F. (2017). Reaction overstepping and re-evaluation of peak p–t conditions of the blueschist unit sifnos, greece: Implications for the cyclades subduction zone. *International Geology Review*, *59*(5-6), 548–562.

Celeux, G., & Govaert, G. (1995). Gaussian parsimonious clustering models. *Pattern Recognition*, *28*(5), 781–793.

Cloos, M., & Shreve, R. (1988). Subduction-channel model of prism accretion, melange formation, sediment subduction, and subduction erosion at convergent plate margins: 1. Background and description. *Pure and Applied Geophysics*, *128*(3), 455–500.

Connolly, J. (2005). Computation of phase equilibria by linear programming: A tool for geodynamic modeling and its application to subduction zone decarbonation. *Earth and Planetary Science Letters*, *236*(1-2), 524–541.

Currie, C., & Hyndman, R. (2006). The thermal structure of subduction zone back arcs. *Journal of Geophysical Research: Solid Earth*, *111*(B8), 1–22.

Currie, C., Wang, K., Hyndman, R., & He, J. (2004). The thermal effects of steady-state slab-driven mantle flow above a subducting plate: The cascadia subduction zone and backarc. *Earth and Planetary Science Letters*, *223*(1-2), 35–48.

Davies, J. (1999). Simple analytic model for subduction zone thermal structure. *Geophysical Journal International*, *139*(3), 823–828.

Delph, J., Thomas, A., & Levander, A. (2021). Subcretionary tectonics: Linking variability in the expression of subduction along the cascadia forearc. *Earth and Planetary Science Letters*, *556*, 116724.

Dempster, A., Laird, N., & Rubin, D. (1977). Maximum likelihood from incomplete data via the EM algorithm. *Journal of the Royal Statistical Society: Series B (Methodological)*, *39*(1), 1–22.

Dragovic, B., Baxter, E., & Caddick, M. (2015). Pulsed dehydration and garnet growth during subduction revealed by zoned garnet geochronology and thermodynamic modeling, sifnos, greece. *Earth and Planetary Science Letters*, *413*, 111–122.

England, P., Engdahl, R., & Thatcher, W. (2004). Systematic variation in the depths of slabs beneath arc volcanoes. *Geophysical Journal International*, *156*(2), 377–408.

Faccenda, M., Gerya, T., & Chakraborty, S. (2008). Styles of post-subduction collisional orogeny: Influence of convergence velocity, crustal rheology and radiogenic heat production. *Lithos*, *103*(1-2), 257–287.

Ferris, A., Abers, G., Christensen, D., & Veenstra, E. (2003). High resolution image of the subducted pacific (?) Plate beneath central alaska, 50–150 km depth. *Earth and Planetary Science Letters*, *214*(3-4), 575–588.

Ferry, J., & Watson, E. (2007). New thermodynamic models and revised calibrations for the ti-in-zircon and zr-in-rutile thermometers. *Contributions to Mineralogy and Petrology*, *154*(4), 429–437.

Figueiredo, M., & Jain, A. (2002). Unsupervised learning of finite mixture models. *IEEE Transactions on Pattern Analysis and Machine Intelligence*, *24*(3), 381–396.

Fisher, D., Hooker, J., Smye, A., & Chen, T. (2021). Insights from the geological record of deformation along the subduction interface at depths of seismogenesis. *Geosphere*, *17*(6), 1686–1703.

Fraley, C., & Raftery, A. (2002). Model-based clustering, discriminant analysis, and density estimation. *Journal of the American Statistical Association*, *97*(458), 611–631.

Furukawa, Y. (1993). Depth of the decoupling plate interface and thermal structure under arcs. *Journal of Geophysical Research: Solid Earth*, *98*(B11), 20005–20013.

Gao, X., & Wang, K. (2014). Strength of stick-slip and creeping subduction megathrusts from heat flow observations. *Science*, *345*(6200), 1038–1041.

Gerya, T. (2019). *Introduction to numerical geodynamic modelling.* Cambridge University Press.

Gerya, T., & Stöckhert, B. (2006). Two-dimensional numerical modeling of tectonic and metamorphic histories at active continental margins. *International Journal of Earth Sciences*, *95*(2), 250–274.

Gerya, T., & Yuen, D. (2003). Characteristics-based marker-in-cell method with conservative finite-differences schemes for modeling geological flows with strongly variable transport properties. *Physics of the Earth and Planetary Interiors*, *140*(4), 293–318.

Gerya, T., Stöckhert, B., & Perchuk, A. (2002). Exhumation of high-pressure metamorphic rocks in a subduction channel: A numerical simulation. *Tectonics*, *21*(6), 6–1.

Gerya, T., Connolly, J., & Yuen, D. (2008). Why is terrestrial subduction one-sided? *Geology*, *36*(1), 43–46.

Gorczyk, W., Willner, A., Gerya, T., Connolly, J., & Burg, J. (2007). Physical controls of magmatic productivity at pacific-type convergent margins: Numerical modelling. *Physics of the Earth and Planetary Interiors*, *163*(1-4), 209–232.

Groppo, C., Rolfo, F., Sachan, H., & Rai, S. (2016). Petrology of blueschist from the western himalaya (ladakh, NW india): Exploring the complex behavior of a lawsonite-bearing system in a paleo-accretionary setting. *Lithos*, *252*, 41–56.

Hacker, B. (1996). Eclogite formation and the rheology, buoyancy, seismicity, and h˜ 2O content of oceanic crust. *GEOPHYSICAL MONOGRAPH-AMERICAN GEOPHYSICAL UNION*, *96*, 337–346.

Hacker, B. (2008). H2O subduction beyond arcs. *Geochemistry, Geophysics, Geosystems*, *9*(3).

Hacker, B., Abers, G., & Peacock, S. (2003). Subduction factory 1. Theoretical mineralogy, densities, seismic wave speeds, and H_2O contents. *Journal of Geophysical Research: Solid Earth*, *108*(B1).

Harlow, F. (1962). *The particle-in-cell method for numerical solution of problems in fluid dynamics*. Los Alamos Scientific Lab., N. Mex.

Harlow, F. (1964). The particle-in-cell computing method for fluid dynamics. *Methods Comput. Phys.*, *3*, 319–343.

Harlow, F., & Welch, J. (1965). Numerical calculation of time-dependent viscous incompressible flow of fluid with free surface. *The Physics of Fluids*, *8*(12), 2182–2189.

Hilairet, N., Reynard, B., Wang, Y., Daniel, I., Merkel, S., Nishiyama, N., & Petitgirard, S. (2007). High-pressure creep of serpentine, interseismic deformation, and initiation of subduction. *Science*, *318*(5858), 1910–1913.

Holt, A., & Condit, C. (2021). Slab temperature evolution over the lifetime of a subduction zone. *Geochemistry, Geophysics, Geosystems*, e2020GC009476.

Hu, J., & Gurnis, M. (2020). Subduction duration and slab dip. *Geochemistry, Geophysics, Geosystems*, *21*(4), e2019GC008862.

Hyndman, R., & Peacock, S. (2003). Serpentinization of the forearc mantle. *Earth and Planetary Science Letters*, *212*(3-4), 417–432.

Hyndman, R., Currie, C., & Mazzotti, S. (2005). Subduction zone backarcs, mobile belts, and orogenic heat. *GSA Today*, *15*(2), 4–10.

Ioannidi, P., Angiboust, S., Oncken, O., Agard, P., Glodny, J., & Sudo, M. (2020). Deformation along the roof of a fossil subduction interface in the transition zone below seismogenic coupling: The austroalpine case and new insights from the malenco massif (central alps). *Geosphere*, *16*(2), 510–532.

Ioannidi, P., Le Pourhiet, L., Agard, P., Angiboust, S., & Oncken, O. (2021). Effective rheology of a two-phase subduction shear zone: Insights from numerical simple shear experiments and implications for subduction zone interfaces. *Earth and Planetary Science Letters*, *566*, 116913.

Ito, K., & Kennedy, G. (1971). An experimental study of the basalt-garnet granulite-eclogite transition. *The Structure and Physical Properties of the Earth's Crust*, *14*, 303–314.

Karato, S., & Wu, P. (1993). Rheology of the upper mantle: A synthesis. *Science*, *260*(5109), 771–778.

Kerswell, B., & Kohn, M. (2022). A comparison of surface heat flow interpolations near subduction zones. *Submitted to Geochemistry, Geophysics, Geosystems.*

Kerswell, B., Kohn, M., & Gerya, T. (2021). Backarc lithospheric thickness and serpentine stability control slab-mantle coupling depths in subduction zones. *Geochemistry, Geophysics, Geosystems*, *22*(6), e2020GC009304.

Kitamura, Y., & Kimura, G. (2012). Dynamic role of tectonic mélange during interseismic process of plate boundary mega earthquakes. *Tectonophysics*, *568*, 39–52.

Kohn, M. (2020). A refined zirconium-in-rutile thermometer. *American Mineralogist: Journal of Earth and Planetary Materials*, *105*(6), 963–971.

Kohn, M., Castro, A., Kerswell, B., Ranero, C. R., & Spear, F. (2018). Shear heating reconciles thermal models with the metamorphic rock record of subduction. *Proceedings of the National Academy of Sciences*, *115*(46), 11706–11711.

Kotowski, A., & Behr, W. (2019). Length scales and types of heterogeneities along the deep subduction interface: Insights from exhumed rocks on syros island, greece. *Geosphere*, *15*(4), 1038–1065.

Locatelli, M., Federico, L., Agard, P., & Verlaguet, A. (2019). Geology of the southern monviso metaophiolite complex (w-alps, italy). *Journal of Maps*, *15*(2), 283–297.

Mann, M., Abers, G., Daly, K., & Christensen, D. (2022). Subduction of an oceanic plateau across southcentral alaska: Scattered-wave imaging. *Journal of Geophysical Research: Solid Earth*, e2021JB022697.

McKenzie, D. (1969). Speculations on the consequences and causes of plate motions. *Geophysical Journal International*, *18*(1), 1–32.

Molnar, P., & England, P. (1990). Temperatures, heat flux, and frictional stress near major thrust faults. *Journal of Geophysical Research: Solid Earth*, *95*(B4), 4833–4856.

Monie, P., & Agard, P. (2009). Coeval blueschist exhumation along thousands of kilometers: Implications for subduction channel processes. *Geochemistry, Geophysics, Geosystems*, *10*(7).

Moresi, L., Dufour, F., & Mühlhaus, H. (2003). A lagrangian integration point finite element method for large deformation modeling of viscoelastic geomaterials. *Journal of Computational Physics*, *184*(2), 476–497.

Morishige, M., & Kuwatani, T. (2020). Bayesian inversion of surface heat flow in subduction zones: A framework to refine geodynamic models based on observational constraints. *Geophysical Journal International*, *222*(1), 103–109.

Naif, S., Key, K., Constable, S., & Evans, R. (2015). Water-rich bending faults at the m iddle a merica t rench. *Geochemistry, Geophysics, Geosystems*, *16*(8), 2582–2597.

Okay, A. (1989). Alpine-himalayan blueschists. *Annual Review of Earth and Planetary Sciences*, *17*(1), 55–87.

Peacock, S. (1990). Fluid processes in subduction zones. *Science*, *248*(4953), 329–337.

Peacock, S. (1996). Thermal and petrologic structure of subduction zones. *Subduction: Top to Bottom*, *96*, 119–133.

Peacock, S., & Wang, K. (1999). Seismic consequences of warm versus cool subduction metamorphism: Examples from southwest and northeast japan. *Science*, *286*(5441), 937–939.

Penniston-Dorland, S., Kohn, M., & Manning, C. (2015). The global range of subduction zone thermal structures from exhumed blueschists and eclogites: Rocks are hotter than models. *Earth and Planetary Science Letters*, *428*, 243–254.

Platt, J. (1986). Dynamics of orogenic wedges and the uplift of high-pressure metamorphic rocks. *Geological Society of America Bulletin*, *97*(9), 1037–1053.

Plunder, A., Agard, P., Chopin, C., & Okay, A. (2013). Geodynamics of the tavşanlı zone, western turkey: Insights into subduction/obduction processes. *Tectonophysics*, *608*, 884–903.

Plunder, A., Agard, P., Chopin, C., Pourteau, A., & Okay, A. (2015). Accretion, underplating and exhumation along a subduction interface: From subduction initiation to continental subduction (tavşanlı zone, w. turkey). *Lithos*, *226*, 233–254.

Plunder, A., Thieulot, C., & Van Hinsbergen, D. (2018). The effect of obliquity on temperature in subduction zones: Insights from 3-d numerical modeling. *Solid Earth*, *9*(3), 759–776.

Ranalli, G. (1995). *Rheology of the earth*. Springer Science & Business Media.

Reynolds, D. (2009). Gaussian mixture models. *Encyclopedia of Biometrics*, *741*, 659–663.

Roda, M., Marotta, A., & Spalla, M. (2010). Numerical simulations of an ocean-continent convergent system: Influence of subduction geometry and mantle wedge hydration on crustal recycling. *Geochemistry, Geophysics, Geosystems*, *11*(5).

Roda, M., Spalla, M., & Marotta, A. (2012). Integration of natural data within a numerical model of ablative subduction: A possible interpretation for the alpine dynamics of the austroalpine crust. *Journal of Metamorphic Geology*, *30*(9), 973–996.

Roda, M., Zucali, M., Regorda, A., & Spalla, M. (2020). Formation and evolution of a subduction-related mélange: The example of the rocca canavese thrust sheets (western alps). *Bulletin*, *132*(3-4), 884–896.

Rondenay, S., Abers, G., & van Keken, P. (2008). Seismic imaging of subduction zone metamorphism. *Geology*, *36*(4), 275–278.

Ruh, J., Le Pourhiet, L., Agard, P., Burov, E., & Gerya, T. (2015). Tectonic slicing of subducting oceanic crust along plate interfaces: Numerical modeling. *Geochemistry, Geophysics, Geosystems*, *16*(10), 3505–3531.

Schmidt, M., & Poli, S. (1998). Experimentally based water budgets for dehydrating slabs and consequences for arc magma generation. *Earth and Planetary Science Letters*, *163*(1-4), 361–379.

Schwarz, G. (1978). Estimating the dimension of a model. *The Annals of Statistics*, 461–464.

Scrucca, L., Fop, M., Murphy, T., & Raftery, A. (2016). Mclust 5: Clustering, classification and density estimation using gaussian finite mixture models. *The R Journal*, *8*(1), 289.

Shreve, R., & Cloos, M. (1986). Dynamics of sediment subduction, melange formation, and prism accretion. *Journal of Geophysical Research: Solid Earth*, *91*(B10), 10229–10245.

Sizova, E., Gerya, T., Brown, M., & Perchuk, L. (2010). Subduction styles in the precambrian: Insight from numerical experiments. *Lithos*, *116*(3-4), 209–229.

Soret, M., Bonnet, G., Agard, P., Larson, K., Cottle, J., Dubacq, B., et al. (2022). Timescales of subduction initiation and evolution of subduction thermal regimes. *Earth and Planetary Science Letters*, *584*, 117521.

Spear, F., & Selverstone, J. (1983). Quantitative PT paths from zoned minerals: Theory and tectonic applications. *Contributions to Mineralogy and Petrology*, *83*(3), 348–357.

Stöckhert, B. (2002). Stress and deformation in subduction zones: Insight from the record of exhumed metamorphic rocks. *Geological Society, London, Special Publications*, *200*(1), 255–274.

Syracuse, E., & Abers, G. (2006). Global compilation of variations in slab depth beneath arc volcanoes and implications. *Geochemistry, Geophysics, Geosystems*, *7*(5).

Syracuse, E., van Keken, P., Abers, G., Suetsugu, D., Bina, C., Inoue, T., et al. (2010). The global range of subduction zone thermal models. *Physics of the Earth and Planetary Interiors*, *183*(1-2), 73–90.

Tewksbury-Christle, C., & Behr, W. (2021). Constraints from exhumed rocks on the seismic signature of the deep subduction interface. *Geophysical Research Letters*, *48*(18).

Tewksbury-Christle, C., Behr, W., & Helper, M. (2021). Tracking deep sediment underplating in a fossil subduction margin: Implications for interface rheology and mass and volatile recycling. *Geochemistry, Geophysics, Geosystems*, *22*(3).

Turcotte, D., & Schubert, G. (2002). *Geodynamics*. Cambridge university press.

van Keken, P., Hacker, B., Syracuse, E., & Abers, G. (2011). Subduction factory: 4. Depth-dependent flux of H_2O from subducting slabs worldwide. *Journal of Geophysical Research*, *116*(b1), b01401.

van Keken, P., Wada, I., Abers, G., Hacker, B., & Wang, K. (2018). Mafic high-pressure rocks are preferentially exhumed from warm subduction settings. *Geochemistry, Geophysics, Geosystems*, *19*(9), 2934–2961.

van Keken, P., Wada, I., Sime, N., & Abers, G. (2019). Thermal structure of the forearc in subduction zones: A comparison of methodologies. *Geochemistry, Geophysics, Geosystems*, *20*(7), 3268–3288.

Vermeesch, P. (2018). IsoplotR: A free and open toolbox for geochronology. *Geoscience Frontiers*, *9*(5), 1479–1493.

Wada, I., & Wang, K. (2009). Common depth of slab-mantle decoupling: Reconciling diversity and uniformity of subduction zones. *Geochemistry, Geophysics, Geosystems*, *10*(10).

Wakabayashi, J. (2015). Anatomy of a subduction complex: Architecture of the franciscan complex, california, at multiple length and time scales. *International Geology Review*, *57*(5-8), 669–746.

Yamato, P., Agard, P., Burov, E., Le Pourhiet, L., Jolivet, L., & Tiberi, C. (2007). Burial and exhumation in a subduction wedge: Mutual constraints from thermomechanical modeling and natural p-t-t data (schistes lustrés, western alps). *Journal of Geophysical Research: Solid Earth*, *112*(B7).

Yamato, P., Burov, E., Agard, P., Le Pourhiet, L., & Jolivet, L. (2008). HP-UHP exhumation during slow continental subduction: Self-consistent thermodynamically and thermomechanically coupled model with application to the western alps. *Earth and Planetary Science Letters*, *271*(1-4), 63–74.

A Appendix

A.1 Gaussian Mixture Models

Let the traced markers represent a d-dimensional array of n random independent variables $x_i \in \mathbb{R}^{n \times d}$. Assume markers x_i were drawn from k discrete probability distributions with parameters Φ. The probability distribution of markers x_i can be modeled with a mixture of k components:

$$p(x_i|\Phi) = \sum_{j=1}^{k} \pi_j p(x_i|\Theta_j) \tag{A.1}$$

where $p(x_i|\Theta_j)$ is the probability of x_i under the j^{th} mixture component and π_j is the mixture proportion representing the probability that x_i belongs to the j^{th} component ($\pi_j \geq 0; \sum_{j=1}^{k} \pi_j = 1$).

Assuming Θ_j describes a Gaussian probability distributions with mean μ_j and covariance Σ_j, Equation (A.1) becomes:

$$p(x_i|\Phi) = \sum_{j=1}^{k} \pi_j \mathcal{N}(x_i|\mu_j, \Sigma_j) \tag{A.2}$$

where

$$\mathcal{N}(x_i|\mu_j, \Sigma_j) = \frac{exp\{-\frac{1}{2}(x_i - \mu_j)(x_i - \mu_j)^T \Sigma_j^{-1}\}}{\sqrt{det(2\pi\Sigma_j)}} \tag{A.3}$$

The parameters μ_j and Σ_j, representing the center and shape of each cluster, are estimated by maximizing the log of the likelihood function, $L(x_i|\Phi) = \prod_{i=1}^{n} p(x_i|\Phi)$:

$$log\ L(x_i|\Phi) = log \prod_{i=1}^{n} p(x_i|\Phi) = \sum_{i=1}^{n} log \left[\sum_{j=1}^{k} \pi_j p(x_i|\Theta_j) \right] \tag{A.4}$$

Taking the derivative of Equation (A.4) with respect to each parameter, π, μ, Σ, setting the equation to zero, and solving for each parameter gives the maximum likelihood estimators:

$$\begin{aligned} N_j &= \sum_{i=1}^{n} \omega_i \\ \pi_j &= \frac{N_j}{n} \\ \mu_j &= \frac{1}{N_j} \sum_{i=1}^{n} \omega_i x_i \\ \Sigma_j &= \frac{1}{N_j} \sum_{i=1}^{n} \omega_i (x_i - \mu_j)(x_i - \mu_j)^T \end{aligned} \tag{A.5}$$

where ω_i ($\omega_i \geq 0; \sum_{j=1}^{k} \omega_i = 1$) are membership weights representing the probability of an observation x_i belonging to the j^{th} Gaussian and N_j represents the number of observations belonging to the j^{th} Gaussian. Please note that ω_i is unknown for markers so maximum likelihood estimator cannot be computed with Equation (A.5). The solution to this problem is the Expectation-Maximization algorithm, which is defined below.

General purpose functions in the R package `Mclust` (Scrucca et al., 2016) are used to fit Gaussian mixture models. "Fitting" refers to adjusting all k Gaussian parameters μ_j and Σ_j until the data and Gaussian ellipsoids achieve maximum likelihood defined by Equation (A.4). After Banfield & Raftery (1993), covariance matrices Σ in `Mclust` are parameterized to be flexible in their shape, volume, and orientation (Scrucca et al., 2016):

$$\Sigma_j = \lambda_j D_j A_j D_j^T \tag{A.6}$$

where D_j is the orthogonal eigenvector matrix, A_j and λ_j are diagonal matrices of values proportional to the eigenvalues. This implementation allows fixing one, two, or three geometric elements of the covariance matrices. That is, the volume λ_j, shape A_j, and orientation D_j of Gaussian clusters can change or be fixed among all k clusters (e.g. Celeux & Govaert, 1995; Fraley & Raftery, 2002). Fourteen parameterizations of Equation (A.6) are tried, representing different geometric combinations of the covariance matrices Σ (see Scrucca et al., 2016) and the Bayesian information criterion is computed (Schwarz, 1978). The parameterization for Equation (A.6) is chosen by Bayesian information criterion.

A.2 Expectation-Maximization

The Expectation-Maximization algorithm estimates Gaussian mixture model parameters by initializing k Gaussians with parameters (π_j, μ_j, Σ_j), then iteratively computing membership weights with Equation (A.7) and updating Gaussian parameters with Equation (A.5) until reaching a convergence threshold (Dempster et al., 1977).

The *expectation* (E-)step involves a "latent" multinomial variable $z_i \in \{1, 2, \ldots, k\}$ representing the unknown classifications of x_i with a joint distribution $p(x_i, z_i) = p(x_i|z_i)p(z_j)$. Membership weights ω_i are equivalent to the conditional probability $p(z_i|x_i)$, which represents the probability of observation x_i belonging to the j^{th} Gaussian. Given initial guesses for Gaussian parameters π_j, μ_j, Σ_j, membership weights are computed using Bayes The-orem (E-step):

$$p(z_i|x_i) = \frac{p(x_i|z_i)p(z_j)}{p(x_i)} = \frac{\pi_j \mathcal{N}(\mu_j, \Sigma_j)}{\sum_{j=1}^{k} \pi_j \mathcal{N}(\mu_j, \Sigma_j)} = \omega_i \quad \text{(A.7)}$$

and Gaussian estimates are updated during the *maximization* (M-)step by applying ω_i to Equation (A.5). This step gives markers x_i class labels $z_i \in \{1, \ldots, k\}$ representing assignment to one of k clusters (Figure 2).

Computing Rates and Distributions of Rock Recovery in Subduction Zones

Buchanan C. Kerswell [1] Matthew J. Kohn [2] Taras V. Gerya [3]

[1] Department of Geology & Environmental Earth Science, Miami University, Oxford, OH 45056

[2] Department of Geosicences, Boise State University, Boise, ID 83725

[3] Department of Earth Sciences, ETH-Zurich, Sonneggstrasse 5, Zurich 8092, Switzerland

Key Points:

- Simulated rocks detach at depths consistent with major mechanical transitions along subduction interfaces
- Simulated rock PT distributions and recovery rates correlate with boundary conditions
- Few simulated rocks detach from the PT region of highest natural sample density

Corresponding author: Buchanan C. Kerswell, `buchanankerswell@u.boisestate.edu`

Abstract

Bodies of rock that are detached (recovered) from subducting oceanic plates, and exhumed to Earth's surface, become invaluable records of the mechanical and chemical processing of rock along subduction interfaces. Exposures of interface rocks with high-pressure (HP) mineral assemblages provide insights into the nature of rock recovery, yet various interpretations concerning thermal gradients, recovery rates, and recovery depths arise when directly comparing the rock record with numerical simulations of subduction. Constraining recovery rates and depths from the rock record presents a major challenge because small sample sizes of HP rocks makes statistical inference weak. As an alternative approach, this study implements numerical simulations of oceanic-continental convergence and applies a classification algorithm to identify rock recovery. Over one million markers are classified from 64 simulations representing a large range of subduction zones. We find recovery P's (depths) correlate strongly with convergence velocity and moderately with oceanic plate age, while PT gradients correlate strongly with oceanic plate age and upper-plate thickness. Recovery rates strongly correlate with upper-plate thickness, yet show no correlation with other boundary conditions. Likewise, PT distributions of recovered markers vary among numerical experiments and generally show poor overlap with the rock record. A significant gap in predicted marker recovery is found near 2 GPa and 550 °C, coinciding with the highest density of exhumed HP rocks. Implications for such a gap in marker recovery include numerical modeling uncertainties, petrologic uncertainties, selective sampling of exhumed HP rocks, or natural geodynamic factors not accounted for in numerical experiments.

Plain language summary

Converging tectonic plates leads to subduction of the denser plate beneath the other. Bodies of subducted rock that return to Earth's surface bring information about the deep subduction interface, yet the rates, depths, and mechanisms that detach rock from the subducting plate are not well-understood. As an alternative to studying rock samples, this study implements a machine learning algorithm to identify rock detachment in numerical simulations. Over one million simulated rocks are classified from 64 simulations representing a large range of possible subduction zones. Marker pressure-temperature (PT) conditions are compared across models and with the rock record. Correlations are drawn among important model parameters, including plate velocities and plate thick-

ness, that reveal strong and weak effects on marker detachment. Recovery rates strongly correlate with upper-plate thickness, yet show no correlation with other parameters. Likewise, PT distributions of markers show variable compatibility with the rock record depending on the comparison. A significant gap marker recovery coincides with a large proportion of exhumed HP rocks. Implications for such a gap in marker recovery include numerical modeling uncertainties, petrologic uncertainties, selective sampling of exhumed HP rocks, or natural geodynamic factors not accounted for in numerical experiments.

1 Introduction

Maximum pressure-temperature (PT) conditions have been estimated for hundreds of high-pressure (HP) metamorphic rocks exhumed from subduction zones (Figure 1, Agard et al., 2018; Hacker, 1996; Penniston-Dorland et al., 2015). These samples represent fragments of oceanic crust, continental crust, seafloor sediments, and upper mantle that have detached from subducting oceanic and continental lithospheres at various depths along the interface between subducting and overriding tectonic plates (referred to as "recovery" after Agard et al. (2018). This *rock record* is the only tangible evidence of PT-strain fields, deep seismic cycling, and fluid flow within Earth's lithosphere during deformation and chemical processing in subduction zones. Together with geophysical imaging (e.g. Bostock, 2013; Ferris et al., 2003; Hyndman & Peacock, 2003; Mann et al., 2022; Naif et al., 2015; Rondenay et al., 2008; Syracuse & Abers, 2006), analysis of surface heat flow data (e.g. Currie & Hyndman, 2006; Gao & Wang, 2014; Hyndman et al., 2005; Kohn et al., 2018; Morishige & Kuwatani, 2020; Wada & Wang, 2009), and forward numerical geodynamic modeling (e.g. Gerya et al., 2002, 2008; Gerya & Stöckhert, 2006; Hacker et al., 2003; Kerswell et al., 2021; McKenzie, 1969; Peacock, 1990, 1996; Sizova et al., 2010; Syracuse et al., 2010; Yamato et al., 2007, 2008), investigation of the rock record underpins contemporary understandings of subduction geodynamics (e.g. Agard et al., 2009; Agard, 2021; Bebout, 2007).

However, it remains difficult to directly interpret the rock record in terms of recovery rates and distributions along the subduction interface. For example, compilations of PT estimates representing the global distribution of HP rocks exhumed during the Phanerozoic (the pd15 and ag18 datasets, Agard et al., 2018; Penniston-Dorland et al., 2015) reveal an abrupt decrease in relative sample abundance at P's above 2.3-2.4 GPa (Figure 1). For pd15 and ag18, a nearly-constant cumulative distribution (CDF) curve interrupted

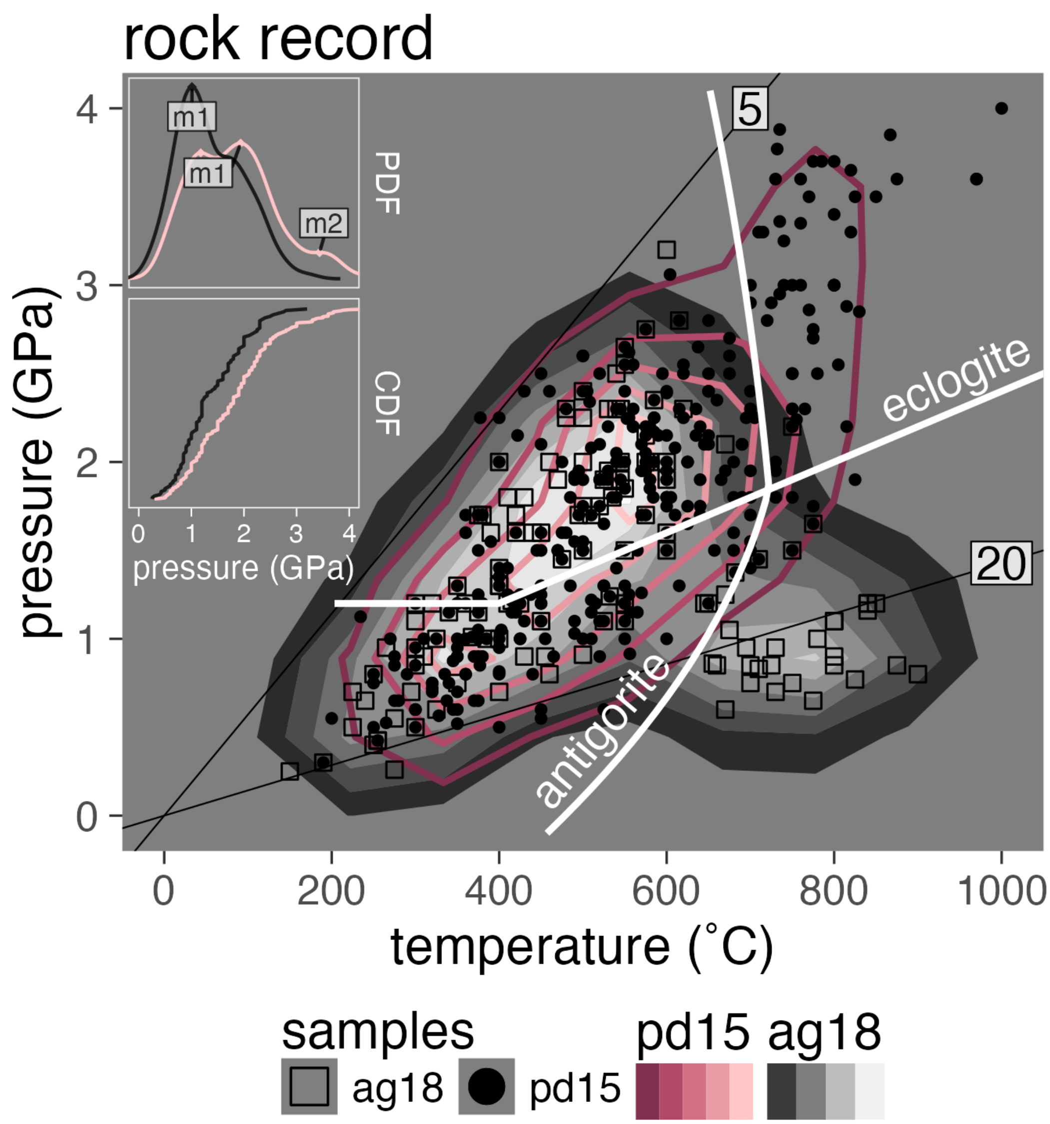

Figure 1: PT diagram showing distributions of PT estimates for exhumed HP metamorphic rock samples compiled in the pd15 (solid contours, Penniston-Dorland et al., 2015) and ag18 (filled contours, Agard et al., 2018) datasets. (insets) Probability distribution diagrams of pd15 and ag18 samples showing broad bimodal and trimodal sample distributions with respect to P (top inset) and a kinked CDF (bottom inset) indicating that a substantial proportion of markers are recovered from P's between 0.5-2.5 GPa with very few rocks reaching maximum P's above 3 GPa. Thin lines are thermal gradients labeled in °C/km. Reaction boundaries for eclogitization of oceanic crust and antigorite dehydration are from Ito & Kennedy (1971) and Schmidt & Poli (1998), respectively.

by a sharp change in slope around 2.3-2.4 GPa implies relatively uniform recovery of subducting material up to 2.3-2.4 GPa, but increasingly rare recovery above 2.3-2.4 GPa (Agard et al., 2018; Kerswell et al., 2021; Monie & Agard, 2009; Plunder et al., 2015). On the one hand, evidence for common mechanical coupling depths near 2.3 GPa (Furukawa, 1993; Kerswell et al., 2021; Wada & Wang, 2009) suggests an upper-limit to recovery depths that is consistent with the scarcity of (ultra-)HP samples in the rock record and invariant with respect to key thermo-kinematic parameters (convergence velocity, subduction geometry, plate thickness; Figure 1). On the other hand, substantial variations in lateral (along-strike) upper-plate surface heat flow patterns suggest coupling depths also vary substantially among subduction zone segments (Kerswell & Kohn, 2022) and do impose an invariant upper-limit to recovery depths. Moreover, geophysical constraints on the depths of key mechanical transitions likely to induce rock recovery (e.g. Abers et al., 2020; Audet & Kim, 2016; Audet & Schaeffer, 2018; Morishige & Kuwatani, 2020) suggest high recovery rates should cluster around discrete depths, rather than uniform and widespread recovery along the subduction interface implied by the pd15 and ag18 datasets.

Difficulties in relating complex polymetamorphic rocks from different environments challenge the use of PT distributions of exhumed HP rock samples as robust constraints on key subduction zone parameters. Interpretations of rock recovery mechanisms, subduction interface behavior, metamorphic reactions, seismic cycling, and subduction geodynamics might vary depending on metamorphic terrane (local tectonic environment), sampling strategy (random or targeted outcrops), sample size (how many outcrops were observed and sampled in the field), and analytical sample selection (investigating PT's and deformation histories for a subset of samples with a specific scientific question in mind). Different compilations of PT estimates can show different density distributions, in terms of relative abundances of samples across PT space, and thus imply different depths of rock recovery along the subduction interface. For example, Agard et al. (2018) noted that compilations from Plunder et al. (2015) and Groppo et al. (2016) show less dispersion (i.e. a more step-like CDF) than ag18 with tighter bimodal or trimodal distributions clustering around inferred depths of important mechanical transitions along the subduction interface. These peaks (modes) in distributions of exhumed HP rocks coincide with the continental Moho at approximately 25-35 km and the transition to mechanical plate coupling at approximately 80 km (Agard et al., 2018; Monie & Agard, 2009; Plunder et al., 2015). Less consensus explains a smaller, yet significant, intermediate mode at 55-

60 km (Agard et al., 2009, 2018; Plunder et al., 2015), although it is consistent with a high- density region of PT estimates in the pd15 dataset.

Differences in compiled PT datasets notwithstanding, key observations regarding rock recovery in subduction zones emerge from pd15 and ag18:

1. Rocks are recovered with relatively similar frequency up to 2.5 GPa
2. 64-66% of recovered rocks equilibrated between 1-2.5 GPa
3. 5-19% of recovered rocks equilibrated above 2.5 GPa
4. 32-34% of recovered rocks equilibrated between 350-525 °C
5. 50-56% of recovered rocks equilibrated above 525 °C
6. 52-62% of recovered rocks record gradients between 5-10 °C/km
7. 18-31% of recovered rocks record gradients between 10-15 °C/km
8. 6-30% of recovered rocks record gradients above 15 °C/km

These ranges in the relative abundances of exhumed HP rocks compiled in different datasets raise important questions in subduction zone research: are rocks recovered broadly and uniformly along the subduction interface or discretely from certain depths? How do recovery rates and distributions vary among diverse subduction zone settings and through time?

Previous work comparing the rock record directly with numerical models has generally produced ambiguous interpretations concerning recovery rates and distributions along the subduction interface. For example, comparisons of different numerical geodynamic codes with subsets of the rock record show variable agreement in terms of overlapping PT paths and thermal gradients (e.g. Angiboust et al., 2012b; Burov et al., 2014; Holt & Condit, 2021; Penniston-Dorland et al., 2015; Plunder et al., 2018; Roda et al., 2010, 2012, 2020; Ruh et al., 2015; Yamato et al., 2007, 2008). Initial setups for numerical experiments (oceanic plate age, convergence velocity, subduction dip angle, upper-plate thickness, and heating sources; Kohn et al., 2018; Penniston-Dorland et al., 2015; Ruh et al., 2015; van Keken et al., 2019), differential recovery rates from subduction zones with favorable thermo-kinematic boundary conditions (Abers et al., 2017; van Keken et al., 2018), and comparisons among suites of undifferentiated HP rocks (e.g. grouping rocks recovered during subduction initiation with rocks recovered during "steady-state" subduction, see Agard et al., 2018, 2020) all potentially contribute to nonoverlapping PT distributions and thermal gradients between exhumed HP rocks and numerical geodynamic models. Compounding the ambiguity are arguments that material is sporadically recovered during short-lived mechanical transitions (Agard et al., 2016) and/or geodynamic changes (Monie & Agard, 2009)—implying exhumed HP rocks are not random samples of the subduction interface during steady-state subduction. Such ambiguities warrant further investigation into the general response of recovery rates and distributions to broad ranges of thermo-kinematic boundary conditions and various implementations of subduction interface rheologies.

Fortunately, clues about the nature and PT limits of rock recovery are provided by many extensively studied examples of exhumed subduction interfaces (e.g. Agard et al., 2018; Angiboust et al., 2011; 2015; Cloos & Shreve, 1988; Fisher et al., 2021; Ioannidi et al., 2020; Kitamura & Kimura, 2012; Kotowski & Behr, 2019; Locatelli et al., 2019; Monie & Agard, 2009; Okay, 1989; Platt, 1986; Plunder et al., 2013, 2015; Tewksbury-Christle et al., 2021; Wakabayashi, 2015). However, these type localities represent an unknown fraction of subducted material and differ significantly in terms of their geometry (field relationships), composition (rock types), and interpreted deformation histories (both detachment and exhumation). It is also unclear to what extent ag18 and pd15 (and other compilations) represent the full range of recovery conditions and/or represent scientific sampling bias (e.g. undersampling low-grade rocks or oversampling high-grade rocks from the same pristine exposures, Agard et al., 2018). Thus, a primary challenge to inferring recovery rates and distributions accurately from the rock record fundamentally stems from sparse nonrandom samples (typically less than a few dozen PT estimates from any given exhumed terrane) compared to the diversity of thermo-kinematic parameters characterizing subduction zones and petro-thermo-mechanical conditions suitable for rock recovery along the subduction interface.

This study aims at addressing the sparsity and nonrandomness of exhumed HP rock samples by tracing numerous (1,341,729) Lagrangian markers from 64 numerical geodynamic simulations of oceanic-continental subduction (Kerswell et al., 2021). We first generate a PT dataset from instantiations of a particular numerical geodynamic code so large that it was insensitive to noise and outliers—thus representing a statistically robust picture of recovery rates and PT distributions in subduction zones. From such a large dataset of generated samples, we identify correlations among recovery rates, PT distributions, and thermo-kinematic boundary conditions that quantify parameter sensitivities and indicate ranges of plausible conditions for reproducing the rock record. In fact, surprisingly low densities of generated samples, in terms of their relative abundances across PT space, were found coinciding with the highest-density regions of natural samples around 2 GPa and 550 °C. We then discuss implications for poor overlap between generated sample densities and exhumed HP rock densities, including insufficient implementation of recovery mechanisms in numerical geodynamic models (numerical bias) and a potential overabundance of natural samples collected from similar metamorphic grades around 2 GPa and 550 °C (empirical bias).

2 Methods

This study presents a dataset of Lagrangian markers (described below) from numerical experiments that simulated 64 oceanic-continental convergent margins with thermo-kinematic boundary conditions (oceanic plate age, convergence velocity, and upper-plate lithospheric thickness) closely representing the range of presently active subduction zones (Syracuse & Abers, 2006; Wada & Wang, 2009). Initial conditions were modified from previous studies of active margins (Gorczyk et al., 2007; Sizova et al., 2010) using the numerical geodynamic code I2VIS (Gerya & Yuen, 2003). I2VIS models visco-plastic flow of geological materials by solving conservative equations of mass, energy, and momentum on a fully-staggered finite difference grid with a *marker-in-cell* technique (Gerya, 2019; Gerya & Yuen, 2003; e.g. Harlow & Welch, 1965). Complete details about the initial setup, boundary conditions, and rheological model are presented in Kerswell et al. (2021). Complete details about I2VIS and example code are presented in Gerya & Yuen (2003) and Gerya (2019).

The following section defines Lagrangian markers (now referred to as *markers*) and briefly elaborates on their usefulness in understanding flow of geological materials, followed by a description of the marker classification algorithm. A complete mathematical description of the classification algorithm is presented in Appendix A.1.

2.1 Lagrangian Markers

Markers are mathematical objects representing discrete parcels of material flowing in a continuum (Harlow, 1962, 1964). Tracing markers (saving marker information at each timestep) is distinctly advantageous for investigating subduction dynamics in the following two ways.

First, modeling subduction requires solving equations of mass, motion, and heat transport in a partly layered, partly heterogeneous, high-strain region known as the *plate interface*, *subduction interface*, or *subduction channel* (Gerya et al., 2002). Current conceptual models regard the subduction interface as a visco-plastic continuum with complex geometry and structure, sharp thermal, chemical, and strain gradients, strong advection, and abundant fluid flow (Agard et al., 2016, 2018; Bebout, 2007; Bebout & Barton, 2002; Cloos & Shreve, 1988; Gerya & Yuen, 2003; Penniston-Dorland et al., 2015; Shreve & Cloos, 1986; Stöckhert, 2002; Tewksbury-Christle et al., 2021). Finite-difference numerical approaches do not perform well with strong local gradients, and interpolating and updating T, strain, and chemical fields with markers greatly improves accuracy and stability of numerical solutions (Gerya, 2019; Gerya & Yuen, 2003; Moresi et al., 2003).

Second, tracing a marker closely proxies for tracing a rock's PT-time history. Strictly speaking, deviations between calculated PT-time histories of markers and rocks are possible because our numerical geodynamic simulations assume: (1) markers move in an incompressible continuum (Batchelor, 1953; Boussinesq, 1897), (2) material properties are governed by a simplified petrologic model describing eclogitization of oceanic crust (Ito & Kennedy, 1971) and (de)hydration of upper mantle ($antigorite \Leftrightarrow olivine + orthopyroxene + H_2O$, Schmidt & Poli, 1998), and (3) marker stress and strain are related by a highly non-linear rheological model derived from empirical flow laws (Hilairet et al., 2007; Karato & Wu, 1993; Ranalli, 1995; Turcotte & Schubert, 2002). For example, if rocks within a subduction interface shear zone were highly compressible or could sustain large deviatoric stresses, P's and T's might be different from markers. The hydrological model implemented in our numerical simulations, embodied by assumptions 2 and 3, exert particularly strong control on subduction interface strength, and thus the probability and style of detachment. Our simulations developed stable subduction channels (tectonic-mélanges, e.g. Gerya et al., 2002) instead of discrete shear zones that detach large coherent slices of oceanic lithosphere (e.g. Ruh et al., 2015) primarily due to our choice of hydrological model. However, insofar as subduction interface shear zones closely behave as mélange-like channels of incompressible visco-plastic fluids (under the assumptions above, Gerya, 2019; Gerya & Yuen, 2003; Kerswell et al., 2021), comparisons between marker PT distributions and the rock record may be made.

2.2 Marker Classification

For each numerical experiment, 20,986 markers were initially selected from within a 760 km-long and 8 km-deep section of oceanic crust and seafloor sediments at $t = 0$ Ma. Tracing proceeded for 115 timesteps (between 9.3-54.7 Ma depending on convergence velocity), which was sufficient for markers to be potentially subducted very deeply (up to 300 km) from their initial positions. However, only markers that detached from the subducting oceanic plate were relevant for comparison with PT estimates of exhumed HP rocks (because these markers and rocks were not subducted). The main challenge, therefore, was to first develop a method for determining which markers among 20,986 detached and moved away from the subducting plate without knowing their fate *a priori*. Moreover, the method needed to be generalizable to a large range of numerical experiments. Note that detached markers were classified as "recovered" even if they did not exhume to the surface within the modeling domain. Diverse processes can cause exhumation of subduction zone rocks, including later tectonic events, and our goal was to compare only the maximum metamorphic conditions of markers and rocks along their prograde paths.

Classifying unlabelled markers as either "recovered" or "not recovered" based solely on their undifferentiated traced histories defines an unsupervised classification problem (Barlow, 1989). Many methods can be applied to solve the unsupervised classification problem, yet this study implemented a Gaussian mixture model (Reynolds, 2009)—a type of "soft" clustering algorithm used extensively for pattern recognition, anomaly detection, and estimating complex probability distribution functions (e.g. Banfield & Raftery, 1993; Celeux & Govaert, 1995; Figueiredo & Jain, 2002; Fraley & Raftery, 2002; Vermeesch, 2018). "Hard" classification is possible by directly applying simple rules to markers without clustering (e.g. Roda et al., 2012). However, "hard" methods are less generalizable than "soft" approaches like Gaussian mixture models, which can be implemented to study many possible features in numerical simulations with Lagrangian reference frames—not just recovery of subducted material. In this case, a Gaussian mixture model organized markers into groups (clusters) by fitting $k = 14$ bivariate Gaussian ellipsoids to the distribution of markers in PT space. "Fitting" refers to adjusting parameters (centroids and covariance matrices) of all k Gaussian ellipsoids until the ellipsoids and data achieved maximum likelihood (see Appendix A.1 for a complete mathematical description). Finally, marker clusters with centroids located within certain bounds were classified as "recovered". The entire classification algorithm can be summarized as follows:

0. Select markers within a 760 km $\times$ 8 km section of oceanic crust
1. Trace markers for 115 timesteps
2. Identify maximum marker PT conditions (at either maxT or maxP)
3. Apply Gaussian mixture modeling to maximum marker PT conditions
4. Check for cluster centroids within the bounds:
    - $\geq$ 3 °C/km AND
    - $\leq$ 1300 °C AND
    - $\leq$ 120 km (3.4 GPa)
5. Classify marker clusters found in step 4 as "recovered"
6. Classify all other markers as "not recovered"

Note that maximum marker PT conditions used for clustering were assessed before markers transformed (dehydrated or melted) and before the accretionary wedge toe collided with the high-viscosity convergence region positioned at 500 km from the left boundary (to avoid spurious maximum PT conditions from sudden isothermal burial). We also tried applying different prograde PT path positions in step 2 by determining maximum marker T's (maxT) and maximum P's (maxP) independently. Applying maxP vs. maxT conditions to the classifier resulted in distinct PT distributions of recovered markers and distinct correlations among thermo-kinematic boundary conditions and marker recovery modes. For natural samples of exhumed HP rocks, compilations emphasize maxP, not maxT, (Penniston-Dorland et al., 2015), and thus empirical PT estimates are best compared with maxP conditions. Also, many PT paths for exhumed HP rocks have "hairpin" or isothermal decompression retrograde PT paths without significant heating during exhumation (Agard et al., 2009). Figures 2 & 3 illustrate marker classification for 1 of 64 numerical experiments. All other experiments are presented in Supplementary **??**.

2.3 Recovery Modes

To better quantify how rock recovery can vary among subduction zones with different boundary conditions, marker recovery modes (density peaks) were determined with respect to absolute PT and PT gradients. The highest-density peak (mode1) shows where the greatest abundance of markers are recovered. The deepest, or warmest, density peak (mode2) shows where the most deeply subducted markers (or markers with the highest PT gradients) are recovered. In other words, changes in the positions of mode1 and mode2 reflect variations in recovery conditions for “normal” recovery and “extreme cases”, respectively.

Note that correlations are not presented here with respect to the thermal parameter Φ (Φ = oceanic plate age $\cdot$ convergence velocity), unlike many studies. The rationale is three-fold: (1) the aim was to understand how oceanic plate age and convergence velocity affect marker recovery independently, (2) sample sizes of recovered markers were larger when grouped by oceanic plate age and convergence velocity (n = 335,788) compared to grouping by Φ (n = 83,947; implying they do not correlate well with Φ), and (3) and combining oceanic plate age and convergence velocity can draw unnecessarily ambiguous associations with other geodynamic features of subduction zones (e.g. Φ vs. H from England et al., 2004; Wada & Wang, 2009).

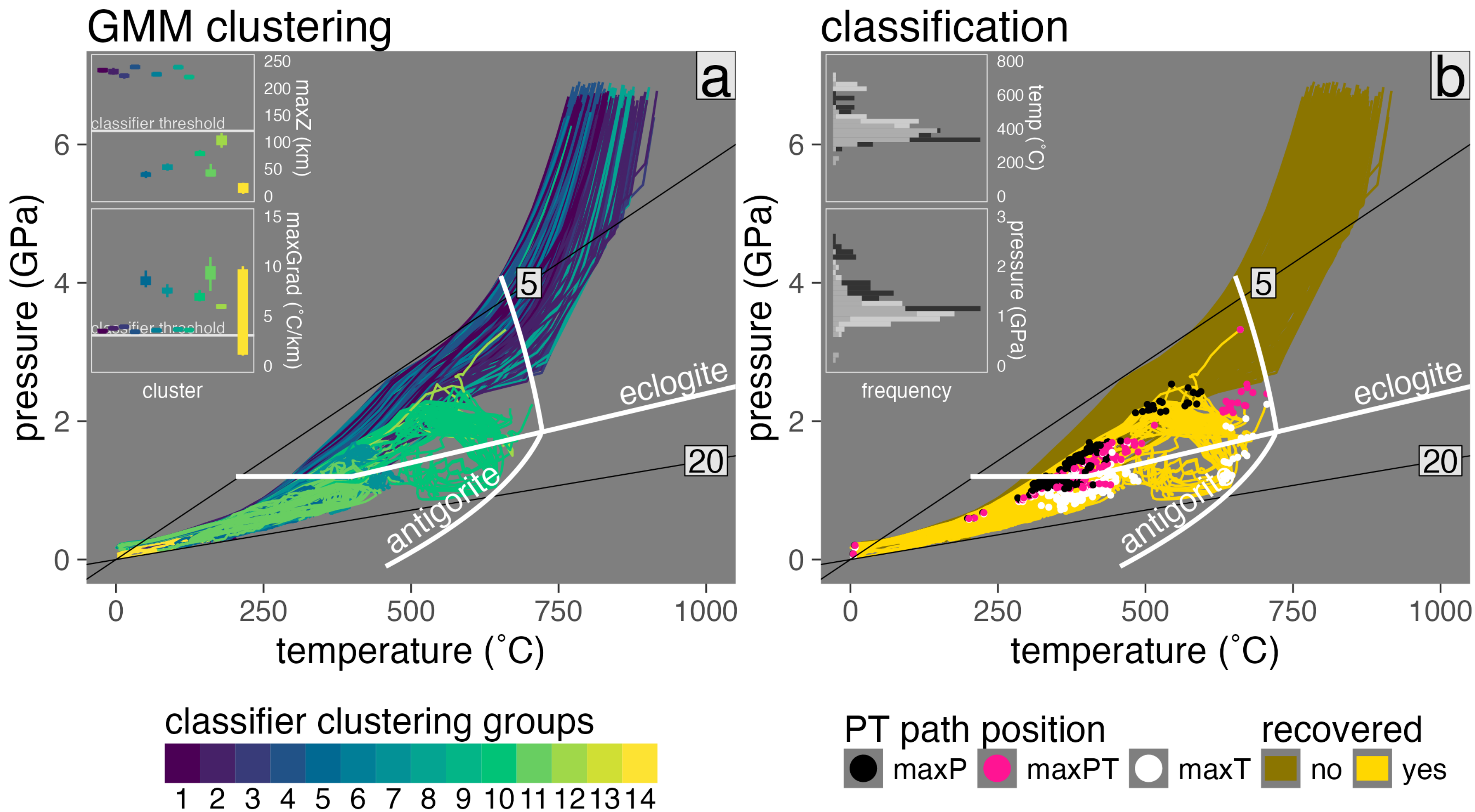

Figure 2: Example of marker classification for model cda62. (a) PT diagram showing marker clusters as assigned by Gaussian mixture modeling (GMM; colored PT paths). Boxplots showing depth and thermal gradient distributions of marker clusters assigned by GMM. Markers belonging to clusters with centroids (means) positioned at ≤ 120 km (top inset) and ≥ 5 °C/km (bottom inset) are classified as recovered. All others are classified as not recovered. (b) PT diagram showing marker classification results (colored PT paths) and various marker positions along their PT paths (black, white, and pink points). (insets) Histograms showing the distribution of T's (top inset) and P's (bottom inset) for recovered markers at maxP (black bars) and maxT (white bars) conditions. In this experiment, a significant number of markers have different peak metamorphic conditions between their maxT and maxP positions. Thin lines are thermal gradients labeled in °C/km. Only a random subset of markers are shown.

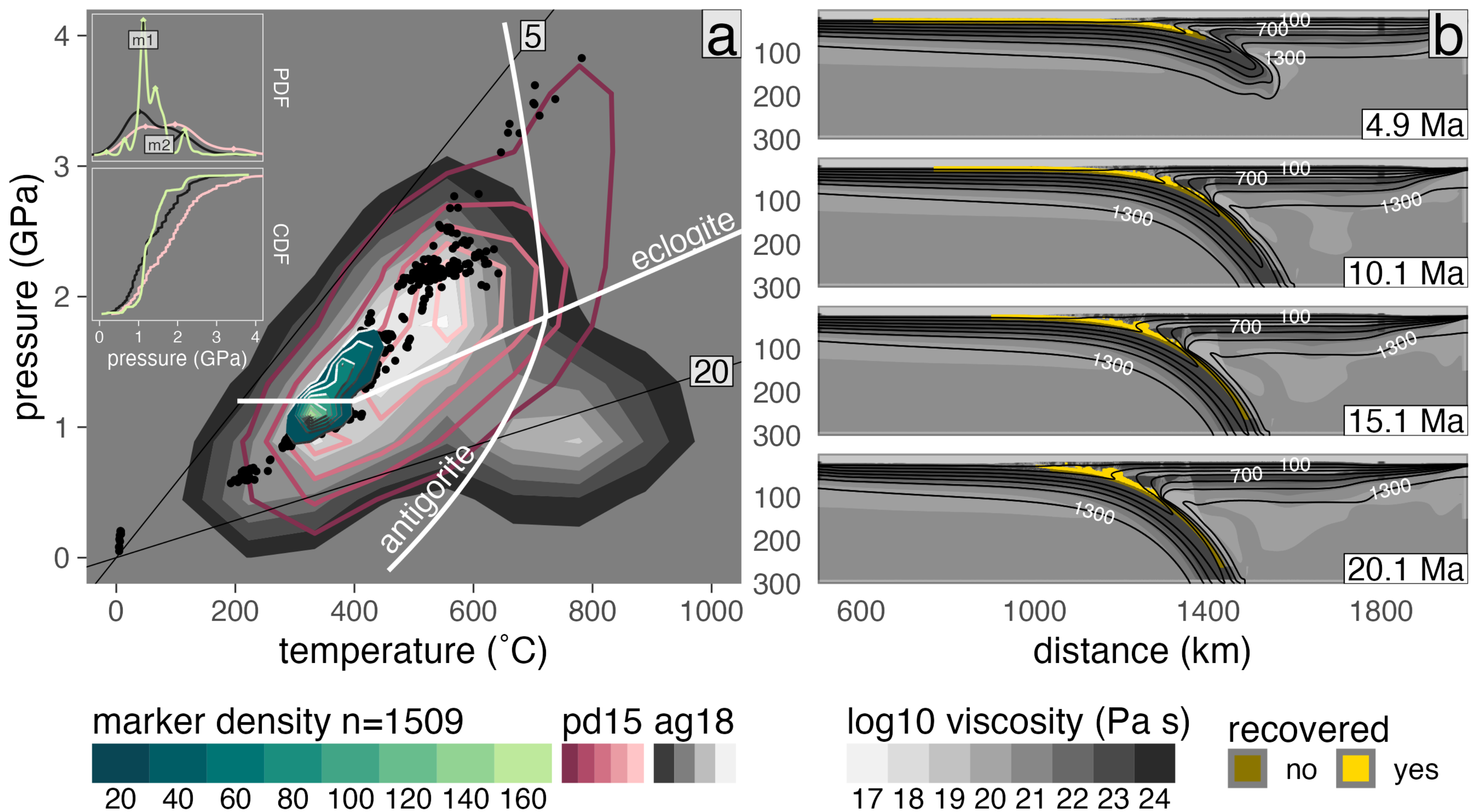

Figure 3: Summary of marker recovery for model cda62. (a) PT diagram showing the density of recovered markers (black points and green Tanaka contours) in comparison with the pd15 (solid red density contours) and ag18 (filled gray density contours) datasets. (insets) Probability distribution diagrams showing trimodal recovery P's (top inset) and a step-like CDF (bottom inset) indicating that a substantial proportion of markers are recovered from depths between 0.5-1.5 GPa. Thin lines are thermal gradients labeled in °C/km. Reaction boundaries for eclogitization of oceanic crust and antigorite dehydration are from Ito & Kennedy (1971) and Schmidt & Poli (1998), respectively. (b) Visualization of log viscosity in the model domain showing the major modes of marker recovery along a relatively thick subduction interface that tapers near the viscous coupling depth.

3 Results

3.1 Comparing Marker PT Distributions with the Rock Record

3.1.1 Global Markers from all Numerical Experiments

While marker recovery can occur at all P's recorded by exhumed metamorphic rocks (Figure 4), large disparities between recovered markers and the rock record are found if considering sample densities with respect to P. For example, pd15 and ag18 show high sample densities centered at 1 GPa—a shared feature common to all 64 numerical experiments— yet sample densities above 1 GPa are much greater in pd15 and ag18 compared to simulations (relative to the total number of samples in each dataset; Figure 4). Samples compiled in pd15 and ag18 also show much broader bimodal or trimodal density distributions across P's compared to a narrow and strong unimodal P distribution centered at 1 GPa for recovered markers. With respect to T, thermal gradients of recovered markers are significantly lower than natural samples. On average, markers recovered from $<$ 2 GPa differ by 173 °C and 3-4 °C/km compared to rocks exhumed from $<$ 2 GPa (excluding the highest-T samples in ag18 that relate to subduction initiation, Agard et al., 2018, 2020; Soret et al., 2022). In fact, relatively poor overlap exists between the high-density peak of recovered markers centered at 1 GPa & 300° C and either high-density peaks of natural sample centered at 1 GPa & 350° C and 2 GPa & 550° C (Figure 4).

3.1.2 Markers from Individual Numerical Experiments

For most experiments, marker recovery is localized and discrete with peaky multimodal density distributions and step-like CDFs. The PT positions of recovery cluster centroids depend on thermo-kinematic boundary conditions, however, so marker PT distributions vary. A few experiments show broad marker distributions that resemble the rock record with respect to P, but not with respect to thermal gradients (Supplementary **??**). Other experiments show the opposite. To compare marker recovery among various subduction zone settings, we combined recovered markers from multiple numerical experiments with similar thermo-kinematic boundary conditions——analogous to randomly sampling exhumed HP rocks from similar subduction zones (Figures 5 & 6).

Whether comparing the rock record with recovered markers from individual numerical experiments, suites of experiments, or all numerical experiments, several key observations emerge (Figure 4):

1. Recovered markers from most individual numerical experiments show discrete multimodal PT distributions with steep step-like CDFs (Figure 3 & Supplementary **??**)
2. Relatively few markers are recovered from PT regions coinciding with high-densities of natural samples around 2 GPa and 550 °C
3. Markers are recovered from a single major P mode near 1 GPa and minor P mode near 2.5 GPa with a higher rate of recovery from lower P's (79% from $\leq$ 1.5 GPa) compared to natural samples (36-59% from $\leq$ 1.5 GPa)
4. Markers are recovered from a single major T mode near 300 °C and minor T mode near 525 °C with a higher rate of recovery from lower T's (97% from $\leq$ 525 °C) compared to natural samples (44-50% from $\leq$ 525 °C)
5. The relative abundance of markers recovered along "typical" thermal gradients for subduction zones (87% from 5-12 °C/km) is high compared to natural samples (59-78% from 5-12 °C/km)
6. Many markers are recovered from the forbidden zone (11% from $\leq$ 5 °C/km)
7. Virtually no markers (0.002%) are recovered from $\geq$ 15 °C/km compared to natural samples (6-30% from $\geq$ 15 °C/km, Figure 4)

3.2 Correlations with Boundary Conditions

3.2.1 Oceanic Plate Age Effect

Thermal gradients of recovered markers respond strongly to changes in oceanic plate age (Figure 7, Table 1). Both PT gradient modes are strongly inversely correlated with oceanic plate age, showing a mean increase from about 5.88 $\pm$ 0.17 °C/km (Grad mode1) and 6.91 $\pm$ 0.68 °C/km (Grad mode2) for older plates ($\geq$ 85 Ma) to about 7.25 $\pm$ 0.05 °C/km (Grad mode1) and 8.84 $\pm$ 0.56 °C/km (Grad mode2) for younger plates ($\leq$ 55 Ma). The dominant P mode (P mode1) moderately correlates with oceanic plate age, indicating a slightly higher possibility of recovering material from beyond the continental Moho for the oldest oceanic plates ($\geq$ 85 Ma). Neither T modes, nor recovery rate

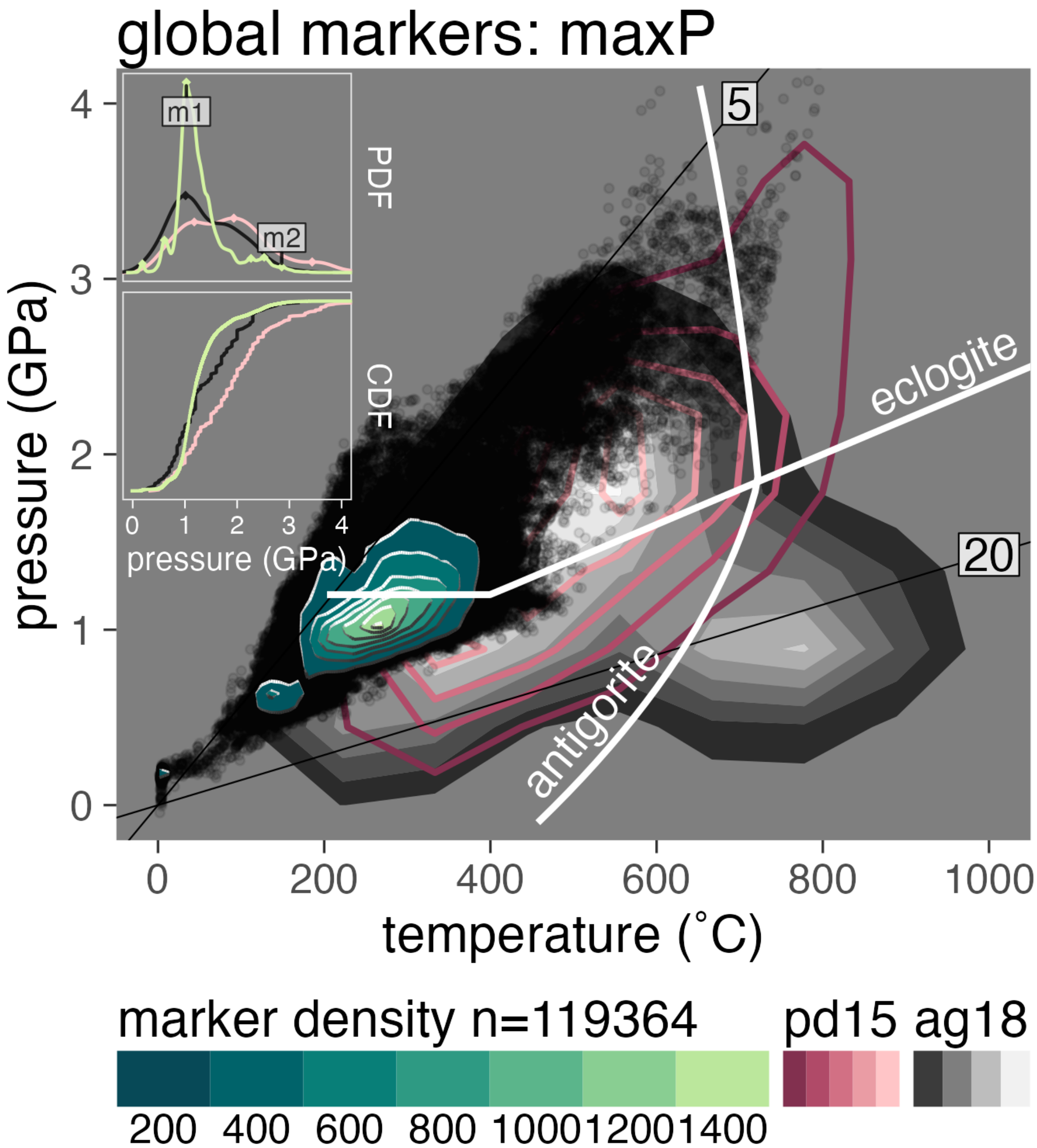

Figure 4: Recovered markers from all 64 numerical experiments. (a) PT diagram showing the density of recovered markers (black points and green Tanaka contours) in comparison with the pd15 (solid red density contours) and ag18 (filled gray density contours) datasets. Marker density is concentrated along relatively cool thermal gradients, primarily near the continental Moho (1 GPa), with minor recovery modes centered near the onset of plate coupling (2.3-2.5 GPa). (insets) Probability distribution diagrams showing discrete multimodal recovery P's (top inset) and a steep CDF (bottom inset) indicating that a substantial proportion of markers are recovered from depths between 0.5-1.5 GPa. Note the higher-abundance of pd15 and ag18 samples at > 1.5 GPa compared to markers. Thin lines are thermal gradients labeled in °C/km. Reaction boundaries for eclogitization of oceanic crust and antigorite dehydration are from Ito & Kennedy (1971) and Schmidt & Poli (1998), respectively.

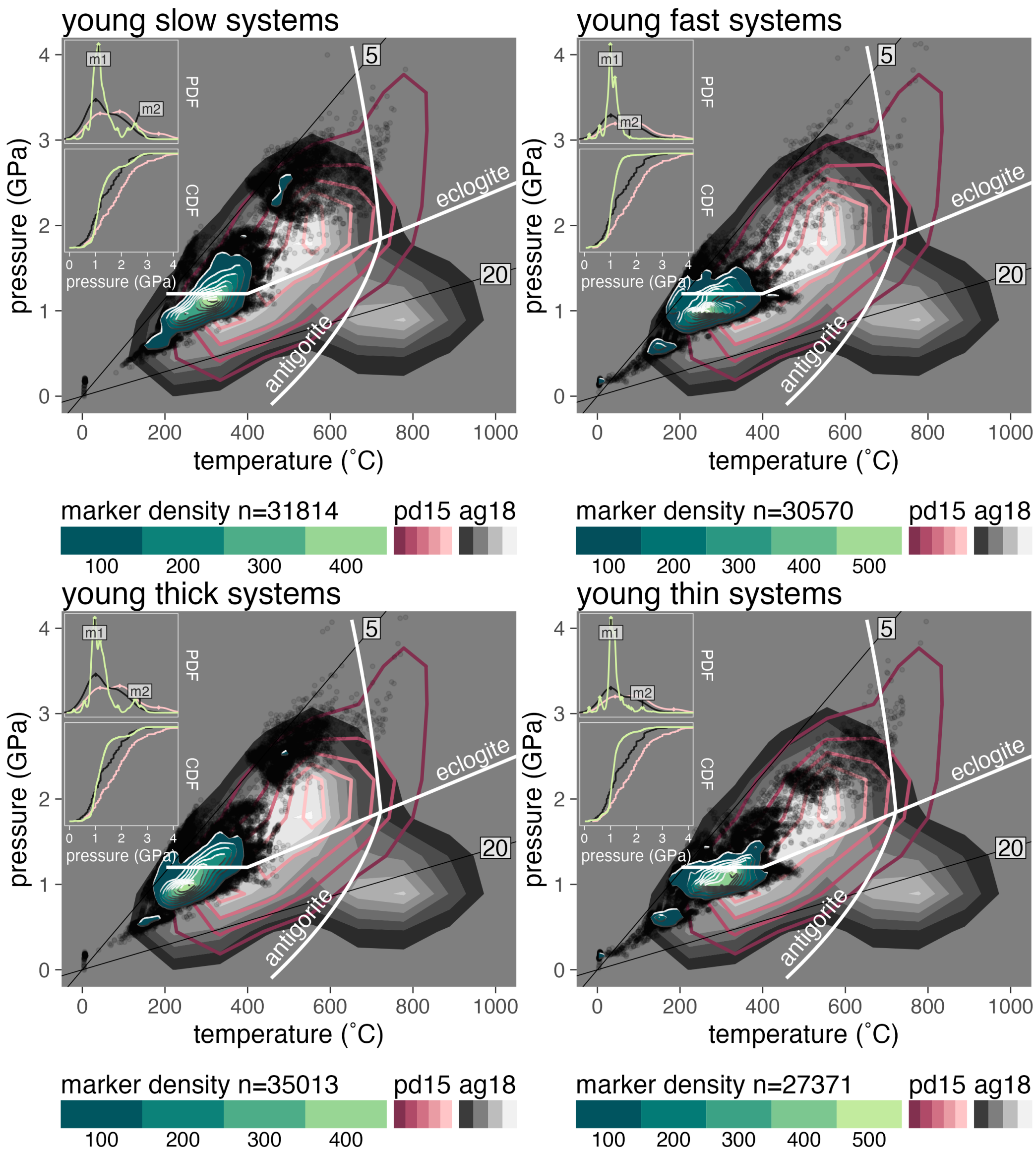

Figure 5: Recovered markers from numerical experiments with young oceanic plates (32.6-55 Ma). PT diagrams showing the densities of recovered markers (black points cloud and green Tanaka contours) in comparison with the pd15 (solid red density contours) and ag18 (filled gray density contours) datasets, grouped by thermo-kinematic boundary conditions (16 experiments per plot; boundary conditions summarized in Kerswell et al., 2021). (insets) Probability distribution (top inset) and CDF diagrams with respect to P. Thin lines are thermal gradients labeled in °C/km. Reaction boundaries for eclogitization of oceanic crust and antigorite dehydration are from Ito & Kennedy (1971) and Schmidt & Poli (1998), respectively.

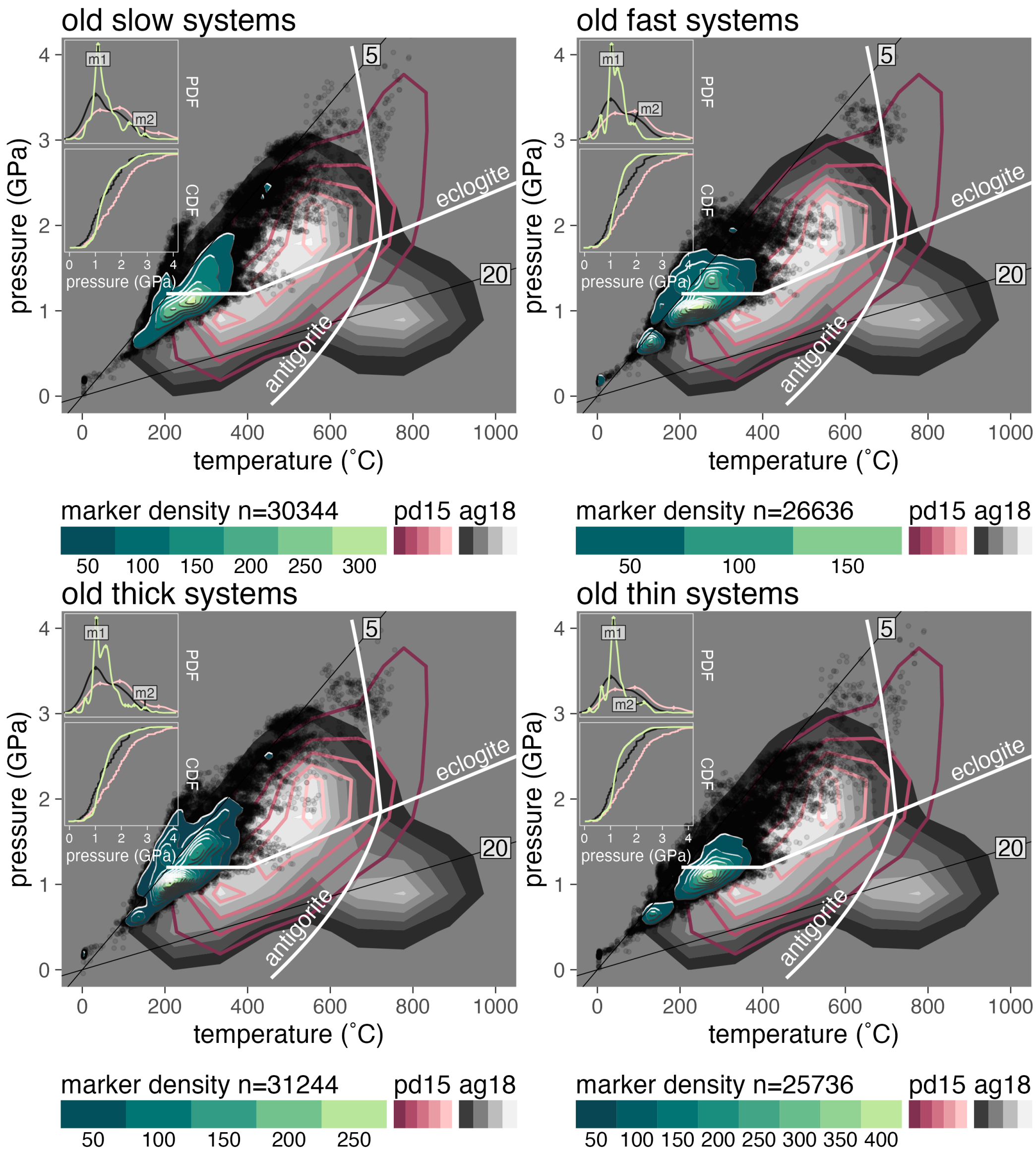

Figure 6: Recovered markers from numerical experiments with older oceanic plates (85-110 Ma). PT diagrams showing the densities of recovered markers (black points cloud and green Tanaka contours) in comparison with the pd15 (solid red density contours) and ag18 (filled gray density contours) datasets, grouped by thermo-kinematic boundary conditions (16 experiments per plot; boundary conditions summarized in Kerswell et al., 2021). (insets) Probability distribution (top inset) and CDF diagrams with respect to P. Thin lines are thermal gradients labeled in °C/km. Reaction boundaries for eclogitization of oceanic crust and antigorite dehydration are from Ito & Kennedy (1971) and Schmidt & Poli (1998), respectively.

correlate with oceanic plate age. Although oceanic plate age strongly affects the average PT gradients of recovered material, it does not strongly shift marker recovery up or down the subduction interface.

3.2.2 Convergence Velocity Effect

P's and T's of recovered markers respond strongly to changes in convergence velocity (Figure 7, Table 1). Both P modes are strongly inversely correlated with convergence velocity, showing a mean increase from 1.09 ± 0.03 GPa (P mode1) and 1.91 ± 0.33 GPa (P mode2) for fast moving plates (100 km/Ma) to about 1.37 ± 0.06 GPa (P mode1) and 2.64 ± 0.08 GPa (P mode2) for slow moving plates (40 km/Ma). However, the dominant P mode (P mode1) does not change significantly until convergence velocity drops below 66 km/Ma (Table 1). Both T modes are strongly inversely correlated with convergence velocity, showing a mean increase from 249.3 ± 6.6 °C (T mode1) and 371.8 ± 60.8 °C (T mode2) for fast moving plates (100 km/Ma) to about 311.6 ± 1.5 °C (T mode1) and 542.5 ± 74.3 °C (T mode2) for slow moving plates (40 km/Ma). Neither PT gradient modes, nor recovery rate correlate with convergence velocity. In summary, decreasing convergence velocity shifts marker recovery to warmer and deeper conditions along the subduction interface without significantly changing the average thermal gradient of subducted material.

3.2.3 Upper-plate Thickness Effect

From the same numerical experiments used to trace markers, an association between upper-plate thickness and mechanical coupling depths was demonstrated (Kerswell et al., 2021). P distributions of markers were thus expected to respond strongly to changes in upper-plate thickness. However, a surprisingly negligible effect was observed (Figure 7). For example, neither of the P modes, nor T mode2 (usually the most deeply subducted markers) correlate with upper-plate thickness. In contrast, both PT gradient modes and the dominant T mode (T mode1) inversely correlate with upper-plate thickness. Recovery rate is correlated with upper-plate thickness and not with any other boundary condition, indicating higher recovery rates are more likely underneath thick upper-plates. Recovery rates show a mean decrease from 10.65 ± 0.32 % for thicker plates ($\geq$ 78 km-thick) to 8.09 ± 0.3 % for thinner upper-plates ($\leq$ 62 km-thick). In summary, thin upper-plates are more likely to produce warmer thermal gradients, higher T's, and lower recovery rates.

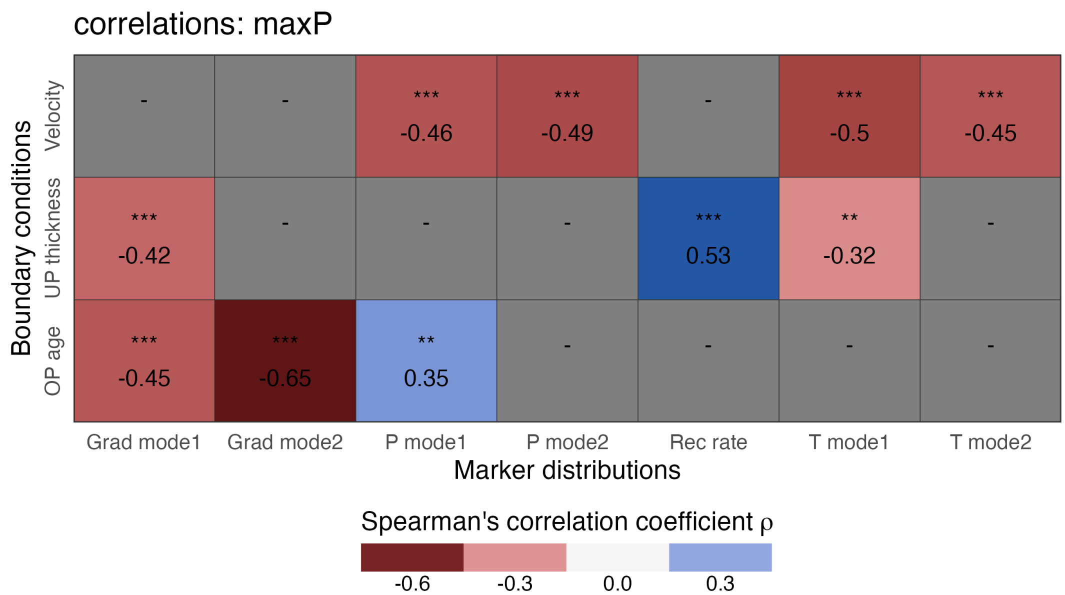

Figure 7: Correlations among marker recovery modes and thermo-kinematic boundary conditions. The dominant recovery mode (mode1) indicates the position of the tallest density peak with respect to P, T, or thermal gradient (i.e. conditions from which the greatest number of markers are recovered), while mode2 indicates the position of the warmest, deepest, or highest gradient density peak (i.e. conditions from which deeply subducted markers are recovered). While oceanic plate age and upper-plate thickness more strongly affect the average thermal gradients of recovered markers (stronger correlations with gradient modes and T mode1), convergence velocity more strongly affects the depths of recovery along the subduction interface, especially for deeply subducted markers (stronger correlation with P modes and T mode2). The dominant T mode (T mode1) and recovery rate are correlated with upper-plate thickness, but not with any other boundary condition. Symbols indicate the Spearman's rank correlation coefficient that measures the significance of monotonic correlations. *** $\rho \leq 0.001$, ** $\rho \leq 0.01$, * $\rho \leq 0.05$, - $\rho \geq 0.05$.

Table 1: Subduction zone parameters and marker classification summary

Initial Boundary Conditions					Marker Classification Summary							
model	Φ	Z_{UP}	age	$\vec{v}$	recovered	rec. rate	P mode1	P mode2	T mode1	T mode2	grad mode1	grad mode2
	km	km	Ma	km/Ma		%	GPa	GPa	°C	°C	°C/km	°C/km
cda46	13.0	46	32.6	40	1482±28	7.8±0.14	1.12±0.00	2.46±0.04	336±2	584±138	8.2±0.02	9.5±0.04
cda62	13.0	62	32.6	40	1351±24	7.2±0.12	1.12±0.00	2.24±0.26	332±2	534±36	8.3±0.02	8.3±0.02
cda78	13.0	78	32.6	40	1863±30	9.9±0.16	1.39±0.00	2.38±0.02	352±2	477±2	5.9±0.02	9.3±1.66
cda94	13.0	94	32.6	40	1932±28	10.2±0.14	1.24±0.00	2.65±0.02	341±2	502±26	5.6±0.02	7.8±0.04
cdb46	21.5	46	32.6	66	1806±34	9.6±0.18	1.04±0.00	2.37±0.74	334±2	657±2	8.3±0.04	8.4±0.38
cdb62	21.5	62	32.6	66	1405±20	7.4±0.10	1±0.00	2.16±0.00	281±2	531±32	7.8±0.04	10±0.06
cdb78	21.5	78	32.6	66	1884±32	10±0.18	0.92±0.00	2.49±0.08	264±2	541±6	8.1±0.04	8.1±0.04
cdb94	21.5	94	32.6	66	2330±124	12.3±0.66	1.16±0.16	2.64±0.12	291±2	464±44	7.5±0.02	7.9±1.10
cdc46	26.1	46	32.6	80	1736±46	9.2±0.24	1.02±0.00	1.27±0.68	320±0	475±162	8.8±0.40	9.1±0.98
cdc62	26.1	62	32.6	80	1288±28	6.8±0.16	0.99±0.00	2.01±0.00	264±2	531±2	6.7±0.02	8.6±0.92
cdc78	26.1	78	32.6	80	1801±24	9.5±0.14	0.94±0.10	2.88±0.16	283±2	519±28	7.8±0.02	8.1±2.00
cdc94	26.1	94	32.6	80	2158±26	11.4±0.14	1.14±0.00	3.01±0.02	274±0	533±2	6.7±0.04	9.8±0.04

Table 1: Subduction zone parameters and marker classification summary *(continued)*

Initial Boundary Conditions					Marker Classification Summary							
model	Φ	Z_{UP}	age	$\vec{v}$	recovered	rec. rate	P mode1	P mode2	T mode1	T mode2	grad mode1	grad mode2
	km	km	Ma	km/Ma		%	GPa	GPa	°C	°C	°C/km	°C/km
cdd46	32.6	46	32.6	100	1055±58	5.6±0.30	1±0.00	1.76±0.14	226±0	465±50	5.9±0.02	8.5±0.06
cdd62	32.6	62	32.6	100	1365±28	7.2±0.14	0.99±0.00	1.63±0.16	262±2	342±30	5.6±0.04	8.9±0.04
cdd78	32.6	78	32.6	100	1889±28	10±0.16	1±0.00	1.93±0.08	264±2	512±2	7.5±0.04	11.8±1.56
cdd94	32.6	94	32.6	100	2716±32	14.4±0.16	1.23±0.00	2.9±0.00	242±38	660±6	7.3±0.02	7.3±0.02
cde46	22.0	46	55.0	40	1612±36	8.5±0.18	1.11±0.00	2.83±0.54	315±2	675±90	6.7±0.02	7.9±0.94
cde62	22.0	62	55.0	40	1794±50	9.5±0.26	1.08±0.00	2.24±0.00	285±2	485±2	6.1±0.00	7.4±0.64
cde78	22.0	78	55.0	40	1866±34	9.9±0.18	1.37±0.00	2.52±0.00	315±2	507±98	5.9±0.06	7.5±0.02
cde94	22.0	94	55.0	40	1808±20	9.6±0.10	2.33±0.86	2.54±0.00	319±2	431±0	5±0.02	7.2±0.02
cdf46	36.3	46	55.0	66	2246±56	11.9±0.30	1.11±0.04	2.68±0.28	308±2	673±14	7.6±0.02	7.6±0.02
cdf62	36.3	62	55.0	66	1569±38	8.3±0.20	1.14±0.00	2.2±0.06	265±2	582±130	6.9±0.02	6.9±0.02
cdf78	36.3	78	55.0	66	1621±26	8.6±0.14	0.99±0.00	2.75±0.18	228±2	545±8	7±0.02	7.5±1.16
cdf94	36.3	94	55.0	66	1964±30	10.4±0.16	0.93±0.00	2.79±0.02	216±0	597±212	6.6±0.02	6.6±0.02

Table 1: Subduction zone parameters and marker classification summary *(continued)*

Initial Boundary Conditions					Marker Classification Summary							
model	Φ	Z_{UP}	age	$\vec{v}$	recovered	rec. rate	P mode1	P mode2	T mode1	T mode2	grad mode1	grad mode2
	km	km	Ma	km/Ma		%	GPa	GPa	°C	°C	°C/km	°C/km
cdg46	44.0	46	55.0	80	2101±74	11.1±0.40	1.2±0.00	1.96±0.04	338±2	338±2	8.1±0.16	8.2±1.26
cdg62	44.0	62	55.0	80	1334±24	7.1±0.12	1±0.00	1.74±0.06	218±4	277±48	5.2±0.02	7.5±0.04
cdg78	44.0	78	55.0	80	1585±26	8.4±0.14	1.01±0.00	2.21±0.02	238±2	529±210	4.9±0.02	7.1±0.02
cdg94	44.0	94	55.0	80	2132±22	11.3±0.12	0.98±0.00	2.69±0.02	209±0	402±36	6.4±0.02	9.4±0.10
cdh46	55.0	46	55.0	100	947±16	5±0.08	0.95±0.00	1.63±0.26	273±4	368±98	7±0.18	9.2±0.48
cdh62	55.0	62	55.0	100	1448±24	7.7±0.12	0.99±0.00	1.73±0.00	237±36	243±2	6.9±1.46	7.1±0.02
cdh78	55.0	78	55.0	100	1631±22	8.6±0.12	0.99±0.02	1.59±0.26	215±10	256±84	6.6±1.36	6.8±0.16
cdh94	55.0	94	55.0	100	2281±28	12.1±0.14	0.88±0.00	1.24±0.14	203±0	275±2	6.7±0.02	10.3±0.62
cdi46	34.0	46	85.0	40	1275±24	6.8±0.14	1.17±0.00	3.55±0.32	287±2	721±72	6.6±0.02	6.6±0.02
cdi62	34.0	62	85.0	40	1915±34	10.1±0.18	1.09±0.00	2.28±0.00	257±2	494±286	5.6±0.76	6.7±0.04
cdi78	34.0	78	85.0	40	2043±24	10.8±0.12	1.65±0.02	2.56±0.00	320±2	443±4	5.4±0.02	6.5±0.02
cdi94	34.0	94	85.0	40	2007±38	10.6±0.20	1.66±0.02	2.94±0.00	292±2	493±6	5.1±0.02	6.4±0.02

Table 1: Subduction zone parameters and marker classification summary *(continued)*

Initial Boundary Conditions					Marker Classification Summary								
model	Φ	Z_{UP}	age	$\vec{v}$	recovered	rec. rate	P mode1	P mode2	T mode1	T mode2	grad mode1	grad mode2
	km	km	Ma	km/Ma		%	GPa	GPa	°C	°C	°C/km	°C/km
cdj46	56.1	46	85.0	66	1656±100	8.8±0.52	1.07±0.00	2.55±0.58	273±2	616±318	6.4±0.06	7.4±0.12
cdj62	56.1	62	85.0	66	1364±28	7.2±0.14	1.09±0.00	2.13±0.04	238±2	516±24	6.3±0.02	6.3±0.02
cdj78	56.1	78	85.0	66	1326±28	7±0.14	1.22±0.00	1.97±0.02	202±0	315±0	4.5±0.02	6.5±0.06
cdj94	56.1	94	85.0	66	1849±26	9.8±0.14	1.03±0.00	1.52±0.00	206±0	206±0	5.9±0.02	5.9±0.02
cdk46	68.0	46	85.0	80	1463±24	7.8±0.14	1.06±0.02	1.11±0.26	270±2	400±120	7.5±0.02	7.5±0.02
cdk62	68.0	62	85.0	80	1204±20	6.4±0.10	1.07±0.00	1.83±0.00	220±2	452±170	4.7±0.02	6.7±0.04
cdk78	68.0	78	85.0	80	1540±36	8.2±0.20	1.02±0.04	1.78±0.34	214±8	214±8	6±1.58	6.9±0.90
cdk94	68.0	94	85.0	80	2032±32	10.8±0.16	1.04±0.00	3.19±0.06	265±2	677±30	6±0.02	6±0.02
cdl46	85.0	46	85.0	100	714±16	3.8±0.08	1.1±0.00	1.56±0.02	268±2	268±2	6±0.06	6.5±2.78
cdl62	85.0	62	85.0	100	1096±22	5.8±0.12	1.02±0.00	2.23±0.02	246±2	466±126	6.8±0.18	6.8±0.18
cdl78	85.0	78	85.0	100	1663±42	8.8±0.22	1.08±0.18	1.94±0.02	273±2	273±2	4±0.02	8.9±2.46
cdl94	85.0	94	85.0	100	1508±218	8±1.16	1.23±0.16	1.27±0.08	225±4	370±70	5.8±0.06	7.4±2.74

Table 1: Subduction zone parameters and marker classification summary *(continued)*

Initial Boundary Conditions					Marker Classification Summary								
model	Φ	Z_{UP}	age	$\vec{v}$	recovered	rec. rate	P mode1	P mode2	T mode1	T mode2	grad mode1	grad mode2
	km	km	Ma	km/Ma		%	GPa	GPa	°C	°C	°C/km	°C/km
cdm46	44.0	46	110.0	40	1390±24	7.4±0.12	1.39±0.00	3.14±0.02	320±2	711±6	6.1±0.02	8.1±1.94
cdm62	44.0	62	110.0	40	2326±28	12.3±0.14	1.21±0.00	2.45±0.00	281±0	439±2	5.5±0.38	5.7±0.04
cdm78	44.0	78	110.0	40	1828±36	9.7±0.18	1.48±0.00	2.51±0.00	331±4	668±208	5.5±0.02	6.4±1.04
cdm94	44.0	94	110.0	40	1901±28	10.1±0.14	1.53±0.00	2.87±0.00	302±2	517±210	5.3±0.02	6±0.02
cdn46	72.6	46	110.0	66	1942±88	10.3±0.46	1.25±0.00	2.3±0.08	283±2	637±70	7.1±0.06	7.1±0.06
cdn62	72.6	62	110.0	66	1217±24	6.5±0.14	1.13±0.00	2.15±0.24	269±0	559±136	6.9±0.06	6.9±0.06
cdn78	72.6	78	110.0	66	1684±38	8.9±0.20	1.38±0.00	1.38±0.00	212±2	429±4	3.9±0.02	7±1.22
cdn94	72.6	94	110.0	66	1685±26	8.9±0.14	1.06±0.00	1.77±0.36	203±2	299±144	5.6±0.04	6.6±0.44
cdo46	88.0	46	110.0	80	1476±128	7.8±0.68	1.21±0.04	1.75±0.86	280±2	343±74	7.4±0.08	7.4±0.08
cdo62	88.0	62	110.0	80	1328±82	7.1±0.44	1.06±0.02	2.31±0.60	252±4	577±230	7.1±0.08	7.1±0.08
cdo78	88.0	78	110.0	80	1629±34	8.7±0.18	0.92±0.00	1.38±0.02	194±2	376±90	4.1±0.02	6.9±1.58
cdo94	88.0	94	110.0	80	1997±152	10.6±0.80	1.07±0.22	2.68±1.86	252±26	526±410	5.7±0.02	6.9±2.58

Table 1: Subduction zone parameters and marker classification summary *(continued)*

Initial Boundary Conditions					Marker Classification Summary							
model	Φ	Z_{UP}	age	$\vec{v}$	recovered	rec. rate	P mode1	P mode2	T mode1	T mode2	grad mode1	grad mode2
	km	km	Ma	km/Ma		%	GPa	GPa	°C	°C	°C/km	°C/km
cdp46	110.0	46	110.0	100	1518±144	8±0.76	1.27±0.00	2.15±3.24	301±2	306±30	7±0.06	7±0.06
cdp62	110.0	62	110.0	100	1371±114	7.3±0.60	1.12±0.00	2.06±0.00	234±2	346±312	5.2±0.78	9.6±1.62
cdp78	110.0	78	110.0	100	1650±36	8.8±0.20	1.11±0.00	1.82±0.24	274±2	541±70	6.1±1.08	6.3±0.06
cdp94	110.0	94	110.0	100	1848±156	9.8±0.84	1.41±0.12	3.17±0.66	244±0	259±90	5.7±0.02	5.7±0.02

Classifier uncertainties (2σ) estimated by running the classifier 30 times with random marker samples (jackknife sample proportion: 90%)

4 Discussion

4.1 Thermo-Kinematic Controls on Rock Recovery

While the combined distribution of markers recovered from all numerical experiments shows appreciable deviations from PT estimates compiled by Penniston-Dorland et al. (2015) and Agard et al. (2018), markers recovered from simulations with the youngest oceanic plates (32.6-55 Ma) and the slowest convergence velocities (40-66 km/Ma) begin to resemble the distribution of exhumed HP rocks (compare Figure 4 with Figures 5 & 6) with respect to thermal gradients and P distributions. Slower subduction of younger plates increases marker thermal gradients and strongly shifts marker recovery down the subduction interface (strong correlations with Grad mode1 and P mode1 & mode2, Figure 7). The correlations in Figure 7 also suggest a shift towards warmer recovery conditions should be complemented by thin upper-plates—implying systems with thin upper-plates, slow convergence, and young oceanic plates should be most consistent with the distribution of rock recovery implied by pd15 and ag18 (Figure 5). This correspondence might appear consistent with inferences that the rock record is composed primarily of rock bodies exhumed from “warm” subduction settings (Abers et al., 2017; van Keken et al., 2018). However, our numerical experiments also show that recovery rates do not correlate with oceanic plate age or convergence velocity, and that recovery rates are poorer for thinner upper-plates (Figure 7). Correlations between thermo-kinematic boundary conditions and recovery rates drawn from many tens of thousands of recovered markers across numerous simulations counter the notion that preferential recovery is happening in “warm” subduction settings.

Besides recovery rates of subducting markers, other dynamic characteristics appear to correlate with oceanic plate age and convergence velocity. For example, simulations with slow convergence velocities (e.g. models: cda, cde, cdi, cdm) tend to have higher subduction angles (see Supplementary **??**)with thicker subduction interfaces that allow more markers to subduct to deeper, and thus warmer, conditions compared to other experiments (e.g. models: cdd, cdh, cdl, cdp) that form narrow interfaces with shallow choke points (e.g. see Supplementary **??**). Observationally, the angle of subduction does not correlate significantly with oceanic plate age or convergence velocity, but rather inversely with the duration of subduction (Hu & Gurnis, 2020). Thus, the rock record might indicate preferential exhumation during the earlier stages of subduction when subduction angles were steeper (although not necessarily during subduction initiation), even for older oceanic plates. More generally, differences in plate flexibility, overall subduction geometry, and velocity of plate motions strongly affect PT distributions of rock recovery (Monie & Agard, 2009)—rather than strictly "warm" versus "cool" subduction settings *per se*. In other words, thermo-kinematic boundary conditions typically inferred to strictly regulate *thermal* effects (e.g. young-slow oceanic plates supporting warmer thermal gradients) may indeed be regulating more *dynamic* effects (e.g. young-slow oceanic plates flexibly rolling back to support deeper subduction of material along thicker interfaces) that are subsequently *observed* as thermal effects (average increase in marker PT's).

4.2 Comparison with other Numerical Experiments

Marker PT distributions and their correlations with thermo-kinematic boundary conditions presented above are determined directly from large samples of recovered material evolving dynamically in a deforming subduction interface (analogous to reconstructing thermal gradients from large random samples of exhumed HP rocks). In contrast, other studies investigating thermal responses to variable boundary conditions typically determine PT gradients statically along discrete surfaces representing megathrust faults (e.g. Abers et al., 2006; Currie et al., 2004; Davies, 1999; Furukawa, 1993; Gao & Wang, 2014; McKenzie, 1969; Molnar & England, 1990; Peacock & Wang, 1999; Syracuse et al., 2010; van Keken et al., 2011, 2019; Wada & Wang, 2009) or dynamically by "finding" the subduction interface heuristically at each timestep (e.g. Arcay, 2017; Holt & Condit, 2021; Ruh et al., 2015). Other studies using similar geodynamic codes have traced many fewer markers (typically dozens vs. ˜ 120,000; Faccenda et al., 2008; Gerya et al., 2002; Sizova et al., 2010; Yamato et al., 2007, 2008) from a narrower range of thermo-kinematic boundary conditions, so they implicitly have less statistical rigor. This study stresses the importance of large sample sizes because individual marker PT paths can vary considerably within a single simulation, yet important modes of recovery become apparent from density peaks as more markers are traced. Furthermore, most other studies make no attempt to determine peak PT conditions related to detachment and *recovery* (with some exceptions, e.g. Roda et al., 2012, 2020), so marker PT paths are less analogous to PT paths determined by applying petrologic modeling.

4.3 Comparison with Geophysical Observations

The locations of important recovery modes determined from numerical experiments correspond closely with the depths of important mechanical transitions inferred from seismic imaging studies and surface heat flow observations. For example, the dominant recovery mode common among all numerical experiments at about 1 GPa (Table 1 & Figure 4) is consistent with a layer of low seismic velocities and high V_p/V_s ratios observed at numerous subduction zones between 20-50 km depth (Bostock, 2013). While considerable unknowns persist about the nature of deformation in this region (Bostock, 2013; Tewksbury-Christle & Behr, 2021), the low-velocity zone, accompanied by low-frequency and slow-slip seismic events, is often interpreted as a transitional brittle-ductile shear zone actively accommodating underplating of subducted material and/or formation of a tectonic mélange around the base of the continental Moho (Audet & Kim, 2016; Audet & Schaeffer, 2018; Bostock, 2013; Calvert et al., 2011, 2020; Delph et al., 2021).

Formation of low-velocity zones and their geophysical properties are generally attributed to high pore-fluid pressures caused by metamorphic reactions relating to the dehydration of oceanic crust (Hacker, 2008; Rondenay et al., 2008; van Keken et al., 2011). Surprisingly, despite our numerical implementation of a relatively simple model for dehydration of oceanic crust (Ito & Kennedy, 1971; Kerswell et al., 2021), and a relatively simple visco-plastic rheological model (Gerya & Yuen, 2003; Kerswell et al., 2021), the primary mode of marker recovery at 1.15 $\pm$ 0.46 GPa (2 σ, Table 1) coincides closely with the expected region for shallow underplating according to geophysical constraints (35 $\pm$ 15 km or 1.0 $\pm$ 0.4 GPa). The size of the markers dataset (n = 119,364 recovered markers) and prevalence of marker recovery from 1 GPa suggest that although dehydration may indeed trigger detachment of subducting rocks, other factors—notably the compositional and mechanical transition in the upper-plate across the Moho—also influence detachment at this depth.

The termination of the low-velocity zone at depths beyond the continental Moho marks another important mechanical transition. This second transition is often interpreted as the onset of mechanical plate coupling near 80 km (or 2.3 GPa) and coincides well with the deeper recovery modes determined from recovered markers at 2.2 $\pm$ 1.1 GPa (2 σ, Table 1). Between these two modes of recovery at $\sim$ 40 and $\sim$ 80 km lies a gap that coincides with the highest sample density of exhumed HP rocks compiled in pd15 and ag18 (Figure 4). This recovery gap is discussed in the following section.

4.4 The Marker Recovery Gap

Although recovered markers partially overlap with the range of PT estimates compiled in the pd15 and ag18 datasets, the differences between distributions of recovered markers and natural samples are numerous, including: (1) an obvious lack of markers recovered from ≥ 15 °C/km (0.002%) compared to pd15 and ag18 (37-48%, Figure 4), (2) recovery of markers from a single dominant mode near 1 GPa and 300 °C compared to more broadly distributed multimodal recovery across PT space for natural samples (Figure 4), (3) a general shift towards lower T's and cooler thermal gradients for markers compared to natural samples, and (4) a remarkable gap in marker recovery near 2 GPa and 550 °C that coincides with the highest density of natural samples (Figure 4). In fact, across 64 numerical experiments with wide-ranging initial conditions less than 1% (0.63%) of markers are recovered from between 1.8-2.2 GPa and 475-625 °C. Why might this gap occur? Four possibilities are considered:

1. Simple rheological models preclude certain recovery mechanisms (poor implementation of subduction interface mechanics, i.e., modeling uncertainty, Section 4.3)
2. Peak metamorphic conditions are systematically misinterpreted (peak metamorphic conditions do not correspond to maxP or PT paths are not well constrained, i.e., petrologic uncertainties, e.g., see Penniston-Dorland et al., 2015)
3. Rocks are frequently (re)sampled from the same peak metamorphic conditions and other rocks from different metamorphic grades are infrequently sampled (selective nonrandom sampling, i.e., scientific bias, e.g., see Agard et al., 2018)
4. Rocks are recovered during short-lived events (e.g., subduction of seamounts, Agard et al., 2009) that are not implemented in our numerical experiments, rather than recovered during steady-state subduction within a serpentine-rich tectonic mélange that is characteristic of our numerical experiments (i.e., geodynamic uncertainties)

4.4.1 Numerical Modeling Uncertainties

Simplifying assumptions in our numerical experiments influence thermal gradients and dynamics of rock recovery from the subducting oceanic plate. Substantially lower T's and thermal gradients in numerical experiments compared to natural samples (Figure 4) might indicate imperfect implementation of heat generation and transfer (Kohn et al., 2018; Penniston-Dorland et al., 2015). Our hydrologic model and implementation of serpentine rheology in the numerical experiments creates a weak interface. A stronger rheology (e.g., quartz or a mixed melange zone Beall et al., 2019; Ioannidi et al., 2021), or a stronger serpentine flow law (Burdette & Hirth, 2022), would yield greater heating and higher T's from enhanced viscous dissipation along the subduction interface (Kohn et al., 2018). In principle, a stronger rheology might shift the overall PT distribution of markers to higher T's and help fill in the marker recovery gap around 2 GPa and 550 °C, and/or possibly change flow to extract rocks more broadly along the subduction interface. Although the effects of different interface rheologies on thermal structure or rock recovery were not explicitly explored in this study, even numerical simulations with the smallest PT discrepancies between markers and natural samples (youngest oceanic plates and slowest convergence velocities, Figures 5 & 6) exhibit the same sizeable gap in marker recovery around 2 GPa and 550 °C. Thus, higher T's alone would not seem to close the gap.

4.4.2 Petrologic Uncertainties

Interpreting peak metamorphic conditions of complex polymetamorphic rocks is challenging with many sources of uncertainties. However, a global shift in PT estimates of natural samples towards warmer conditions compared to recovered markers would imply that decades of field observations, conventional thermobarometry (e.g. Spear & Selverstone, 1983), phase equilibria modeling (e.g. Connolly, 2005), trace element thermometry (e.g. Ferry & Watson, 2007; Kohn, 2020), and Raman Spectroscopy of Carbonaceous Material thermometry (Beyssac et al., 2002) from many independent localities worldwide (e.g. Agard et al., 2009, 2018; Angiboust et al., 2009, 2012a, 2016; Avigad & Garfunkel, 1991; Monie & Agard, 2009; Plunder et al., 2013, 2015) have systematically misinterpreted the prograde and retrograde histories of exhumed HP rocks. The consistency of independent analytical techniques suggests systematic bias is unlikely and estimated uncertainties are generally too small for this argument to be viable (Penniston-Dorland et al., 2015).

4.4.3 Selective Sampling and Scientific Bias

At least two factors might lead to scientific bias. First, the application of conventional thermobarometry is easier for certain rock types and mineral assemblages (e.g. eclogite-facies metabasites and metapelitic schists) than for others (e.g. quartzites, metagraywackes). Second, certain subduction complexes expose more rocks than others. These factors lead to sampling bias, both in the rocks that are selected for analysis and which subduction complexes contribute most to compilations. For example, a PT condition of ~ 2 GPa and 550 °C typically yields assemblages that are both recognizable in the field (eclogites, *sensu stricto*, and kyanite- or chloritoid-schists) and amenable to thermobarometric calculations and petrologic modeling. This fact may lead to oversampling of the rocks that yield these PT conditions and the subduction zones that expose these rocks. In Penniston-Dorland et al. (2015), the western and central European Alps, which contain many rocks that equilibrated near this PT condition, represented ~ 90 samples across < 1000 km (~ 1 sample per 100 km), whereas the Himalaya and Andes, which contained more diverse PT conditions, represented only ~ 1 sample per 300-400 km. Some subduction zones are not represented at all in these datasets (e.g. central and western Aleutians, Kamchatka, Izu-Bonin-Marianas, Philippines, Indonesia, etc.), either because metamorphic rocks are not exposed or rock types are not amenable to petrologic investigation. Correcting for this type of bias is challenging because it would require large random samples of exhumed HP rocks from localities worldwide and development of new techniques for quantifying PT conditions in diverse rock types.

4.4.4 Short-lived Events and Geodynamic Uncertainties

Detachment of rocks from the subducting slab might not occur randomly, but rather in response to specific events, such as subduction of asperities or seamounts (e.g. Agard et al., 2009) or abrupt fluid events. Yet no numerical models have attempted to model these events. In the case of seamounts, high surface roughness correlates with higher coefficients of friction (Gao & Wang, 2014). Higher friction increases heating and T's, driving subduction interface thermal gradients into the field of PT conditions defined by the pd15 and ag18 datasets (Kohn et al., 2018). If asperities become mechanically unstable at depths of $\sim$ 50-70 km, preferential detachment would create an "overabundance" of recorded PT conditions at moderate T ($\sim$ 550 °C) at $\sim$ 2 GPa, as observed.

Alternatively, although fluid release is modeled in our numerical experiments as continuous, it may occur sporadically. Two dehydration reactions along the subduction interface are particularly relevant: the transformation of lawsonite to epidote, and the transformation of chlorite (plus quartz) to garnet. Although dehydration of lawsonite is nearly discontinuous in PT space, few rocks show clear evidence for lawsonite immediately prior to peak metamorphism (although such evidence can be subtle). In the context of equilibrium thermodynamics, chlorite dehydration should occur continuously below depths of $\sim$ 35 km, consistent with assumptions of many numerical geodynamic models. However, research suggests substantial overstepping of this reaction, resulting in the abrupt formation of abundant garnet and release of water (Castro & Spear, 2017). Direct geochronology of garnet growth rates in subduction complexes also suggests abrupt growth and water release (Dragovic et al., 2015). Because fluids are thought to help trigger brittle failure (earthquakes) that could detach rocks from the subducting slab surface, abrupt release at a depth of $\sim$ 50-70 km might again result in an "overabundance" of recorded PT conditions at P's of $\sim$ 2 GPa. This mechanism would require relatively consistent degrees of overstepping in rocks of similar bulk composition and would not directly explain higher T's, however.

5 Conclusion

This study traces PT paths of more than one million markers from 64 subduction simulations representing a large range of presently active subduction zones worldwide. Marker recovery is identified by implementing a "soft" clustering algorithm, and PT distributions of recovered markers are compared among models and with the rock record. Such a large dataset presents a statistically-robust portrait of important recovery modes (where most markers are detached) along the subduction interface. The three most important findings are as follows:

1. Numerical simulations with relatively simple (de)hydration models and visco-plastic interface rheologies simulate important recovery mechanisms near the base of the continental Moho around 1 GPa and 300 °C (underplating and/or formation of

tectonic mélanges) and near the depth of mechanical plate coupling around 2.5 GPa and 525 °C.

2. Subduction systems with young oceanic plates, slow convergence velocities, and thin upper-plate lithospheres are most consistent with the rock record, but it is unclear to what extent kinematic effects (young flexible oceanic plates with high subduction angles accommodating deeper subduction of material) rather than thermal effects (young oceanic plates supporting higher thermal gradients) drive changes in marker PT distributions. Comparing young-slow-thin numerical experiments to the rock record is not straightforward, however, because recovery rates do not correlate with either oceanic plate age or convergence velocity, and warmer subduction zones yield poorer recovery rates.
3. A gap in marker recovery near 2 GPa and 550 °C coinciding with the highest densities of natural samples suggests an "overabundance" of samples are studied from this PT region. Explanations for this "overabundance" might include selective sampling of rocks amenable to petrologic investigation (scientific bias), reaction overstepping (abrupt release of water triggering detachment of rock near 2 GPa and 550 °C), or processes such as subduction of seamounts that are not included in numerical simulations. Future work investigating natural samples from a larger range of peak PT conditions and analyzing marker recovery from numerical geodynamic models that include new hydrologic models and interface rheologies might help resolve this discrepancy.

Open Research

All data, code, and relevant information for reproducing this work can be found at `https://github.com/buchanankerswell/kerswell_et_al_marx`, and at `https://doi.org/10.17605/OSF.IO/3EMWF`, the official Open Science Framework data repository. All code is MIT Licensed and free for use and distribution (see license details).

Acknowledgments

We gratefully acknowledge high-performance computing support from the Borah compute cluster (DOI: `10.18122/oit/3/boisestate`) provided by Boise State University's Research Computing Department. This work was supported by the National Science Foundation grant OIA1545903 to M. Kohn, S. Penniston-Dorland, and M. Feineman.

References

Abers, G., Keken, P. van, Kneller, E., Ferris, A., & Stachnik, J. (2006). The thermal structure of subduction zones constrained by seismic imaging: Implications for slab dehydration and wedge flow. *Earth and Planetary Science Letters*, *241*(3-4), 387–397.

Abers, G., van Keken, P., & Hacker, B. (2017). The cold and relatively dry nature of mantle forearcs in subduction zones. *Nature Geoscience*, *10*(5), 333–337.

Abers, G., Keken, P. van, & Wilson, C. (2020). Deep decoupling in subduction zones: Observations and temperature limits. *Geosphere*, *16*(6), 1408–1424.

Agard, P. (2021). Subduction of oceanic lithosphere in the alps: Selective and archetypal from (slow-spreading) oceans. *Earth-Science Reviews*, *214*, 103517.

Agard, P., Yamato, P., Jolivet, L., & Burov, E. (2009). Exhumation of oceanic blueschists and eclogites in subduction zones: Timing and mechanisms. *Earth-Science Reviews*, *92*(1-2), 53–79.

Agard, P., Yamato, P., Soret, M., Prigent, C., Guillot, S., Plunder, A., et al. (2016). Plate interface rheological switches during subduction infancy: Control on slab penetration and metamorphic sole formation. *Earth and Planetary Science Letters*, *451*, 208–220.

Agard, P., Plunder, A., Angiboust, S., Bonnet, G., & Ruh, J. (2018). The subduction plate interface: Rock record and mechanical coupling (from long to short time scales). *Lithos*, *320-321*, 537–566.

Agard, P., Prigent, C., Soret, M., Dubacq, B., Guillot, S., & Deldicque, D. (2020). Slabitization: Mechanisms controlling subduction development and viscous coupling. *Earth-Science Reviews*, *208*, 103259.

Angiboust, S., Agard, P., Jolivet, L., & Beyssac, O. (2009). The zermatt-saas ophiolite: The largest (60-km wide) and deepest (c. 70–80 km) continuous slice of oceanic lithosphere detached from a subduction zone? *Terra Nova*, *21*(3), 171–180.

Angiboust, S., Agard, P., Raimbourg, H., Yamato, P., & Huet, B. (2011). Subduction interface processes recorded by eclogite-facies shear zones (monviso, w. alps). *Lithos*, *127*(1-2), 222–238.

Angiboust, S., Langdon, R., Agard, P., Waters, D., & Chopin, C. (2012a). Eclogitization of the monviso ophiolite (w. Alps) and implications on subduction dynamics. *Journal of Metamorphic Geology*, *30*(1), 37–61.

Angiboust, S., Wolf, S., Burov, E., Agard, P., & Yamato, P. (2012b). Effect of fluid circulation on subduction interface tectonic processes: Insights from thermo-mechanical numerical modelling. *Earth and Planetary Science Letters*, *357*, 238–248.

Angiboust, S., Kirsch, J., Oncken, O., Glodny, J., Monié, P., & Rybacki, E. (2015). Probing the transition between seismically coupled and decoupled segments along an ancient subduction interface. *Geochemistry, Geophysics, Geosystems*, *16*(6), 1905–1922.

Angiboust, S., Agard, P., Glodny, J., Omrani, J., & Oncken, O. (2016). Zagros blueschists: Episodic underplating and long-lived cooling of a subduction zone. *Earth and Planetary Science Letters*, *443*, 48–58.

Arcay, D. (2017). Modelling the interplate domain in thermo-mechanical simulations of subduction: Critical effects of resolution and rheology, and consequences on wet mantle melting. *Physics of the Earth and Planetary Interiors*, *269*, 112–132.

Audet, P., & Kim, Y. (2016). Teleseismic constraints on the geological environment of deep episodic slow earthquakes in subduction zone forearcs: A review. *Tectonophysics*, *670*, 1–15.

Audet, P., & Schaeffer, A. (2018). Fluid pressure and shear zone development over the locked to slow slip region in cascadia. *Science Advances*, *4*(3), eaar2982.

Avigad, D., & Garfunkel, Z. (1991). Uplift and exhumation of high-pressure metamorphic terrains: The example of the cycladic blueschist belt (aegean sea). *Tectonophysics*, *188*(3-4), 357–372.

Banfield, J., & Raftery, A. (1993). Model-based gaussian and non-gaussian clustering. *Biometrics*, 803–821.

Barlow, H. (1989). Unsupervised learning. *Neural Computation*, *1*(3), 295–311.

Batchelor, G. (1953). *The theory of homogeneous turbulence*. Cambridge university press.

Beall, A., Fagereng, Å., & Ellis, S. (2019). Strength of strained two-phase mixtures: Application to rapid creep and stress amplification in subduction zone mélange. *Geophysical Research Letters*, *46*(1), 169–178.

Bebout, G. (2007). Metamorphic chemical geodynamics of subduction zones. *Earth and Planetary Science Letters*, *260*(3-4), 373–393.

Bebout, G., & Barton, M. (2002). Tectonic and metasomatic mixing in a high-t, subduction-zone mélange—insights into the geochemical evolution of the slab–mantle interface. *Chemical Geology*, *187*(1-2), 79–106.

Beyssac, O., Goffé, B., Chopin, C., & Rouzaud, J. (2002). Raman spectra of carbonaceous material in metasediments: A new geothermometer. *Journal of Metamorphic Geology*, *20*(9), 859–871.

Bostock, M. (2013). The moho in subduction zones. *Tectonophysics*, *609*, 547–557.

Boussinesq, J. (1897). *Théorie de l'écoulement tourbillonnant et tumultueux des liquides dans les lits rectilignes a grande section* (Vol. 1). Gauthier-Villars.

Burdette, E., & Hirth, G. (2022). Creep rheology of antigorite: Experiments at subduction zone conditions. *Journal of Geophysical Research: Solid Earth*, *127*(7), e2022JB024260.

Burov, E., François, T., Agard, P., Le Pourhiet, L., Meyer, B., Tirel, C., et al. (2014). Rheological and geodynamic controls on the mechanisms of subduction and HP/UHP exhumation of crustal rocks during continental collision: Insights from numerical models. *Tectonophysics*, *631*, 212–250.

Calvert, A., Preston, L., & Farahbod, A. (2011). Sedimentary underplating at the cascadia mantle-wedge corner revealed by seismic imaging. *Nature Geoscience*, *4*(8), 545–548.

Calvert, A., Bostock, M., Savard, G., & Unsworth, M. (2020). Cascadia low frequency earthquakes at the base of an overpressured subduction shear zone. *Nature Communications*, *11*(1), 1–10.

Castro, A., & Spear, F. (2017). Reaction overstepping and re-evaluation of peak p–t conditions of the blueschist unit sifnos, greece: Implications for the cyclades subduction zone. *International Geology Review*, *59*(5-6), 548–562.

Celeux, G., & Govaert, G. (1995). Gaussian parsimonious clustering models. *Pattern Recognition*, *28*(5), 781–793.

Cloos, M., & Shreve, R. (1988). Subduction-channel model of prism accretion, melange formation, sediment subduction, and subduction erosion at convergent plate margins: 1. Background and description. *Pure and Applied Geophysics*, *128*(3), 455–500.

Connolly, J. (2005). Computation of phase equilibria by linear programming: A tool for geodynamic modeling and its application to subduction zone decarbonation. *Earth and Planetary Science Letters*, *236*(1-2), 524–541.

Currie, C., & Hyndman, R. (2006). The thermal structure of subduction zone back arcs. *Journal of Geophysical Research: Solid Earth*, *111*(B8), 1–22.

Currie, C., Wang, K., Hyndman, R., & He, J. (2004). The thermal effects of steady-state slab-driven mantle flow above a subducting plate: The cascadia subduction zone and backarc. *Earth and Planetary Science Letters*, *223*(1-2), 35–48.

Davies, J. (1999). Simple analytic model for subduction zone thermal structure. *Geophysical Journal International*, *139*(3), 823–828.

Delph, J., Thomas, A., & Levander, A. (2021). Subcretionary tectonics: Linking variability in the expression of subduction along the cascadia forearc. *Earth and Planetary Science Letters*, *556*, 116724.

Dempster, A., Laird, N., & Rubin, D. (1977). Maximum likelihood from incomplete data via the EM algorithm. *Journal of the Royal Statistical Society: Series B (Methodological)*, *39*(1), 1–22.

Dragovic, B., Baxter, E., & Caddick, M. (2015). Pulsed dehydration and garnet growth during subduction revealed by zoned garnet geochronology and thermodynamic modeling, sifnos, greece. *Earth and Planetary Science Letters*, *413*, 111–122.

England, P., Engdahl, R., & Thatcher, W. (2004). Systematic variation in the depths of slabs beneath arc volcanoes. *Geophysical Journal International*, *156*(2), 377–408.

Faccenda, M., Gerya, T., & Chakraborty, S. (2008). Styles of post-subduction collisional orogeny: Influence of convergence velocity, crustal rheology and radiogenic heat production. *Lithos*, *103*(1-2), 257–287.

Ferris, A., Abers, G., Christensen, D., & Veenstra, E. (2003). High resolution image of the subducted pacific (?) Plate beneath central alaska, 50–150 km depth. *Earth and Planetary Science Letters*, *214*(3-4), 575–588.

Ferry, J., & Watson, E. (2007). New thermodynamic models and revised calibrations for the ti-in-zircon and zr-in-rutile thermometers. *Contributions to Mineralogy and Petrology*, *154*(4), 429–437.

Figueiredo, M., & Jain, A. (2002). Unsupervised learning of finite mixture models. *IEEE Transactions on Pattern Analysis and Machine Intelligence*, *24*(3), 381–396.

Fisher, D., Hooker, J., Smye, A., & Chen, T. (2021). Insights from the geological record of deformation along the subduction interface at depths of seismogenesis. *Geosphere*, *17*(6), 1686–1703.

Fraley, C., & Raftery, A. (2002). Model-based clustering, discriminant analysis, and density estimation. *Journal of the American Statistical Association*, *97*(458), 611–631.

Furukawa, Y. (1993). Depth of the decoupling plate interface and thermal structure under arcs. *Journal of Geophysical Research: Solid Earth*, *98*(B11), 20005–20013.

Gao, X., & Wang, K. (2014). Strength of stick-slip and creeping subduction megathrusts from heat flow observations. *Science*, *345*(6200), 1038–1041.

Gerya, T. (2019). *Introduction to numerical geodynamic modelling*. Cambridge University Press.

Gerya, T., & Stöckhert, B. (2006). Two-dimensional numerical modeling of tectonic and metamorphic histories at active continental margins. *International Journal of Earth Sciences*, *95*(2), 250–274.

Gerya, T., & Yuen, D. (2003). Characteristics-based marker-in-cell method with conservative finite-differences schemes for modeling geological flows with strongly variable transport properties. *Physics of the Earth and Planetary Interiors*, *140*(4), 293–318.

Gerya, T., Stöckhert, B., & Perchuk, A. (2002). Exhumation of high-pressure metamorphic rocks in a subduction channel: A numerical simulation. *Tectonics*, *21*(6), 6–1.

Gerya, T., Connolly, J., & Yuen, D. (2008). Why is terrestrial subduction one-sided? *Geology*, *36*(1), 43–46.

Gorczyk, W., Willner, A., Gerya, T., Connolly, J., & Burg, J. (2007). Physical controls of magmatic productivity at pacific-type convergent margins: Numerical modelling. *Physics of the Earth and Planetary Interiors*, *163*(1-4), 209–232.

Groppo, C., Rolfo, F., Sachan, H., & Rai, S. (2016). Petrology of blueschist from the western himalaya (ladakh, NW india): Exploring the complex behavior of a lawsonite-bearing system in a paleo-accretionary setting. *Lithos*, *252*, 41–56.

Hacker, B. (1996). Eclogite formation and the rheology, buoyancy, seismicity, and h˜ 2O content of oceanic crust. *GEOPHYSICAL MONOGRAPH-AMERICAN GEOPHYSICAL UNION*, *96*, 337–346.

Hacker, B. (2008). H2O subduction beyond arcs. *Geochemistry, Geophysics, Geosystems*, *9*(3).

Hacker, B., Abers, G., & Peacock, S. (2003). Subduction factory 1. Theoretical mineralogy, densities, seismic wave speeds, and H_2O contents. *Journal of Geophysical Research: Solid Earth*, *108*(B1).

Harlow, F. (1962). *The particle-in-cell method for numerical solution of problems in fluid dynamics*. Los Alamos Scientific Lab., N. Mex.

Harlow, F. (1964). The particle-in-cell computing method for fluid dynamics. *Methods Comput. Phys.*, *3*, 319–343.

Harlow, F., & Welch, J. (1965). Numerical calculation of time-dependent viscous incompressible flow of fluid with free surface. *The Physics of Fluids*, *8*(12), 2182–2189.

Hilairet, N., Reynard, B., Wang, Y., Daniel, I., Merkel, S., Nishiyama, N., & Petitgirard, S. (2007). High-pressure creep of serpentine, interseismic deformation, and initiation of subduction. *Science*, *318*(5858), 1910–1913.

Holt, A., & Condit, C. (2021). Slab temperature evolution over the lifetime of a subduction zone. *Geochemistry, Geophysics, Geosystems*, e2020GC009476.

Hu, J., & Gurnis, M. (2020). Subduction duration and slab dip. *Geochemistry, Geophysics, Geosystems*, *21*(4), e2019GC008862.

Hyndman, R., & Peacock, S. (2003). Serpentinization of the forearc mantle. *Earth and Planetary Science Letters*, *212*(3-4), 417–432.

Hyndman, R., Currie, C., & Mazzotti, S. (2005). Subduction zone backarcs, mobile belts, and orogenic heat. *GSA Today*, *15*(2), 4–10.

Ioannidi, P., Angiboust, S., Oncken, O., Agard, P., Glodny, J., & Sudo, M. (2020). Deformation along the roof of a fossil subduction interface in the transition zone below seismogenic coupling: The austroalpine case and new insights from the malenco massif (central alps). *Geosphere*, *16*(2), 510–532.

Ioannidi, P., Le Pourhiet, L., Agard, P., Angiboust, S., & Oncken, O. (2021). Effective rheology of a two-phase subduction shear zone: Insights from numerical simple shear experiments and implications for subduction zone interfaces. *Earth and Planetary Science Letters*, *566*, 116913.

Ito, K., & Kennedy, G. (1971). An experimental study of the basalt-garnet granulite-eclogite transition. *The Structure and Physical Properties of the Earth's Crust*, *14*, 303–314.

Karato, S., & Wu, P. (1993). Rheology of the upper mantle: A synthesis. *Science*, *260*(5109), 771–778.

Kerswell, B., & Kohn, M. (2022). A comparison of surface heat flow interpolations near subduction zones. *Submitted to Geochemistry, Geophysics, Geosystems.*

Kerswell, B., Kohn, M., & Gerya, T. (2021). Backarc lithospheric thickness and serpentine stability control slab-mantle coupling depths in subduction zones. *Geochemistry, Geophysics, Geosystems*, *22*(6), e2020GC009304.

Kitamura, Y., & Kimura, G. (2012). Dynamic role of tectonic mélange during interseismic process of plate boundary mega earthquakes. *Tectonophysics*, *568*, 39–52.

Kohn, M. (2020). A refined zirconium-in-rutile thermometer. *American Mineralogist: Journal of Earth and Planetary Materials*, *105*(6), 963–971.

Kohn, M., Castro, A., Kerswell, B., Ranero, C. R., & Spear, F. (2018). Shear heating reconciles thermal models with the metamorphic rock record of subduction. *Proceedings of the National Academy of Sciences*, *115*(46), 11706–11711.

Kotowski, A., & Behr, W. (2019). Length scales and types of heterogeneities along the deep subduction interface: Insights from exhumed rocks on syros island, greece. *Geosphere*, *15*(4), 1038–1065.

Locatelli, M., Federico, L., Agard, P., & Verlaguet, A. (2019). Geology of the southern monviso metaophiolite complex (w-alps, italy). *Journal of Maps*, *15*(2), 283–297.

Mann, M., Abers, G., Daly, K., & Christensen, D. (2022). Subduction of an oceanic plateau across southcentral alaska: Scattered-wave imaging. *Journal of Geophysical Research: Solid Earth*, e2021JB022697.

McKenzie, D. (1969). Speculations on the consequences and causes of plate motions. *Geophysical Journal International*, *18*(1), 1–32.

Molnar, P., & England, P. (1990). Temperatures, heat flux, and frictional stress near major thrust faults. *Journal of Geophysical Research: Solid Earth*, *95*(B4), 4833–4856.

Monie, P., & Agard, P. (2009). Coeval blueschist exhumation along thousands of kilometers: Implications for subduction channel processes. *Geochemistry, Geophysics, Geosystems*, *10*(7).

Moresi, L., Dufour, F., & Mühlhaus, H. (2003). A lagrangian integration point finite element method for large deformation modeling of viscoelastic geomaterials. *Journal of Computational Physics*, *184*(2), 476–497.

Morishige, M., & Kuwatani, T. (2020). Bayesian inversion of surface heat flow in subduction zones: A framework to refine geodynamic models based on observational constraints. *Geophysical Journal International*, *222*(1), 103–109.

Naif, S., Key, K., Constable, S., & Evans, R. (2015). Water-rich bending faults at the m iddle a merica t rench. *Geochemistry, Geophysics, Geosystems*, *16*(8), 2582–2597.

Okay, A. (1989). Alpine-himalayan blueschists. *Annual Review of Earth and Planetary Sciences*, *17*(1), 55–87.

Peacock, S. (1990). Fluid processes in subduction zones. *Science*, *248*(4953), 329–337.

Peacock, S. (1996). Thermal and petrologic structure of subduction zones. *Subduction: Top to Bottom*, *96*, 119–133.

Peacock, S., & Wang, K. (1999). Seismic consequences of warm versus cool subduction metamorphism: Examples from southwest and northeast japan. *Science*, *286*(5441), 937–939.

Penniston-Dorland, S., Kohn, M., & Manning, C. (2015). The global range of subduction zone thermal structures from exhumed blueschists and eclogites: Rocks are hotter than models. *Earth and Planetary Science Letters*, *428*, 243–254.

Platt, J. (1986). Dynamics of orogenic wedges and the uplift of high-pressure metamorphic rocks. *Geological Society of America Bulletin*, *97*(9), 1037–1053.

Plunder, A., Agard, P., Chopin, C., & Okay, A. (2013). Geodynamics of the tavşanlı zone, western turkey: Insights into subduction/obduction processes. *Tectonophysics*, *608*, 884–903.

Plunder, A., Agard, P., Chopin, C., Pourteau, A., & Okay, A. (2015). Accretion, underplating and exhumation along a subduction interface: From subduction initiation to continental subduction (tavşanlı zone, w. turkey). *Lithos*, *226*, 233–254.

Plunder, A., Thieulot, C., & Van Hinsbergen, D. (2018). The effect of obliquity on temperature in subduction zones: Insights from 3-d numerical modeling. *Solid Earth*, *9*(3), 759–776.

Ranalli, G. (1995). *Rheology of the earth*. Springer Science & Business Media.

Reynolds, D. (2009). Gaussian mixture models. *Encyclopedia of Biometrics*, *741*, 659–663.

Roda, M., Marotta, A., & Spalla, M. (2010). Numerical simulations of an ocean-continent convergent system: Influence of subduction geometry and mantle wedge hydration on crustal recycling. *Geochemistry, Geophysics, Geosystems*, *11*(5).

Roda, M., Spalla, M., & Marotta, A. (2012). Integration of natural data within a numerical model of ablative subduction: A possible interpretation for the alpine dynamics of the austroalpine crust. *Journal of Metamorphic Geology*, *30*(9), 973–996.

Roda, M., Zucali, M., Regorda, A., & Spalla, M. (2020). Formation and evolution of a subduction-related mélange: The example of the rocca canavese thrust sheets (western alps). *Bulletin*, *132*(3-4), 884–896.

Rondenay, S., Abers, G., & van Keken, P. (2008). Seismic imaging of subduction zone metamorphism. *Geology*, *36*(4), 275–278.

Ruh, J., Le Pourhiet, L., Agard, P., Burov, E., & Gerya, T. (2015). Tectonic slicing of subducting oceanic crust along plate interfaces: Numerical modeling. *Geochemistry, Geophysics, Geosystems*, *16*(10), 3505–3531.

Schmidt, M., & Poli, S. (1998). Experimentally based water budgets for dehydrating slabs and consequences for arc magma generation. *Earth and Planetary Science Letters*, *163*(1-4), 361–379.

Schwarz, G. (1978). Estimating the dimension of a model. *The Annals of Statistics*, 461–464.

Scrucca, L., Fop, M., Murphy, T., & Raftery, A. (2016). Mclust 5: Clustering, classification and density estimation using gaussian finite mixture models. *The R Journal*, *8*(1), 289.

Shreve, R., & Cloos, M. (1986). Dynamics of sediment subduction, melange formation, and prism accretion. *Journal of Geophysical Research: Solid Earth*, *91*(B10), 10229–10245.

Sizova, E., Gerya, T., Brown, M., & Perchuk, L. (2010). Subduction styles in the precambrian: Insight from numerical experiments. *Lithos*, *116*(3-4), 209–229.

Soret, M., Bonnet, G., Agard, P., Larson, K., Cottle, J., Dubacq, B., et al. (2022). Timescales of subduction initiation and evolution of subduction thermal regimes. *Earth and Planetary Science Letters*, *584*, 117521.

Spear, F., & Selverstone, J. (1983). Quantitative PT paths from zoned minerals: Theory and tectonic applications. *Contributions to Mineralogy and Petrology*, *83*(3), 348–357.

Stöckhert, B. (2002). Stress and deformation in subduction zones: Insight from the record of exhumed metamorphic rocks. *Geological Society, London, Special Publications*, *200*(1), 255–274.

Syracuse, E., & Abers, G. (2006). Global compilation of variations in slab depth beneath arc volcanoes and implications. *Geochemistry, Geophysics, Geosystems*, *7*(5).

Syracuse, E., van Keken, P., Abers, G., Suetsugu, D., Bina, C., Inoue, T., et al. (2010). The global range of subduction zone thermal models. *Physics of the Earth and Planetary Interiors*, *183*(1-2), 73–90.

Tewksbury-Christle, C., & Behr, W. (2021). Constraints from exhumed rocks on the seismic signature of the deep subduction interface. *Geophysical Research Letters*, *48*(18).

Tewksbury-Christle, C., Behr, W., & Helper, M. (2021). Tracking deep sediment underplating in a fossil subduction margin: Implications for interface rheology and mass and volatile recycling. *Geochemistry, Geophysics, Geosystems*, *22*(3).

Turcotte, D., & Schubert, G. (2002). *Geodynamics*. Cambridge university press.

van Keken, P., Hacker, B., Syracuse, E., & Abers, G. (2011). Subduction factory: 4. Depth-dependent flux of H_2O from subducting slabs worldwide. *Journal of Geophysical Research*, *116*(b1), b01401.

van Keken, P., Wada, I., Abers, G., Hacker, B., & Wang, K. (2018). Mafic high-pressure rocks are preferentially exhumed from warm subduction settings. *Geochemistry, Geophysics, Geosystems*, *19*(9), 2934–2961.

van Keken, P., Wada, I., Sime, N., & Abers, G. (2019). Thermal structure of the forearc in subduction zones: A comparison of methodologies. *Geochemistry, Geophysics, Geosystems*, *20*(7), 3268–3288.

Vermeesch, P. (2018). IsoplotR: A free and open toolbox for geochronology. *Geoscience Frontiers*, *9*(5), 1479–1493.

Wada, I., & Wang, K. (2009). Common depth of slab-mantle decoupling: Reconciling diversity and uniformity of subduction zones. *Geochemistry, Geophysics, Geosystems*, *10*(10).

Wakabayashi, J. (2015). Anatomy of a subduction complex: Architecture of the franciscan complex, california, at multiple length and time scales. *International Geology Review*, *57*(5-8), 669–746.

Yamato, P., Agard, P., Burov, E., Le Pourhiet, L., Jolivet, L., & Tiberi, C. (2007). Burial and exhumation in a subduction wedge: Mutual constraints from thermomechanical modeling and natural p-t-t data (schistes lustrés, western alps). *Journal of Geophysical Research: Solid Earth*, *112*(B7).

Yamato, P., Burov, E., Agard, P., Le Pourhiet, L., & Jolivet, L. (2008). HP-UHP exhumation during slow continental subduction: Self-consistent thermodynamically and thermomechanically coupled model with application to the western alps. *Earth and Planetary Science Letters*, *271*(1-4), 63–74.

A Appendix

A.1 Gaussian Mixture Models

Let the traced markers represent a d-dimensional array of n random independent variables $x_i \in \mathbb{R}^{n \times d}$. Assume markers x_i were drawn from k discrete probability distributions with parameters Φ. The probability distribution of markers x_i can be modeled with a mixture of k components:

$$p(x_i|\Phi) = \sum_{j=1}^{k} \pi_j p(x_i|\Theta_j) \tag{A.1}$$

where $p(x_i|\Theta_j)$ is the probability of x_i under the j^{th} mixture component and π_j is the mixture proportion representing the probability that x_i belongs to the j^{th} component ($\pi_j \geq 0; \sum_{j=1}^{k} \pi_j = 1$).

Assuming Θ_j describes a Gaussian probability distributions with mean μ_j and covariance Σ_j, Equation (A.1) becomes:

$$p(x_i|\Phi) = \sum_{j=1}^{k} \pi_j \mathcal{N}(x_i|\mu_j, \Sigma_j) \tag{A.2}$$

where

$$\mathcal{N}(x_i|\mu_j, \Sigma_j) = \frac{exp\{-\frac{1}{2}(x_i - \mu_j)(x_i - \mu_j)^T \Sigma_j^{-1}\}}{\sqrt{det(2\pi\Sigma_j)}} \tag{A.3}$$

The parameters μ_j and Σ_j, representing the center and shape of each cluster, are estimated by maximizing the log of the likelihood function, $L(x_i|\Phi) = \prod_{i=1}^{n} p(x_i|\Phi)$:

$$log\ L(x_i|\Phi) = log \prod_{i=1}^{n} p(x_i|\Phi) = \sum_{i=1}^{n} log \left[\sum_{j=1}^{k} \pi_j p(x_i|\Theta_j) \right] \tag{A.4}$$

Taking the derivative of Equation (A.4) with respect to each parameter, π, μ, Σ, setting the equation to zero, and solving for each parameter gives the maximum likelihood estimators:

$$\begin{aligned} N_j &= \sum_{i=1}^{n} \omega_i \\ \pi_j &= \frac{N_j}{n} \\ \mu_j &= \frac{1}{N_j} \sum_{i=1}^{n} \omega_i x_i \\ \Sigma_j &= \frac{1}{N_j} \sum_{i=1}^{n} \omega_i (x_i - \mu_j)(x_i - \mu_j)^T \end{aligned} \tag{A.5}$$

where ω_i ($\omega_i \geq 0; \sum_{j=1}^{k} \omega_i = 1$) are membership weights representing the probability of an observation x_i belonging to the j^{th} Gaussian and N_j represents the number of observations belonging to the j^{th} Gaussian. Please note that ω_i is unknown for markers so maximum likelihood estimator cannot be computed with Equation (A.5). The solution to this problem is the Expectation-Maximization algorithm, which is defined below.

General purpose functions in the R package `Mclust` (Scrucca et al., 2016) are used to fit Gaussian mixture models. "Fitting" refers to adjusting all k Gaussian parameters μ_j and Σ_j until the data and Gaussian ellipsoids achieve maximum likelihood defined by Equation (A.4). After Banfield & Raftery (1993), covariance matrices Σ in `Mclust` are parameterized to be flexible in their shape, volume, and orientation (Scrucca et al., 2016):

$$\Sigma_j = \lambda_j D_j A_j D_j^T \tag{A.6}$$

where D_j is the orthogonal eigenvector matrix, A_j and λ_j are diagonal matrices of values proportional to the eigenvalues. This implementation allows fixing one, two, or three geometric elements of the covariance matrices. That is, the volume λ_j, shape A_j, and orientation D_j of Gaussian clusters can change or be fixed among all k clusters (e.g. Celeux & Govaert, 1995; Fraley & Raftery, 2002). Fourteen parameterizations of Equation (A.6) are tried, representing different geometric combinations of the covariance matrices Σ (see Scrucca et al., 2016) and the Bayesian information criterion is computed (Schwarz, 1978). The parameterization for Equation (A.6) is chosen by Bayesian information criterion.

A.2 Expectation-Maximization

The Expectation-Maximization algorithm estimates Gaussian mixture model parameters by initializing k Gaussians with parameters (π_j, μ_j, Σ_j), then iteratively computing membership weights with Equation (A.7) and updating Gaussian parameters with Equation (A.5) until reaching a convergence threshold (Dempster et al., 1977).

The *expectation* (E-)step involves a "latent" multinomial variable $z_i \in \{1, 2, \ldots, k\}$ representing the unknown classifications of x_i with a joint distribution $p(x_i, z_i) = p(x_i|z_i)p(z_j)$. Membership weights ω_i are equivalent to the conditional probability $p(z_i|x_i)$, which represents the probability of observation x_i belonging to the j^{th} Gaussian. Given initial guesses for Gaussian parameters π_j, μ_j, Σ_j, membership weights are computed using Bayes The-orem (E-step):

$$p(z_i|x_i) = \frac{p(x_i|z_i)p(z_j)}{p(x_i)} = \frac{\pi_j \mathcal{N}(\mu_j, \Sigma_j)}{\sum_{j=1}^{k} \pi_j \mathcal{N}(\mu_j, \Sigma_j)} = \omega_i \tag{A.7}$$

and Gaussian estimates are updated during the *maximization* (M-)step by applying ω_i to Equation (A.5). This step gives markers x_i class labels $z_i \in \{1, \ldots, k\}$ representing assignment to one of k clusters (Figure 2).

Supporting Information for: Computing Rates and Distributions of Rock Recovery in Subduction Zones

Buchanan C. Kerswell [1] Matthew J. Kohn [2] Taras V. Gerya [3]

[1]Department of Geology & Environmental Earth Science, Miami University, Oxford, OH 45056

[2]Department of Geosicences, Boise State University, Boise, ID 83725

[3]Department of Earth Sciences, ETH-Zurich, Sonneggstrasse 5, Zurich 8092, Switzerland

1 Contents of this File

1. Visualizations S1 to S64

2 Introduction

The following pages contain visualizations of marker classifications results for all 64 subduction zone simulations summarized in the main text of this study. Each page contains figures showing marker PT distributions and geodynamic snapshots that supplement the examples used in the manuscript. Data and code for reproducing these visualizations are available online at `https://github.com/buchanankerswell/kerswell_et_al_marx` and `https://osf.io/3emwf/`.

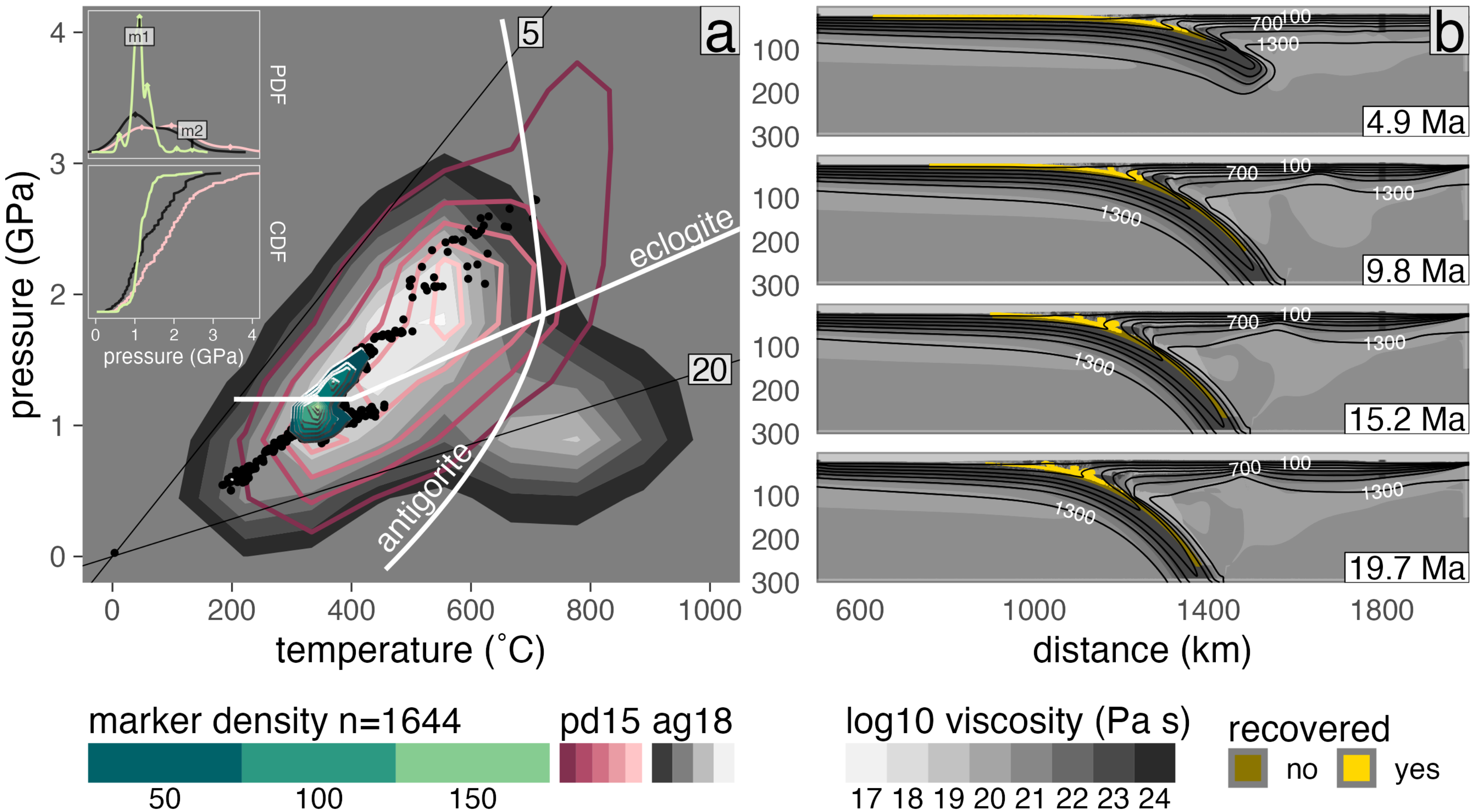

Figure S1: PT distribution of recovered markers from model cda46. Refer to the main text for explanation of panels and colors.

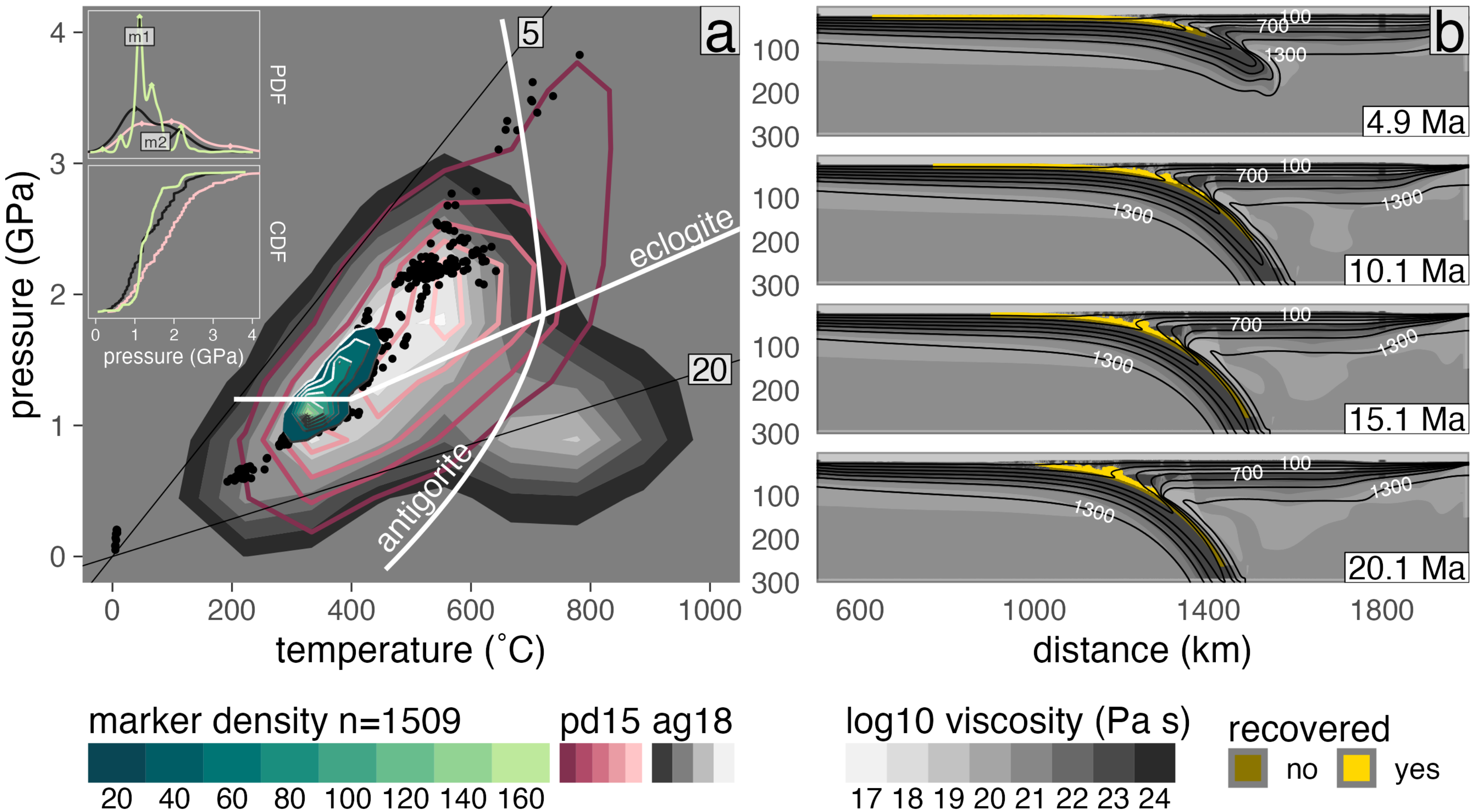

Figure S2: PT distribution of recovered markers from model cda62. Refer to the main text for explanation of panels and colors.

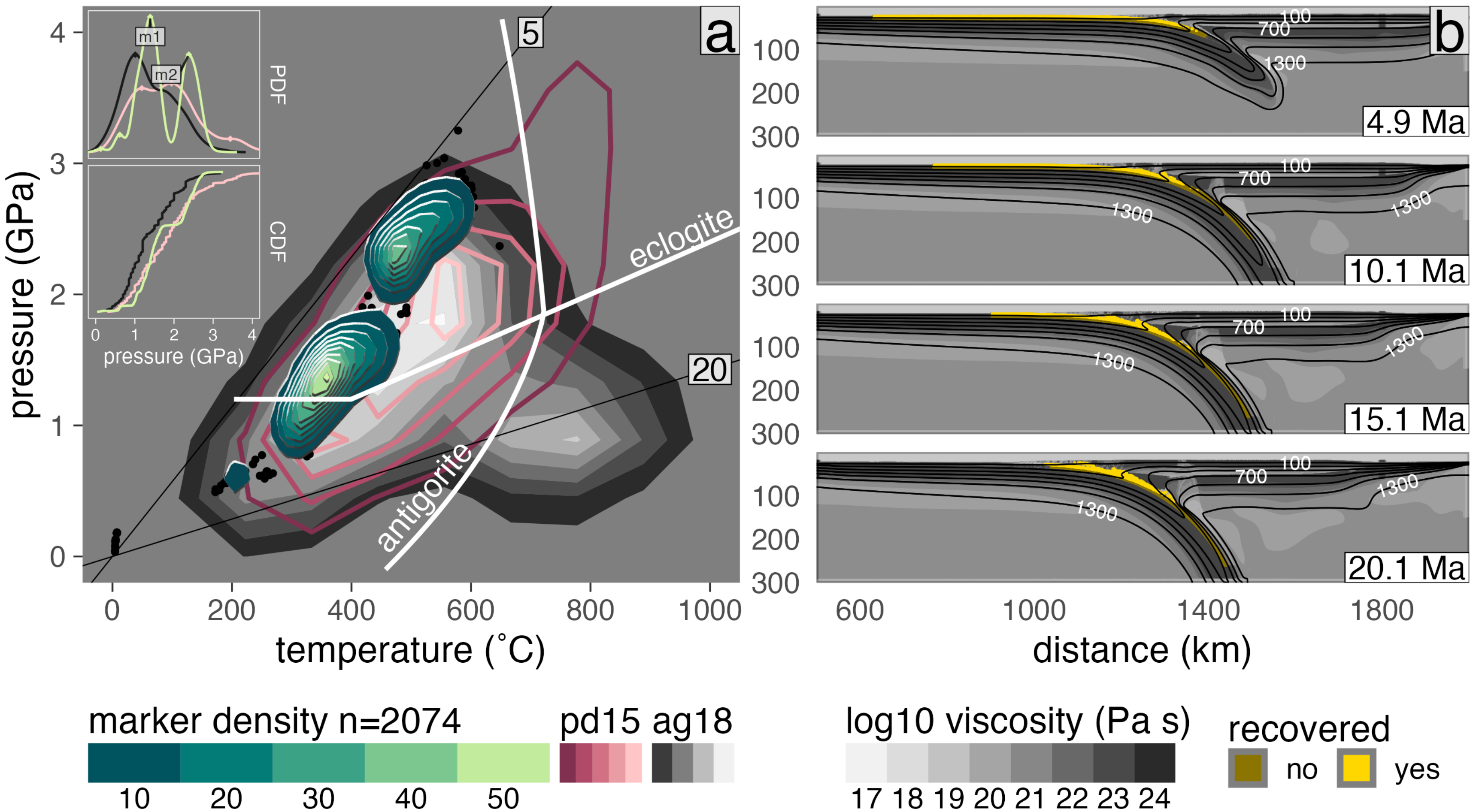

Figure S3: PT distribution of recovered markers from model cda78. Refer to the main text for explanation of panels and colors.

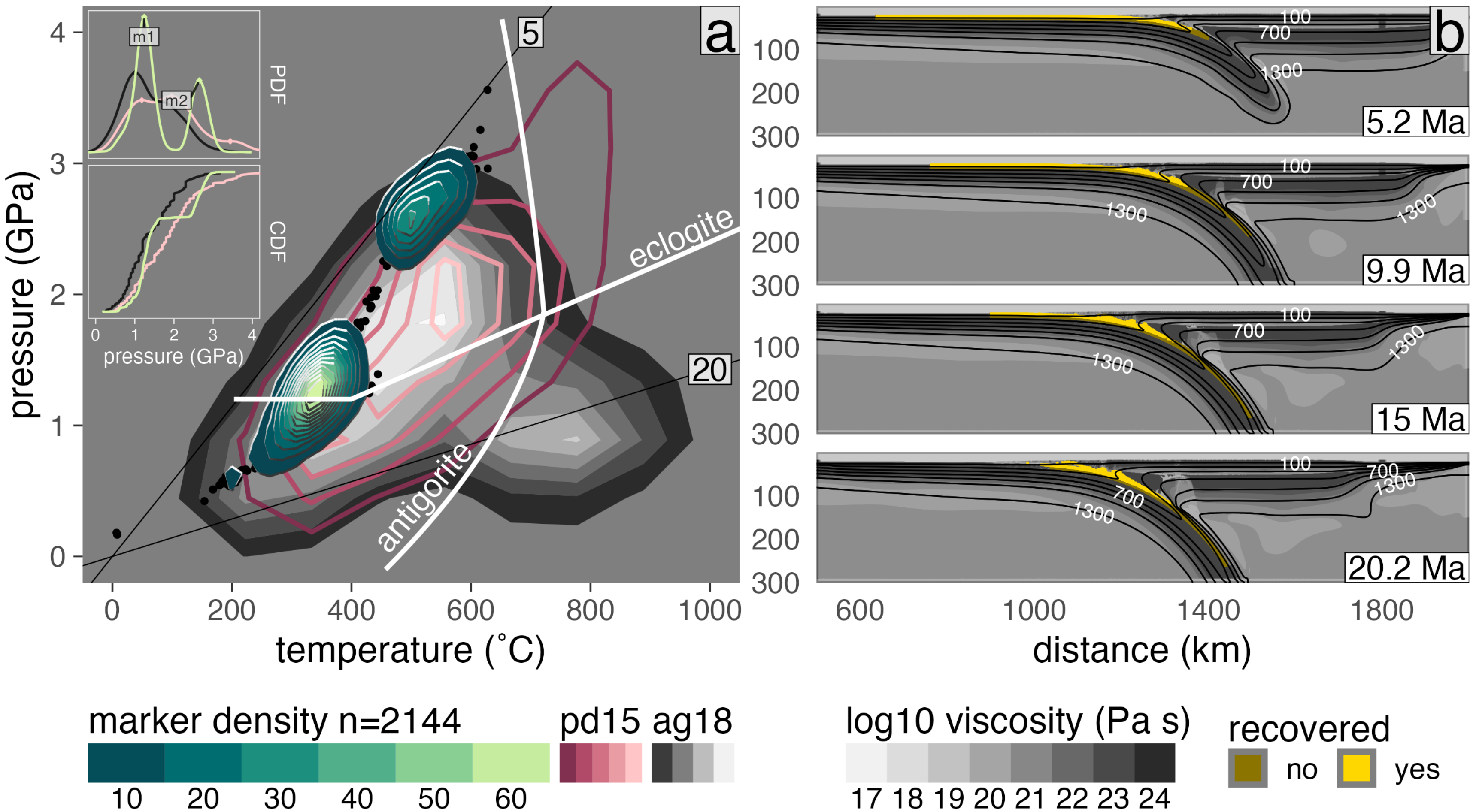

Figure S4: PT distribution of recovered markers from model cda94. Refer to the main text for explanation of panels and colors.

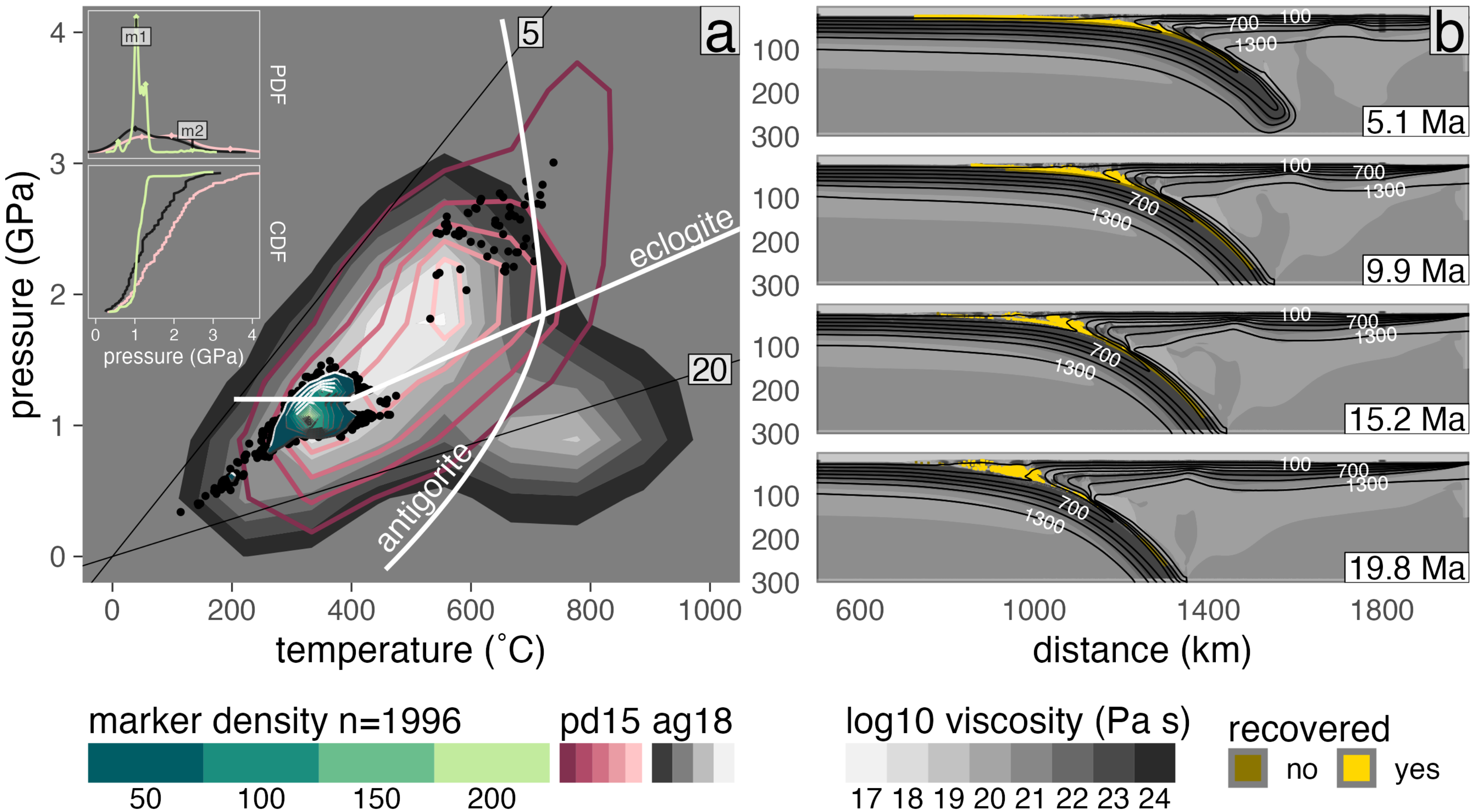

Figure S5: PT distribution of recovered markers from model cdb46. Refer to the main text for explanation of panels and colors.

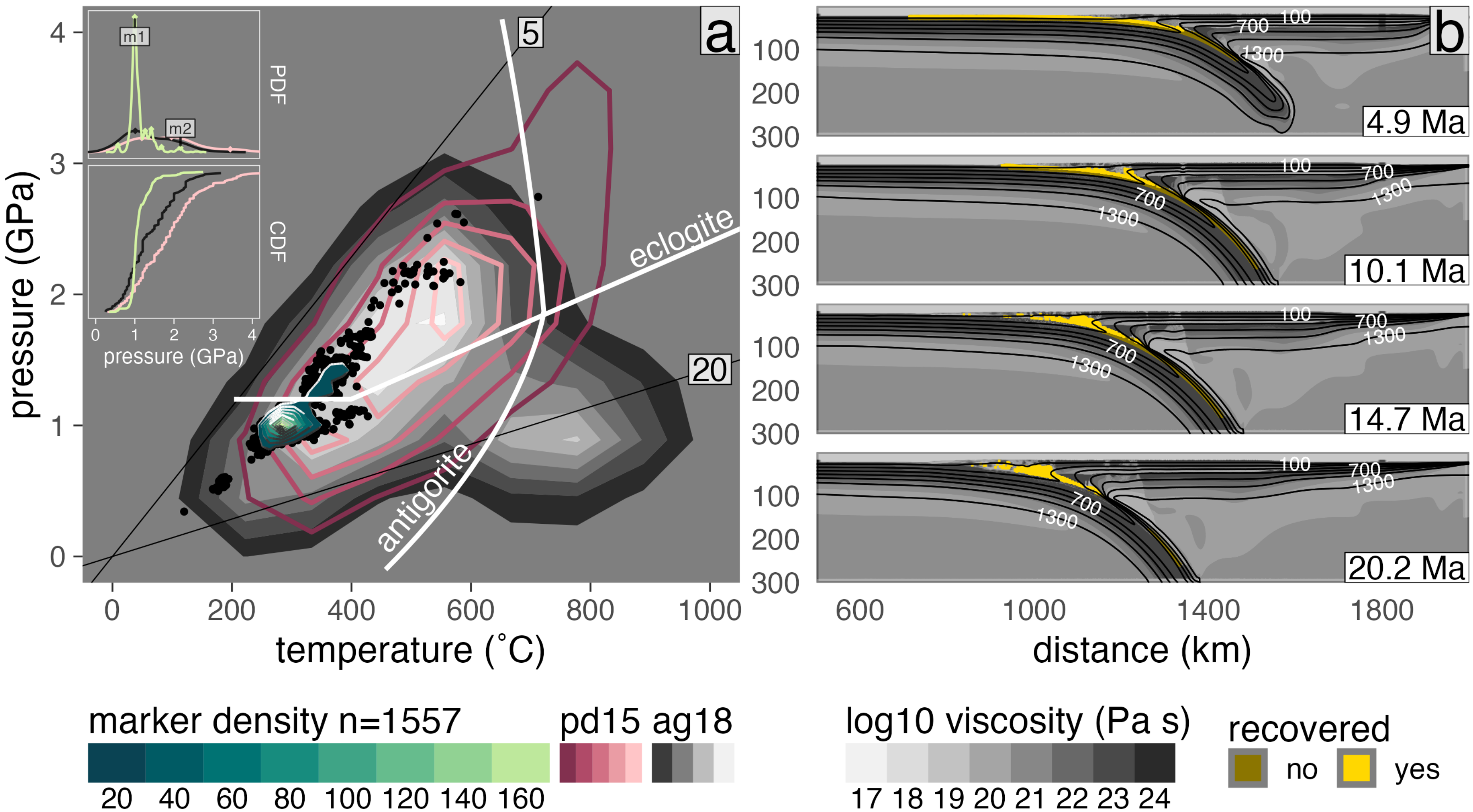

Figure S6: PT distribution of recovered markers from model cdb62. Refer to the main text for explanation of panels and colors.

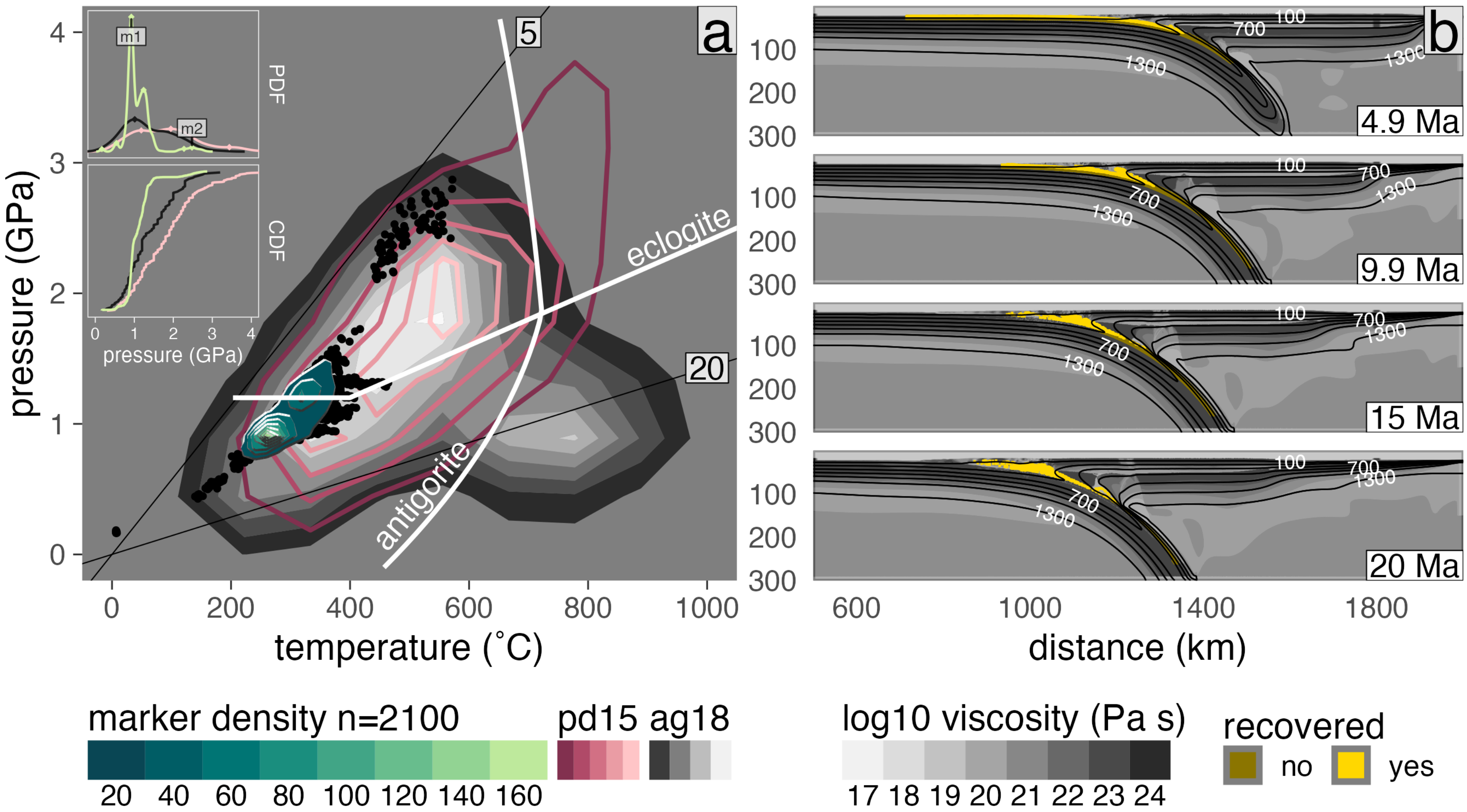

Figure S7: PT distribution of recovered markers from model cdb78. Refer to the main text for explanation of panels and colors.

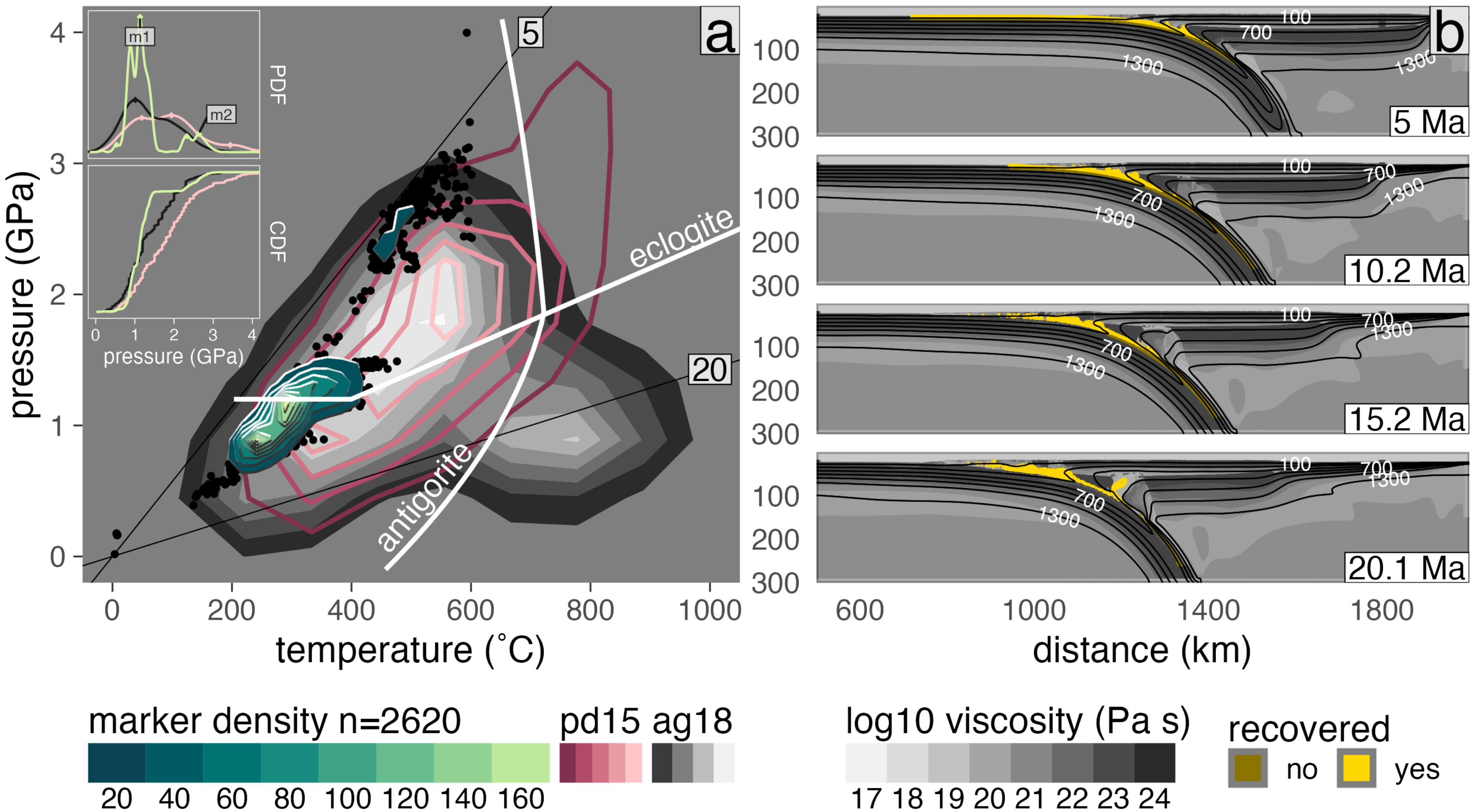

Figure S8: PT distribution of recovered markers from model cdb94. Refer to the main text for explanation of panels and colors.

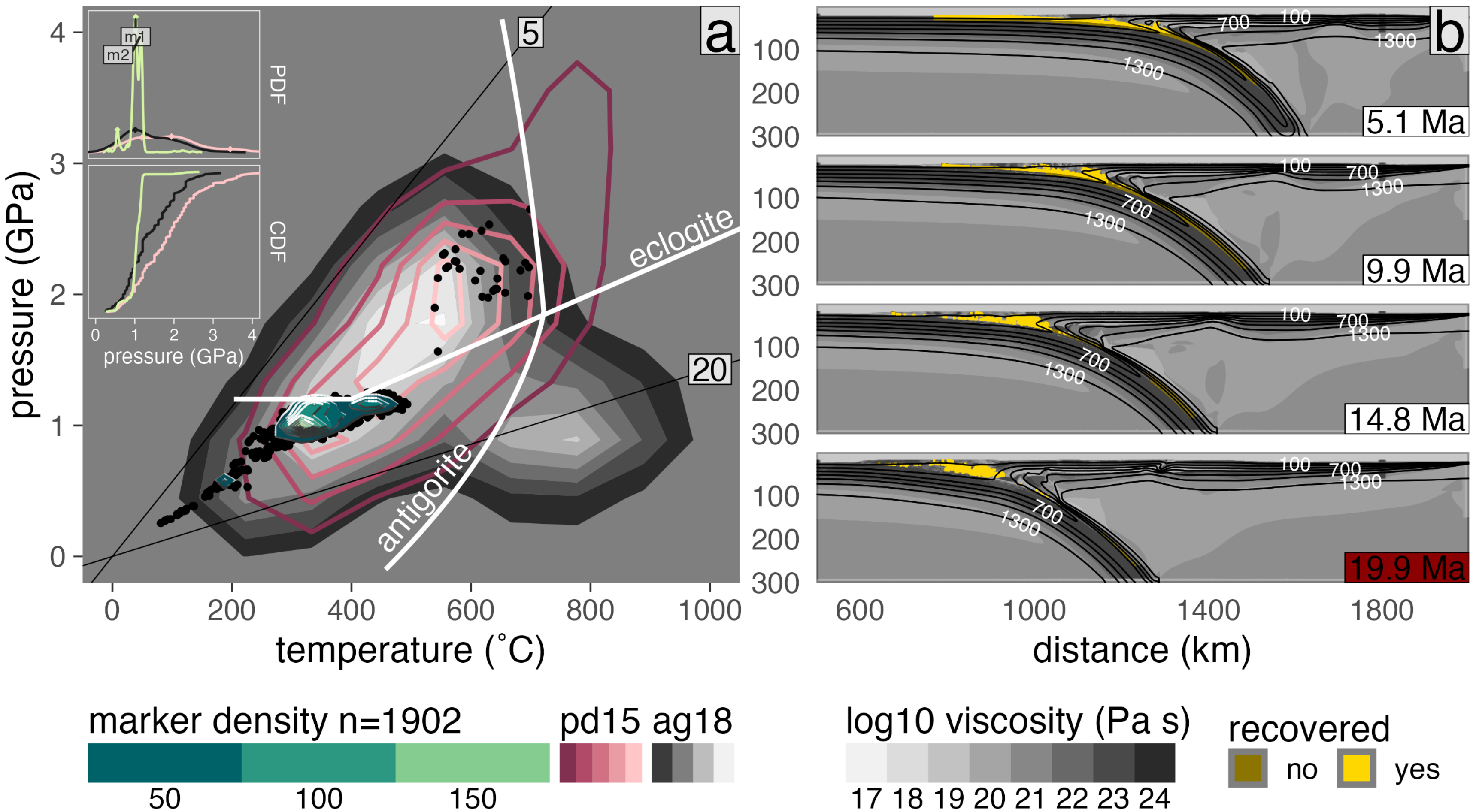

Figure S9: PT distribution of recovered markers from model cdc46. Refer to the main text for explanation of panels and colors.

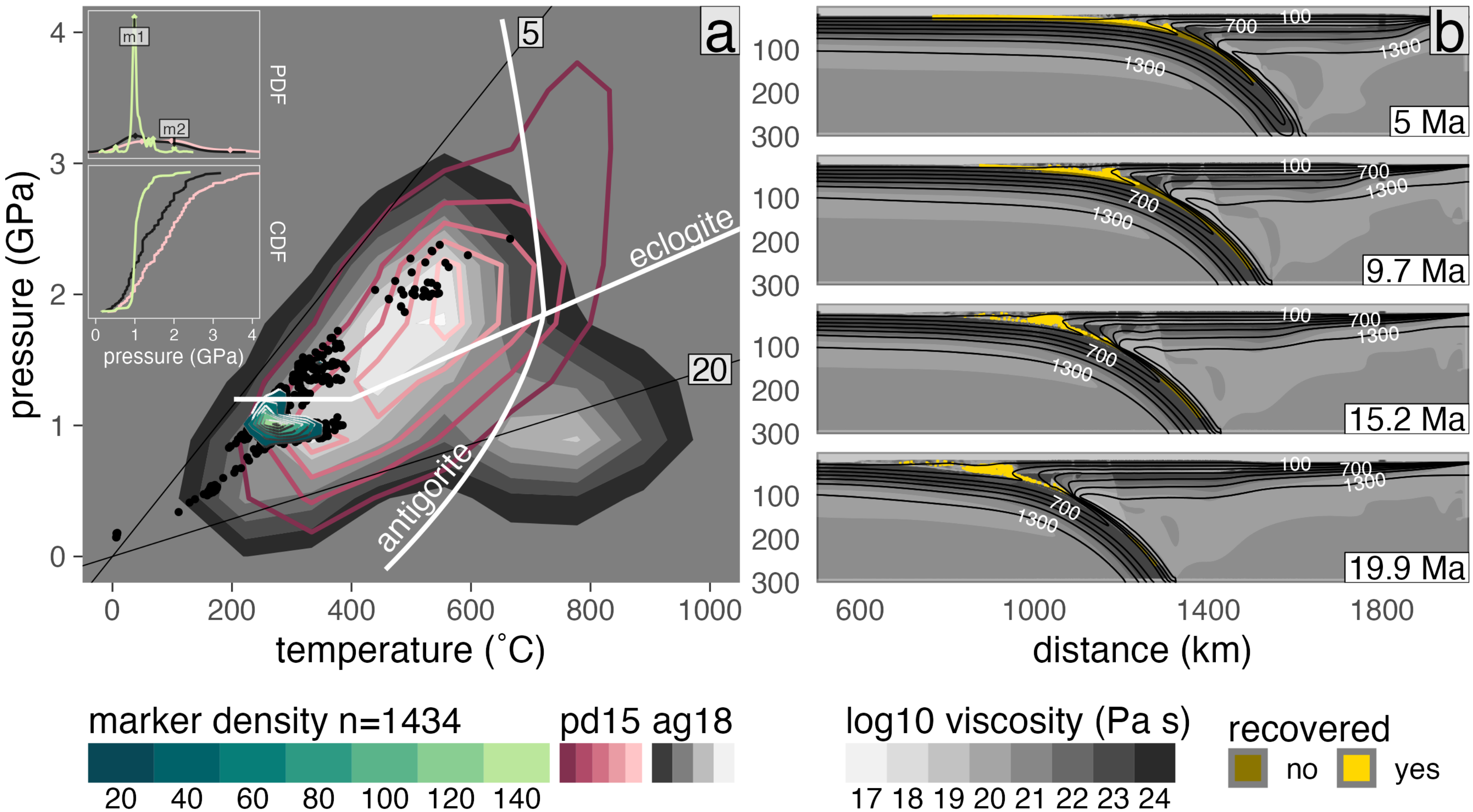

Figure S10: PT distribution of recovered markers from model cdc62. Refer to the main text for explanation of panels and colors.

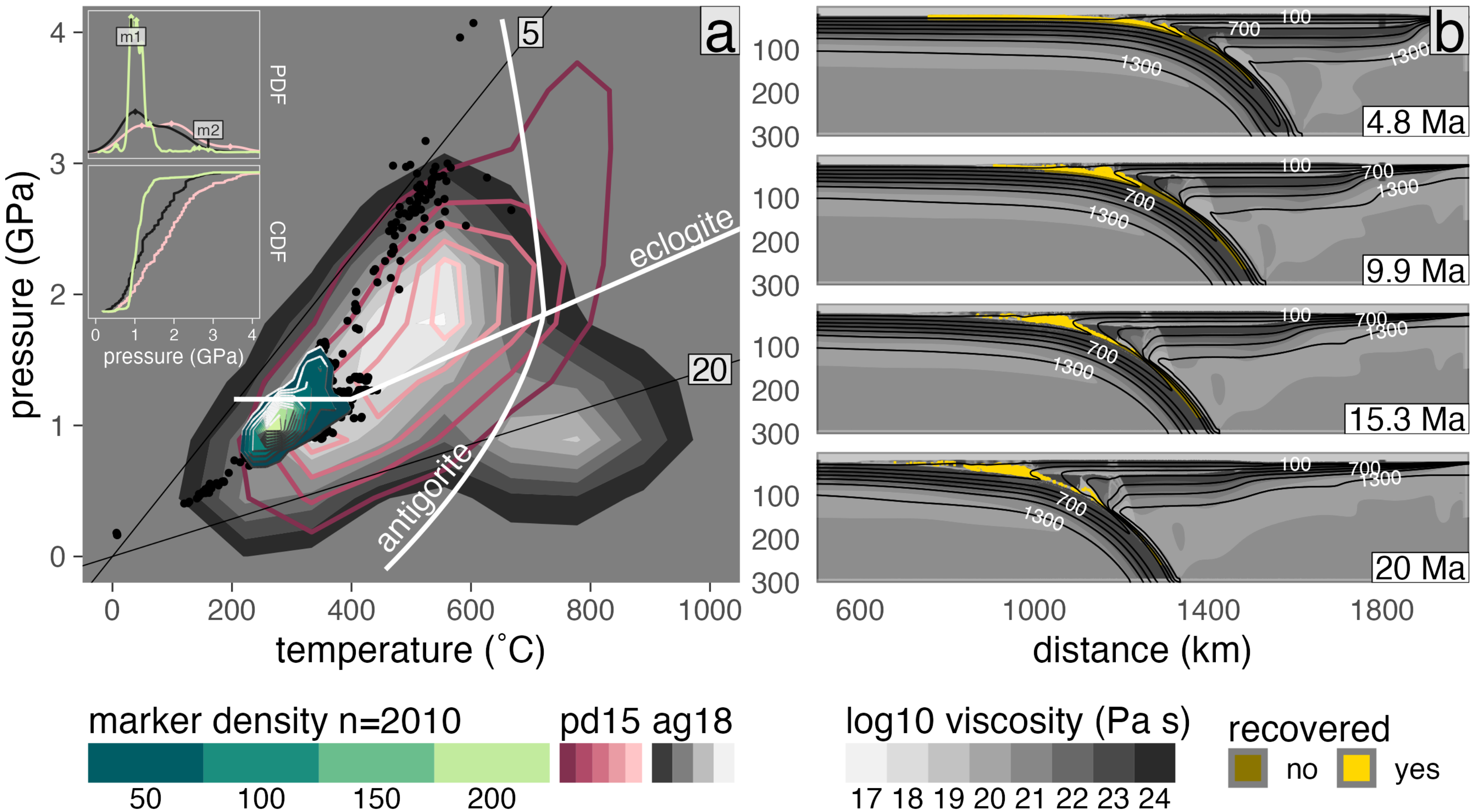

Figure S11: PT distribution of recovered markers from model cdc78. Refer to the main text for explanation of panels and colors.

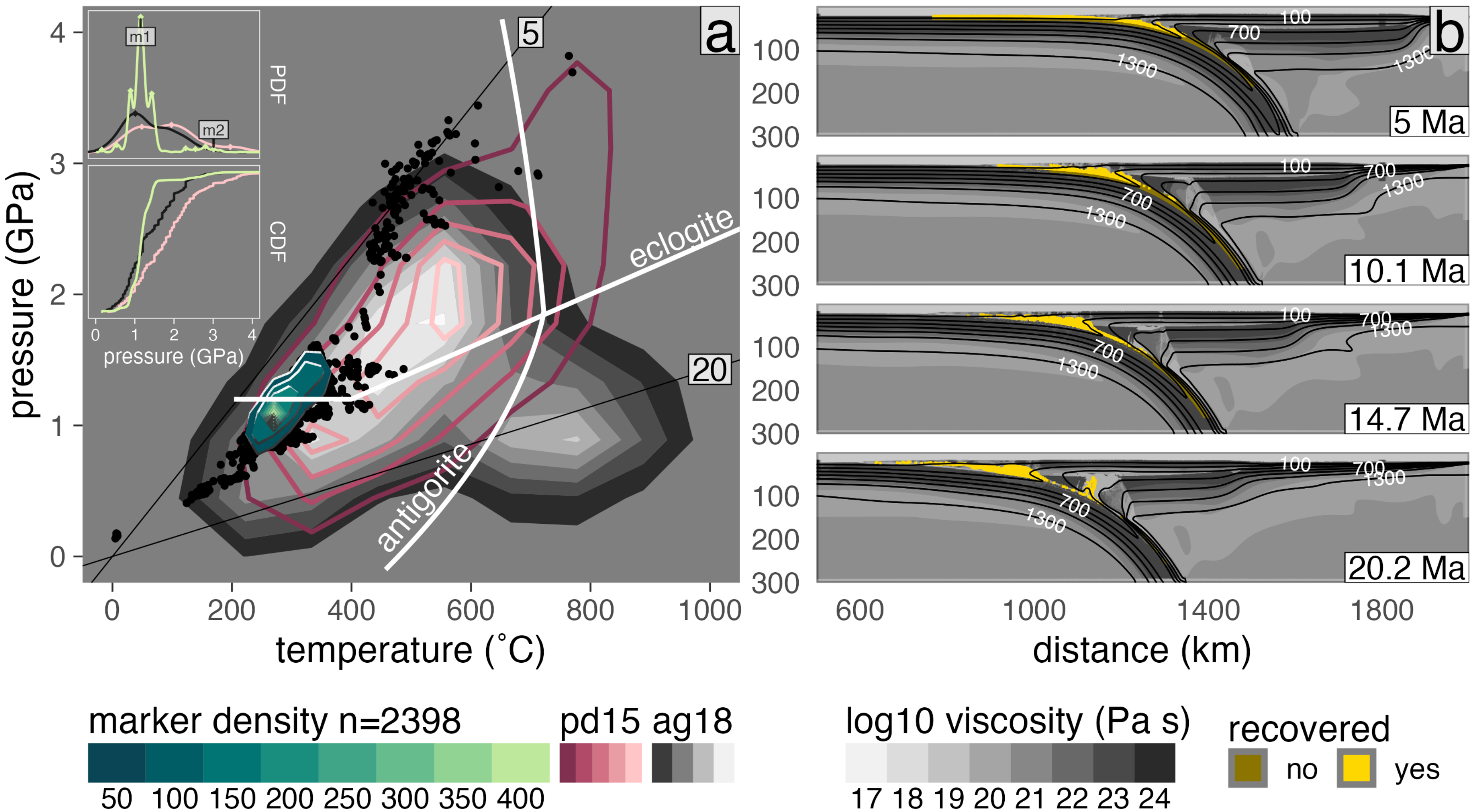

Figure S12: PT distribution of recovered markers from model cdc94. Refer to the main text for explanation of panels and colors.

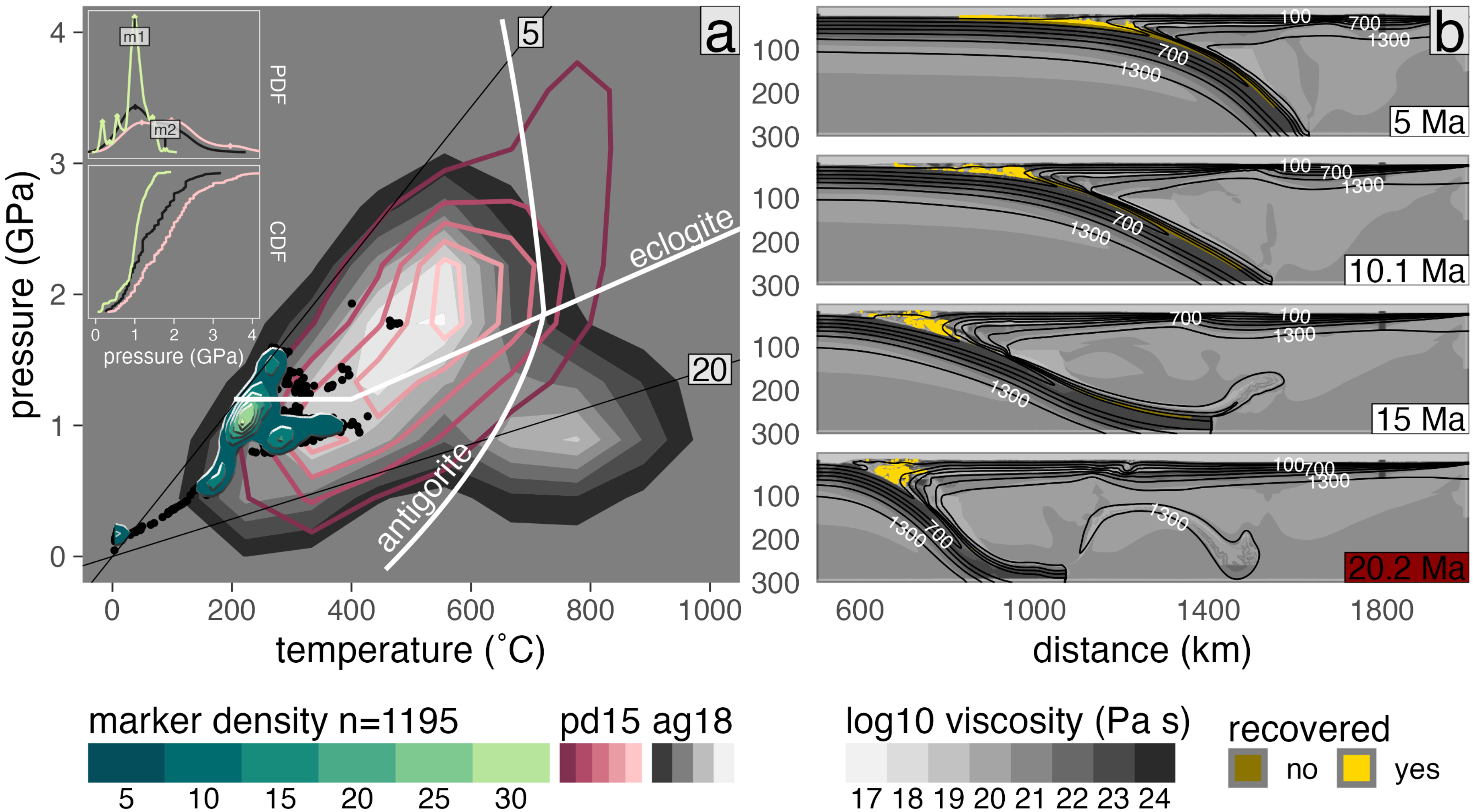

Figure S13: PT distribution of recovered markers from model cdd46. Refer to the main text for explanation of panels and colors.

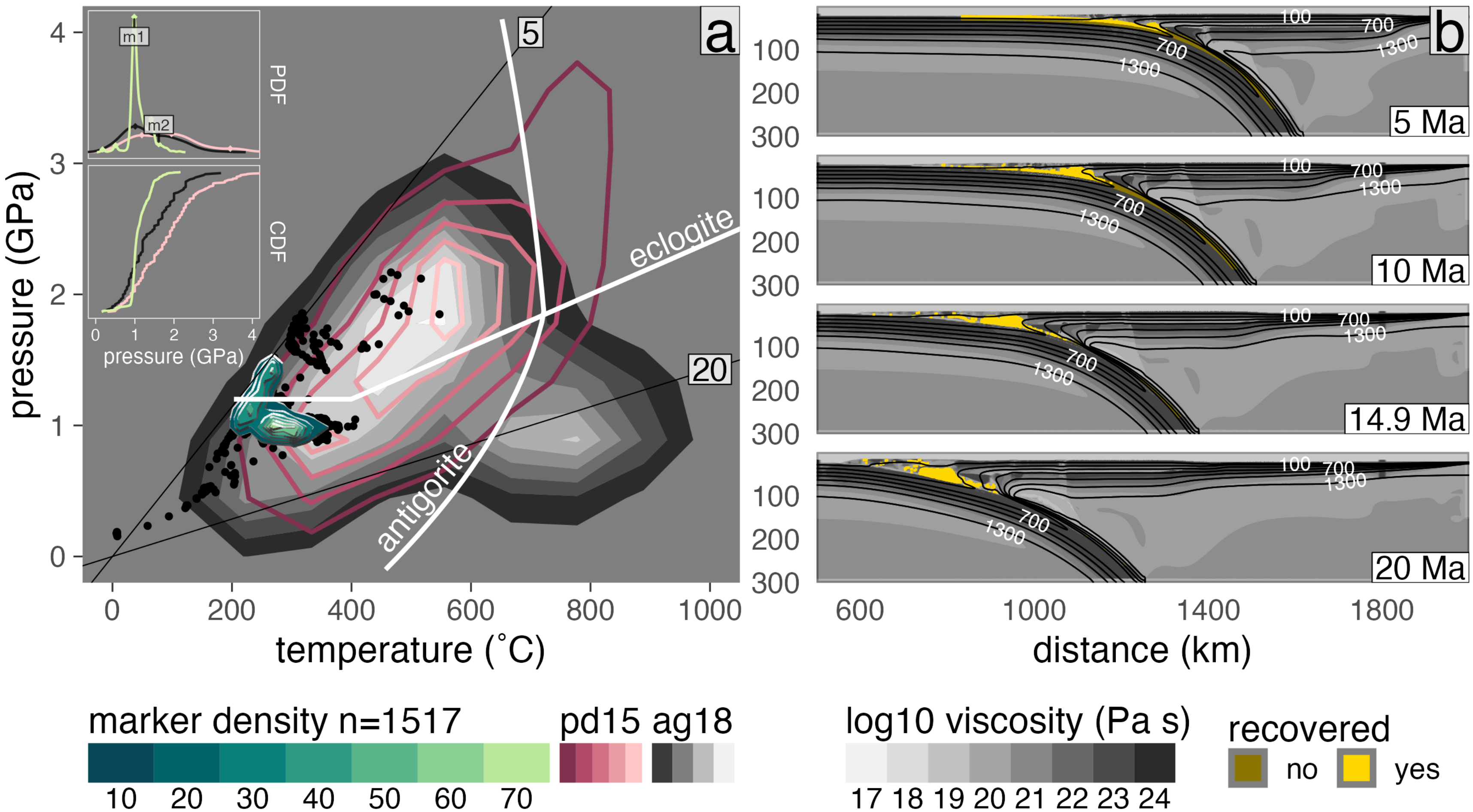

Figure S14: PT distribution of recovered markers from model cdd62. Refer to the main text for explanation of panels and colors.

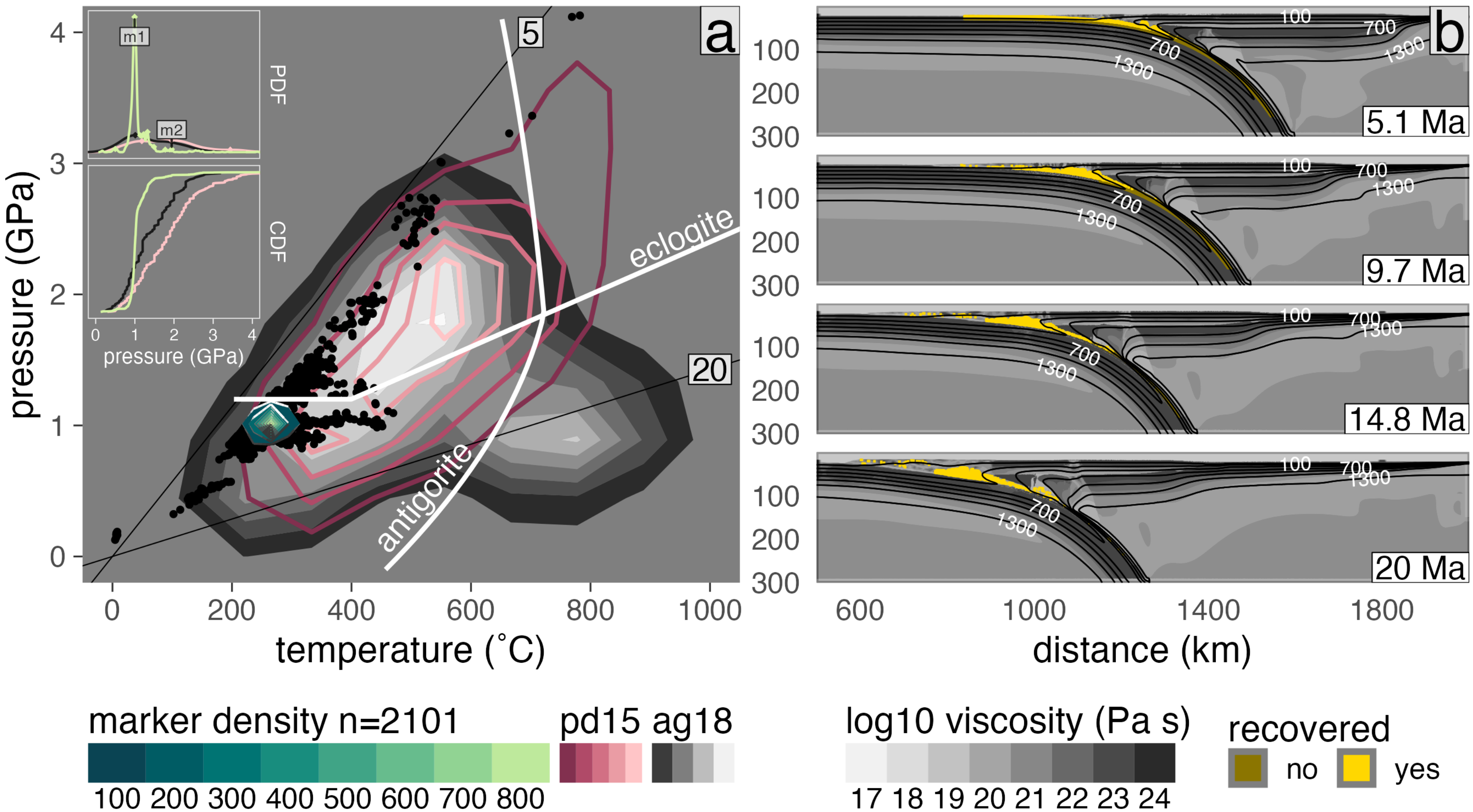

Figure S15: PT distribution of recovered markers from model cdd78. Refer to the main text for explanation of panels and colors.

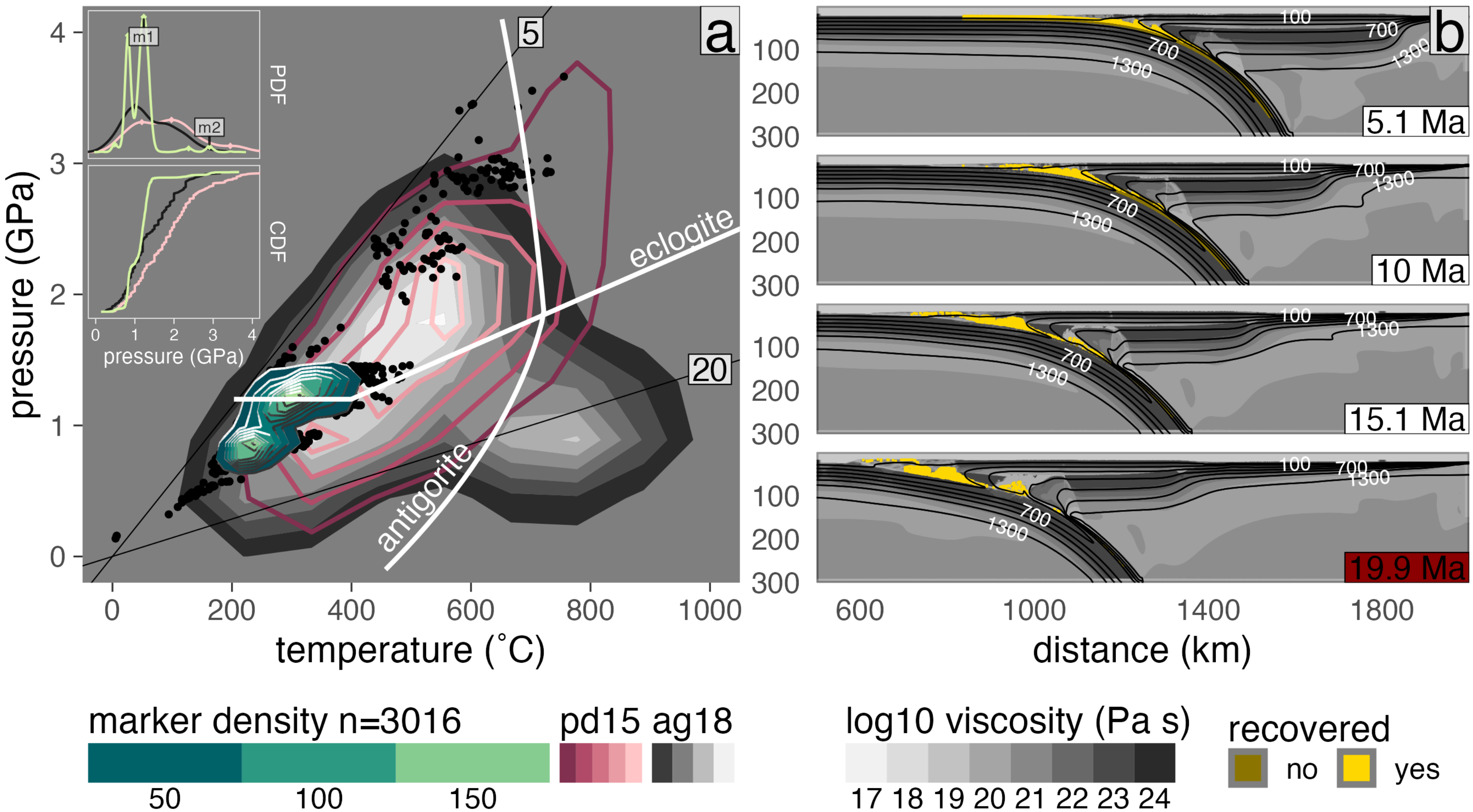

Figure S16: PT distribution of recovered markers from model cdd94. Refer to the main text for explanation of panels and colors.

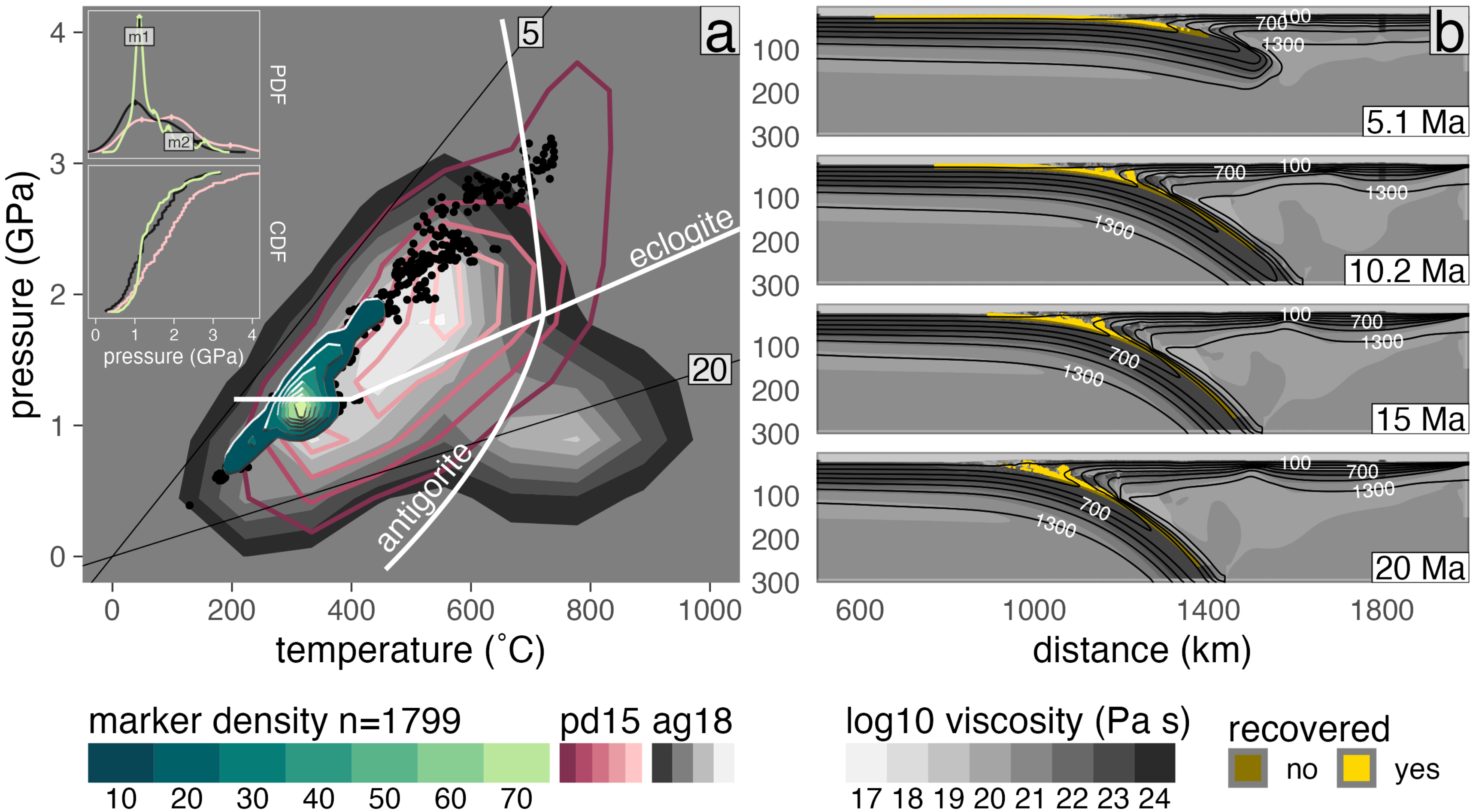

Figure S17: PT distribution of recovered markers from model cde46. Refer to the main text for explanation of panels and colors.

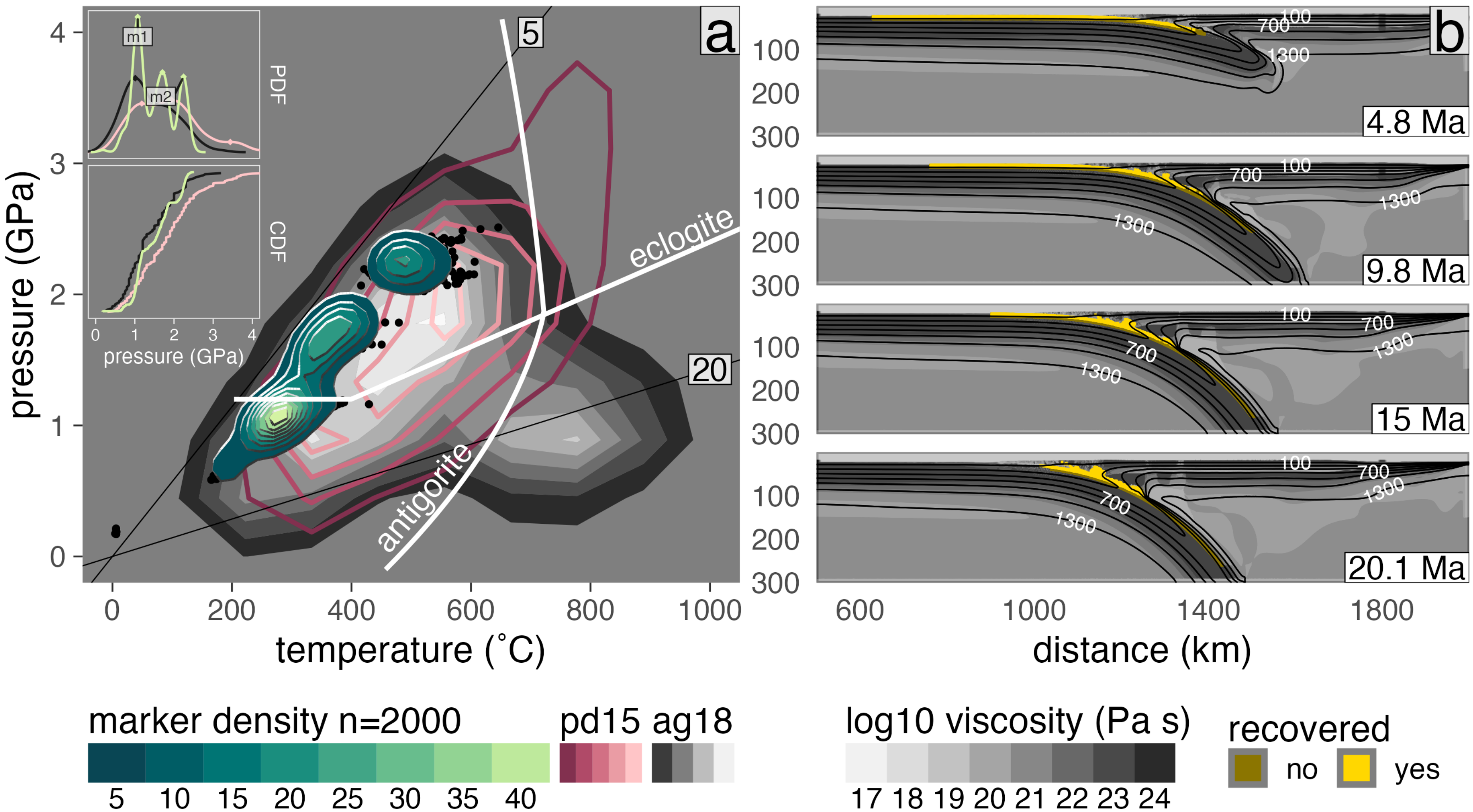

Figure S18: PT distribution of recovered markers from model cde62. Refer to the main text for explanation of panels and colors.

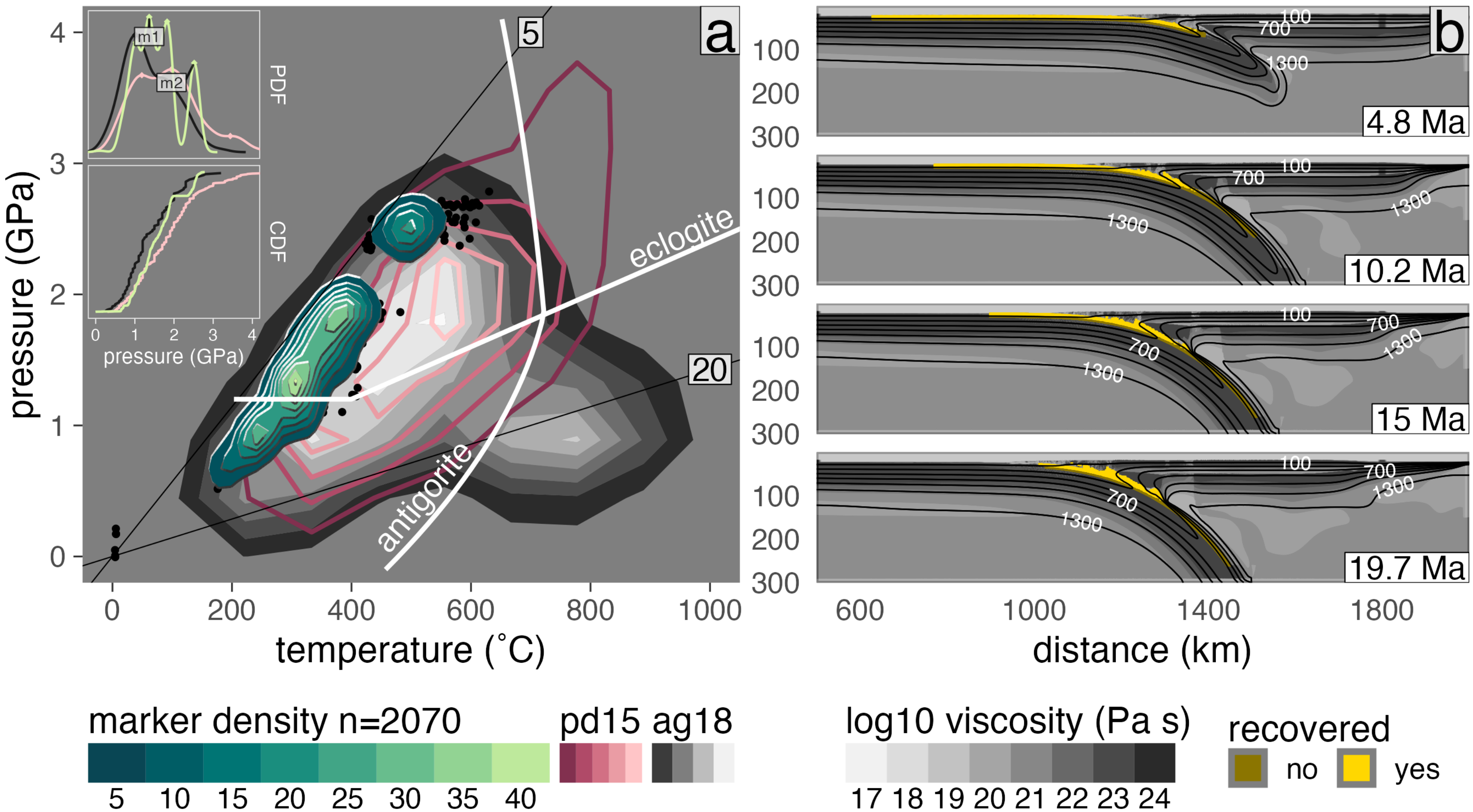

Figure S19: PT distribution of recovered markers from model cde78. Refer to the main text for explanation of panels and colors.

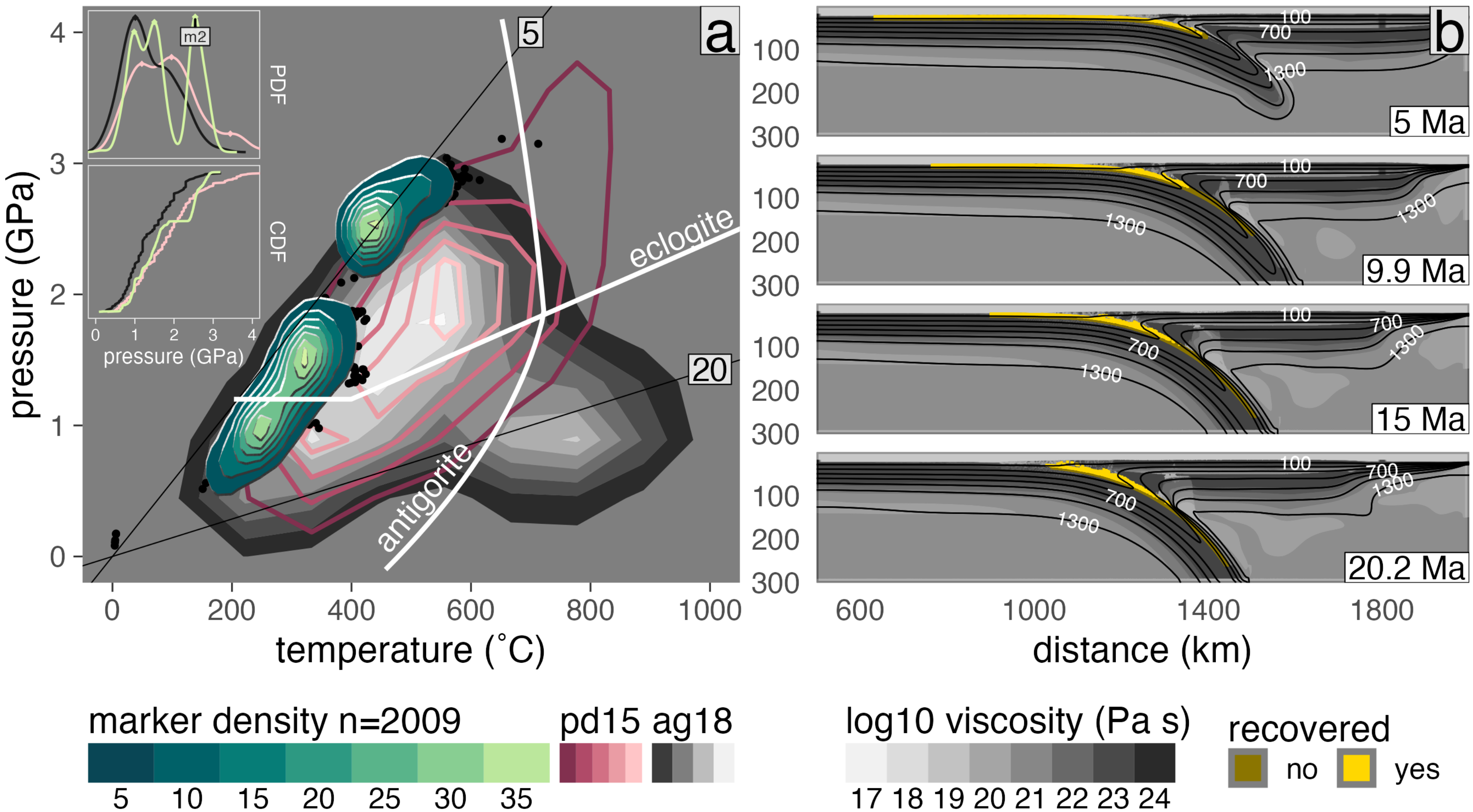

Figure S20: PT distribution of recovered markers from model cde94. Refer to the main text for explanation of panels and colors.

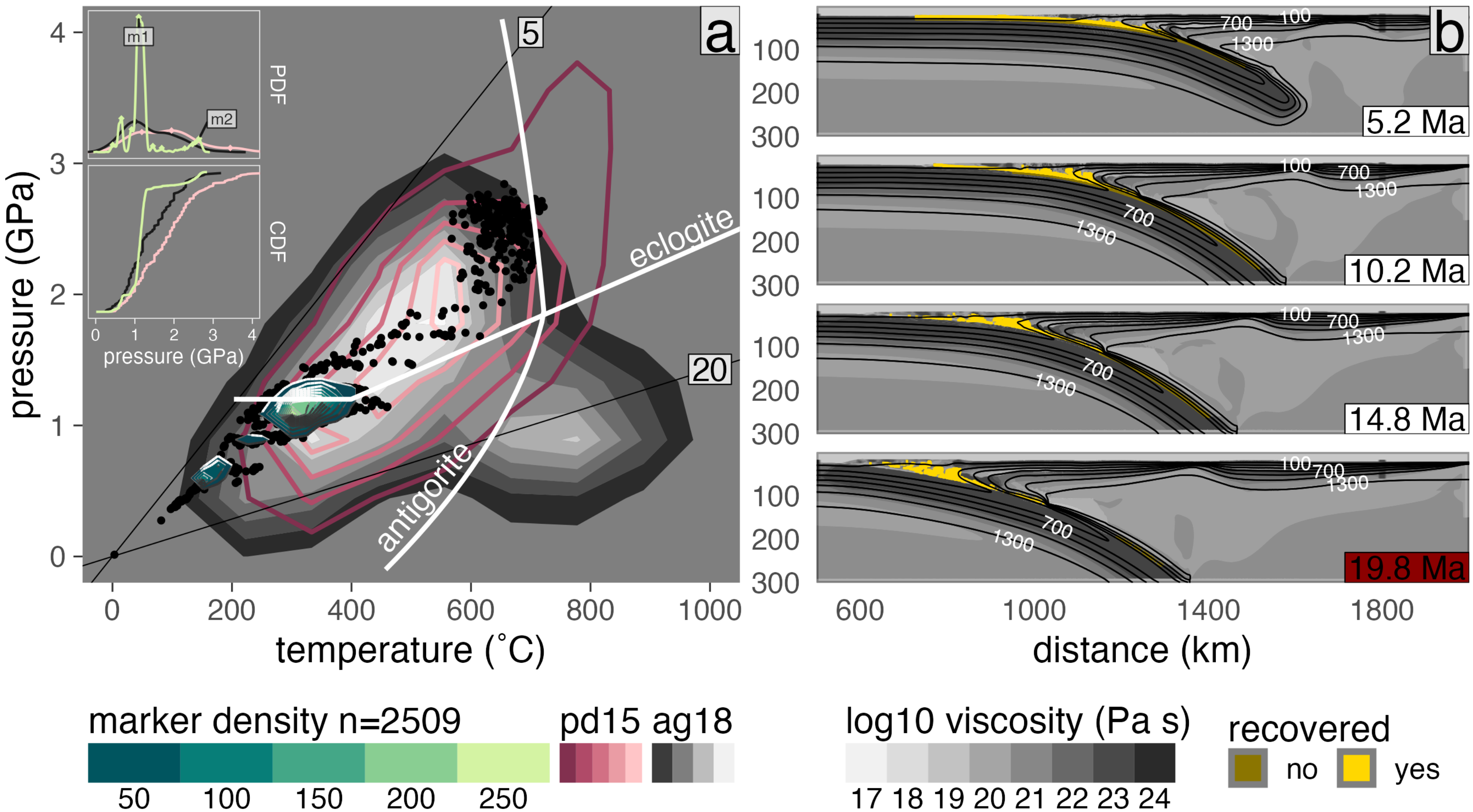

Figure S21: PT distribution of recovered markers from model cdf46. Refer to the main text for explanation of panels and colors.

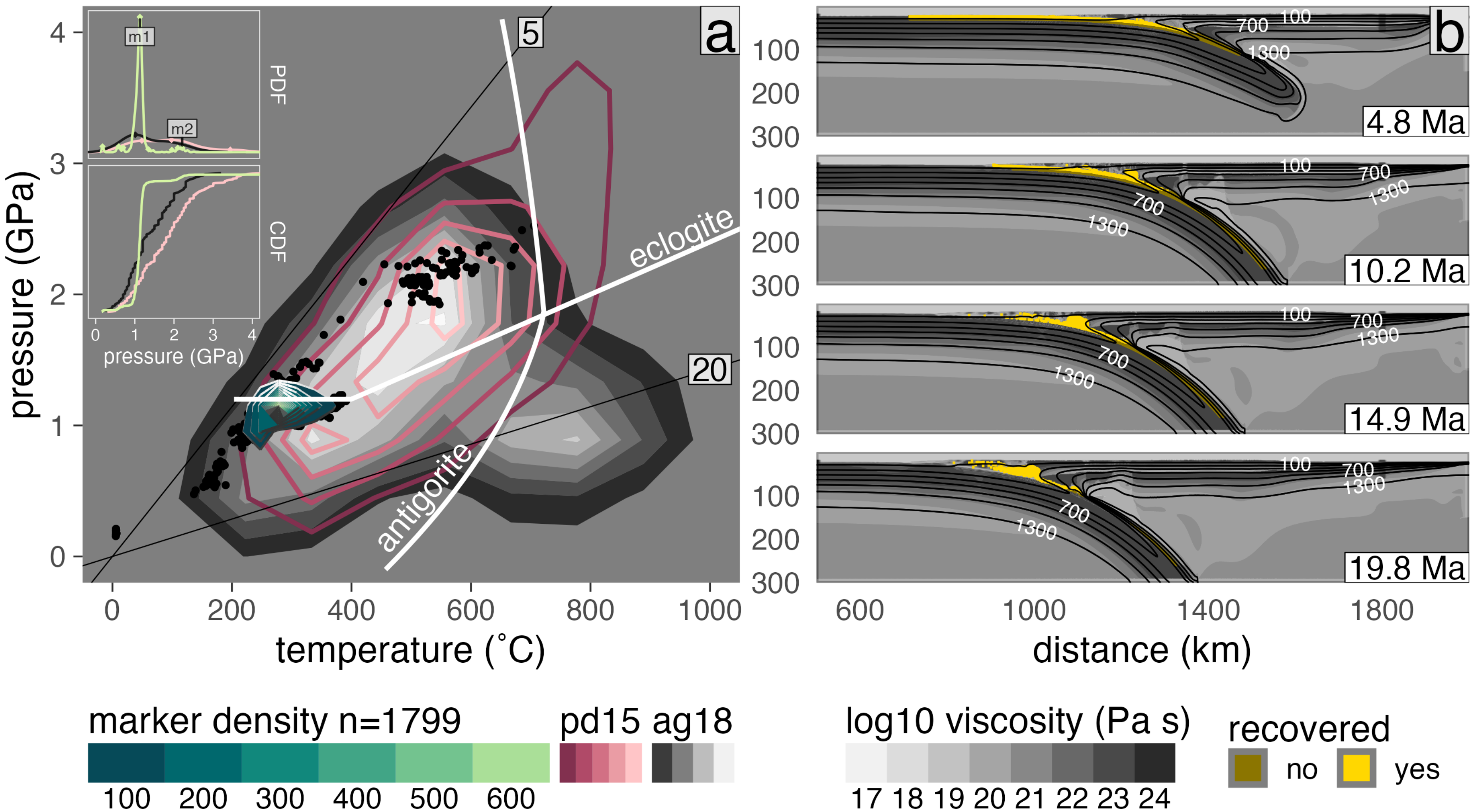

Figure S22: PT distribution of recovered markers from model cdf62. Refer to the main text for explanation of panels and colors.

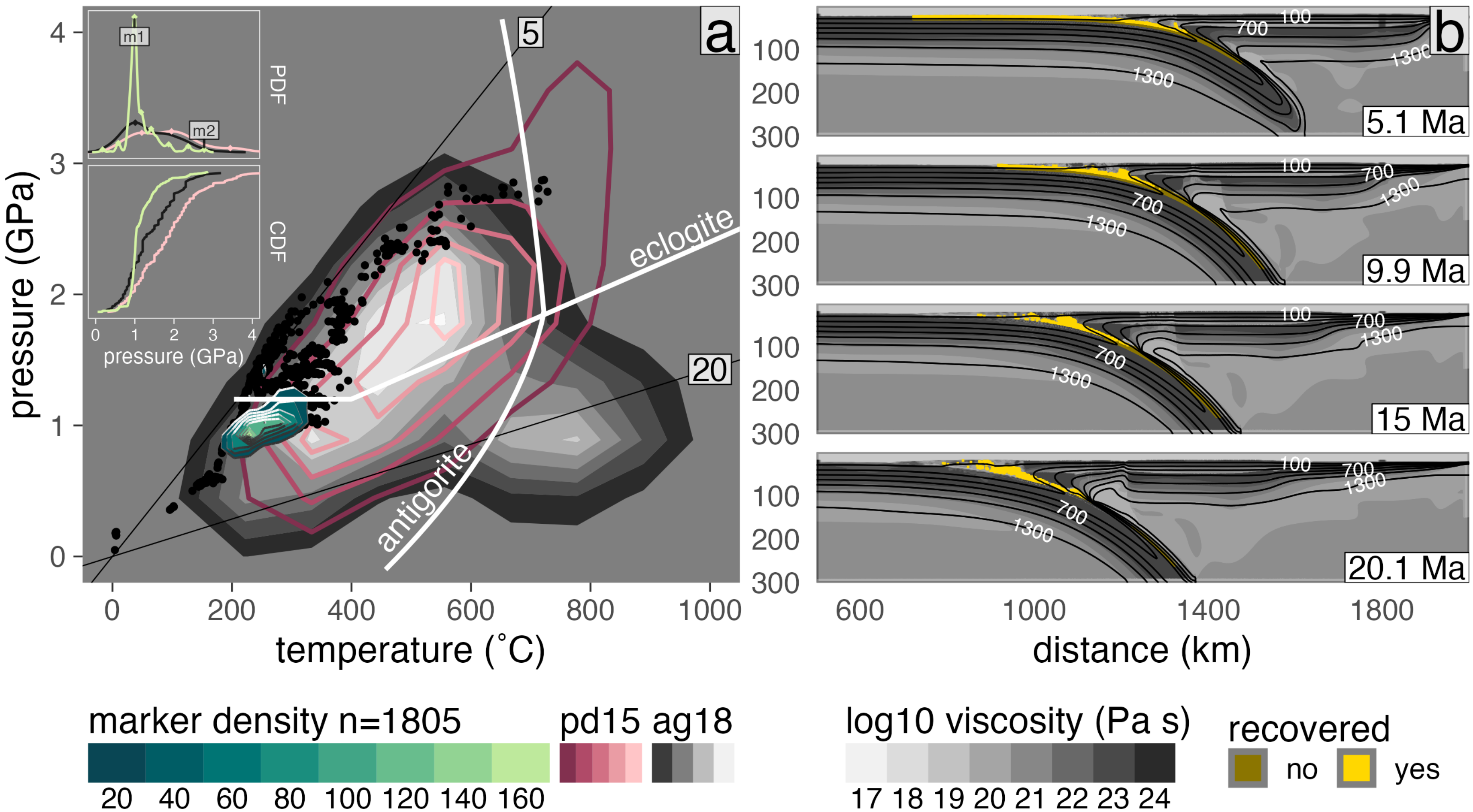

Figure S23: PT distribution of recovered markers from model cdf78. Refer to the main text for explanation of panels and colors.

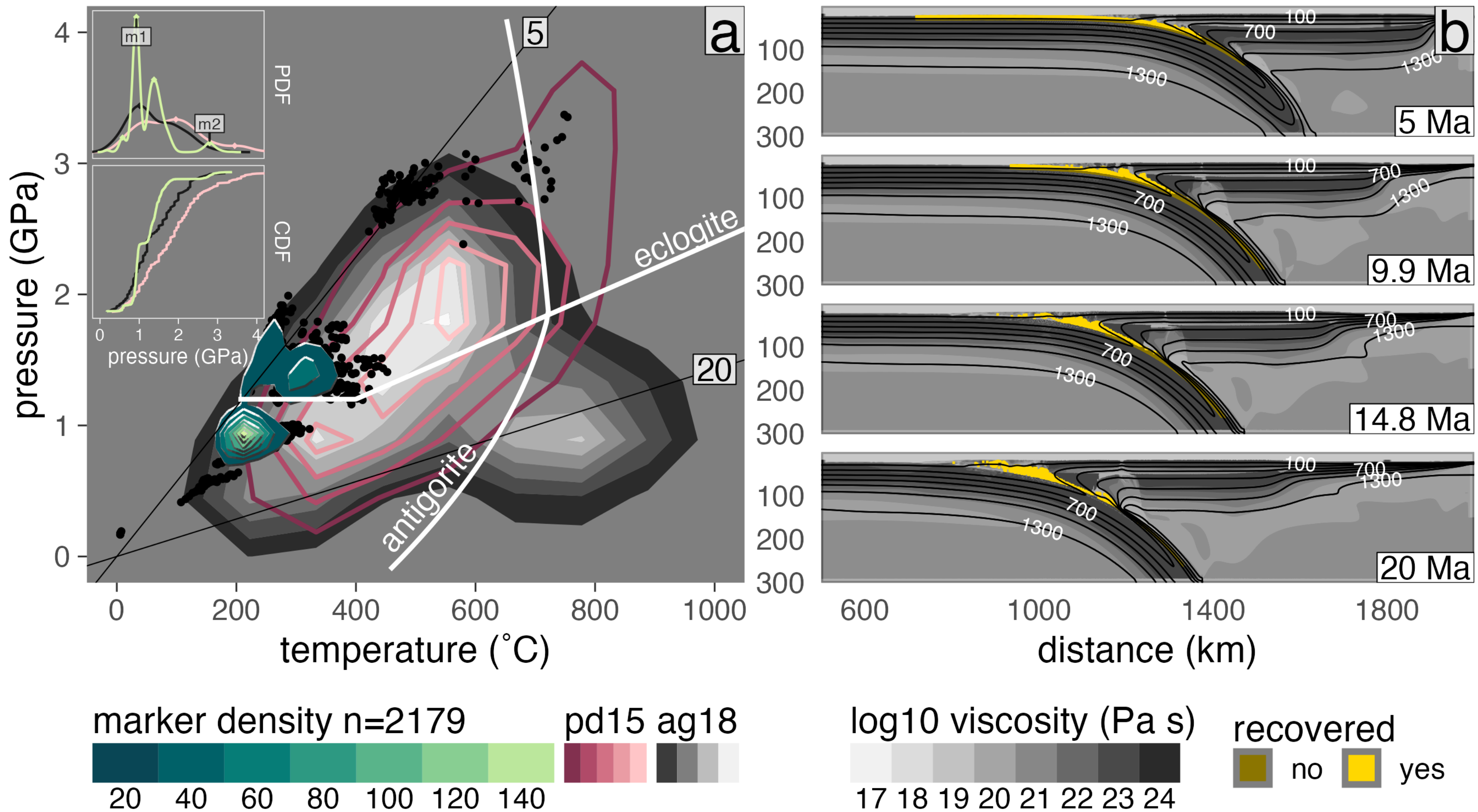

Figure S24: PT distribution of recovered markers from model cdf94. Refer to the main text for explanation of panels and colors.

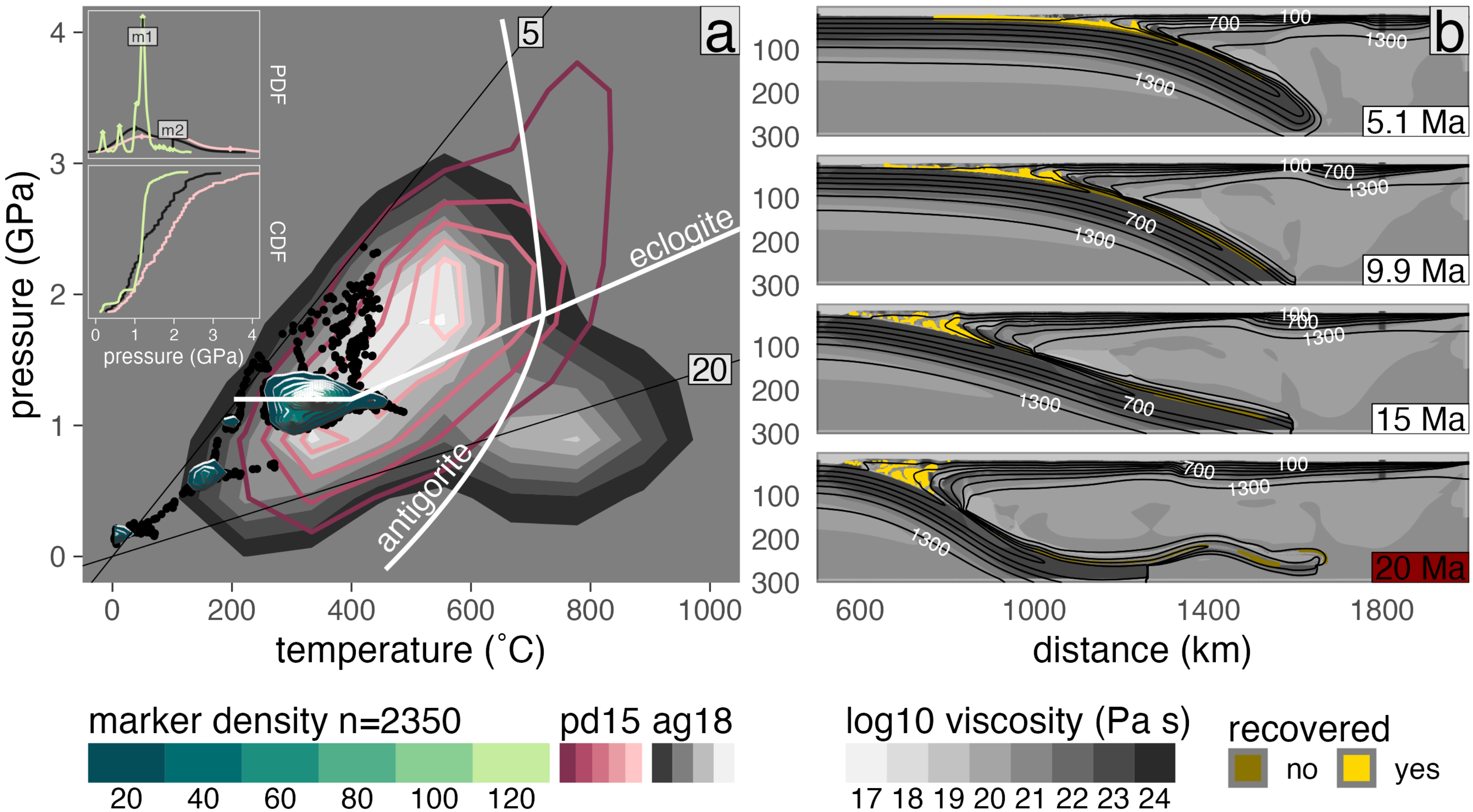

Figure S25: PT distribution of recovered markers from model cdg46. Refer to the main text for explanation of panels and colors.

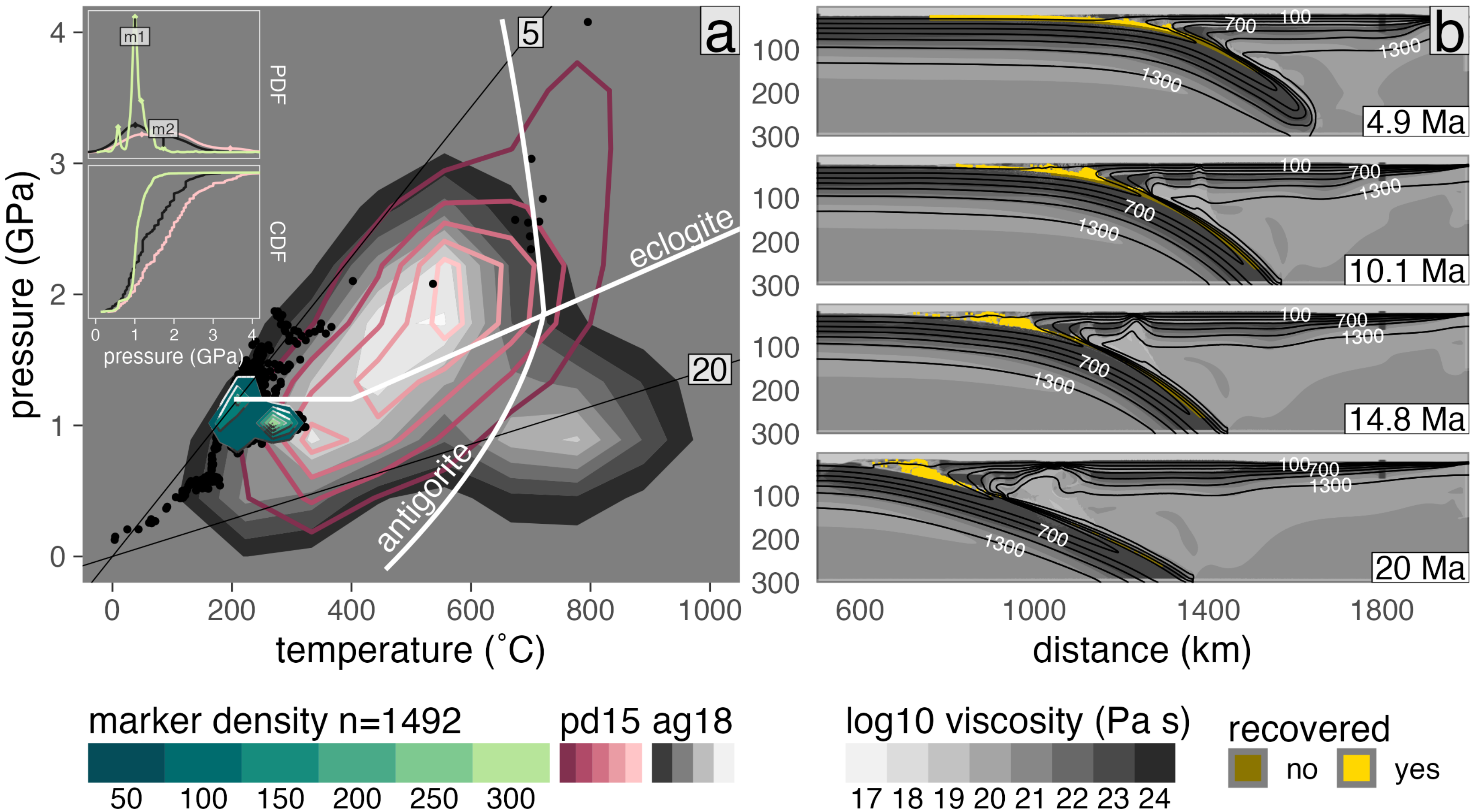

Figure S26: PT distribution of recovered markers from model cdg62. Refer to the main text for explanation of panels and colors.

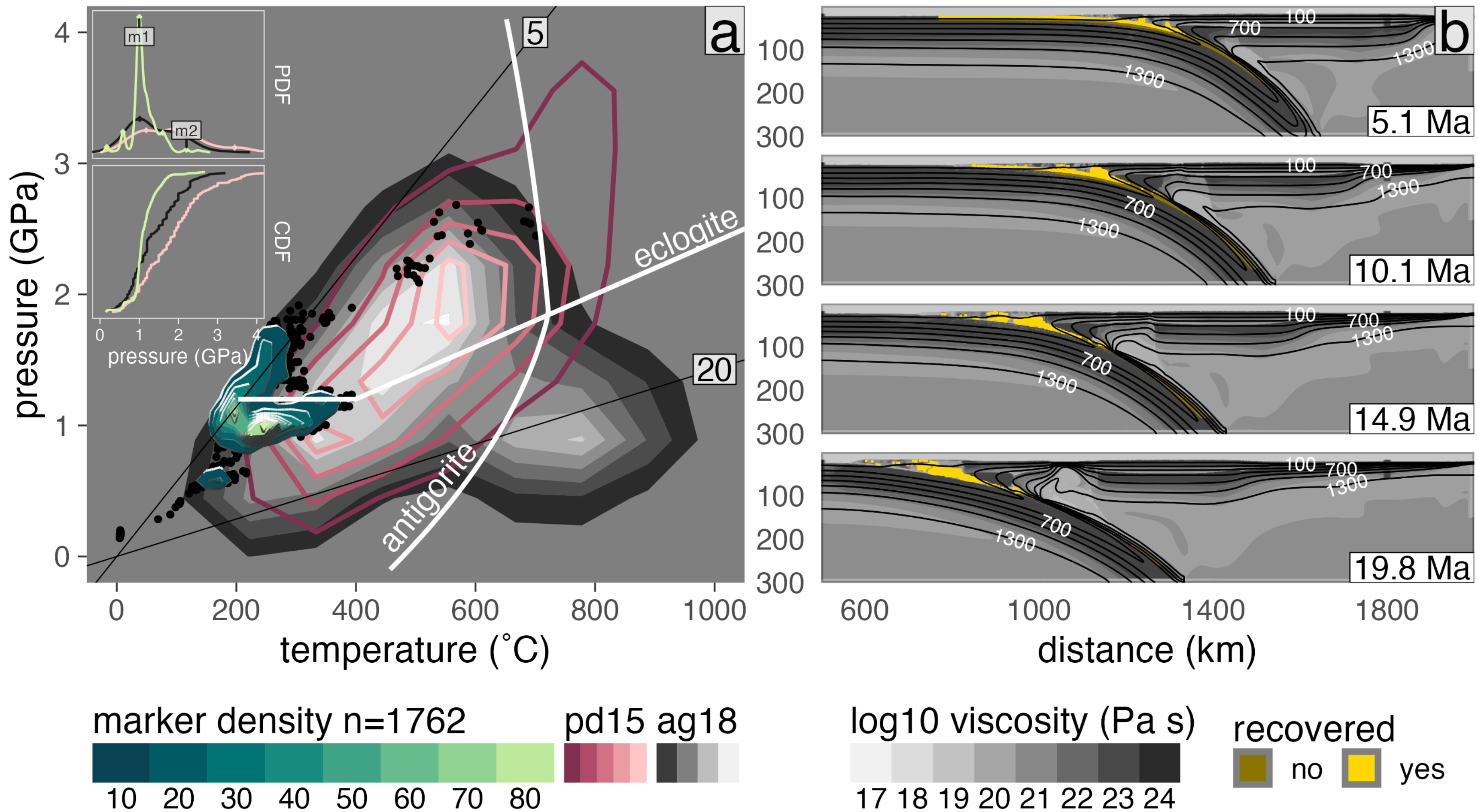

Figure S27: PT distribution of recovered markers from model cdg78. Refer to the main text for explanation of panels and colors.

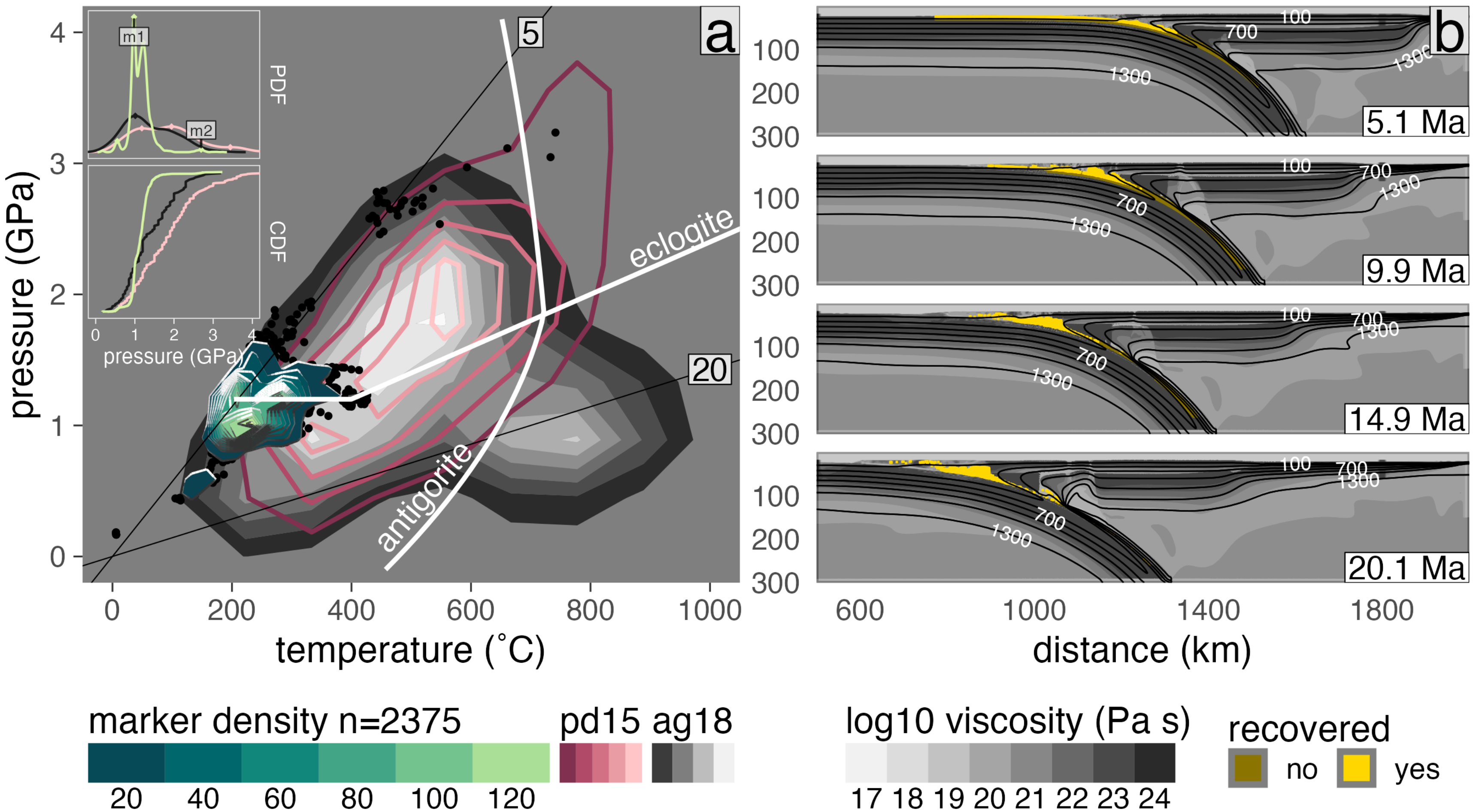

Figure S28: PT distribution of recovered markers from model cdg94. Refer to the main text for explanation of panels and colors.

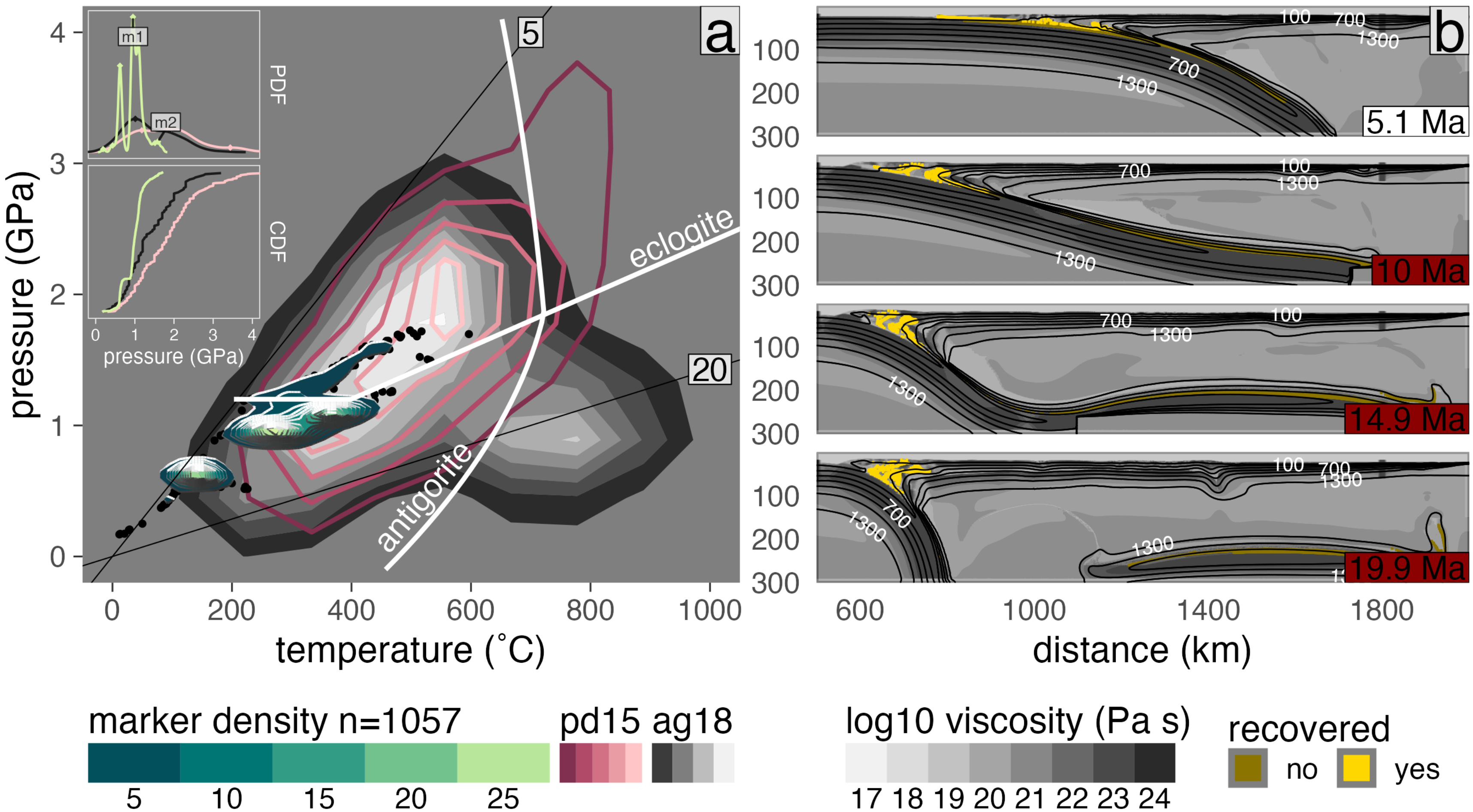

Figure S29: PT distribution of recovered markers from model cdh46. Refer to the main text for explanation of panels and colors.

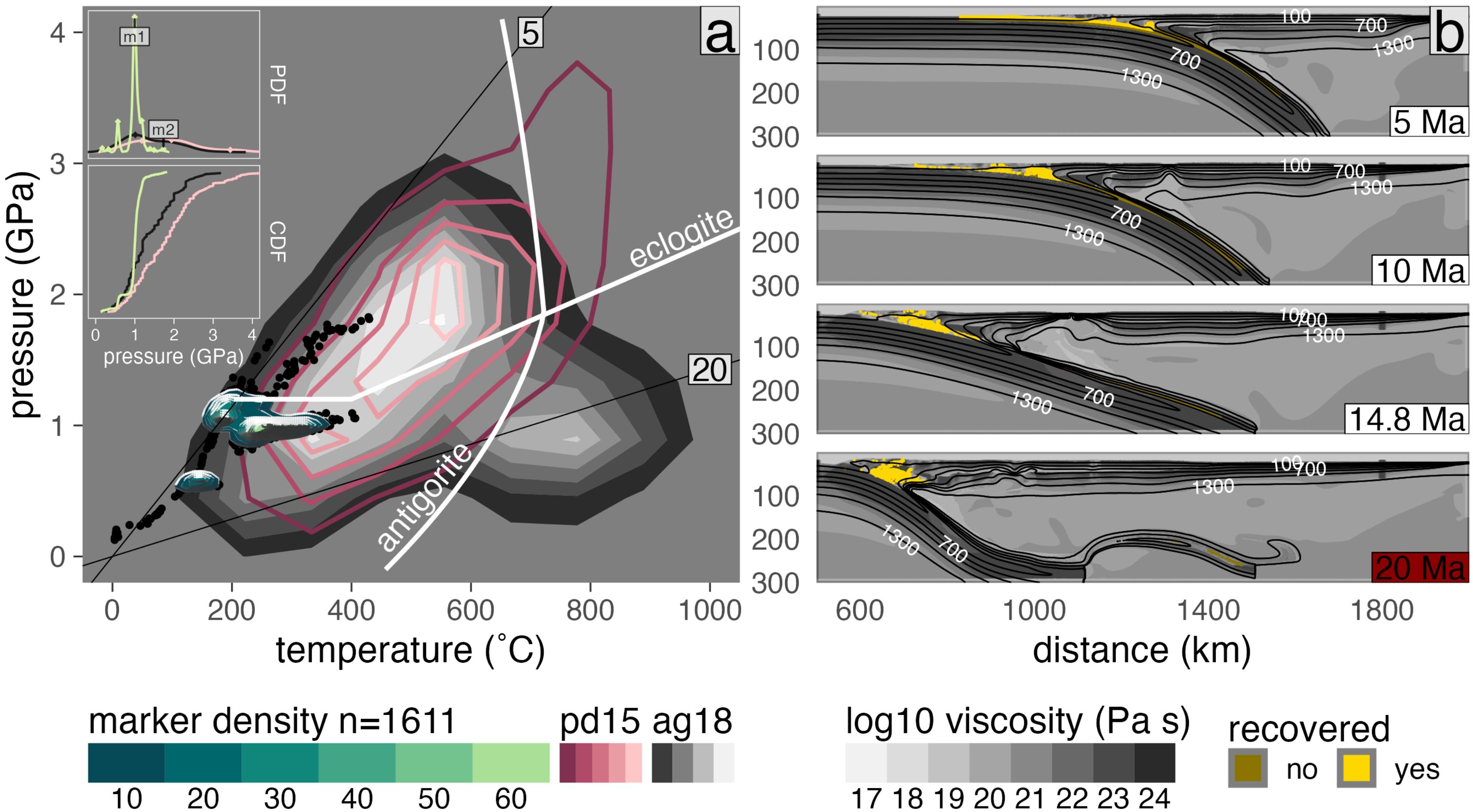

Figure S30: PT distribution of recovered markers from model cdh62. Refer to the main text for explanation of panels and colors.

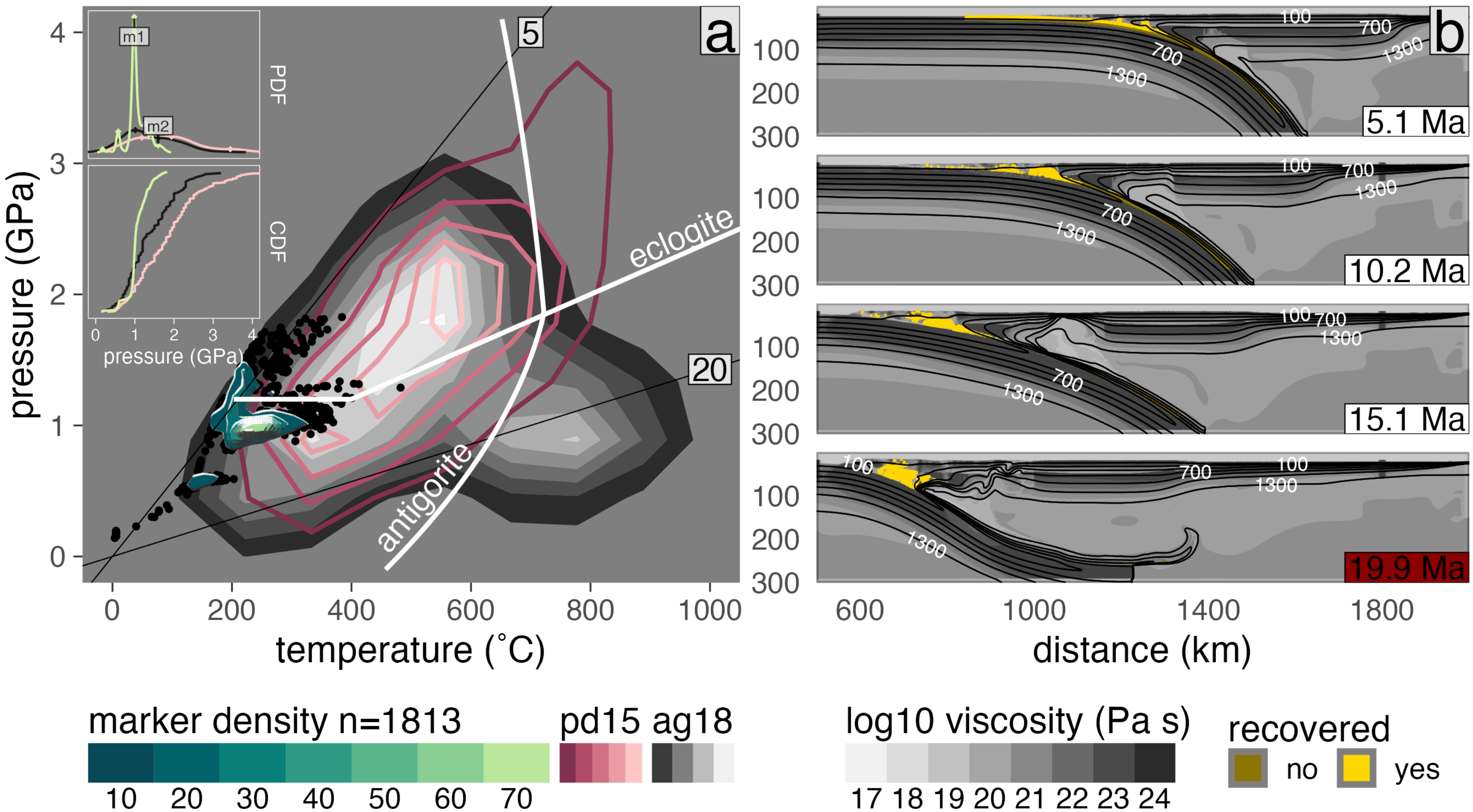

Figure S31: PT distribution of recovered markers from model cdh78. Refer to the main text for explanation of panels and colors.

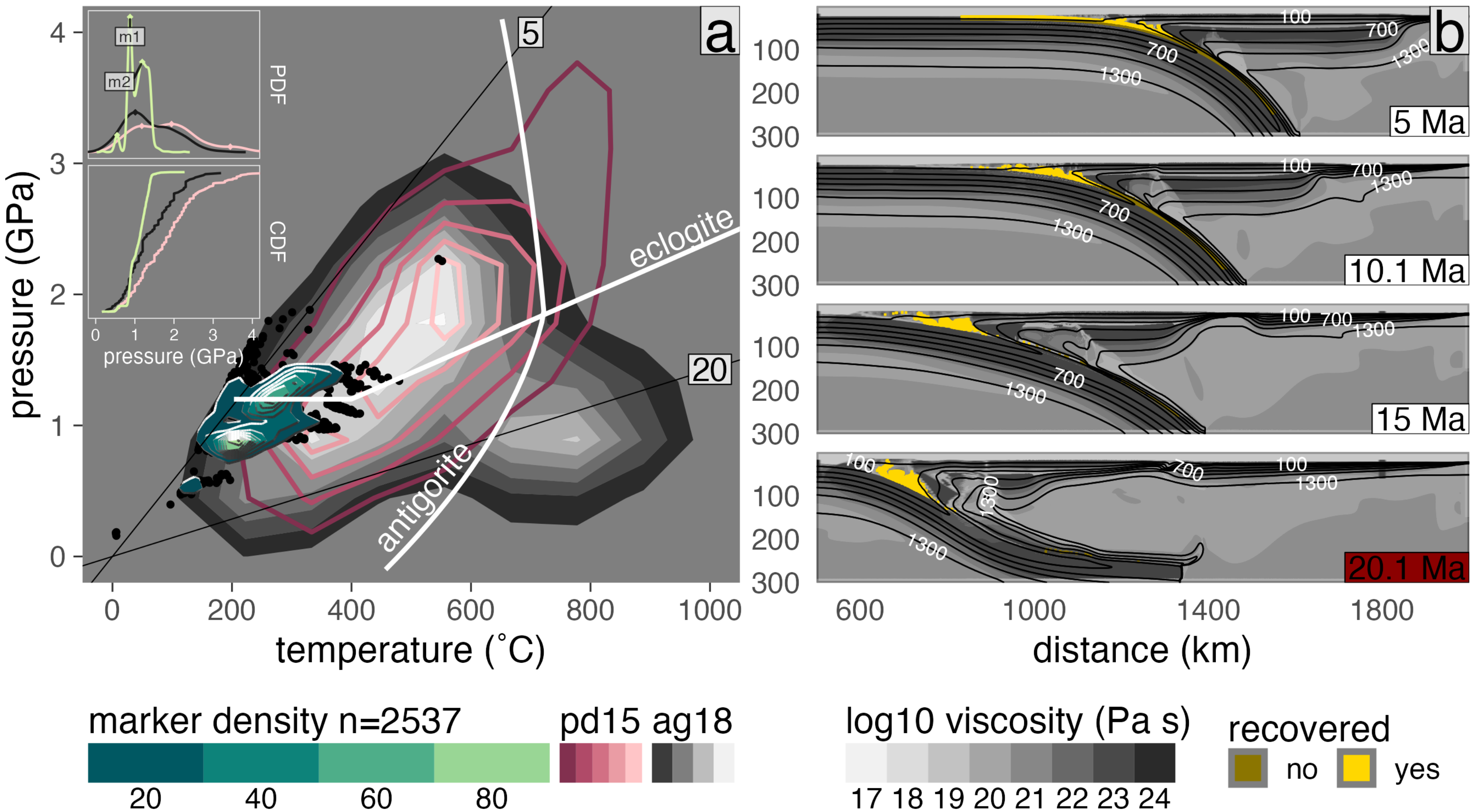

Figure S32: PT distribution of recovered markers from model cdh94. Refer to the main text for explanation of panels and colors.

manuscript submitted to *Geochemistry, Geophysics, Geosystems*

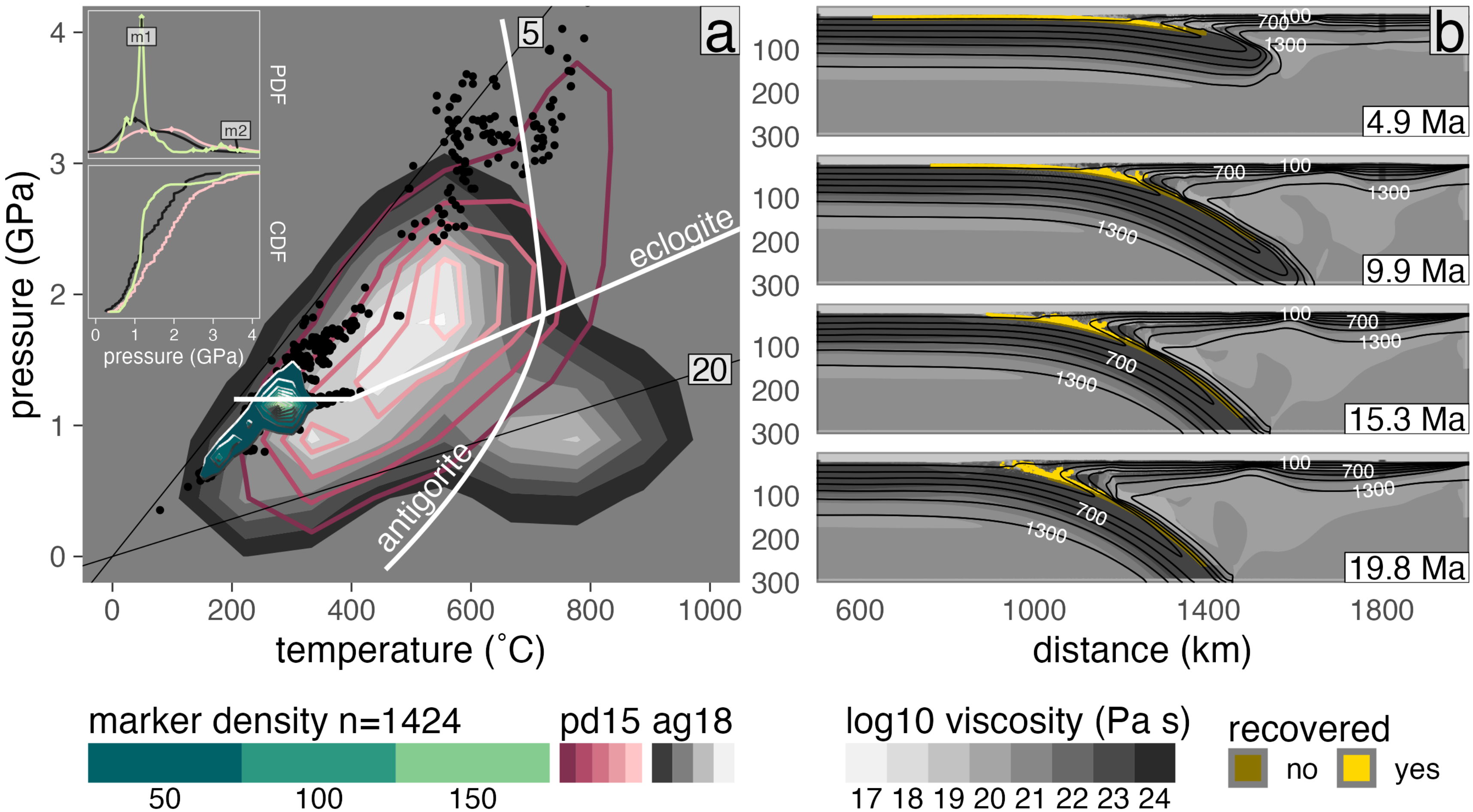

Figure S33: PT distribution of recovered markers from model cdi46. Refer to the main text for explanation of panels and colors.

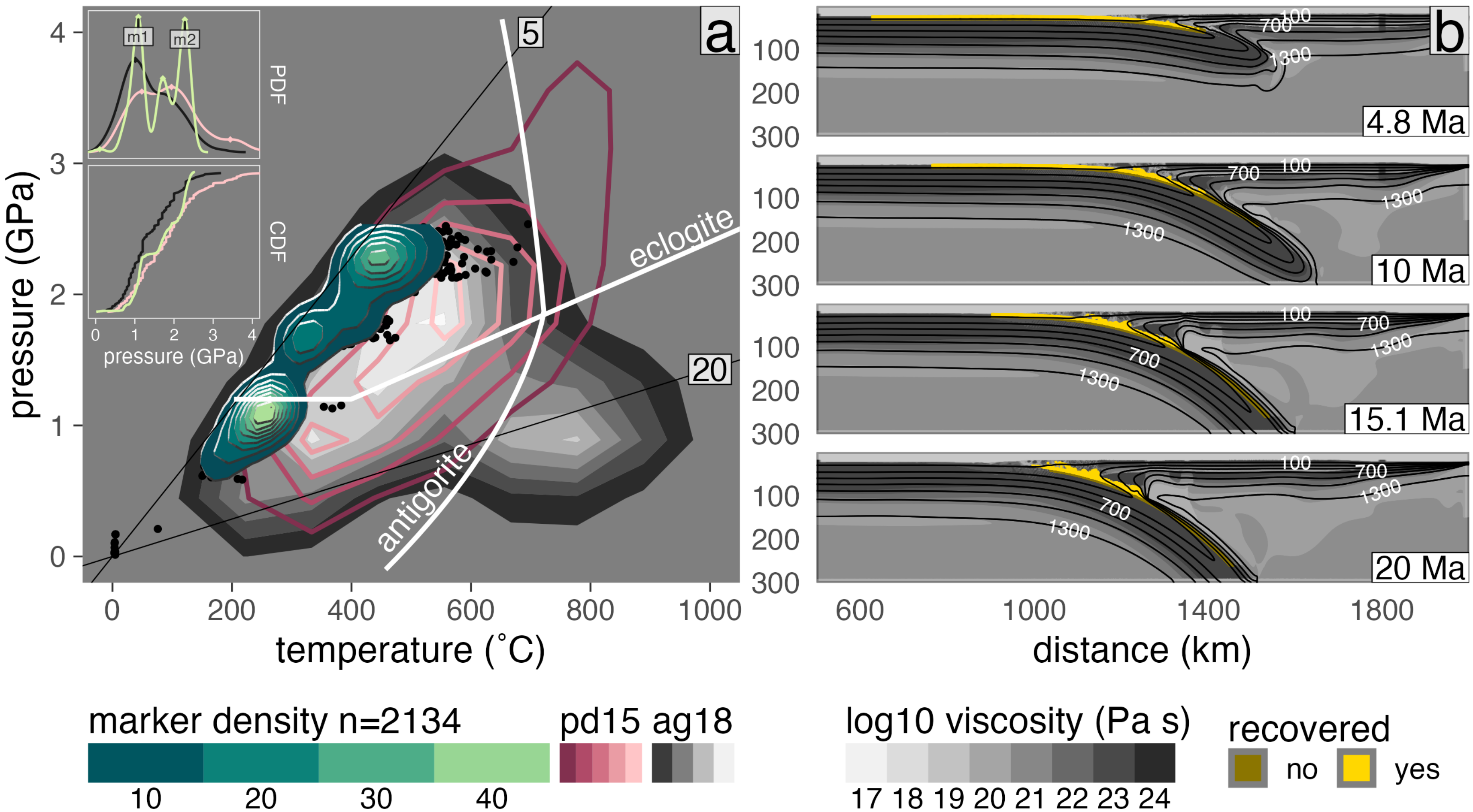

Figure S34: PT distribution of recovered markers from model cdi62. Refer to the main text for explanation of panels and colors.

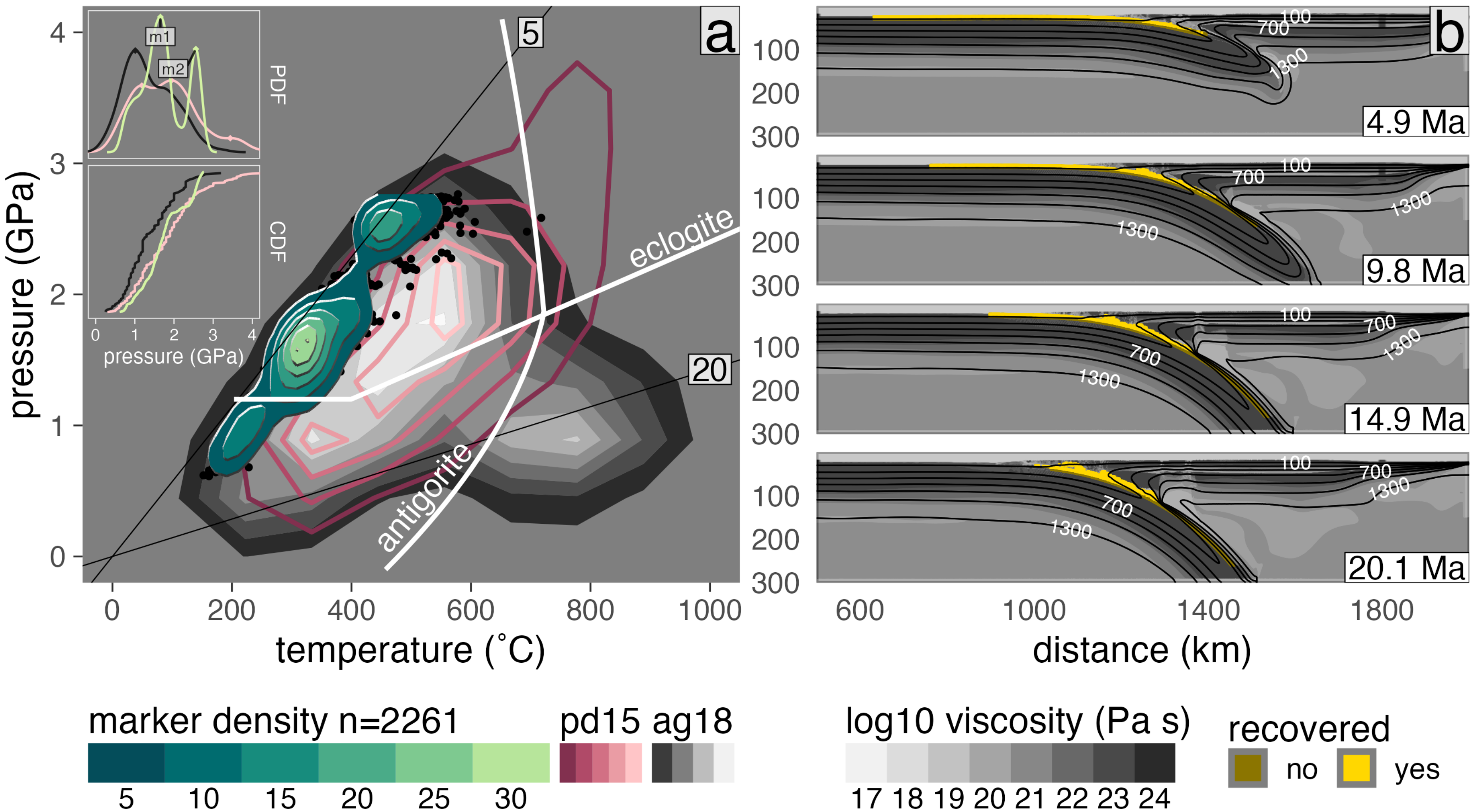

Figure S35: PT distribution of recovered markers from model cdi78. Refer to the main text for explanation of panels and colors.

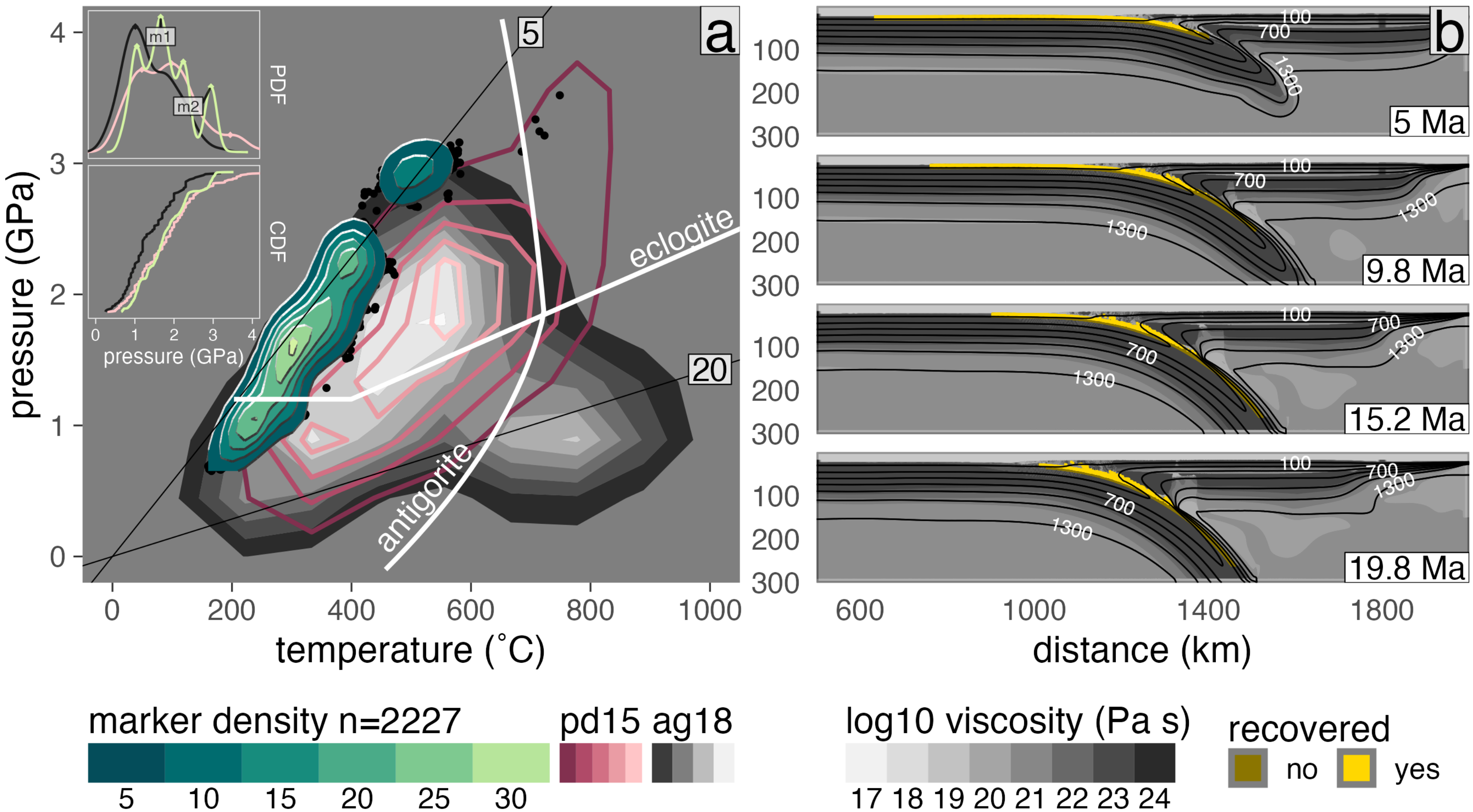

Figure S36: PT distribution of recovered markers from model cdi94. Refer to the main text for explanation of panels and colors.

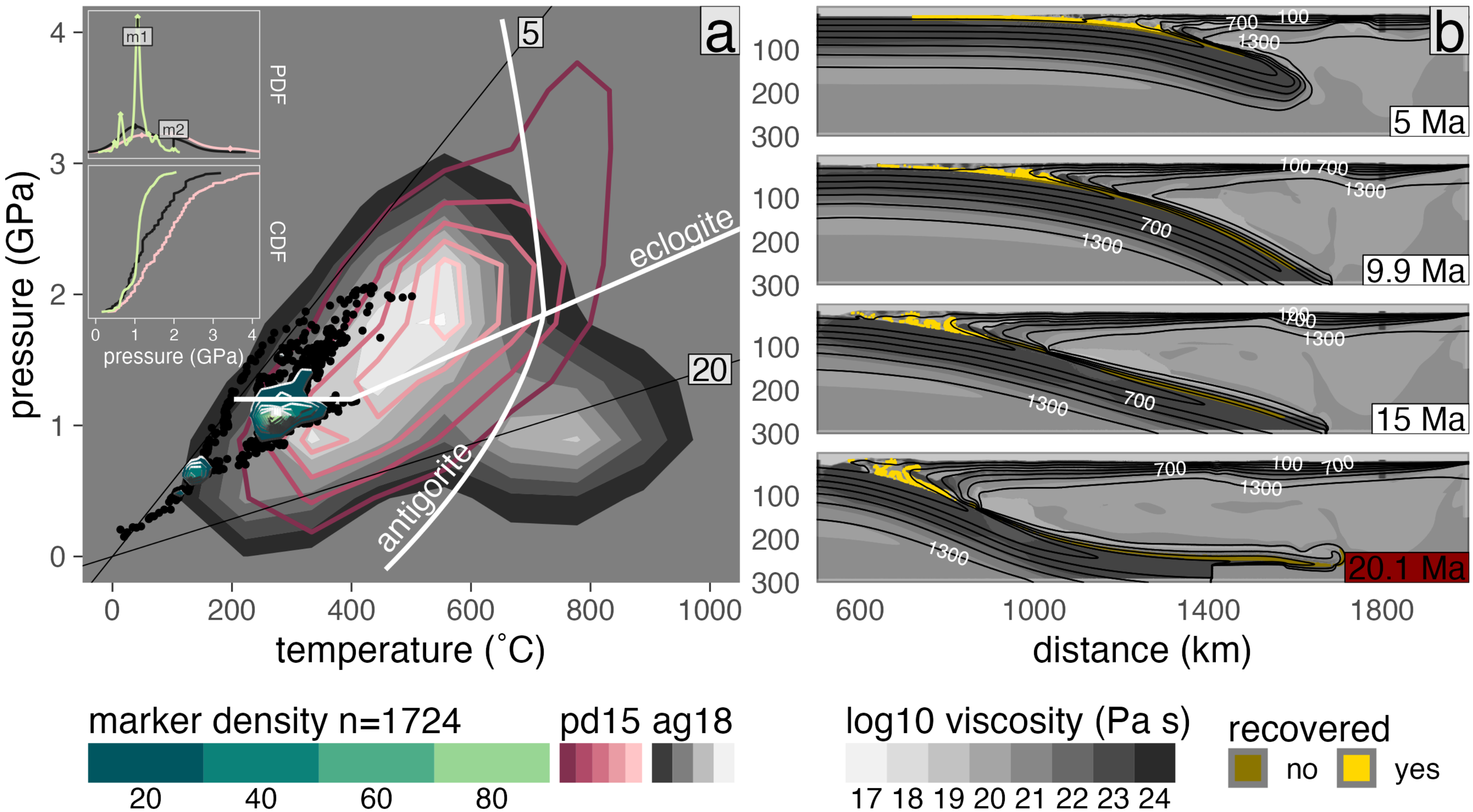

Figure S37: PT distribution of recovered markers from model cdj46. Refer to the main text for explanation of panels and colors.

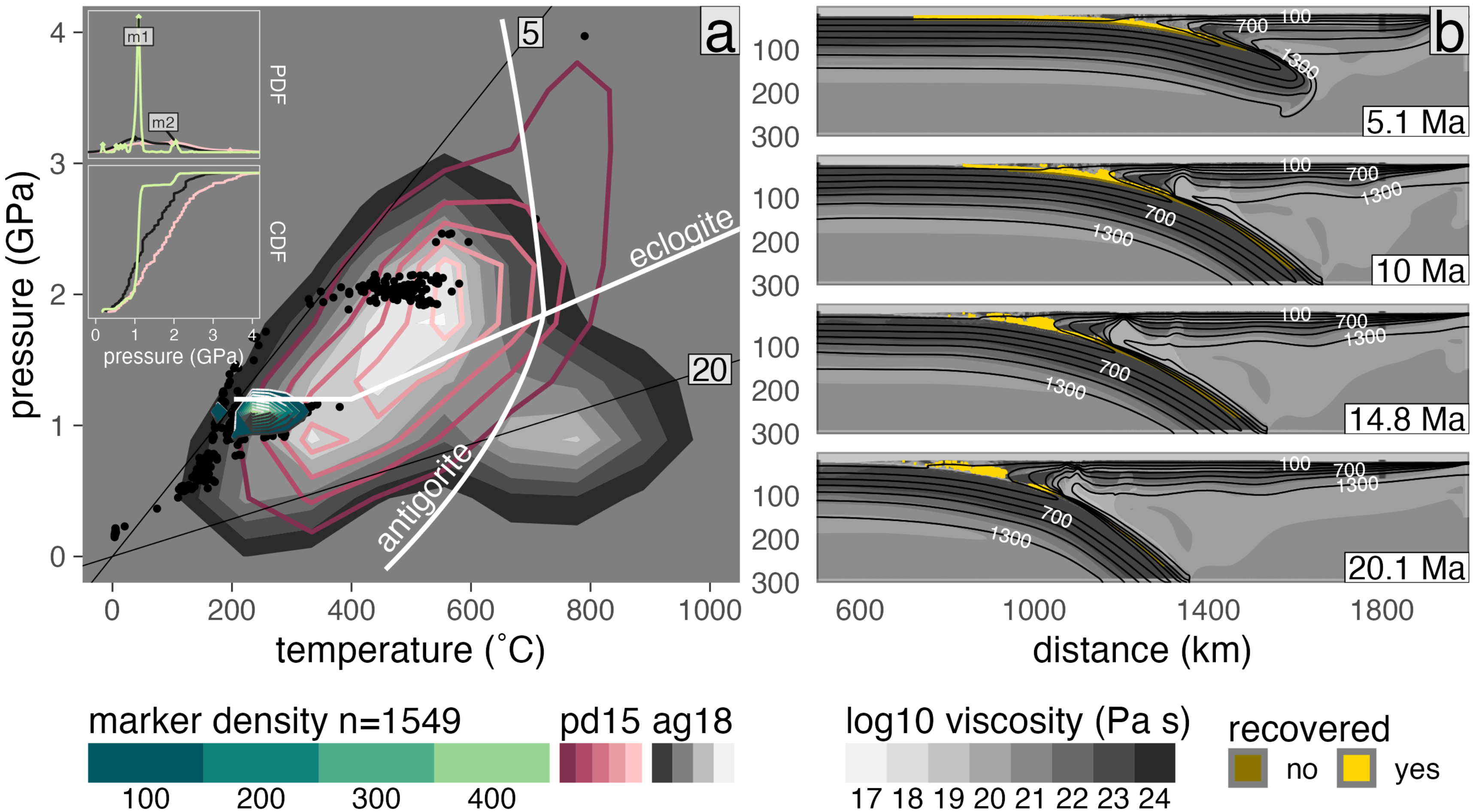

Figure S38: PT distribution of recovered markers from model cdj62. Refer to the main text for explanation of panels and colors.

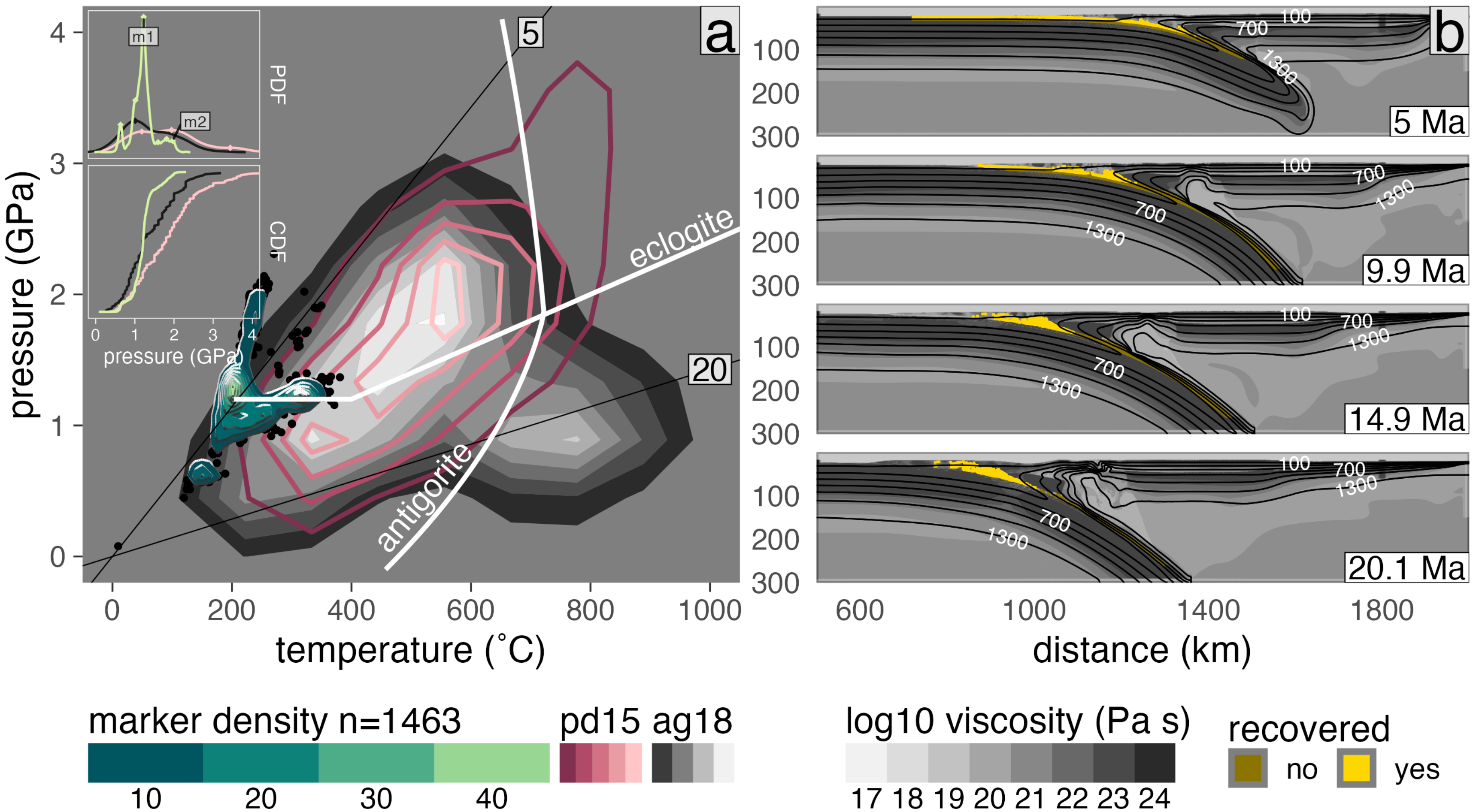

Figure S39: PT distribution of recovered markers from model cdj78. Refer to the main text for explanation of panels and colors.

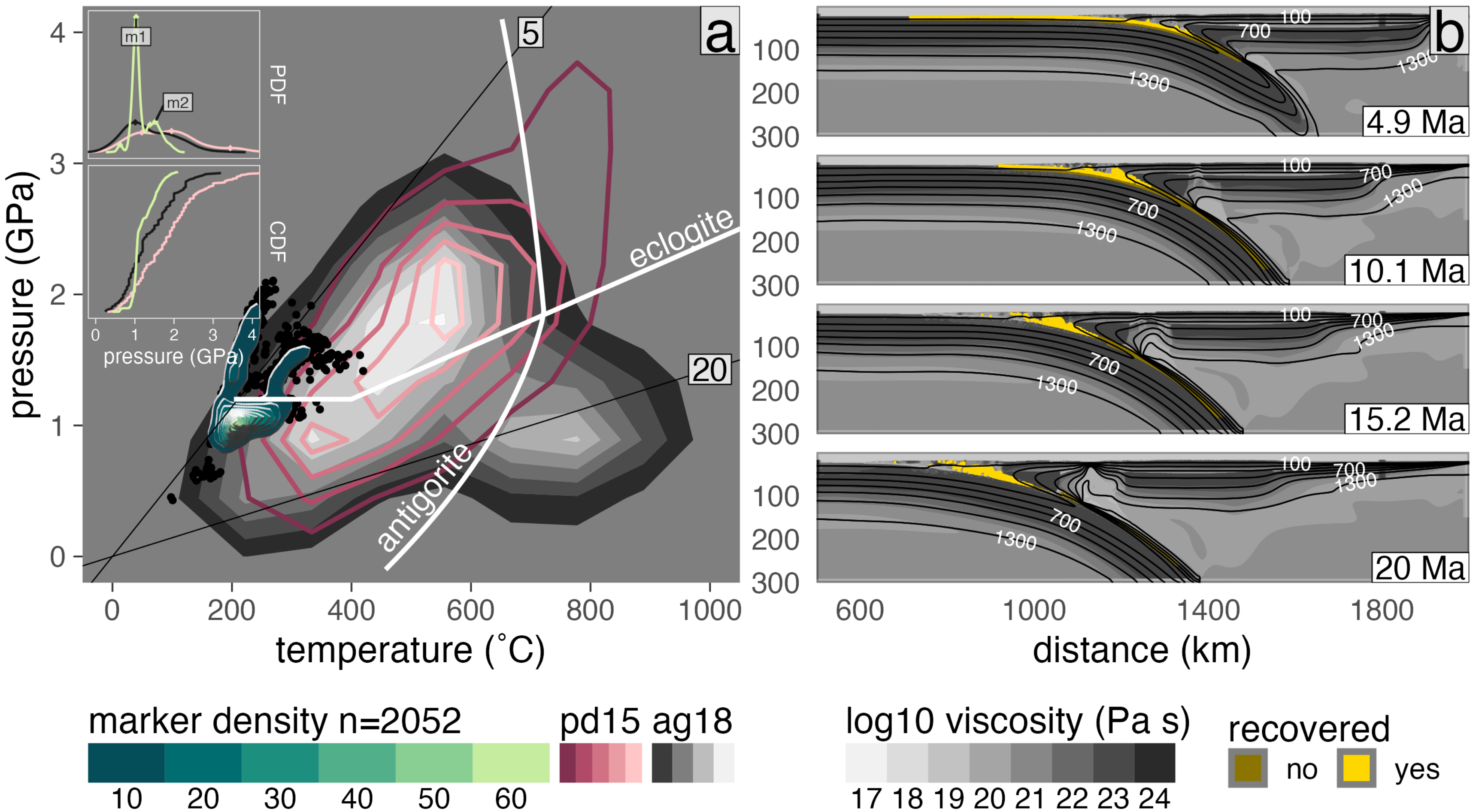

Figure S40: PT distribution of recovered markers from model cdj94. Refer to the main text for explanation of panels and colors.

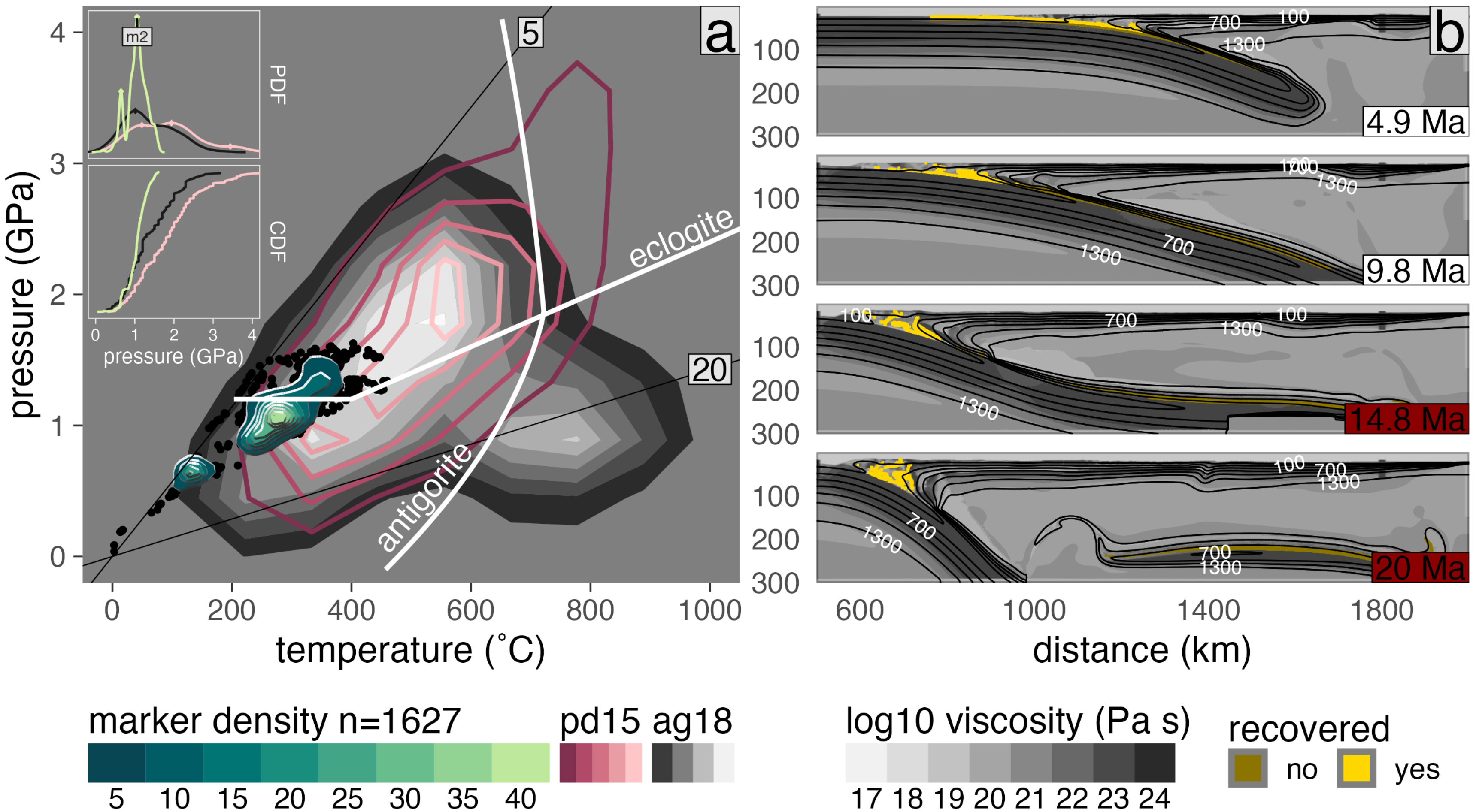

Figure S41: PT distribution of recovered markers from model cdk46. Refer to the main text for explanation of panels and colors.

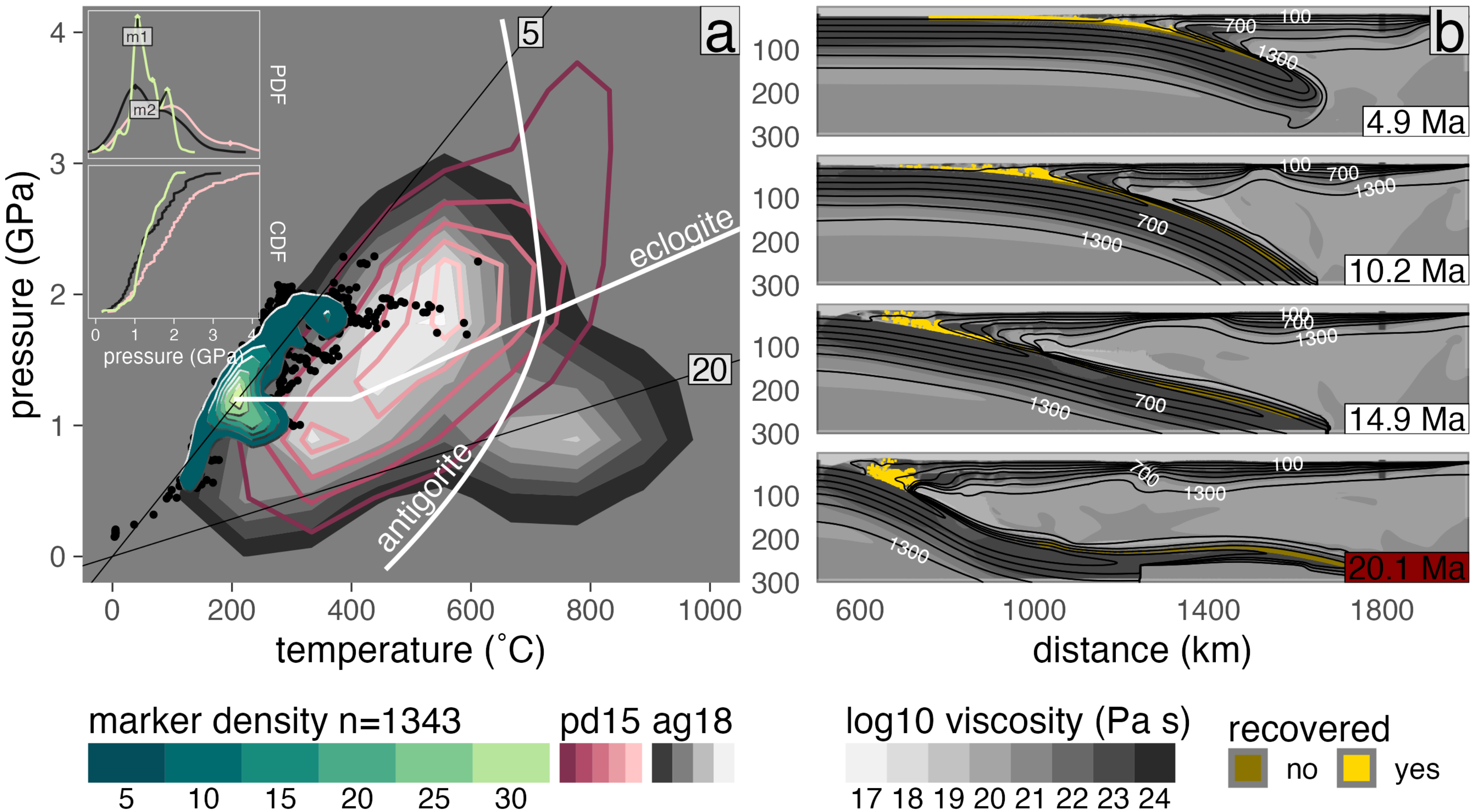

Figure S42: PT distribution of recovered markers from model cdk62. Refer to the main text for explanation of panels and colors.

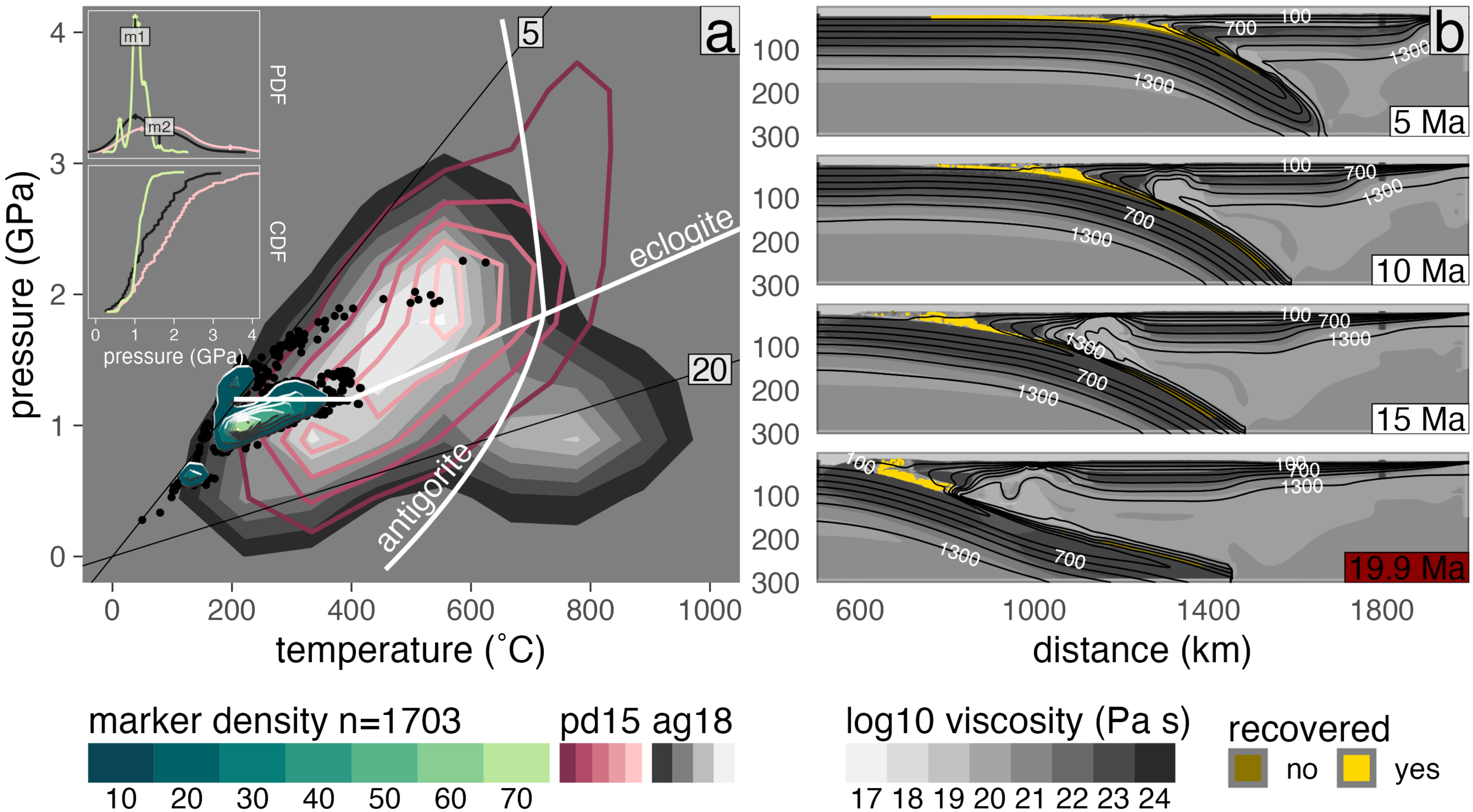

Figure S43: PT distribution of recovered markers from model cdk78. Refer to the main text for explanation of panels and colors.

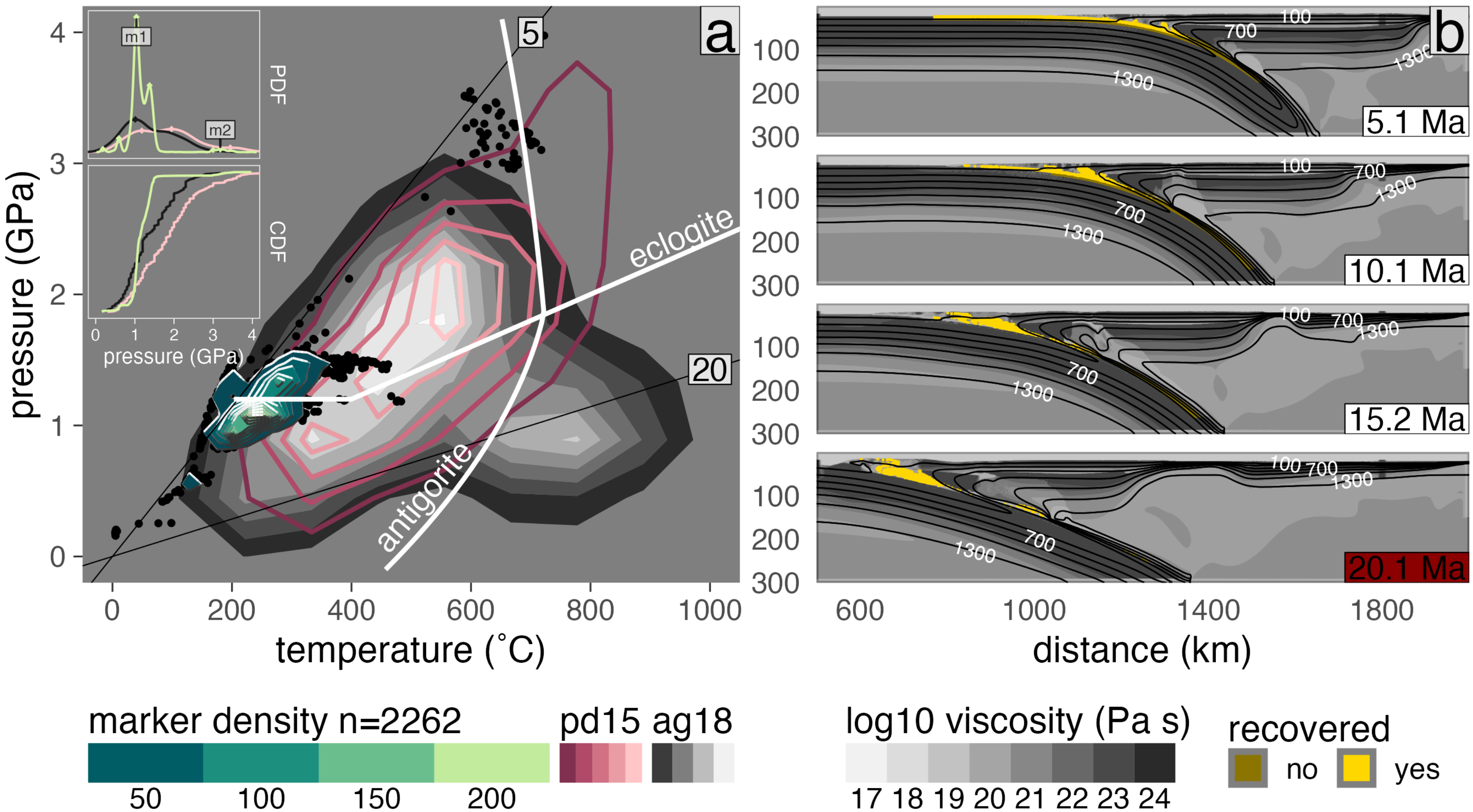

Figure S44: PT distribution of recovered markers from model cdk94. Refer to the main text for explanation of panels and colors.

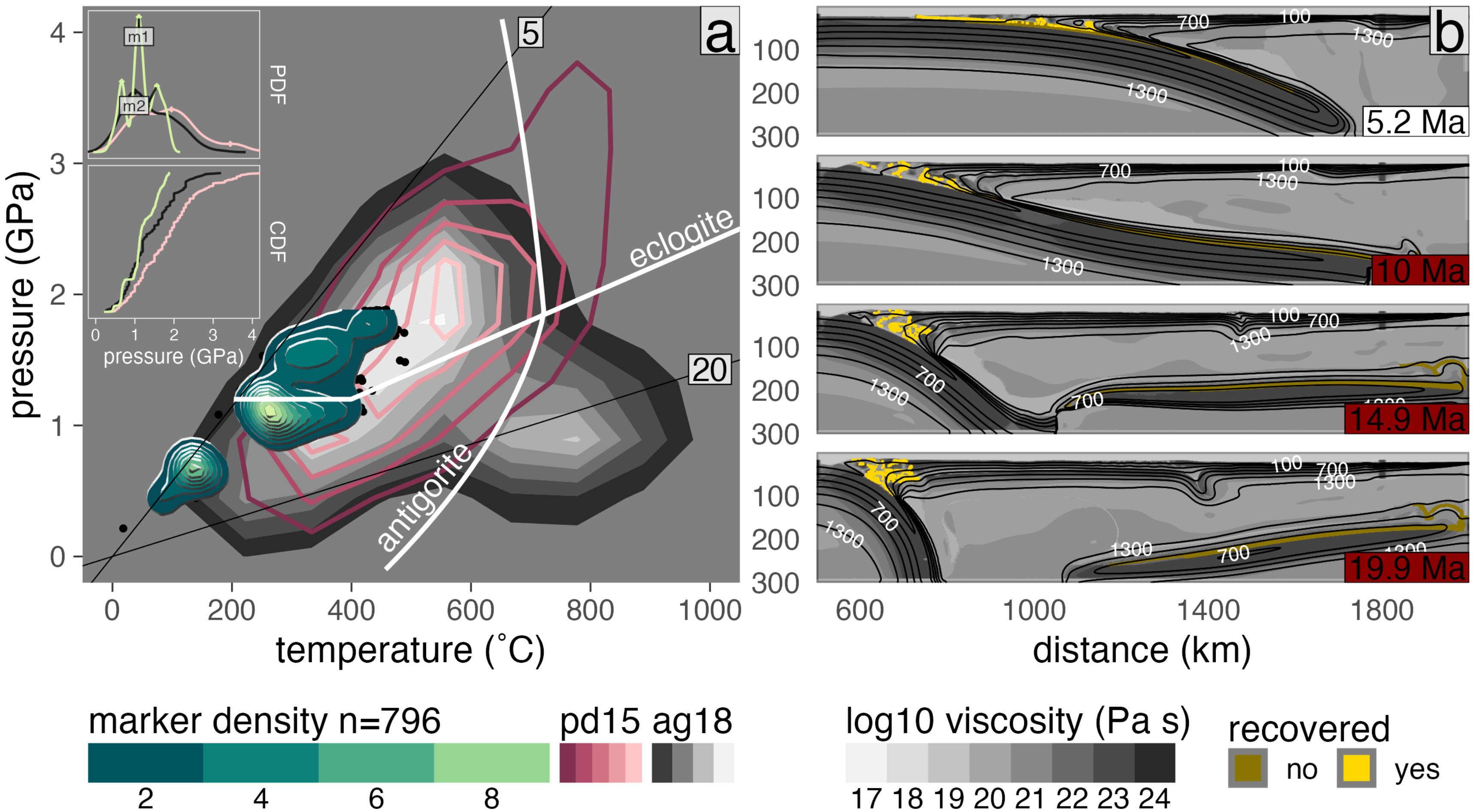

Figure S45: PT distribution of recovered markers from model cdl46. Refer to the main text for explanation of panels and colors.

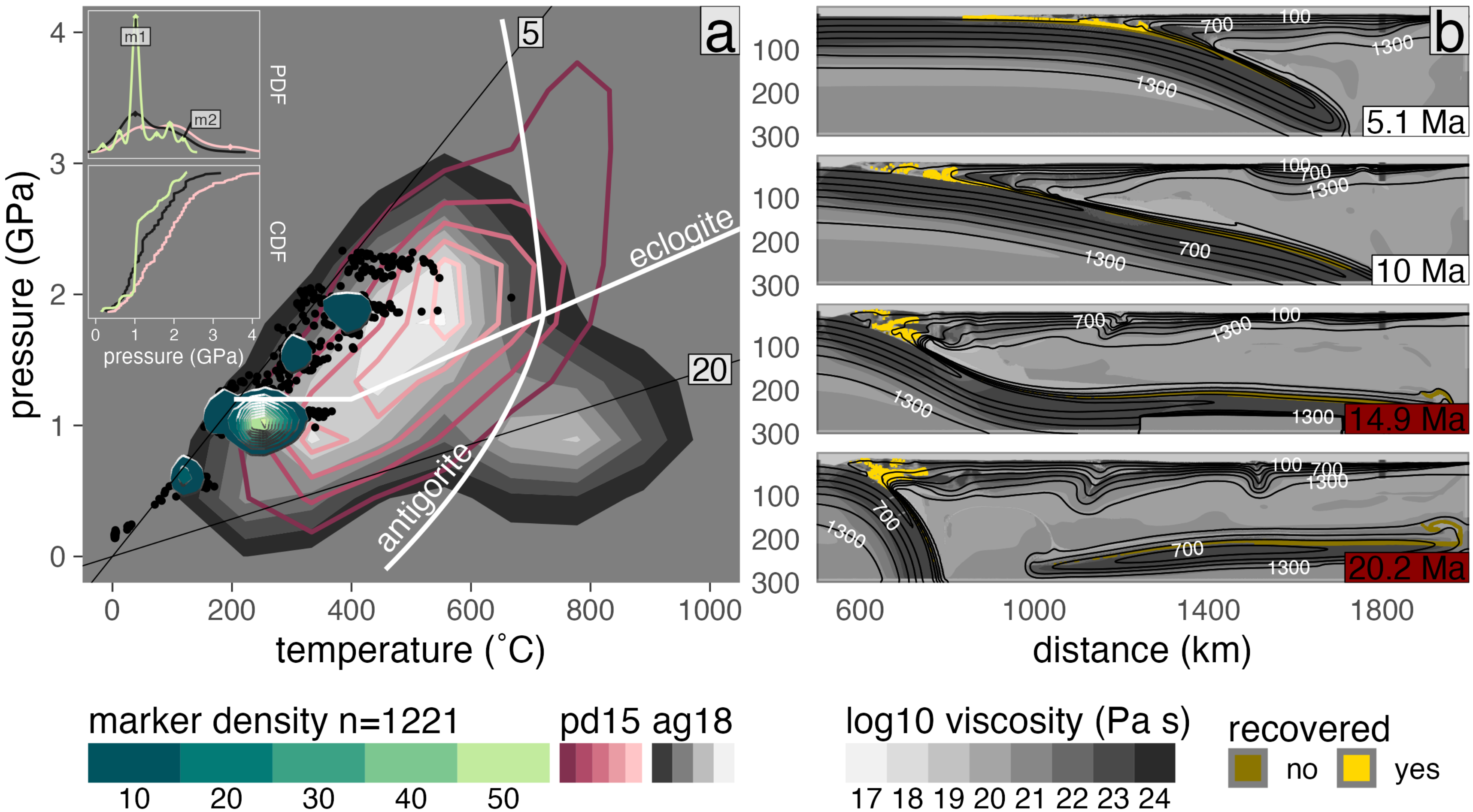

Figure S46: PT distribution of recovered markers from model cdl62. Refer to the main text for explanation of panels and colors.

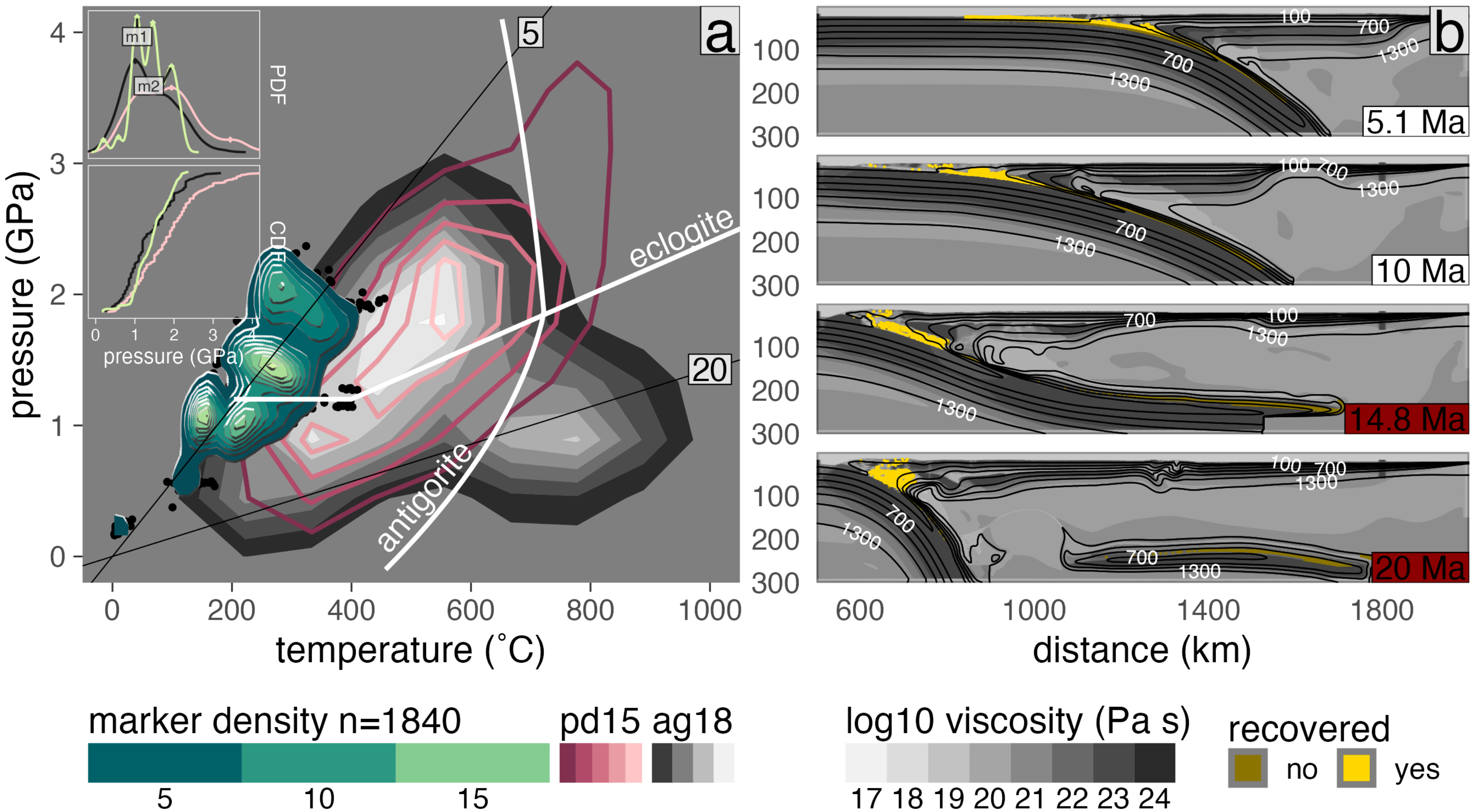

Figure S47: PT distribution of recovered markers from model cdl78. Refer to the main text for explanation of panels and colors.

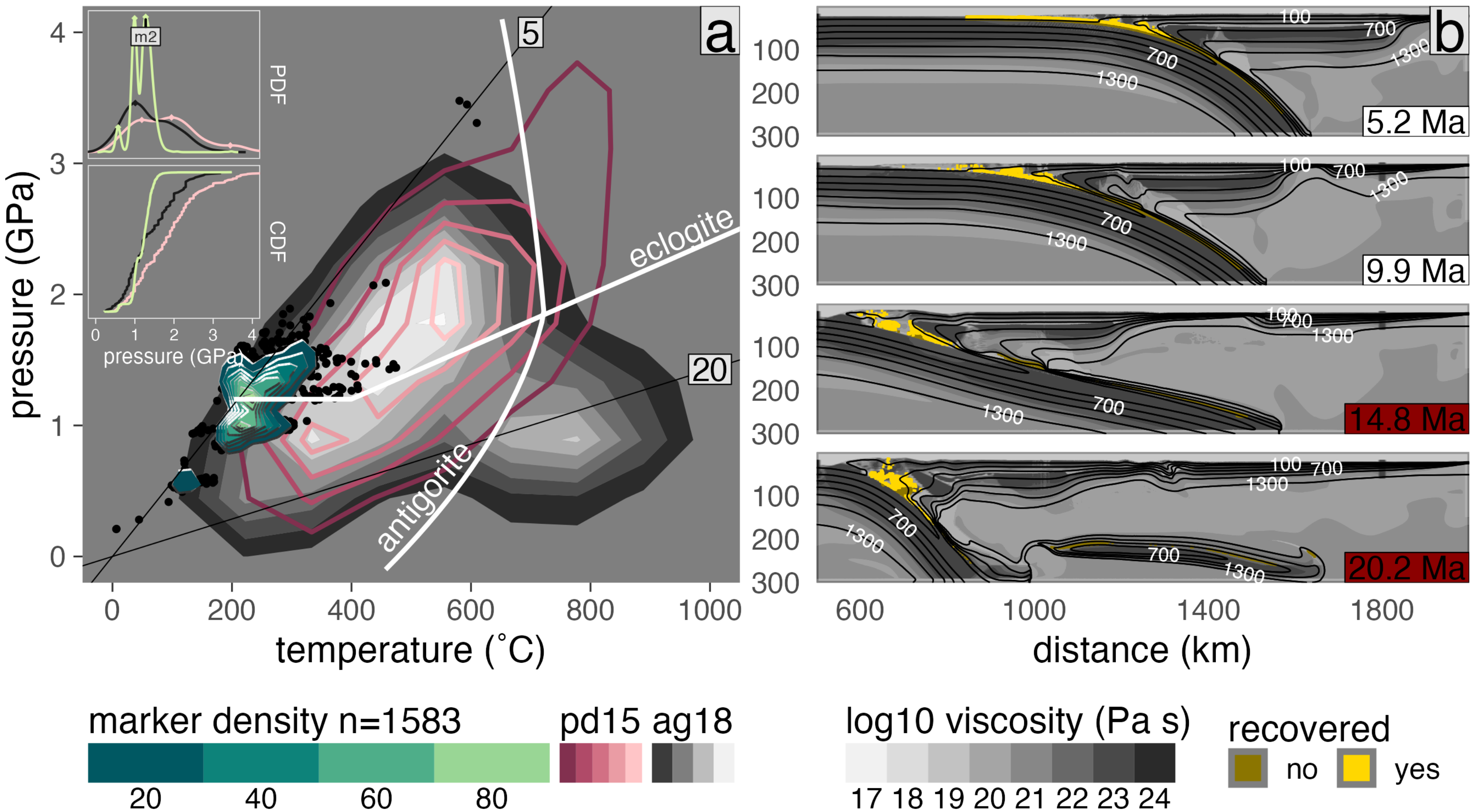

Figure S48: PT distribution of recovered markers from model cdl94. Refer to the main text for explanation of panels and colors.

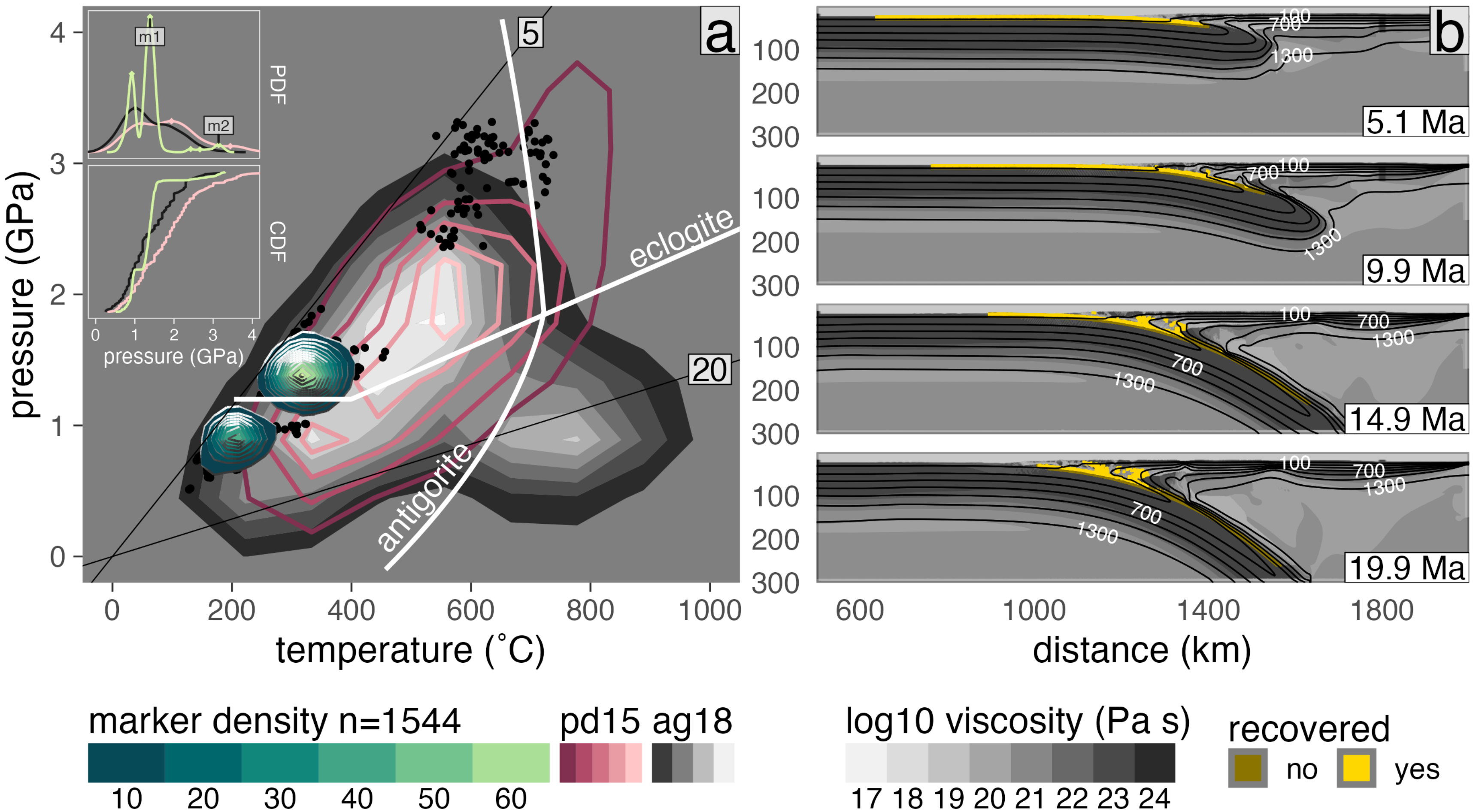

Figure S49: PT distribution of recovered markers from model cdm46. Refer to the main text for explanation of panels and colors.

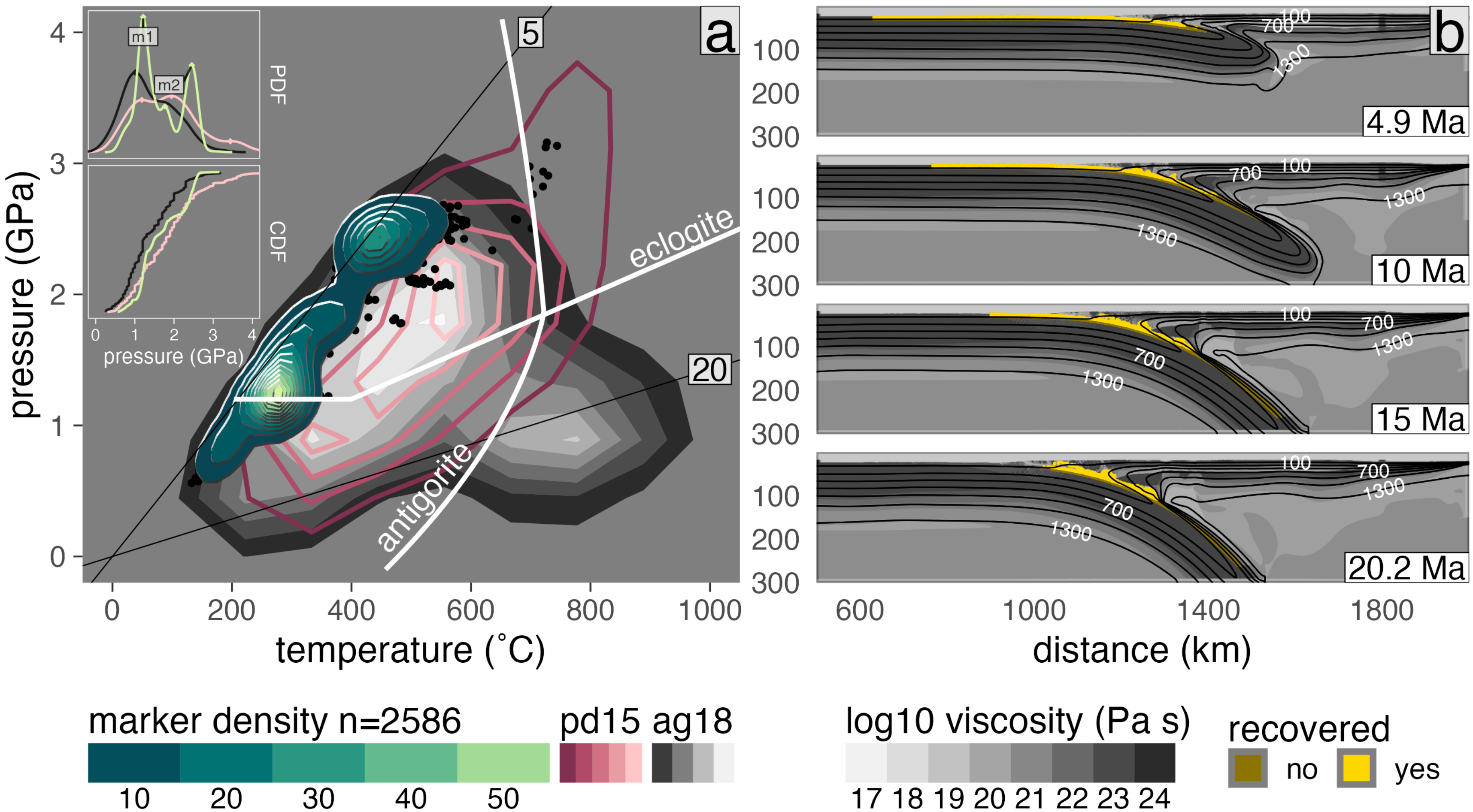

Figure S50: PT distribution of recovered markers from model cdm62. Refer to the main text for explanation of panels and colors.

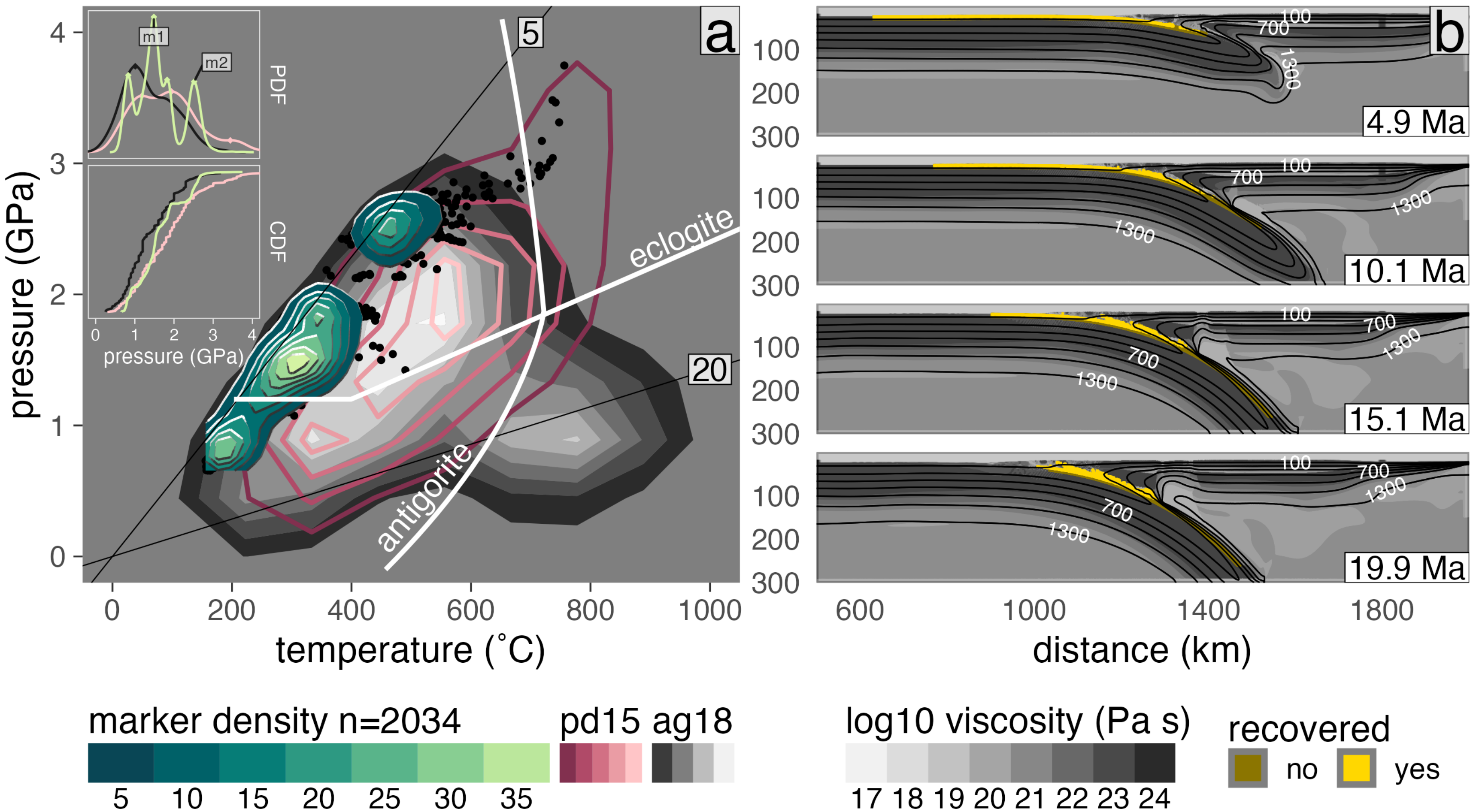

Figure S51: PT distribution of recovered markers from model cdm78. Refer to the main text for explanation of panels and colors.

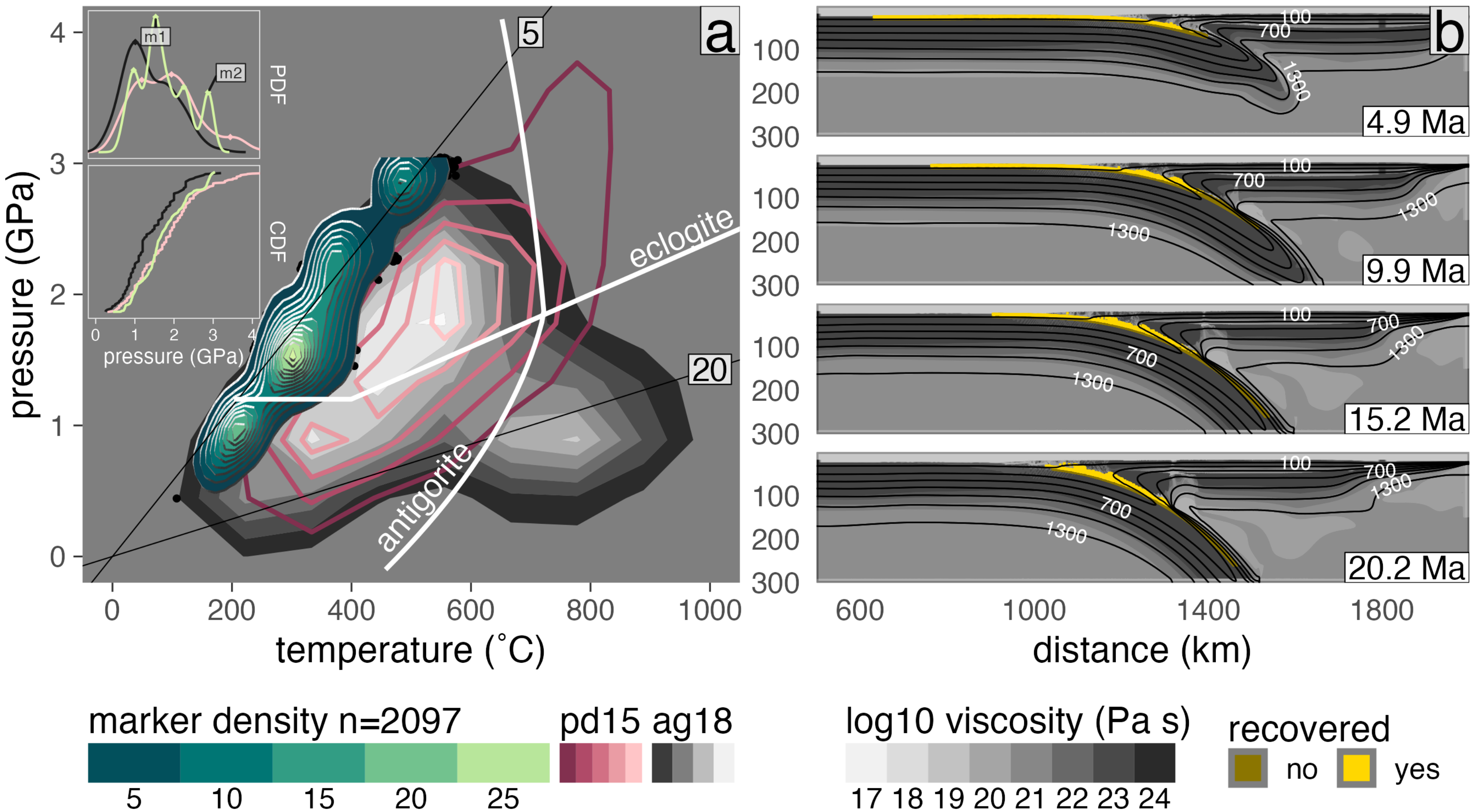

Figure S52: PT distribution of recovered markers from model cdm94. Refer to the main text for explanation of panels and colors.

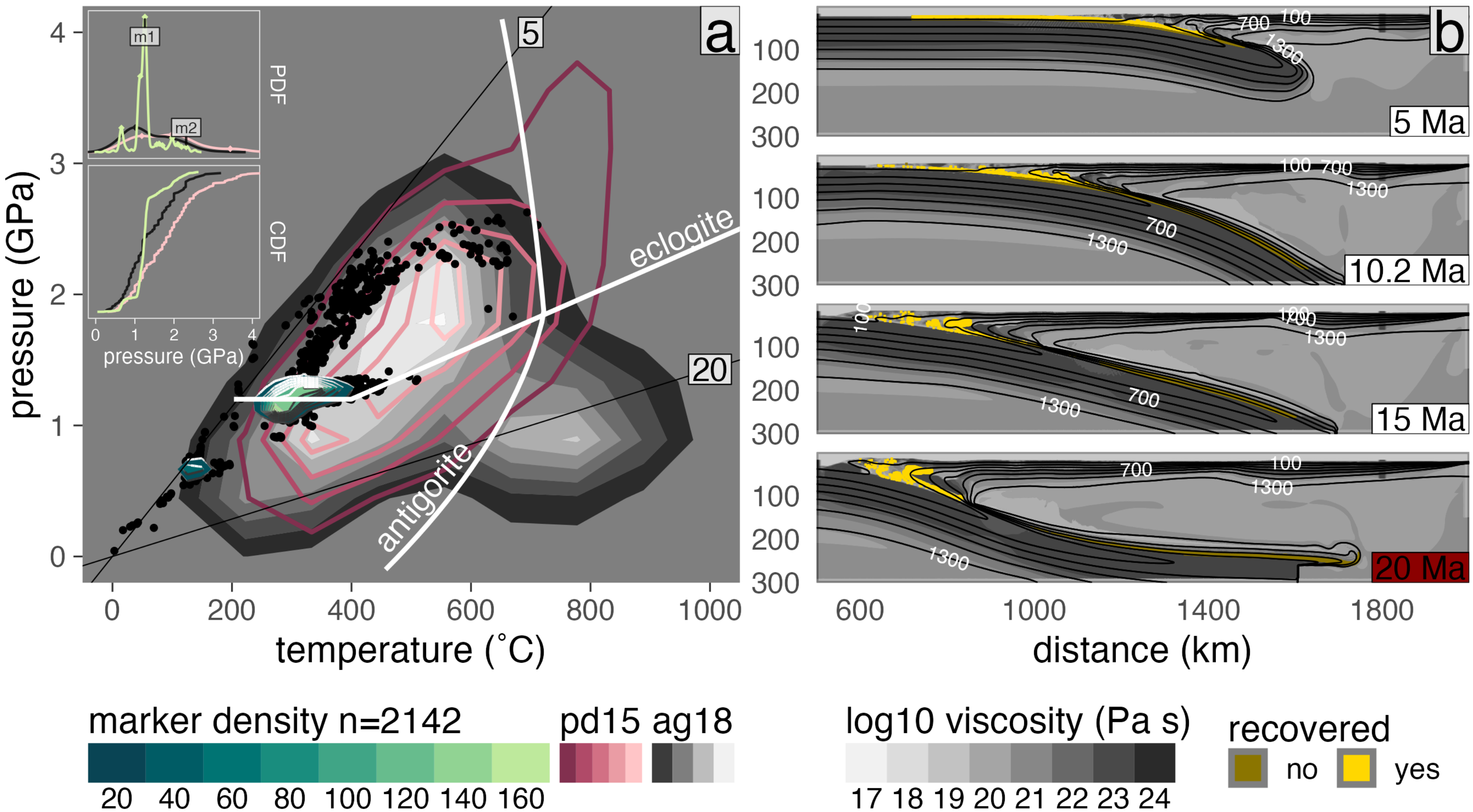

Figure S53: PT distribution of recovered markers from model cdn46. Refer to the main text for explanation of panels and colors.

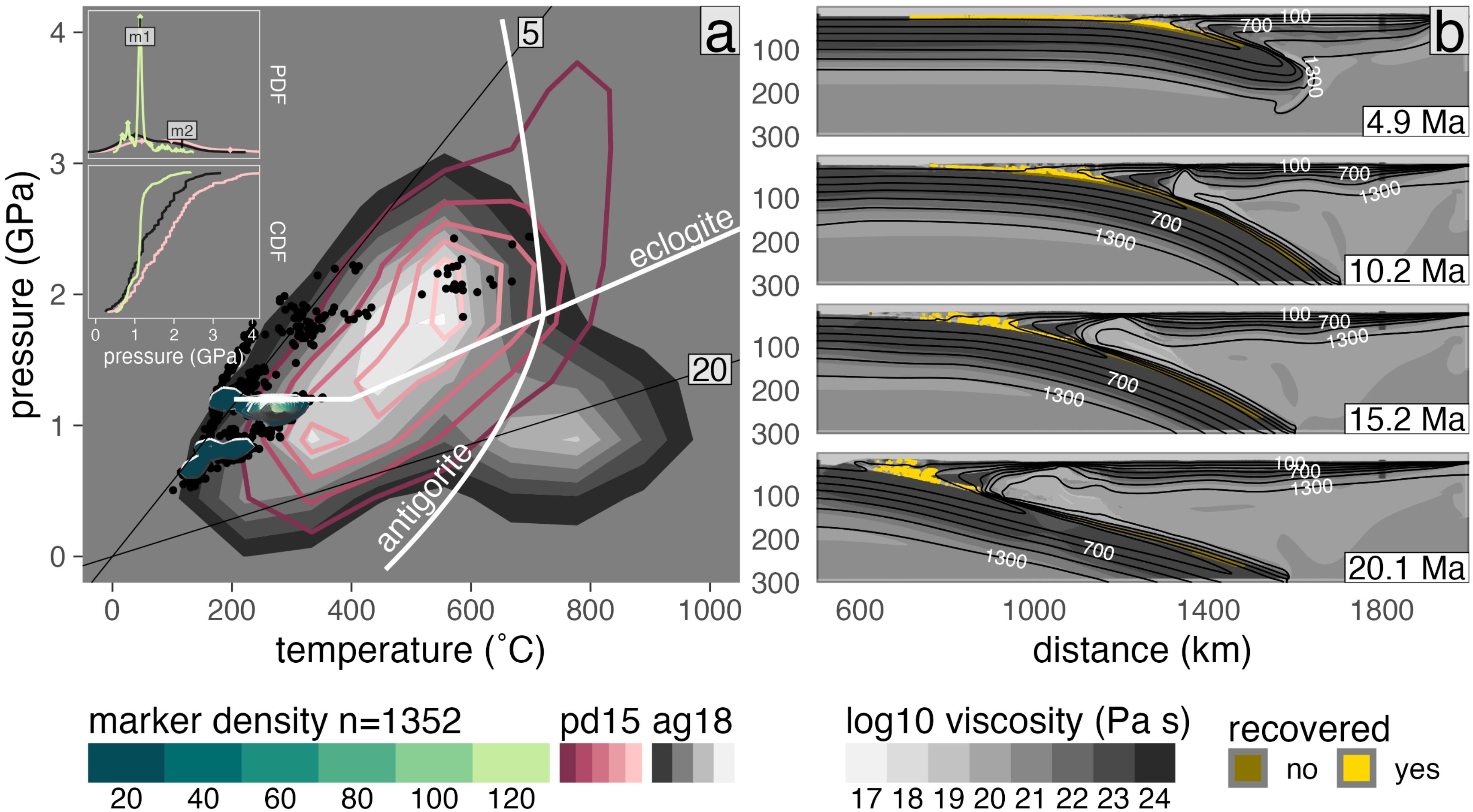

Figure S54: PT distribution of recovered markers from model cdn62. Refer to the main text for explanation of panels and colors.

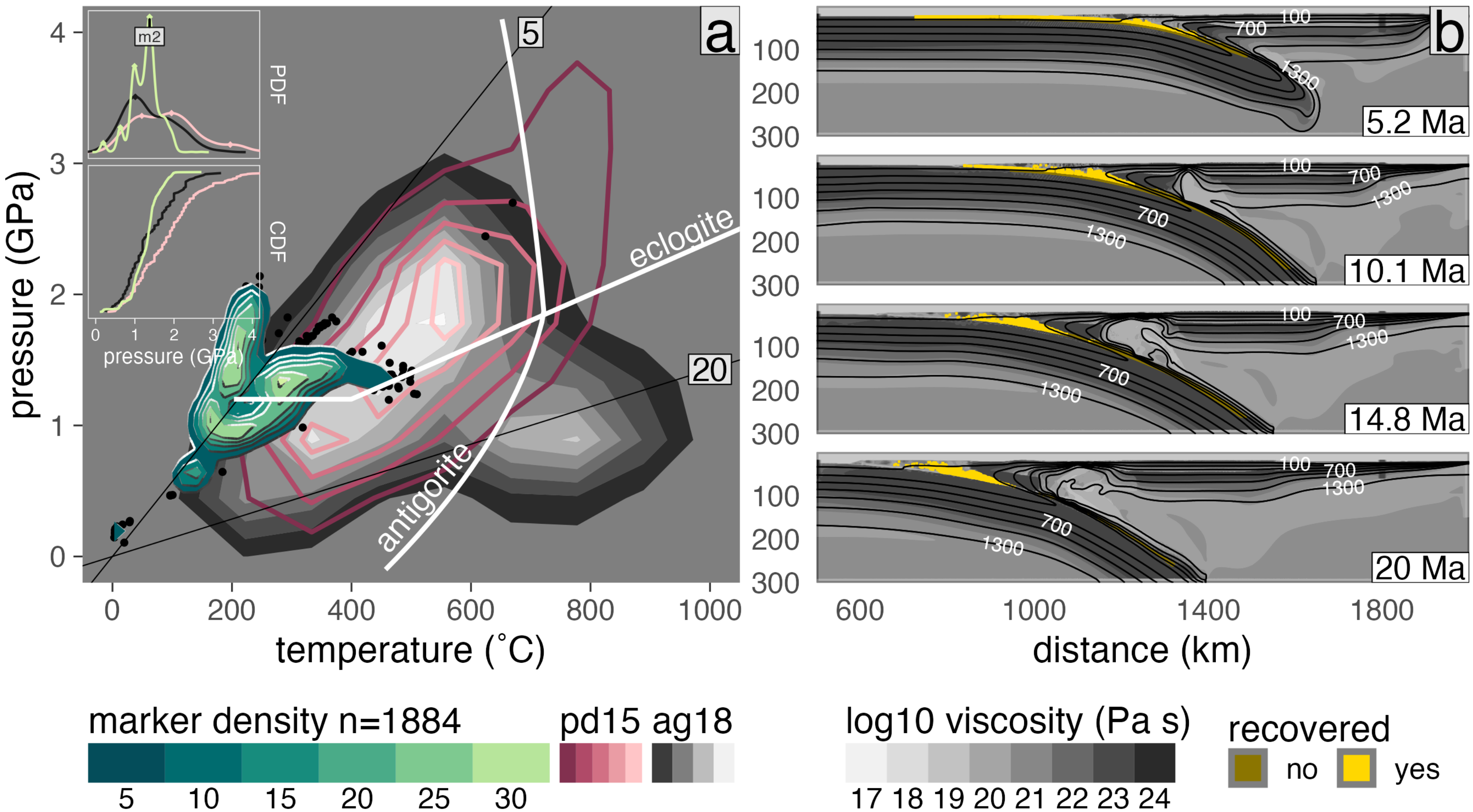

Figure S55: PT distribution of recovered markers from model cdn78. Refer to the main text for explanation of panels and colors.

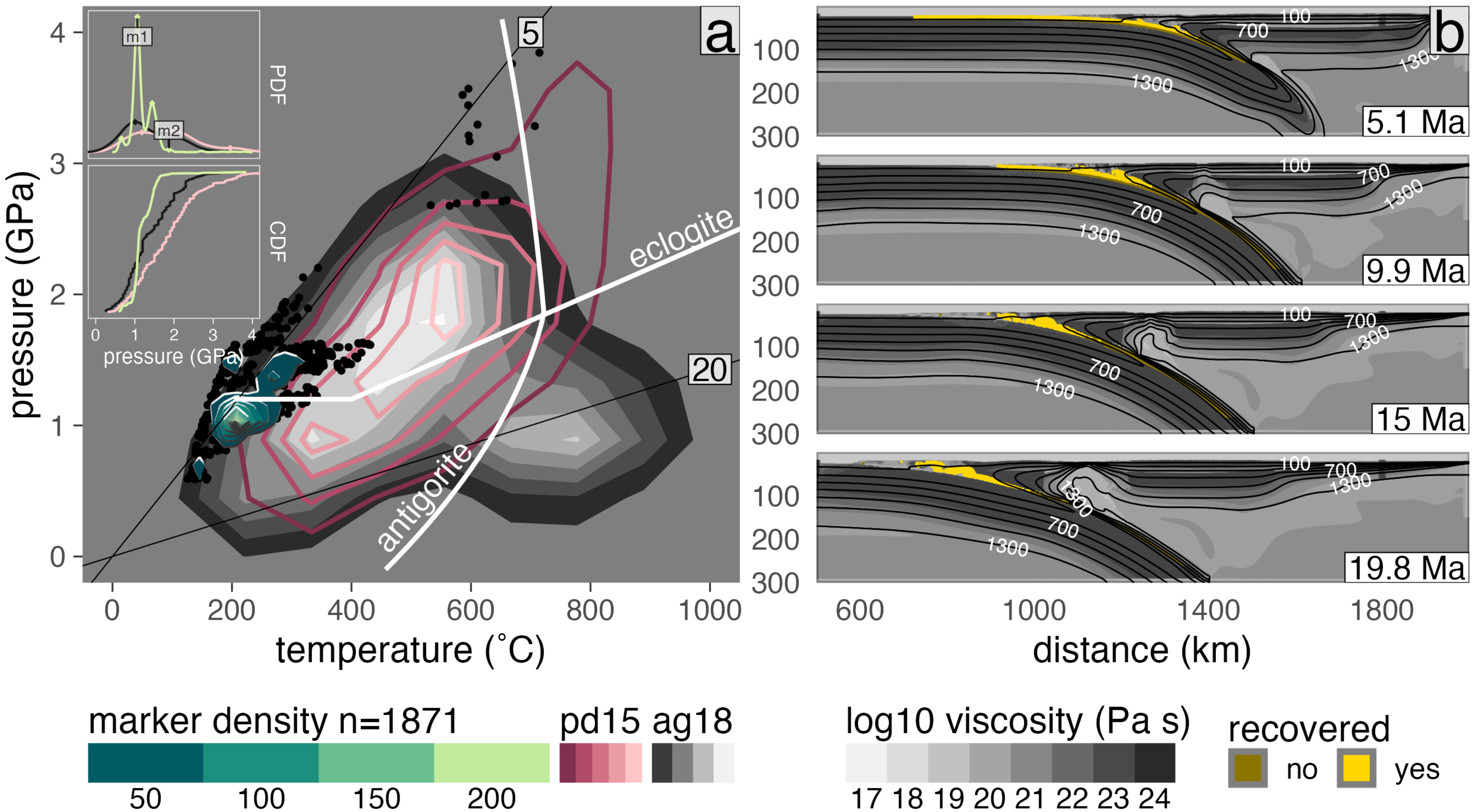

Figure S56: PT distribution of recovered markers from model cdn94. Refer to the main text for explanation of panels and colors.

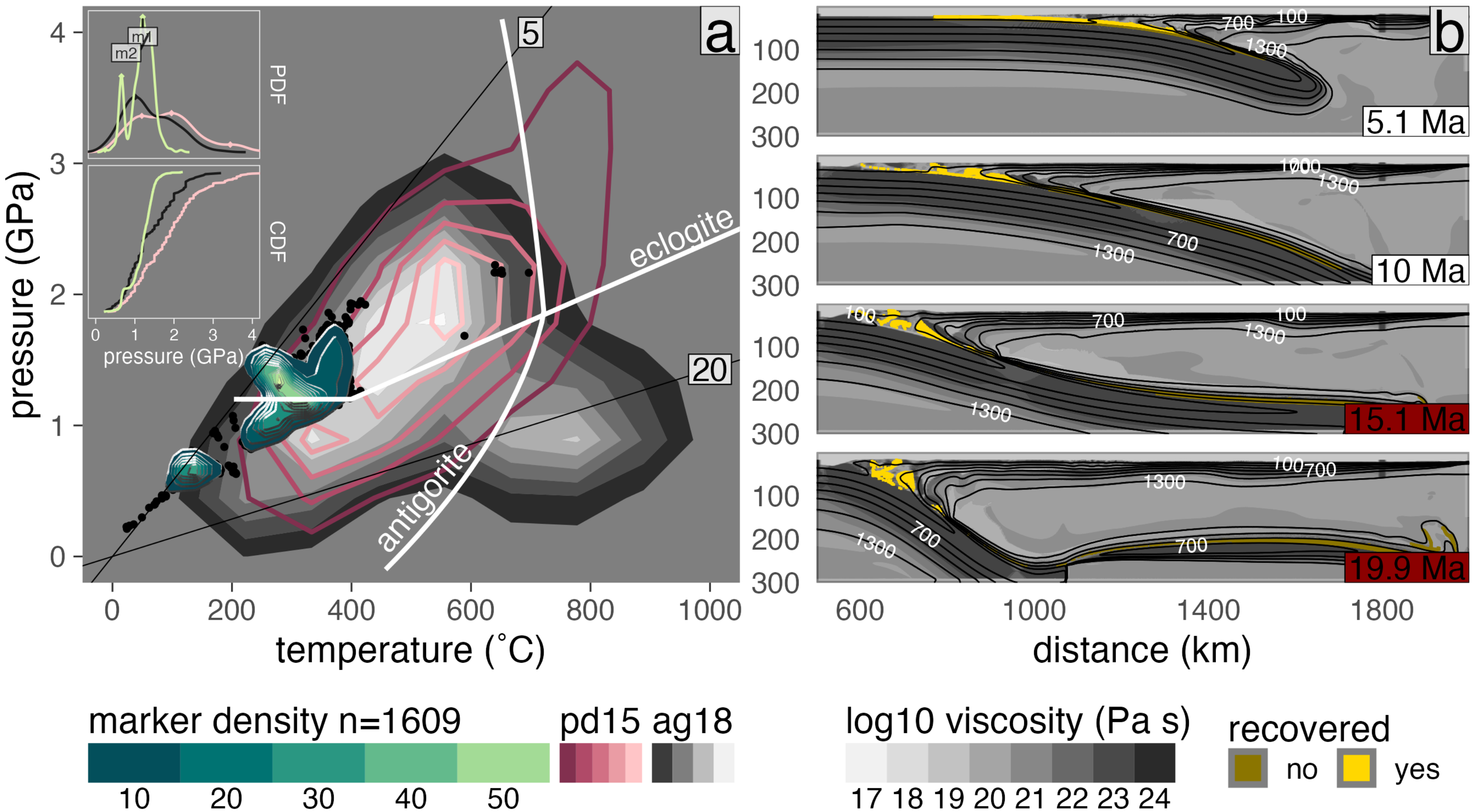

Figure S57: PT distribution of recovered markers from model cdo46. Refer to the main text for explanation of panels and colors.

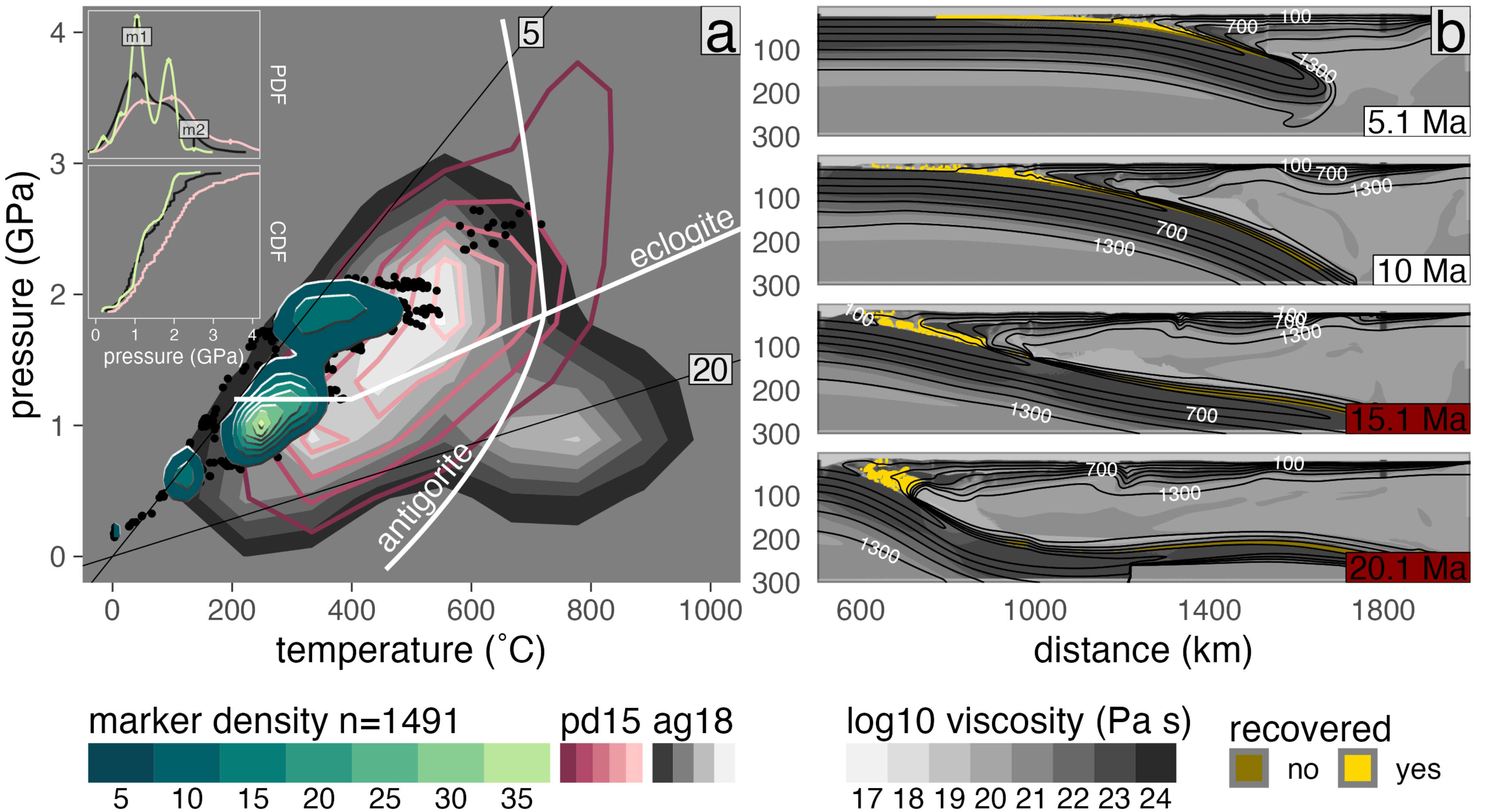

Figure S58: PT distribution of recovered markers from model cdo62. Refer to the main text for explanation of panels and colors.

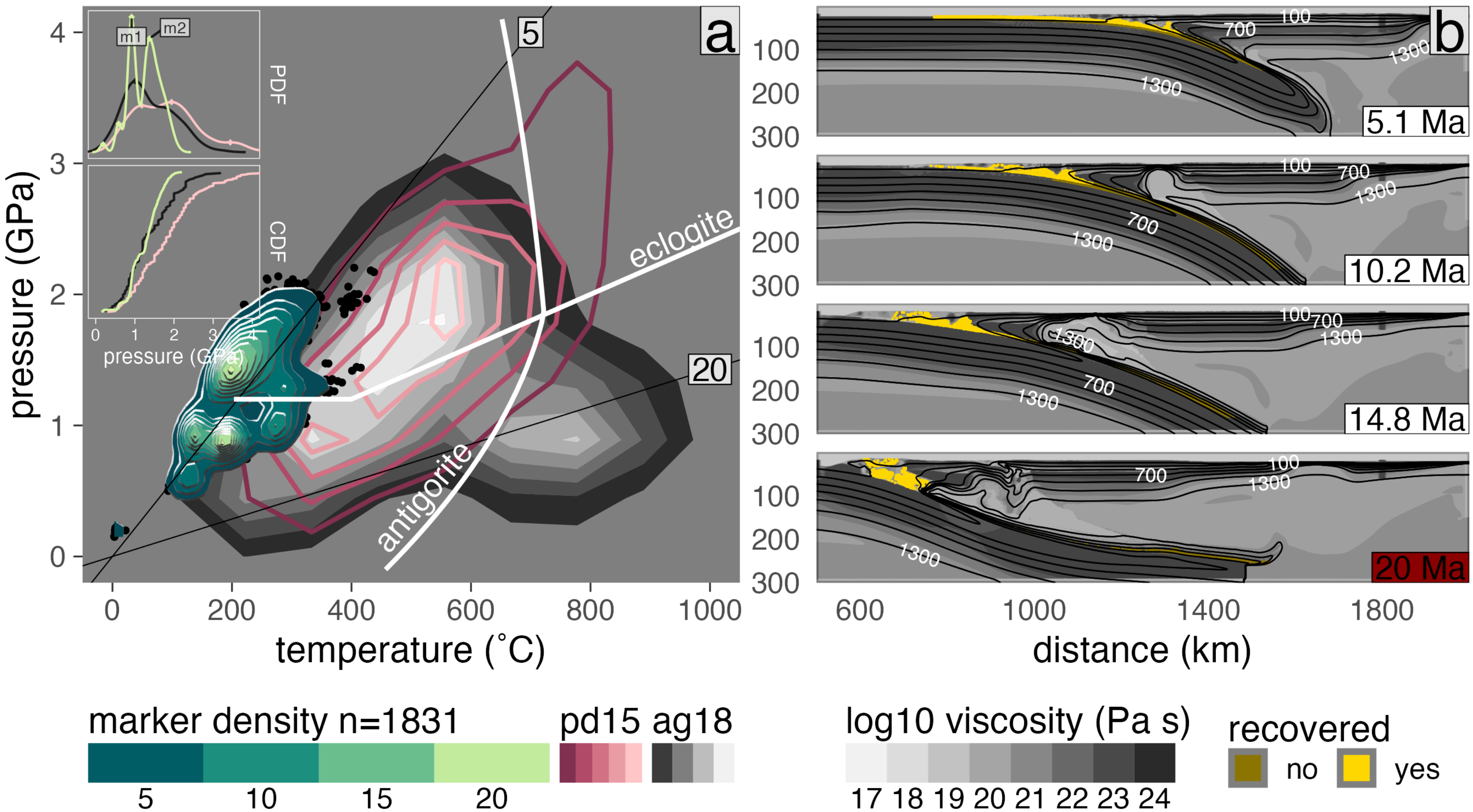

Figure S59: PT distribution of recovered markers from model cdo78. Refer to the main text for explanation of panels and colors.

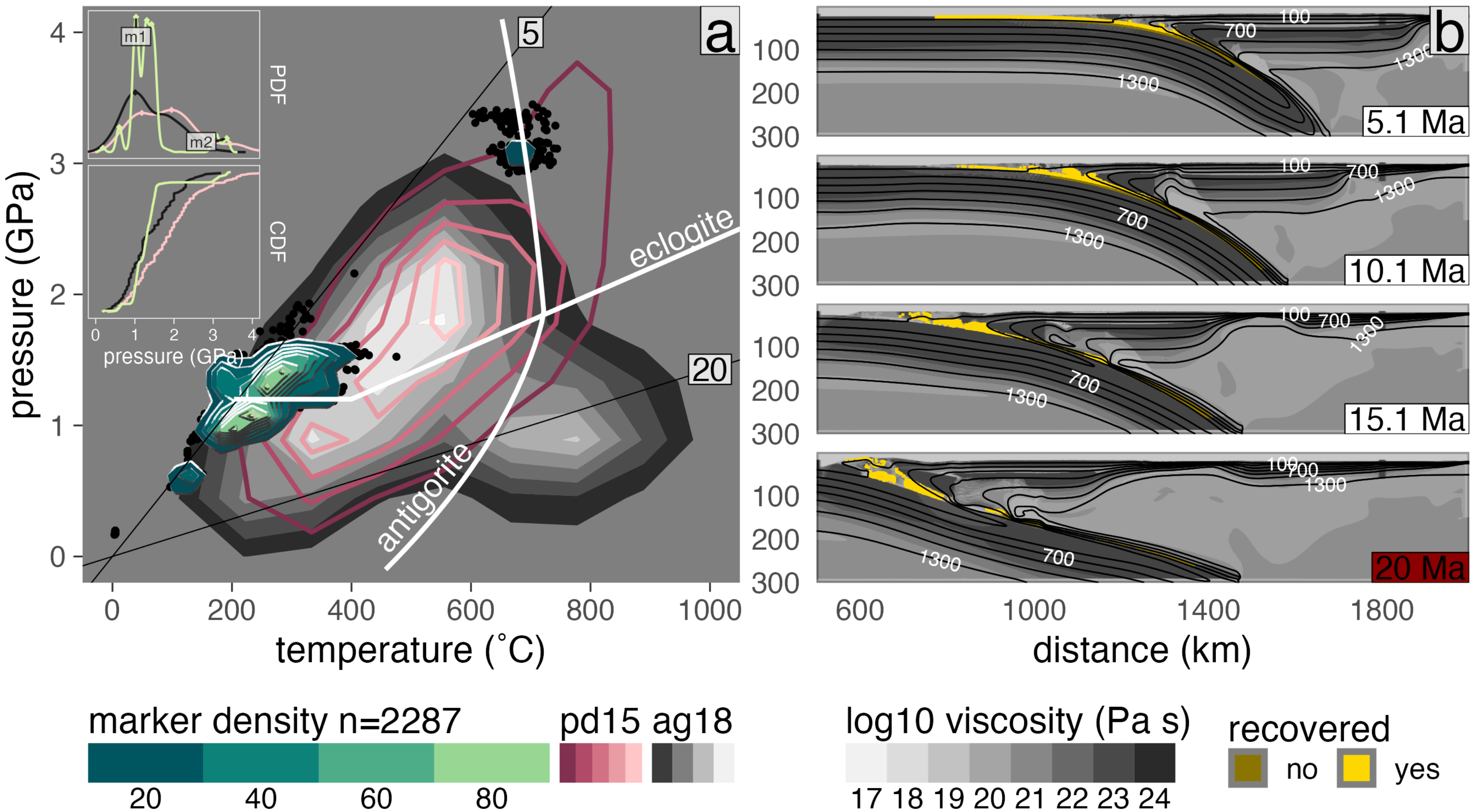

Figure S60: PT distribution of recovered markers from model cdo94. Refer to the main text for explanation of panels and colors.

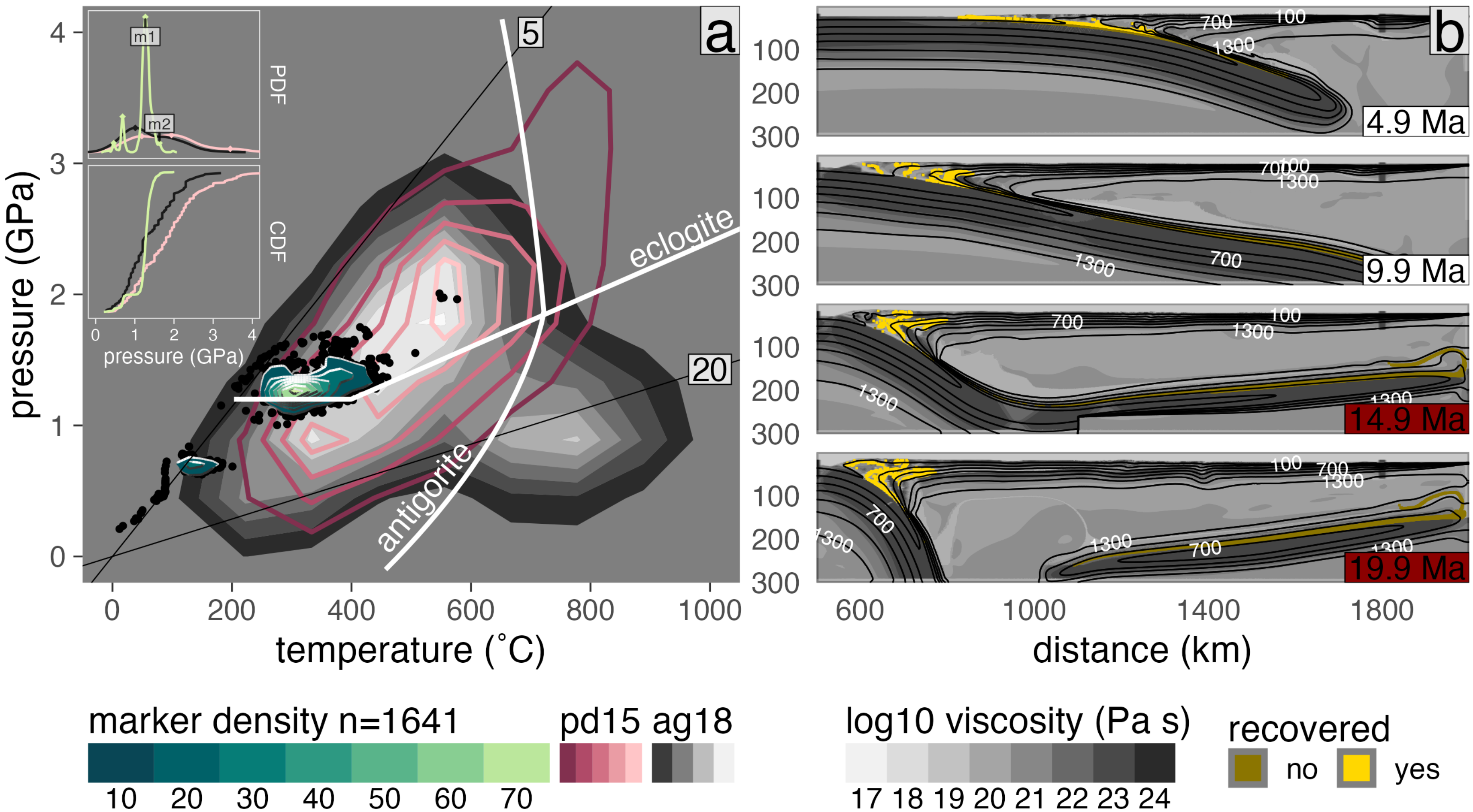

Figure S61: PT distribution of recovered markers from model cdp46. Refer to the main text for explanation of panels and colors.

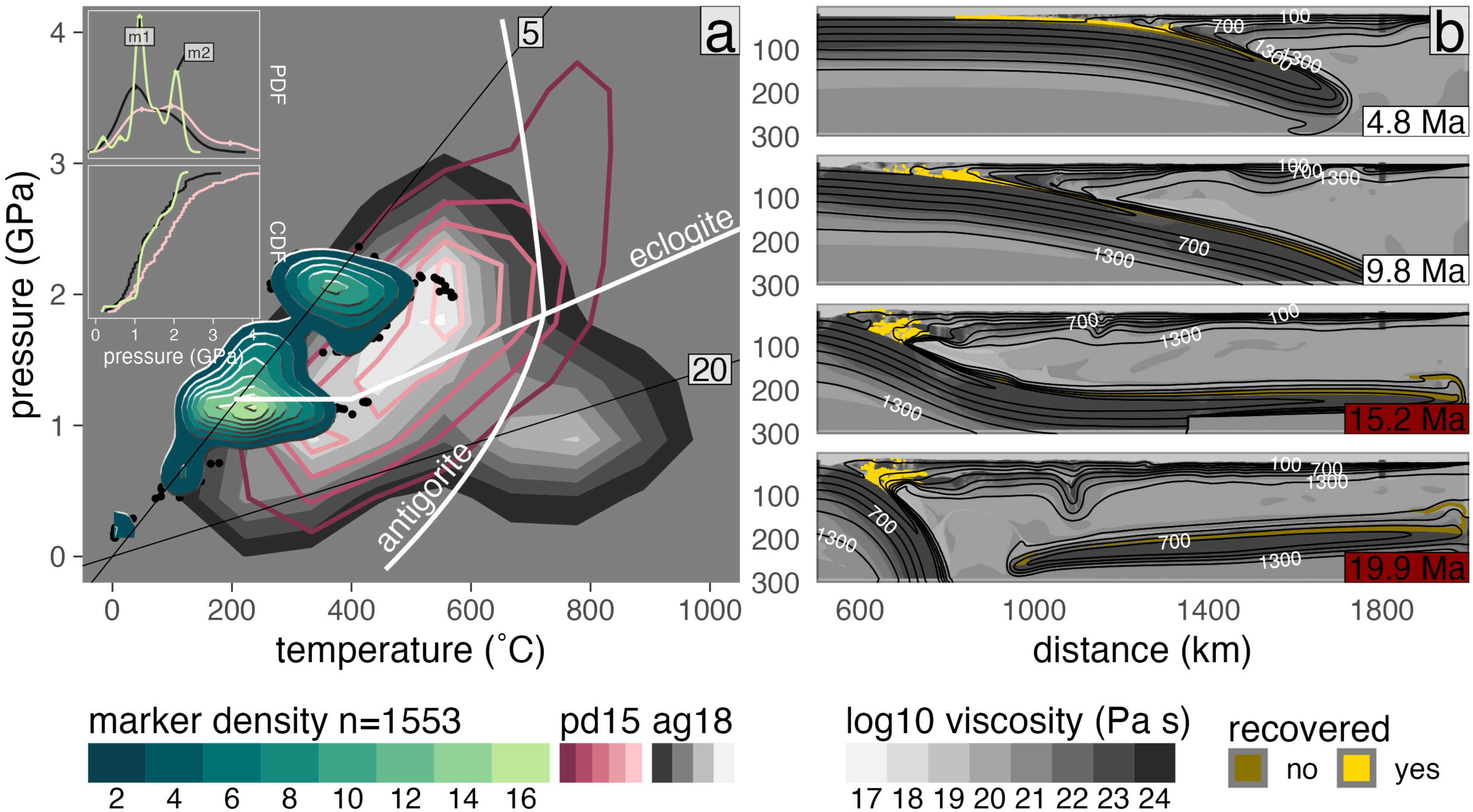

Figure S62: PT distribution of recovered markers from model cdp62. Refer to the main text for explanation of panels and colors.

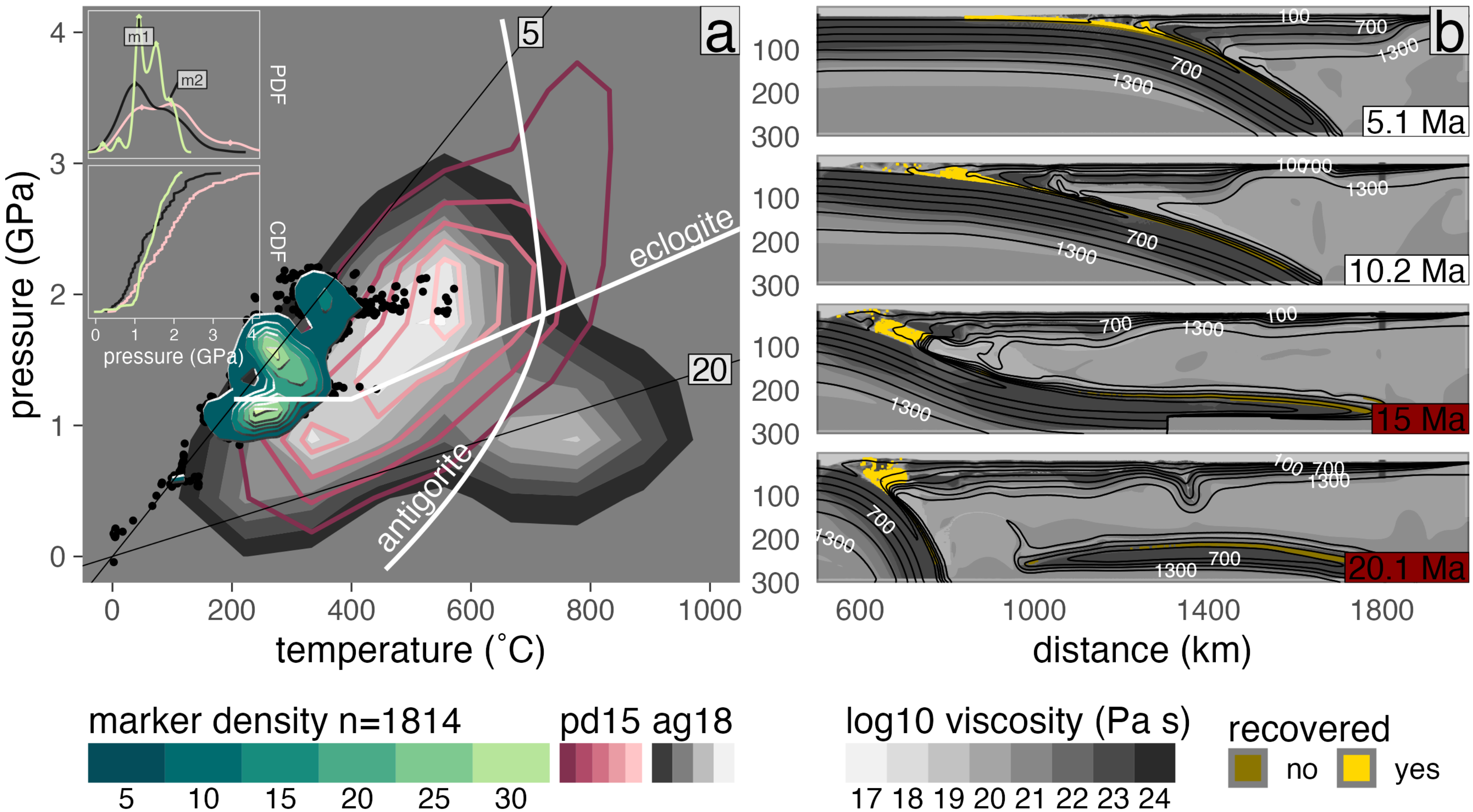

Figure S63: PT distribution of recovered markers from model cdp78. Refer to the main text for explanation of panels and colors.

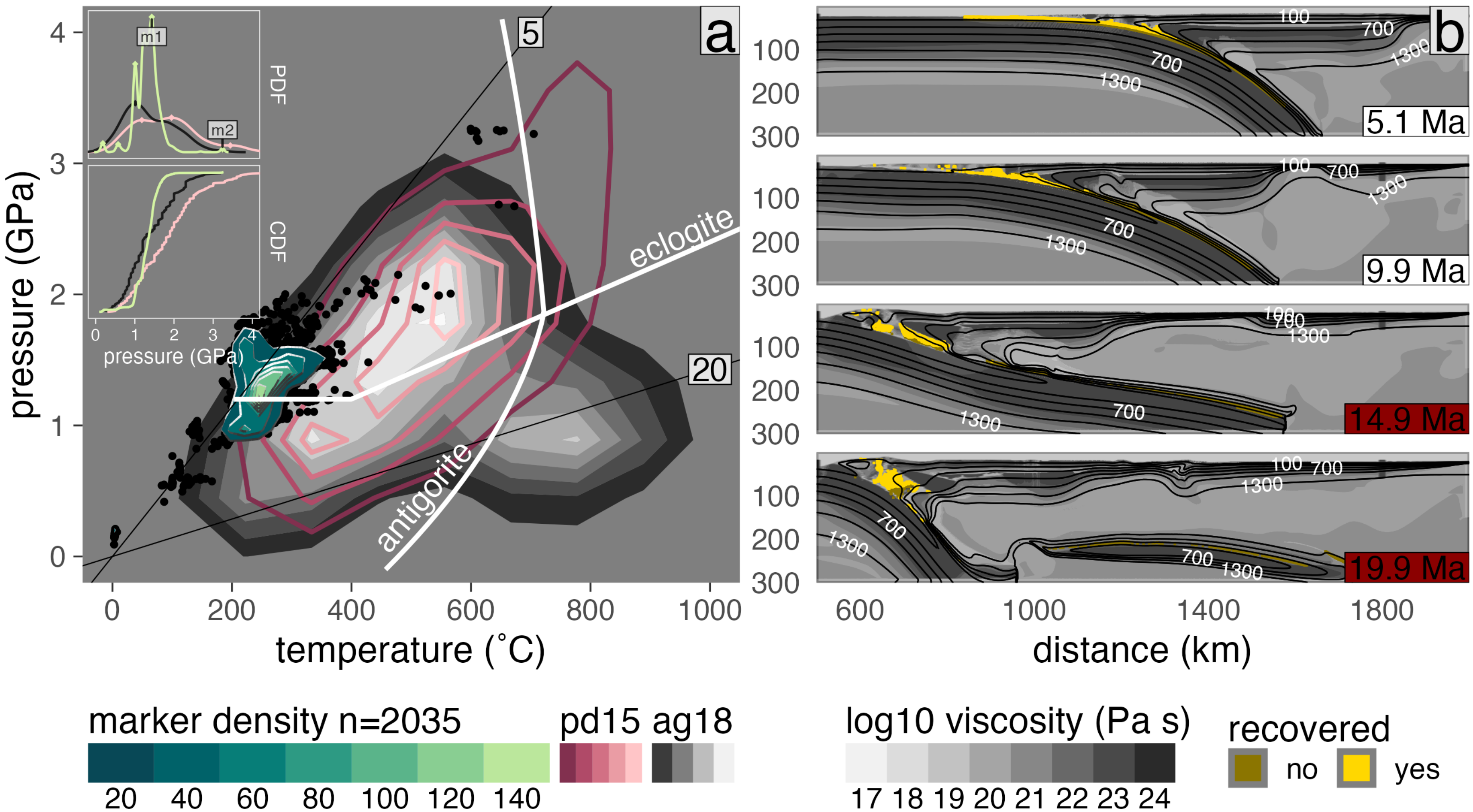

Figure S64: PT distribution of recovered markers from model cdp94. Refer to the main text for explanation of panels and colors.